APPLIED COMPUTATIONAL ELECTROMAGNETICS SOCIETY JOURNAL

June 2018
Vol. 33 No. 6
ISSN 1054-4887

The ACES Journal is abstracted in INSPEC, in Engineering Index, DTIC, Science Citation Index Expanded, the Research Alert, and to Current Contents/Engineering, Computing & Technology.

The illustrations on the front cover have been obtained from the research groups at the Department of Electrical Engineering, The University of Mississippi.

EMERITUS ASSOCIATE EDITORS-IN-CHIEF

EMERITUS EDITORIAL ASSISTANTS

JUNE 2018 REVIEWERS: REGULAR PAPERS

Rusan Barik
Adalbert Beyer
Hai-tao Chen
Xibi Chen
Zhe Chen
Klaus Debes
Qian Ding
Nebojsa Doncov
Zhenhong Fan
Zhengwei Hao
Ahmad Hosseinbeig
Lijun Jiang
Zhaoneng Jiang
Bin Li
Gaosheng Li
Haihui Li
Jian Li
Teng Li
Xin Li
Miaomiao Ma
Peyman Mahouti
Mahdi NaghshvarianJahromi
Arash Nemati
Mohammad Neshati
Jagdishkumar Rathod
Blaise Ravelo
Kubilay Sertel
Yury Shestopalov
Yan Shi
Bruno Stupfel
Christopher Trueman
Hubert Trzaska
Zuo-Min Tsai
Zhonggen Wang
Li Wu
Jinpeng Yang
Ali Yapar
Huan Zhang

JUNE 2018 REVIEWERS: EXPRESS PAPERS

Maokun Li
Ladislau Matekovits
Gregory Mitchell
Quang Nguyen
Edward Rothwell
Zvonimir Sipus
Steven Weiss

THE APPLIED COMPUTATIONAL ELECTROMAGNETICS SOCIETY JOURNAL

Vol. 33 No. 6 June 2018

TABLE OF CONTENTS – REGULAR PAPERS

TABLE OF CONTENTS – EXPRESS PAPERS

Extrema of Two-Port Network Transducer Power Gain and Voltage Gain Under Varying Port Terminations: Semi-Analytical Method and Application to Biotelemetry System

Toni Björninen

BioMediTech Institute and Faculty of Biomedical Sciences and Engineering
Tampere University of Technology, Tampere, 33101, Finland
toni.bjorninen@tut.fi

Abstract ─ Analysis of the structure of the level sets of transducer power gain and voltage gain of a two-port network enables a semi-analytical method for finding the extrema these performance indicators as the port terminations vary in bounded rectangles in the complex plane. In particular, we show that the extrema are necessarily attained in small-dimensional subsets of the given rectangles. This provides efficient means to assess the impact of variability in the port terminations numerically. As an example, we study how variability in the port terminations affects the performance of a biotelemetry system composed of magnetically coupled small loops with highly sensitive impedance matching properties.

Index Terms ─ Sensitivity analysis, tolerance analysis, transducer power gain, two-port networks, voltage gain.

I. INTRODUCTION

Fundamental optimisation approaches aim at maximising the performance of electromagnetic systems in their nominal operating conditions. In two-port microwave networks, which are the focus in this work, a typical goal is the bi-conjugate impedance matching that maximises the power transfer efficiency from the source to the load. This is a relevant goal in virtually all applications, including the recently emerged radio-frequency systems, which operate on harvested energy [1–4]. In such systems, however, also a certain voltage threshold must be exceeded to activate semiconductor devices. This makes the voltage gain another important parameter. A feature shared by both gain parameters in two-port systems is that they are non-linear functions of the complex impedances terminating the ports. Consequently, it is problematic to conclude how variability in the port terminations affect these fundamental performance indicators. In the related previous work, sensitivity of specific two-port networks was characterised through derivative-based approaches [5–6]. In article [7], the authors presented analysis of constant mismatch circles to establish optimum trade-off between input and output mismatch for transistor amplifier design. The authors of [8] investigated the stability of two-port network with terminations varying in elliptic regions in the complex plane. In [4], the minimum of the voltage gain was computed numerically in a special case where the load impedance varied in a disk defined by a given lower bound of the transducer power gain.

In our earlier work [9], we showed that as the port terminations of a two-port network vary in bounded rectangles in the complex plane, the minimisers of the transducer power gain and voltage gain are located necessarily in small-dimensional subsets of the rectangles. In this work, we first summarise the relevant analytical considerations regarding the structure of the level sets of the gain parameters from [9] and then show how this enables identifying the subsets that necessarily contain the maximisers of the gain parameters. This way, we achieve the complete sensitivity analysis of two-port networks. The presented method does not involve differentiation, but is fully based on the analysis of the structure of the level sets of the gain parameters. It provides an efficient computation of the extrema of the gain parameters by restricting the search of both the minimum and maximum in small-dimensional subsets of the given tolerance rectangles. As an example, we apply the method in the analysis of a highly sensitivity biotelemetry system composed of magnetically coupled small loops.

II. LEVEL SETS PF TRANSDUCER POWER GAIN AND VOLTAGE GAIN

Transducer power gain (G_t) of a two-port network is the ratio of the power delivered to the load ($Z_L=R_L+jX_L$) connected to Port 2 of the system to the power available from a Thévenin voltage source with internal impedance of $Z_S=R_S+jX_S$ connected to Port 1. It is given by [10, Ch. 2]:

Submitted On: May 12, 2017
Accepted On: May 21, 2018

$$G_t = \frac{4R_S R_L |z_{21}|^2}{|(Z_S + z_{11})(Z_L + z_{22}) - z_{12}z_{21}|^2}, \quad (1)$$

where z_{mn}, (m=1,2; n=1,2) are the two-port Z-parameters. In this work, only passive port terminations and unconditionally stable systems are considered. In this case we have [10, Ch. 2]:

$$\begin{cases} 0 < R_S \text{ and } 0 < R_L, \\ 0 < \mathrm{Re}(z_{11}) \text{ and } 0 < \mathrm{Re}(z_{22}), \\ |z_{12}z_{21}| < 2\,\mathrm{Re}(z_{11})\mathrm{Re}(z_{22}) - \mathrm{Re}(z_{12}z_{21}), \end{cases} \quad (2)$$

which implies that the input and output impedances given by:

$$Z_i = z_{11} - \frac{z_{12}z_{21}}{z_{22} + Z_L} \text{ and } Z_o = z_{22} - \frac{z_{12}z_{21}}{z_{11} + Z_S}, \quad (3)$$

respectively, have positive real parts.

The voltage gain (A_v) of a two-port system is given by is the ratio of the load (connected to Port 2) voltage amplitude to the amplitude of a Thévenin voltage source with internal impedance of Z_S=R_S+jX_S connected to Port 1. Basic circuit analysis utilising the Z-parameters yield:

$$A_v = \left| \frac{z_{21}Z_L}{(Z_S + z_{11})(Z_L + z_{22}) - z_{12}z_{21}} \right|. \quad (4)$$

A. Level sets of transducer power gain

For further analysis, it is useful to restate Equation (1) as:

$$\begin{cases} G_t = \dfrac{2\Lambda_L R_S}{|Z_S + Z_i|^2}, \quad \Lambda_L = \dfrac{2R_L |z_{21}|^2}{|Z_L + z_{22}|^2}, \\ G_t = \dfrac{2\Lambda_S R_L}{|Z_L + Z_o|^2}, \quad \Lambda_S = \dfrac{2R_S |z_{21}|^2}{|Z_S + z_{11}|^2}. \end{cases} \quad (5)$$

Next, we suppose that Z_S and Z-parameters are fixed and study the condition $\alpha \le G_t(Z_L)$, where $\alpha > 0$. In this case, (5) implies:

$$Z_L Z_L^* + \left(Z_o^* - \frac{\Lambda_S}{\alpha}\right) Z_L + \left(Z_o - \frac{\Lambda_S}{\alpha}\right) Z_L^* + |Z_o|^2 \le 0, \quad (6)$$

which defines a complex plane disk $D_{\alpha L}$ with the centre point ($C_{\alpha L}$) and radius ($r_{\alpha L}$) given by:

$$C_{\alpha L} = -\left(Z_o^* - \frac{\Lambda_S}{\alpha}\right)^* = \frac{\Lambda_S}{\alpha} - Z_o \quad (7)$$

$$\text{and} \quad r_{\alpha L} = \sqrt{|C_{\alpha L}|^2 - |Z_o|^2} = \sqrt{\frac{\Lambda_S}{\alpha}\left(\frac{\Lambda_S}{\alpha} - 2R_o\right)}.$$

Hence, for any Z_S, the load plane level set defined by $\alpha = G_t(Z_L)$ is a circle and $\alpha \le G_t(Z_L)$ holds true in the disk $D_{\alpha L}$ bound by this circle. Analogously we find that for any Z_L, the source plane level set defined by $\alpha = G_t(Z_S)$ is a circle with the centre point ($C_{\alpha S}$) and radius ($r_{\alpha S}$) given by:

$$C_{\alpha S} = \frac{\Lambda_L}{\alpha} - Z_i \quad \text{and} \quad r_{\alpha S} = \sqrt{\frac{\Lambda_L}{\alpha}\left(\frac{\Lambda_L}{\alpha} - 2R_i\right)}, \quad (8)$$

and that $\alpha \le G_t(Z_S)$ holds true in a disk $D_{\alpha S}$ bound by this circle.

By setting the radius to zero in Equations (7)–(8), we find the level sets of $G_t(Z_L)$ and $G_t(Z_S)$ defined by α=Λ_S/(2R_o) and α=Λ_L/(2R_i) to be singletons $\{C_{\alpha L}\}$=$\{Z_o^*\}$ and $\{C_{\alpha S}\}$=$\{Z_i^*\}$, respectively. These special cases correspond to complex-conjugate match at the output and input of the system, respectively, and for a larger α, the level sets are empty. Thus, in the standard terminology of two-port systems, Λ_S/(2R_o) = G_a and Λ_L/(2R_i) = G_p, where G_a and G_p are the available power gain and operating power gain, respectively [10, Ch. 2]. Moreover, (7)–(8) show that the imaginary parts of $C_{\alpha L}$ and $C_{\alpha S}$ are independent of α, whereas their real parts grow monotonically towards infinity as α reduces. At the same time the radii $r_{\alpha L}$ and $r_{\alpha S}$ also tend monotonically towards infinity, but due to the level set property, for any $\alpha_2 < \alpha_1$ we have $D_{\alpha S1} \subset D_{\alpha S2}$ and $D_{\alpha L1} \subset D_{\alpha L2}$. Figure 1 shows an illustration of the level sets of G_t in the source plane.

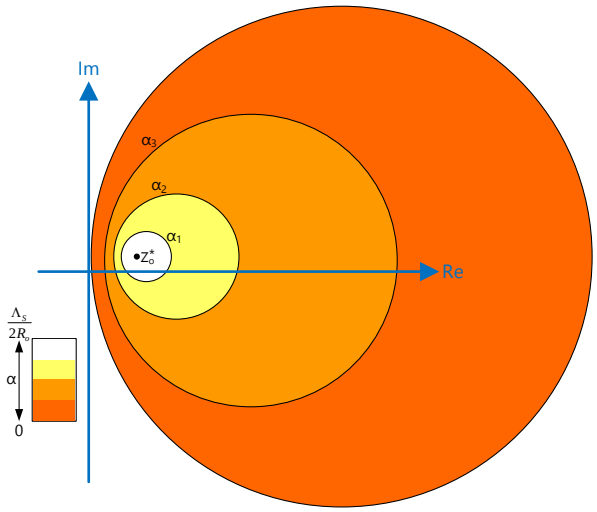

Fig. 1. Illustration of the level sets of G_t in the load plane with $\alpha_1 > \alpha_2 > \alpha_3$ [9].

B. Level sets of voltage gain

First, we note that it is useful to restate Equation (4) as:

$$A_v = \Lambda \left| \frac{Z_L}{Z_L + Z_o} \right|, \quad \Lambda = \left| \frac{z_{21}}{Z_S + z_{11}} \right|. \quad (9)$$

Next, we suppose that Z_L and the Z-parameters are fixed and study the condition $\alpha \le A_v(Z_S)$. In this case, (9) implies:

$$|Z_S - C_{\alpha S}| \le \frac{1}{\alpha} \left| \frac{z_{21}Z_L}{Z_L + z_{22}} \right| = r_{\alpha S}, \; C_{\alpha S} = -Z_i, \quad (10)$$

which defines a disk $D_{\alpha S}$ with the centre point and radius of $C_{\alpha S}$ and $r_{\alpha S}$, respectively. Hence, the level sets defined by $\alpha = A_v(Z_S)$ are circles and $\alpha \le A_v(Z_S)$ holds true in $D_{\alpha S}$.

We suppose next that Z_S and the Z-parameters are fixed and study the condition $\alpha \le A_v(Z_L)$. Now, (10) implies:

$$\mathrm{Z_L Z_L^*} + \frac{\mathrm{Z_o^*}}{\mathrm{P}}\mathrm{Z_L} + \frac{\mathrm{Z_o}}{\mathrm{P}}\mathrm{Z_L^*} + \frac{|\mathrm{Z_o}|^2}{\mathrm{P}} \begin{cases} \le 0, & \mathrm{P} > 0, \\ \ge 0, & \mathrm{P} < 0, \end{cases} \quad (11)$$

where $P = 1-\Lambda^2/\alpha^2$. For $\alpha>\Lambda$, (11) defines a complex plane disk $D_{\alpha L}$ with the centre ($C_{\alpha L}$) and radius ($r_{\alpha L}$) given by:

$$C_{\alpha L} = \frac{-Z_o}{P} \text{ and } r_{\alpha L} = \sqrt{|C_{\alpha L}|^2 - \frac{|Z_o|^2}{P}} = \frac{\Lambda}{\alpha}\left|\frac{Z_o}{P}\right|. \quad (12)$$

For $\alpha<\Lambda$, (11) defines the complex plane excluding $D_{\alpha L}$. Finally, in case $\alpha=\Lambda$, (11) defines a region comprised of the complex plane on and below the line:

$$L_\Lambda = \left\{ x + jy : x = -\frac{X_o}{R_o} y - \frac{|Z_o|^2}{2R_o} \right\}. \quad (13)$$

Figure 3 in Section IV illustrates of the level sets of A_v in the load plane. Finally, the limit processes for the level sets of A_v are summarised as follows:

$$\alpha \to 0 \Rightarrow \begin{cases} r_{aS} \to \infty \text{ and } C_{\alpha S} = -Z_i \\ r_{aL} \to 0 \text{ and } C_{\alpha L} = 0 \end{cases}$$

$$\alpha \uparrow \Lambda \Rightarrow \begin{cases} r_{aL} \to \infty \\ C_{\alpha L} \to \infty \pm j\infty \\ D_{\alpha L} \to \text{Complex plane above } L_\Lambda \end{cases} \quad (14)$$

$$\alpha \downarrow \Lambda \Rightarrow \begin{cases} r_{aL} \to \infty \\ C_{\alpha L} \to -\infty \pm j\infty \\ D_{\alpha L} \to \text{Complex plane below } L_\Lambda \end{cases}$$

$$\alpha \to \infty \Rightarrow \begin{cases} r_{aS} \to 0 \text{ and } C_{\alpha S} \to -Z_i \\ r_{aL} \to 0 \text{ and } C_{\alpha L} \to -Z_o \end{cases}$$

III. EXTREMA OF TRANSDUCER POWER GAIN

In this and the next section, we assume that the port terminations vary in a closed and bounded hyper-rectangle $U = U_S \times U_L$ where U_S and U_L are rectangles in the complex plane given by:

$$\mathrm{U_S} = \left\{ \begin{matrix} \mathrm{x + jy} : 0 < \mathrm{x_{S1}} \le \mathrm{x} \le \mathrm{x_{S2}}, \\ \mathrm{y_{S1}} \le \mathrm{y} \le \mathrm{y_{S2}} \end{matrix} \right\},$$
$$\mathrm{U_L} = \left\{ \begin{matrix} \mathrm{x + jy} : 0 < \mathrm{x_{L1}} \le \mathrm{x} \le \mathrm{x_{L2}}, \\ \mathrm{y_{L1}} \le \mathrm{y} \le \mathrm{y_{L2}} \end{matrix} \right\}. \quad (15)$$

Below, we will detail how the knowledge of the structure of the level sets of G_t and A_v enables the identification of small-dimensional subsets of U where the studied gain parameters necessarily attain their extreme values. To aid the further analysis, we denote the sets of corner and boundary points of U_S and U_L by V_S and V_L, and B_S and B_L, respectively.

Since G_t and A_v are continuous real-valued functions which can also be interpreted as functions of four real variables in a closed and bounded set defined by the intervals of the real and imaginary parts in Equation (15), Extreme Value Theorem guarantees that they attain their extreme values in U [11, Ch. 12.5].

B. Minimum of transducer power gain

The level sets of G_t are circles in both the source and load planes. We focus first on the source plane, where $\alpha \le G_t(Z_S)$ holds true in a disk $D_{\alpha S}$ which is bound by the level set circle. Hence, to bound $G_t(Z_S)$ from below in U_S, we must find the smallest α for which U_S is entirely contained in $D_{\alpha S}$. Since U_S is a rectangle, such α defines a level set circle that passes through a corner of U_S. Hence, for all Z_S in U_S we have $G_t(Z_S) \ge G_t(Z_{S0})$, where $Z_{S0} \in V_S$. With a similar reasoning, for all Z_L in U_L, we have $G_t(Z_L) \ge G_t(Z_{L0})$, where $Z_{L0} \in V_L$. Consequently, for all (Z_S,Z_L) in U: $G_t(Z_S,Z_L) \ge G_t(Z_{S0},Z_L) \ge G_t(Z_{S0},Z_{L0})$. Because this lower bound of G_t over the whole closed and bounded set U is its value evaluated at $(Z_{S0},Z_{L0}) \in U$, then by the Extreme Value Theorem, this point must be the minimiser of G_t in U.

C. Maximum of transducer power gain

For an unconditionally stable two-port, the unique bi-conjugate-matched source and load terminations Z_{mS} and Z_{mL}, respectively, maximise the transducer power gain and the maximum can be computed with the well-known formula [10, Ch. 2]. Clearly, if $(Z_{mS},Z_{mL}) \in U$, this point is the maximiser of G_t in U. Therefore, below we will assume that $(Z_{mS},Z_{mL}) \notin U$. For further analysis, we denote the images of U_L and U_S under the complex conjugate map of the input and output impedances as $Z_i^*[U_L]$ and $Z_o^*[U_S]$, respectively, and make the following definitions: $\Sigma_S = U_S \cap Z_i^*[U_L]$ and $\Sigma_L = U_L \cap Z_o^*[U_S]$.

If Σ_S and Σ_L are both empty, then for an increasing level sets values, the level set circles of G_t must converge towards points outside of U_S and U_L, because neither the input or output can be conjugate-matched. Hence, to bound $G_t(Z_S,Z_S)$ from above in U_S, we must find the largest level set value α for which $D_{\alpha S}$ intersects U_S at a single point only. Such α defines a level set circle that passes through a point in the boundary of U_S. Hence, for all Z_L in U_L, we have $G_t(Z_S,Z_L) \le G_t(Z_{S0},Z_L)$, where $Z_{S0} \in B_S$. With an identical argument, for any $Z_S \in U_S$, we have $G_t(Z_S,Z_L) \le G_t(Z_S,Z_{L0})$, where $Z_{L0} \in B_L$. Consequently, for all (Z_S,Z_L) in U: $G_t(Z_S,Z_L) \le G_t(Z_{S0},Z_L) \le G_t(Z_{S0},Z_{L0})$. Because this upper bound of G_t over the whole closed and bounded set U is its value evaluated at $(Z_{S0},Z_{L0}) \in U$, by the Extreme Value Theorem, this point must be the maximiser of G_t in U.

If either Σ_S or Σ_L or both are non-empty, the maximiser of G_t may be located in the interior of U. To aid the analysis in these cases, we first study the algebraic properties of the map Z_i^* defined as the complex conjugate of the input impedance. Firstly, Z_i^* is clearly continuous in U_L since $\mathrm{Re}(z_{22})$ and R_L are both positive (Equation 2) and thus $z_{22}+Z_L \neq 0$ in Equation (3).

Moreover, it is elementary to show that Z_i^* is injective and thus bijective from its domain to its image. Finally, Equation (3) can be readily solved for Z_L to see that the inverse map Z_i^{*-1} exists and is continuous. These properties make Z_i^* a homeomorphism from U_L to its image. This class of functions map interior and boundary points of their domain to the respective points of the image. Moreover, simply-connectedness is a property that is preserved under a homeomorphic map. Therefore, as the closed and bounded rectangle U_L is clearly simply-connected, so must be the set $Z_i^*[U_L]$.

With analogous arguments as for the map Z_i^*, we find that Z_i^{*-1} is a homeomorphism from Σ_S to its image $Z_i^{*-1}[\Sigma_S]$ and thus this set must be simply-connected and its boundary given by $Z_i^{*-1}[\partial\Sigma_S]$, where $\partial\Sigma_S$ denotes the boundary of Σ_S. Since Z_i^* and Z_o^* have identical structure, all of the above conclusions are true for Z_o^* and its inverse as well. Finally, we note that since we have assumed that the bi-conjugate-matched source and load impedances of the two-port system are not located in U, we must have $\Sigma_S \cap Z_o^{*-1}[\Sigma_L] = \emptyset$ and $\Sigma_L \cap Z_i^{*-1}[\Sigma_S] = \emptyset$.

Next, we suppose Σ_S is non-empty. This implies that there exists $Z_{L1} \in Z_i^{*-1}[\Sigma_S]$ such that $Z_i^*(Z_{L1}) = Z_{S1} \in \Sigma_S$. In general, $G_t(Z_S,Z_L) \le G_p(Z_L)$, where G_p is the operating power gain of the two-port network attained when the input is conjugate-matched. Because the input is conjugate-matched at the point (Z_{S1},Z_{L1}), G_t attains its upper bound $G_p(Z_L)$ w.r.t. the source impedance at this point. However, since $\Sigma_L \cap Z_i^{*-1}[\Sigma_S] = \emptyset$, the level sets of G_t in the load plane converge towards a point outside of $Z_i^{*-1}[\Sigma_S]$. Hence, to bound G_t from above in $\Sigma_S \times Z_i^{*-1}[\Sigma_S]$, we must find the largest α for which $D_{\alpha L}$ intersects $Z_i^{*-1}[\Sigma_S]$ at a single point only. Such α defines a level set circle that passes through a point in the boundary of $Z_i^{*-1}[\Sigma_S]$. Thus, for all $(Z_S,Z_L) \in \Sigma_S \times Z_i^{*-1}[\Sigma_S]$, we have $G_t(Z_S,Z_L) \le G_t(Z_{S1},Z_{L1})$, where $Z_{L1} \in Z_i^{*-1}[\partial\Sigma_S]$ and $Z_{S1} = Z_i^*(Z_{L1})$.

In case Σ_L is non-empty, then by identical arguments as above, we have $G_t(Z_S,Z_L) \le G_a(Z_S)$, where G_a is the available power gain of the two-port network attained when the output is conjugate-matched and we conclude that for all $(Z_S,Z_L) \in Z_o^{*-1}[\Sigma_L] \times \Sigma_L$ we have $G_t(Z_S,Z_L) \le G_t(Z_{S2},Z_{L2})$, where $Z_{S2} \in Z_o^{*-1}[\partial\Sigma_L]$, $Z_{L2} = Z_o^*(Z_{S2})$.

Finally, since $\Sigma_S \times Z_i^{*-1}[\Sigma_S]$ and $\Sigma_L \times Z_o^{*-1}[\Sigma_L]$ are proper subsets of U, the upper bound of G_t in the whole U may be larger than $\max\{G_t(Z_{S1},Z_{L1}),\ G_t(Z_{S2},Z_{L2})\}$. However, for a level set value α that is strictly greater than this value, the level sets of G_t are either empty, if (Z_{S1},Z_{L1}) or (Z_{S2},Z_{L2}) happens to be the maximiser of G_t in U, or converge towards points outside of U_S and U_L. This is because, in all cases where level sets convergence towards a point inside U_S or U_L, G_t is upper bounded by $\max\{G_t(Z_{S1},Z_{L1}), G_t(Z_{S2},Z_{L2})\} < \alpha$ as shown above. Thus, for all (Z_S,Z_L) in U, we have $G_t(Z_S,Z_L) \le \max\{G_t(Z_{S0},Z_{L0}), G_t(Z_{S1},Z_{L1}), G_t(Z_{S2},Z_{L2})\}$, where $(Z_{S0},Z_{L0}) \in B_S \times B_L$.

Based on these findings, we conclude that the maximiser of G_t in U is necessarily located in a small-dimensional subset of U as summarised below. Figure 2 illustrates the search of the maximiser of G_t in U_L in case (d) of the below list.

(a) If $(Z_{mS},Z_{mL}) \in U$, the maximum of G_t in U is $G_t(Z_{mS},Z_{mL})$.

(b) If $\Sigma_S = \emptyset$ and $\Sigma_L = \emptyset$, the maximiser of G_t in U is a point $(Z_{S0},Z_{L0}) \in B_S \times B_L$.

(c) If $\Sigma_S \neq \emptyset$ and $\Sigma_L = \emptyset$, the maximiser of G_t in U is (Z_{S0},Z_{L0}) or a point (Z_{S1},Z_{L1}), where $Z_{L1} \in Z_i^{*-1}[\partial\Sigma_S]$ and $Z_{S1} = Z_i^*(Z_{L1})$.

(d) If $\Sigma_S = \emptyset$ and $\Sigma_L \neq \emptyset$, the maximiser of G_t in U is (Z_{S0},Z_{L0}) or a point (Z_{S2},Z_{L2}), where $Z_{S2} \in Z_o^{*-1}[\partial\Sigma_L]$ and $Z_{L2} = Z_o^*(Z_{S2})$.

(e) If $\Sigma_S \neq \emptyset$ and $\Sigma \neq \emptyset$, the maximiser of G_t in U is (Z_{S0},Z_{L0}), (Z_{S1},Z_{L1}) or (Z_{S2},Z_{L2}).

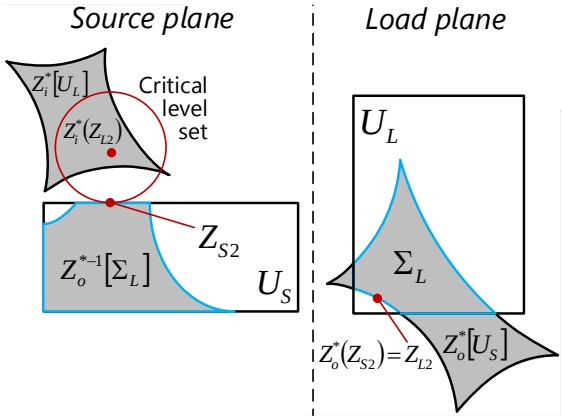

Fig. 2. Illustration of the search of maximiser of G_t in U in the case $\Sigma_S = \emptyset$ and $\Sigma_L \neq \emptyset$. The figure has been drawn supposing the maximiser is (Z_{S2},Z_{L2}).

IV. EXTREMA OF VOLTAGE GAIN

A. Minimum of voltage gain

In the source plane, the level sets defined by $\alpha=A_v(Z_S)$ are circles given in Equation (9) and $\alpha \le A_v(Z_S)$ holds true in a disk $D_{\alpha S}$ which is bound by the level set circle. Hence, to bound $A_v(Z_S)$ from below in U_S, we must find the smallest α for which U_S is contained in $D_{\alpha S}$. Since U_S is a rectangle, such α defines a level set circle which passes through a corner of U_S. As seen from Equation (9), the centre point of the level set circle has a negative real part and the circle radius is inversely proportional to α. Therefore, since every point in U_S has a positive real part, the set of possible corners of intersection are limited to those with larger real parts. We denote these corners as $V_{S+}=\{x_{S2}+jy_{S1}, x_{S2}+jy_{S2}\}$. Hence, for all Z_S in U_S we have $A_v(Z_S) \ge A_v(Z_{S0})$, where $Z_{S0} \in V_{S+}$.

To bound $A_v(Z_L)$ from below in U_L, we first suppose that the minimum of $A_v(Z_L)$ in V_L is attained at a point

Z_{L1}. If $A_v(Z_{L1})>\Lambda$, then the level set circle that passes through Z_{L1} must be the boundary of a disk $D_{\alpha L}$ where $A_v(Z_L)\geq A_v(Z_{L1})$. Given that Z_{L1} is a corner point of U_L and minimises $A_v(Z_L)$ in V_L, then the remaining corners of U_L must be contained in $D_{\alpha L}$. Since U_L is a rectangle, this implies that U_L must be entirely contained $D_{\alpha L}$. Thus, $A_v(Z_L)\geq A_v(Z_{L1})$ for all Z_L in U_L.

If $A_v(Z_{L1})<\Lambda$, there may be more points in U_L for which A_v is smaller than $A_v(Z_{L1})$. For any such point Z_{L2}, $A_v(Z_L)\geq A_v(Z_{L2})$ holds true outside of $D_{\alpha L}$ with the corresponding level set circle passing through Z_{L2}. Thus, to bound $A_v(Z_L)$ from below in U_L, we must find the smallest α such that $D_{\alpha L}$ intersects U_L at a single point only. Based on the limit processes summarised in Equation (14), as α reduces from Λ towards 0, then $C_{\alpha L}\to 0$ and $r_{\alpha L}\to 0$. However, by the definition of U_L given in Equation (15), $0\notin U_L$. Thus, the intersection point must be found in B_L.

By combining the results from the above discussion, since $V_L\subset B_L$, for all (Z_S,Z_L) in U we have $A_v(Z_S,Z_L)\geq A_v(Z_{S0},Z_L)\geq A_v(Z_{S0},Z_{L0})$, where $(Z_{S0},Z_{L0})\in V_{S+}\times B_L$. Because this lower bound of A_v over the whole closed and bounded set U is its value evaluated at $(Z_{S0},Z_{L0})\in U$, then by the Extreme Value Theorem, this point must be the minimiser of A_v in U. Figure 3 illustrates the search of the minimiser of A_v in U_L.

B. Maximum of voltage gain

In the source plane, the level sets defined by $\alpha=A_v(Z_S)$ are circles given in Equation (9) and $\alpha\leq A_v(Z_S)$ holds true in a disk $D_{\alpha S}$ which is bound by the level set circle. Hence, to bound $A_v(Z_S)$ from above in U_S, we must find the largest α for which $D_{\alpha S}$ intersects U_S only at a single point. Since U_S is a rectangle, such α defines a level set circle that passes through a point at the boundary of U_S. As seen from Equation (9), the centre point of the level set circle has a negative real part and the circle radius is inversely proportional to α. Therefore, since every point in U_S has a positive real part, the intersection point must lie on the vertical edge of U_S with the smaller real part. We denote this set as $B_{S-}=\{x+jy: x=x_{S1},\ y_{S1}\leq y\leq y_{S2}\}$. Hence, for all Z_S in U_S we have $A_v(Z_S)\leq A_v(Z_{S0})$, where $Z_{S0}\in B_{S-}$.

To bound $A_v(Z_L)$ from above in U_L, we first suppose that the maximum of $A_v(Z_L)$ in V_L is attained at a point Z_{L1}. If $A_v(Z_{L1})<\Lambda$, the level set circle passing through Z_{L1} defines a disk $D_{\alpha L}$ where $A_v(Z_L)<A_v(Z_{L1})$. Given that Z_{L1} is a corner point of U_L and maximises $A_v(Z_L)$ in V_L, the remaining corners must be contained in $D_{\alpha L}$. Since U_L is a rectangle, this implies that U_L must be entirely contained in $D_{\alpha L}$. Thus, $A_v(Z_L)<A_v(Z_{L1})$ for all Z_L in U_L.

If $A_v(Z_{L1})>\Lambda$, there may be more points in U_L for which A_v is greater than $A_v(Z_{L1})$. For any such point Z_{L2}, $A_v(Z_L)\leq A_v(Z_{L2})$ holds true outside of $D_{\alpha L}$ with the corresponding level set circle passing through Z_{L2}. Thus, to bound $A_v(Z_L)$ from above in U_L, we must find the largest α such that $D_{\alpha L}$ intersects U_L at a single point only. Based on the limit processes summarised in Equation (14), as α grows from Λ towards infinity, $C_{\alpha L}\to 0$ and $r_{\alpha L}\to 0$. By the definition of U_L given in Equation (15), $0\notin U_L$. Thus, the intersection point must be found in B_L.

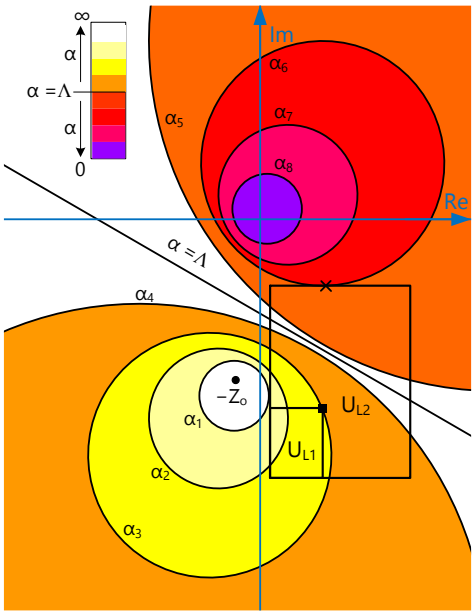

Fig. 3. Illustration of the search of minimiser of A_v in the load plane in rectangles U_{L1} and U_{L2}. In the figure: $\alpha_n>\alpha_{n+1}$ and $\alpha_4>\Lambda>\alpha_5$. The box and cross markers indicate the minimiser of A_v in U_{L1} and U_{L2}, respectively [9].

By combining the results from the above discussion, since $V_L\subset B_L$, for all (Z_S,Z_L) in U we have $A_v(Z_S,Z_L)\leq A_v(Z_{S0},Z_L)\leq A_v(Z_{S0},Z_{L0})$, where $(Z_{S0},Z_{L0})\in B_{S-}\times B_L$. Because this upper bound of A_v over the whole closed and bounded set U is its value evaluated at $(Z_{S0},Z_{L0})\in U$, then by the Extreme Value Theorem, this point must be the minimiser of A_v in U.

In practice, the search for the maximiser of A_v in U is initialised by finding the maximiser (Z_{S0},Z_{L1}) of A_v in $B_{S-}\times V_L$. This is readily done, since this is a small subset of U. Next Λ given in Equation (9) is computed at $Z_S=Z_{S0}$. If $A_v(Z_{S0},Z_{L1})<\Lambda$, then (Z_{S0},Z_{L1}) maximises A_v in U. Otherwise, the maximum value is attained in $B_{S+}\times B_L$ which is also a limited subset of U. The search for the minimiser follows an analogous algorithm.

V. APPLICATION TO ANALYSIS OF A BIOTELEMETRY SYSTEM

The presented technique of finding the extrema of the transducer power gain and voltage gain of a two-port network as the source and load impedances vary in given rectangles in the complex plane is applicable to all two-ports which are unconditionally stable. In this section, we present an example in the analysis of a wireless link

in a biotelemetry system.

We consider a wireless link between a miniature loop antenna formed by metallizing four adjacent faces of a 1×1×1 mm^3 sized cube and a planar circular loop with the inner diameter of 12 mm, which has been developed for a wireless brain-machine interface system [3]. In this application, the cubic loop lies on the cortex harvesting energy for a microsystem that records the electrical activity of the brain. The source of energy is a planar loop placed 5 mm above the scalp transmitting at 300 MHz. A major practical challenge in the implementation and testing of the wireless link is the impedance matching of the small loops. This is because they have very low input resistance and consequently the system is sensitive towards variability in the antenna terminations.

For testing the wireless link, the antennas need to be matched to 50 Ω instruments. To bi-conjugate match the system, we computed the unique matched source and load terminations to achieve this and implement matching circuits comprised of two reactive components for both antennas. This is a generally applicable approach to transform any complex impedance to a given resistance [12, Ch. 5.1]. In this process, we utilised the simulated Z-parameters of the wireless link including the antennas and biological channel that we obtained from simulations in ANSYS HFSS as detailed in [3]. As shown in [3], due to the miniature size of the implanted antenna and the biological environment, the maximum link power efficiency in this system is attained around 300 MHz. At this frequency, the component values to realize the bi-conjugate matching were found to be: C_{in} = 13.0 pF, L_{in} = 1.80 nH, C_{out} = 182 pF, and L_{out} = 0.75 nH, where the capacitors are connected in series with the external and implant antennas and followed by the inductors in parallel. At 300 MHz these circuits transform 50 Ω to the matched source and load impedances Z_{mS}=0.695−j63.616 Ω and Z_{mL}=0.049−j2.489 Ω terminating the implant and external antenna ports, respectively. This means that under ideal conditions the system is bi-conjugate matched at 300 MHz with no impedance mismatch loss.

For the assessment of impact of variability in the antenna terminations, the bounds of impedance variation can be defined in numerous ways. We first considered the tolerance rectangles U_S and U_L to be the largest squares centred at Z_{mS} and Z_{mL}, such that the minimum of G_t at 300 MHz was 3 dB (Case 1a) and 6 dB (Case 2a) below the nominal value. As the presented analysis method is applicable to any rectangle, we then extended the squares to largest rectangles so that the drop in G_t from the nominal value remained at 3 dB (Case 1b) and 6 dB (Case 2b) at 300 MHz. Given that the level sets of G_t are circles with the properties detailed in Section II, this can be understood as an extension of the rectangles until the critical level set circle passes through not only one, but at least two of the corners of the tolerance rectangles. Finally, at other frequencies, U_S and U_L were defined through corner points having the same percentage difference in real and imaginary parts with respect to Z_S and Z_L, as in the case at 300 MHz. Table 1 lists the percentage differences defining the rectangles. Table 2 shows the corner points of the rectangles at 300 MHz. Figures 4 and 5 present the simulated transducer power gain and voltage gain of the system together with the bounds of variation given by the impedance tolerance defined in Table 1.

Table 1: Percentage variation in the source and load impedance for the computation of the minimum and maximum of G_t and A_v in Fig. 4

Case 1a			
Re(Z_S)	Im(Z_S)	Re(Z_L)	Im(Z_L)
±1.17%	±1.17%	±1.17%	±1.17%
Case 1b			
Re(Z_S)	Im(Z_S)	Re(Z_L)	Im(Z_L)
–1.17% +364%	±1.17%	–1.29% +21.1%	–1.21% +1.18%
Case 2a			
Re(Z_S)	Im(Z_S)	Re(Z_L)	Im(Z_L)
±1.94%	±1.94%	±1.94%	±1.94%
Case 2b			
Re(Z_S)	Im(Z_S)	Re(Z_L)	Im(Z_L)
–2.24% +1013%	±1.94%	–1.96% +55.1%	–1.95% +1.94%

Table 2: Corner points of the tolerance rectangles (unit: Ω) at 300 MHz for the computation of the minimum and maximum of G_t and A_v in Fig. 4

Case 1a				
U_S	0.228 −j37.72	0.228 −j36.85	0.233 −j37.72	0.233 −j36.85
U_L	0.039 −j1.517	0.039 −j1.482	0.0404 −j1.517	0.0404 −j1.482
Case 1b				
U_S	0.228 −j37.72	0.228 −j36.85	1.07 −j36.85	1.07 −j36.13
U_L	0.039 −j1.518	0.039 −j1.482	0.0483 −j1.518	0.0483 −j1.482
Case 2a				
U_S	0.226 −j38.0	0.226 −j36.56	0.235 −j38.0	0.235 −j36.56
U_L	0.0391 −j1.529	0.0391 −j1.471	0.0407 −j1.529	0.0407 −j1.471
Case 2b				
U_S	0.225 −j38.0	0.225 −j36.56	2.564 −j38.0	2.564 −j36.56
U_L	0.0391 −j1.529	0.0391 −j1.471	0.0619 −j1.529	0.0619 −j1.471

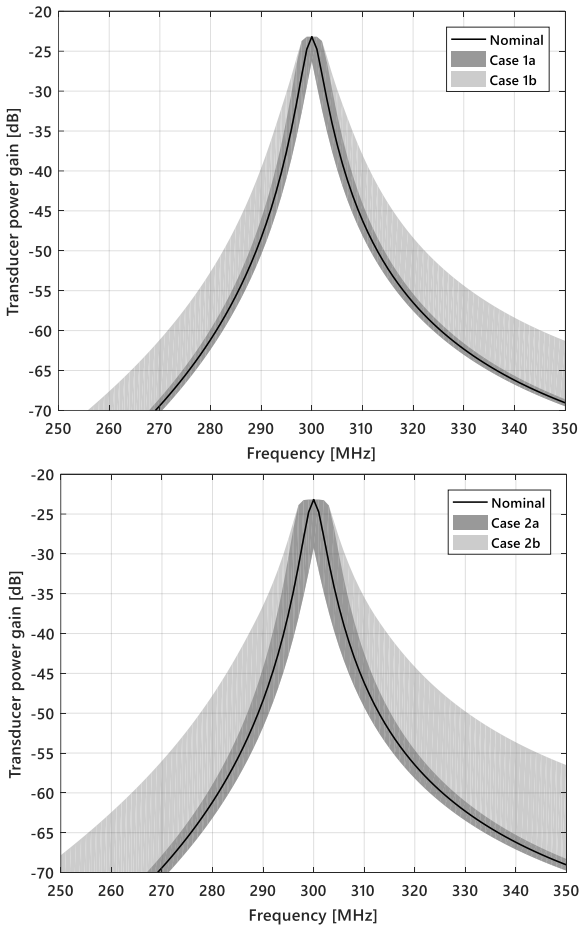

Fig. 4. Transducer power gain of the biotelemetry system and the bounds of variation as the source and load impedances vary in the tolerance rectangles given in Table 1.

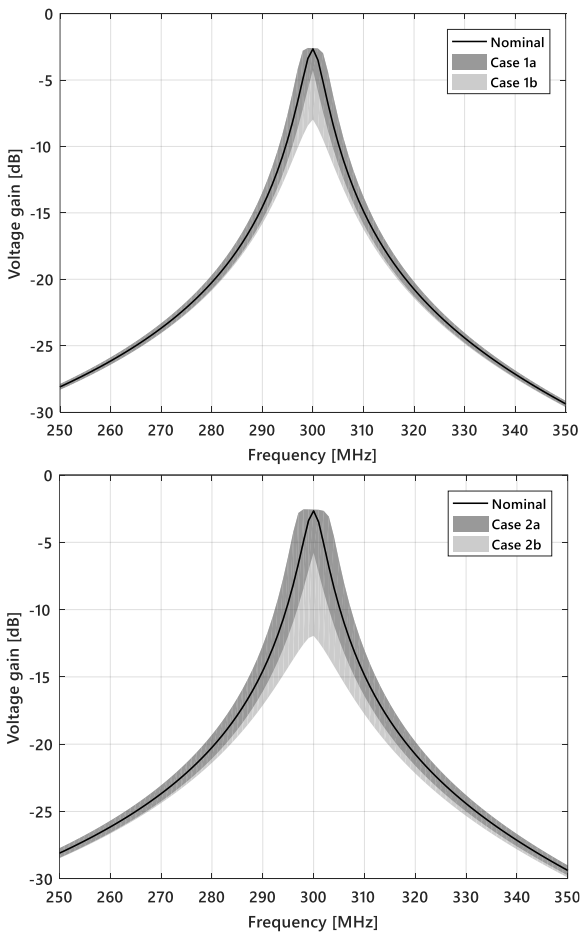

Fig. 5. Voltage gain of the biotelemetry system and the bounds of variation as the source and load impedances vary in the tolerance rectangles given in Table 1.

As seen from Tables 1 and 2, the bounds of variability which correspond to the notable reductions of 3 dB (Case 1) and 6 dB in the transducer power gain compared to the nominal operating conditions, are small. The same conclusion applies to voltage gain, which drops 1.6 dB and 5.3 dB in Case 1a and Case 1b, respectively, and 3.1 dB and 9.3 dB in Case 2a and Case 2b, respectively, at 300 MHz. Overall, it is clear from the results that in this system very small variations in the order of 1-to-2% in the antenna terminations may result in significant reduction in the system's performance. In contrast, however, it tolerates marked deviations in the source and load resistances, towards values higher than the nominal as exemplified by Cases 1b and 2b.

VI. CONCLUSION

Prediction of the performance bounds of electromagnetic systems under non-ideal operating conditions is an important step in achieving reliable devices and conducting reproducible experiments. To aid this process in the context of two-port networks, we developed a semi-analytical method for locating the minimiser and maximiser of the transducer power gain and voltage gain as the port terminations vary in bounded rectangles in the complex plane. Instead of differentiation, the method exploits the knowledge on the structure of the level sets of the gain parameters to limit the numerical search to small-dimensional subsets of the full four-dimension search space. We applied the method in the analysis of a highly sensitive biotelemetry system based

on magnetically coupled small loops. Future work includes comparison of matching circuits to reduce the sensitivity in this type of wireless systems.

ACKNOWLEDGMENT

This research was funded by Academy of Finland funding decision 294616.

REFERENCES

[1] J. Kimionis, M. Isakov, B. S. Koh, A. Georgiadis, and M. M. Tentzeris, "3D-printed origami packaging with inkjet-printed antennas for RF harvesting sensors," *IEEE Trans. Microw. Theory Techn.*, vol. 63, no. 12, pp. 4521-4532, Dec. 2015.

[2] M. Zargham and P. G. Gulak, "Fully integrated on-chip coil in 0.13 µm CMOS for wireless power transfer through biological media," *IEEE Trans. Biomed. Circuits Syst.*, vol. 9, no. 2, pp. 259-271, Apr. 2015.

[3] E. Moradi, S. Amendola, T. Björninen, L. Sydänheimo, J. M. Carmena, J. M. Rabaey, and L. Ukkonen, "Backscattering neural tags for wireless brain-machine interface system," *IEEE Trans. Antennas. Propag.*, vol. 62, no. 2, pp. 719-726, Dec. 2014.

[4] M. Waqas, A. Khan, T. Björninen, L. Sydänheimo, and L. Ukkonen, "Characterization of two-turns external loop antenna with magnetic core for efficient wireless powering of cortical implants," *IEEE Antennas Wireless Propag. Lett.*, vol. 15, pp. 1410-1413, Dec. 2015.

[5] G. I. Vasilescu and T. Redon, "A new approach to sensitivity computation of microwave circuits," *IEEE Intl. Symp. Circuits and Systems*, Espoo, Finland, pp. 1167-1170, June 1988.

[6] F. Güneş and S. Altunç, "Gain-sensitivity analysis for cascaded two-ports and application to distributed-parameter amplifiers," *Intl. J. RF and Microw. Computer-Aided Eng*., vol. 14, no. 5, pp. 462-474, Sep. 2004.

[7] W. Ciccognani, P. E. Longhi, S. Colangeli, and E. Limiti, "Constant mismatch circles and application to low-noise microwave amplifier design," *IEEE Trans. Microw. Theory Techn.*, vol. 61, no. 12, pp. 4154-4167, Dec. 2013.

[8] P. Marietti, G. Scotti, A. Trifiletti, and G. Viviani, "Stability criterion for two-port network with input and output terminations varying in elliptic regions," *IEEE Trans. Microw. Theory Techn.*, vol. 54, no. 12, pp. 4049-4055, Dec. 2006.

[9] T. Björninen, E. Moradi, M. Waqas, A. Khan, and L. Ukkonen, "Minimum of two-port voltage and power gain under varying terminations: Semi-analytic method and application to biotelemetry systems," *URSI Commission B Intl. Symp. On Electromagnetic Theory*, Espoo, Finland, pp. 869-872, Aug. 2016.

[10] Ralph S. Carson, *High-Frequency Amplifiers*. John Wiley & Sons, USA, 1975.

[11] Patrick M. Fitzpatrick, *Advanced Calculus*. 2nd ed., Thomson Brooks/Cole, USA, 2006.

[12] David M. Pozar, *Microwave Engineering*. 4th ed., John Wiley & Sons, Inc., USA, 2012.

Toni Björninen received the M.Sc. and doctoral degrees in Electrical Engineering in 2009 and 2012, respectively, from Tampere University of Technology (TUT), Tampere, Finland. He is currently an Academy of Finland Research Fellow in BioMediTech Institute and Faculty of Biomedical Sciences and Engineering in TUT. He has been a Visiting Postdoctoral Scholar in Berkeley Wireless Research Center in UC Berkeley and in Microwave and Antenna Institute in Electronic Engineering Dept., Tsinghua University, Beijing. His research focuses on technology for wireless health including implantable and wearable antennas and sensors, and RFID-inspired wireless solutions. Björninen is an author of 140 peer-reviewed scientific publications. He serves as an Associate Editor in IET Electronics Letters and IEEE Journal of Radio Frequency Identification, and as an Editor in International Journal of Antennas and Propagation. In 2016, IEEE Antennas and Propagation Society selected him among the top 10 Reviewers of IEEE Transactions on Antennas and Propagation for his input during 06/2015–04/2016.

First and Second Order Mur Type ABCs for DNG Media

Ayşegül Pekmezci [1], Ercan Topuz [1], and Levent Sevgi [2]

[1] Department of Electronics and Communications Engineering
Dogus University, 34722 Kadikoy, Istanbul, Turkey
apekmezci@dogus.edu.tr, etopuz@dogus.edu.tr

[2] Department of Electrical and Electronics Engineering
Okan University, 34959 Tuzla, Istanbul, Turkey
levent.sevgi@okan.edu.tr

Abstract ─ Reflections from boundaries of the FDTD computational domain lead to inaccurate, even unstable codes when dealing with problems involving double negative (DNG) materials. Here, an efficient and simple algorithm is presented for terminating FDTD in DNG medium which is based on first and second order Mur's absorbing boundary conditions (ABC). FDTD update equations for Mur's ABC formulations are obtained from frequency domain one-way wave equations using piecewise linear recursive convolution (PLRC) method. Numerical examples are given both for 1D and 2D scenarios to demonstrate the validity and stability of the proposed Mur formulations, and its advantages over uniaxial perfectly matched layer (UPML) in reducing computational time and memory requirements.

Index Terms ─ Absorbing Boundary Conditions (ABC), Double Negative Media (DNG), Finite Difference Time Domain (FDTD), Lorentz model, MUR, one-way wave equation.

I. INTRODUCTION

FDTD formulation is a convenient tool for solution of electromagnetic wave problems. Often it becomes necessary to terminate computational domain at fictitious boundaries which ideally absorb all incident radiation without producing any reflection. The most widely used ABCs are Mur [1], perfectly matched layer (PML) [2-5] types and the recently proposed surface impedance ABCs [6,7]. Although PML performance is significantly better than Mur's ABC particularly when dealing with a wider range of incident angles, Mur's ABC may be preferred due to its computational efficiency and ease of implementation whenever the level of reflections can be tolerated.

In the presence of DNG medium special care is required in implementing Mur or PML ABCs to ensure stability. In literature, one can find several studies on the use of PML in DNG media [8-11]. Kosmas et al. presented an ABC based on Mur's approach using dispersive media with a single pole conductivity z-transform model [12]. In this study, a novel formulation of first and second order Mur's ABC has been developed for truncating the DNG media for 1D and 2D problems using PLRC-FDTD algorithm [13]. In the following sections, formulation of the proposed method is presented and its validity and stability as well as its computational advantages over UPML is demonstrated via numerical examples considering a domain filled entirely with Lorentz type DNG material.

It should be noted two factors limit the applicability domain of the formulation presented in this paper. The first one is the assumption of identical dispersion models for electric and magnetic susceptibilities to enable the Fourier transform of the refractive index $n(\omega)=\sqrt{\varepsilon_r(\omega)\mu_r(\omega)}$ to be performed analytically. The second one is the approximation of the square root terms in the one-way split-operator form of the wave equation in 2nd order Mur formulation by two term Taylor series expansion. Thereby introduced limitations are discussed in the following sections.

II. NUMERICAL METHOD

A. Formulation of first-order DNG-Mur ABC

In linear, isotropic, and homogenous DNG media the wave equation becomes:

$$\nabla^2 E(\omega)+k^2(\omega)E(\omega)=0;\; k(\omega)=\frac{\omega}{c}n(\omega), \qquad (1)$$

where E is a field component, $k(\omega)$ is the wave number and c is free space wave velocity. The frequency dependent refractive index $n(\omega)$ is written as:

$$n(\omega)=\sqrt{\varepsilon_r(\omega)\mu_r(\omega)}=\sqrt{\left[1+\chi_e(\omega)\right]\left[1+\chi_m(\omega)\right]}. \qquad (2)$$

In numerical calculations single pole Lorentz model is used for electric and magnetic susceptibilities, $\chi_e(\omega),\chi_m(\omega)$ as in [14]:

Submitted On: July 31, 2017
Accepted On: April 27, 2018

$$\chi_{e,m}(\omega)=\frac{\omega_{pe,pm}^2}{\omega_{oe,om}^2-\omega^2+j\Gamma_{e,m}\omega}, \quad (3)$$

where $\omega_{pe,pm}$ is the plasma frequency, $\omega_{oe,om}$ is the resonance frequency, and $\Gamma_{e,m}$ is the damping coefficient, respectively. Considering a 1D case, where $\partial/\partial y \equiv \partial/\partial z \equiv 0$, right and left going waves can be separated as:

$$\left(\frac{\partial^2}{\partial x^2}+\frac{\omega^2}{c^2}n(\omega)^2\right)E(\omega)=\left(\frac{\partial}{\partial x}+\frac{j\omega}{c}n(\omega)\right)\cdot\left(\frac{\partial}{\partial x}-\frac{j\omega}{c}n(\omega)\right)E(\omega)=0 \quad (4)$$

The functional form of (2) complicates inverse Fourier transform of the operators in (4). A convenient way of avoiding this complication is to approximate geometric mean in (2) by its arithmetic mean. This approach is found to be rather effective when source spectrum is centered close to the intersection point of the $\chi_e(\omega)$ and $\chi_m(\omega)$. However, for purposes of brevity, in this letter we present the formulations for the case of identical models for $\varepsilon_r(\omega)$ and $\mu_r(\omega)$ to write the refractive index as $n(\omega)=1+\chi_e(\omega)$. Then the left going waves in (4) yields:

$$\frac{\partial E(\omega)}{\partial x}-\frac{j\omega}{c}E(\omega)-\frac{j\omega}{c}P(\omega)=0, \quad (5)$$

$$P(\omega)=\chi_e(\omega)E(\omega). \quad (6)$$

Inverse Fourier transform of (5-6) yields:

$$\frac{\partial E(t)}{\partial x}-\frac{1}{c}\frac{\partial E(t)}{\partial t}-\frac{1}{c}\frac{\partial P(t)}{\partial t}=0, \quad (7)$$

$$P(t)=\chi_e(t)*E(t), \quad (8)$$

where '$*$' denotes convolution in time domain and electric susceptibility function in time domain $\chi_e(t)$ is obtained from (3) as:

$$\chi_e(t)=\gamma_e e^{-\alpha_e t}\sin(\beta_e t)u(t), \quad (9)$$

where $\alpha_e=\Gamma_e/2$, $\beta_e=\sqrt{\omega_{oe}^2-\Gamma_e^2/4}$ and $\gamma_e=\omega_{pe}^2/\beta_e$. To derive an FDTD update equation for implementing one-way absorbing boundary condition, (7) is discretized using two-point centered difference approximation at mesh point i+1/2 and at time index n+1/2:

$$E\big|_i^{n+1}=E\big|_{i+1}^{n}+\left(\frac{c\Delta t-\Delta x}{c\Delta t+\Delta x}\right)\left[E\big|_{i+1}^{n+1}-E\big|_i^{n}\right]-\left(\frac{\Delta x}{c\Delta t+\Delta x}\right)\left[P\big|_{i+1}^{n+1}-P\big|_{i+1}^{n}+P\big|_i^{n+1}-P\big|_i^{n}\right] \quad (10)$$

Here, i and n are the indices of discrete space and time variables, Δx and Δt are spatial and temporal discretization step sizes, respectively. The discrete form of P^n is obtained by using PLRC method [13] where the multiplication in frequency domain corresponds to the convolution integral in time domain and discretized as a running sum. Imposing causality, the convolution term in (8) can be defined as:

$$P(t)=\chi_e(t)*E(t)=\int_0^t E(t-\tau)\chi_e(\tau)d\tau. \quad (11)$$

The discretized convolution integral is then obtained by inserting $t=n\Delta t$ into (11):

$$P\big|_i^n=\int_0^{n\Delta t}E(n\Delta t-\tau)\chi_e(\tau)\,d\tau\Big|_i. \quad (12)$$

Approximating the variation of E fields with a linear function in successive Δt interval $q\Delta t\le\tau\le(q+1)\Delta t$, one can write:

$$E(n\Delta t-\tau)=E^{n-q}+\frac{E^{n-q-1}-E^{n-q}}{\Delta t}(\tau-q\Delta t). \quad (13)$$

Substitution of (13) into (12) yields:

$$P\big|_i^n=\sum_{q=0}^{n-1}\int_{q\Delta t}^{(q+1)\Delta t}\left[E^{n-q}+\frac{E^{n-q-1}-E^{n-q}}{\Delta t}(\tau-q\Delta t)\right]\chi_e(\tau)\,d\tau\Big|_i, =\sum_{q=0}^{n-1}\left\{E\big|_i^{n-q}\,\chi_e^q+\left(E\big|_i^{n-q-1}-E\big|_i^{n-q}\right)\xi_e^q\right\} \quad (14)$$

where

$$\chi_e^q=\int_{q\Delta t}^{(q+1)\Delta t}\chi_e(\tau)\,d\tau, \quad (15a)$$

$$\xi_e^q=\frac{1}{\Delta t}\int_{q\Delta t}^{(q+1)\Delta t}(\tau-q\Delta t)\chi_e(\tau)\,d\tau, \quad (15b)$$

which can be evaluated using (9) and following the steps given in [13,14]. The P terms in the right side of (10) can then be expressed as:

$$P\big|_{i+1}^{n+1}-P\big|_{i+1}^{n}+P\big|_i^{n+1}-P\big|_i^{n}=\xi_e^0\left[E\big|_{i+1}^{n}+E\big|_i^{n}\right]+\left(\chi_e^0-\xi_e^0\right)\left[E\big|_{i+1}^{n+1}+E\big|_i^{n+1}\right]-\psi_e\big|_{i+1}^{n}-\psi_e\big|_i^{n}, \quad (16)$$

where ψ_e^n is known as the recursive accumulator and given by:

$$\psi_e\big|_i^n=\sum_{q=0}^{n-1}\left[\left(\Delta\chi_e^q-\Delta\xi_e^q\right)E\big|_i^{n-q}+\Delta\xi_e^q\,E\big|_i^{n-q-1}\right], \quad (17a)$$

with

$$\Delta\chi_e^q=\chi_e^q-\chi_e^{q+1}\;;\;\Delta\xi_e^q=\xi_e^q-\xi_e^{q+1}. \quad (17b)$$

Substituting (16) into (10) and rearranging the discrete equation, one obtains FDTD update equations for left (i=1) and right (i=K) side boundaries:

$$E\big|_1^{n+1}=a_1E\big|_2^{n+1}+a_2E\big|_2^{n}-a_3E\big|_1^{n}+a_4\left[\psi_e\big|_2^{n}+\psi_e\big|_1^{n}\right]$$
$$E\big|_K^{n+1}=a_1E\big|_{K-1}^{n+1}+a_2E\big|_{K-1}^{n}-a_3E\big|_K^{n}+a_4\left[\psi_e\big|_{K-1}^{n}+\psi_e\big|_K^{n}\right], \quad (18)$$

with

$$c_1=\left(\frac{c\Delta t-\Delta x}{c\Delta t+\Delta x}\right);c_2=\left(\frac{\Delta x}{c\Delta t+\Delta x}\right);\ c_3=\left(\chi_e^0-\xi_e^0\right);c_4=\xi_e^0;$$
$$a_1=\left(\frac{c_1-c_2c_3}{1+c_2c_3}\right);a_2=\left(\frac{1-c_2c_4}{1+c_2c_3}\right);\ a_3=\left(\frac{c_1+c_2c_4}{1+c_2c_3}\right);a_4=\left(\frac{c_2}{1+c_2c_3}\right)$$

.

B. Formulation of second-order DNG-Mur ABC

The first-order DNG-Mur's boundary is suitable for 1D problem, where the wave is propagating normal to boundaries. In more general problems, wave propagates toward boundaries at an arbitrary angle. In those cases, obviously, 2nd order approximation is superior to the 1st order approximation in reducing reflections from boundaries of the computational domain. Considering 2D case $\left(\partial/\partial z\equiv 0\right)$ where only the E_z field components impinge on the left and right boundaries along x-direction (i.e., on x=0 and x=h), the wave equation is factored as in the following:

$$\left(\frac{\partial^2}{\partial x^2}+\frac{\partial^2}{\partial y^2}+\frac{\omega^2}{c^2}n(\omega)^2\right)E(\omega)=\left(D_x^2+D_y^2-D_\omega^2 n(\omega)^2\right)E(\omega)$$
$$=\left(D_x+D_\omega n(\omega)\sqrt{1-S_x^2}\right)\left(D_x-D_\omega n(\omega)\sqrt{1-S_x^2}\right)E(\omega)=0 \quad (19)$$

where

$$S_x^2=\frac{D_y^2}{n(\omega)^2\,D_\omega^2}, \quad (20a)$$

$$D_x\equiv\frac{\partial}{\partial x},D_y^2\equiv\frac{\partial^2}{\partial y^2},D_\omega\equiv\frac{j\omega}{c},D_\omega^2\equiv-\frac{\omega^2}{c^2}. \quad (20b)$$

Approximating the square root term with a two-term Taylor series expansion as $\sqrt{1-S_x^2}\cong 1-S_x^2/2$ and substituting S_x^2 and $n(\omega)$ into (19) one can write the one-way wave equation which satisfies the backward wave condition along x-direction as:

$$\left(D_x-D_\omega n(\omega)\left(1-\frac{S_x^2}{2}\right)\right)E(\omega)$$
$$=j\omega\frac{\partial E(\omega)}{\partial x}+\frac{\omega^2}{c}E(\omega)+\frac{\omega^2}{c}P(\omega)+\frac{c}{2}R(\omega)=0 \quad (21)$$

where

$$P(\omega)=\chi_e(\omega)E(\omega)$$
$$R(\omega)=\frac{\partial^2E(\omega)}{\partial y^2}-Q(\omega). \quad (22)$$
$$Q(\omega)=R(\omega)\chi_e(\omega)$$

Taking the inverse Fourier transform of (21) yields:

$$c\frac{\partial^2E(t)}{\partial t\partial x}-\frac{\partial^2E(t)}{\partial t^2}-\frac{\partial^2P(t)}{\partial t^2}+\frac{c^2}{2}R(t)=0, \quad (23)$$

where

$$P(t)=\chi_e(t)*E(t)$$
$$R(t)=\frac{\partial^2E(t)}{\partial y^2}-Q(t). \quad (24)$$
$$Q(t)=\chi_e(t)*R(t)$$

Similar to 1D formulation, discrete forms of P, Q and R are obtained using PLRC algorithm:

$$P\big|_{(i,j)}^{n+1}=\left\{2P^n-P^{n-1}+p_1E^{n+1}+p_2E^n+p_3E^{n-1}+\psi_e^n\right\}\Big|_{(i,j)}$$
$$Q\big|_{(i,j)}^{n+1}=\left\{Q^n+p_1R^{n+1}+\xi_e^0R^n-\phi_e^n\right\}\Big|_{(i,j)} \quad (25)$$
$$R\big|_{(i,j)}^{n+1}=\left[\frac{E\big|_{(i,j+1)}^{n+1}-2E\big|_{(i,j)}^{n+1}+E\big|_{(i,j-1)}^{n+1}}{\Delta y^2}\right]-Q\big|_{(i,j)}^{n+1}$$

Here, ψ_e^n and ϕ_e^n are known as the recursive accumulator and given by:

$$\psi_e^n(i,j)=\sum_{q=0}^{n-2}\left[\begin{matrix}\left(\Delta\chi_e^q-\Delta\xi_e^q\right)E^{n-q-1}(i,j)\\+\Delta\xi_e^qE^{n-q-2}(i,j)\end{matrix}\right], \quad (26a)$$

$$\phi_e^n(i,j)=\sum_{q=0}^{n-1}\left[\begin{matrix}\left(\Delta\chi_{ee}^q-\Delta\xi_{ee}^q\right)R^{n-q}(i,j)\\+\Delta\xi_{ee}^qR^{n-q-1}(i,j)\end{matrix}\right], \quad (26b)$$

where

$$\Delta\chi_e^q=\chi_e^{q+2}-2\chi_e^{q+1}+\chi_e^q;\Delta\chi_{ee}^q=\chi_e^q-\chi_e^{q+1}, \quad (27a)$$
$$\Delta\xi_e^q=\xi_e^{q+2}-2\xi_e^{q+1}+\xi_e^q;\ \Delta\xi_{ee}^q=\xi_e^q-\xi_e^{q+1}. \quad (27b)$$

Using central-difference expressions for the space and time derivatives in (23) and substituting discrete form of P, Q and R from (25) one obtains:

$$E\big|_{(1,j)}^{n+1}=e_1E\big|_{(2,j)}^{n+1}+e_2E\big|_{(2,j)}^{n}+e_3E\big|_{(1,j)}^{n}-e_4E\big|_{(2,j)}^{n-1}$$
$$+e_5E\big|_{(1,j)}^{n-1}-e_6\left[\psi_e\big|_{(2,j)}^{n}+\psi_e\big|_{(1,j)}^{n}\right]$$
$$+e_7\left[R\big|_{(2,j)}^{n}+R\big|_{(1,j)}^{n}\right] \quad (28)$$

with

$$p_1=\left(\chi_e^0-\xi_e^0\right);\ p_2=\left(\chi_e^1-\xi_e^1-2\chi_e^0+3\xi_e^0\right);\ p_3=\left(\xi_e^1-2\xi_e^0\right)$$
$$e_0=\frac{c\Delta t/\Delta x+1+p_1}{2\Delta t^2};e_1=\frac{c\Delta t/\Delta x-1-p_1}{2\Delta t^2e_0};e_2=e_3=\frac{2-p_2}{2\Delta t^2e_0};$$
$$e_4=\frac{c\Delta t/\Delta x+1+p_3}{2\Delta t^2e_0};e_5=\frac{c\Delta t/\Delta x-1-p_3}{2\Delta t^2e_0};e_6=\frac{1}{2\Delta t^2e_0};e_7=\frac{c^2}{4e_0}.$$

Analogous FDTD expressions for the 2nd order DNG-Mur ABC on the other boundaries can be derived in the same manner.

III. NUMERICAL RESULTS

In this section, first numerical results are presented both for 1D and 2D cases where the problem space is filled entirely with DNG medium modelled by identical Lorentz parameters for $\varepsilon_r(\omega),\mu_r(\omega)$ and boundaries on both sides are terminated with proposed DNG-Mur ABCs. In all simulations, a tapered sinusoidal pulse (5-10-5 pulse described in [15]) is used as excitation with a center frequency of $f_s=7.5$ GHz, and inserted at the center of the FDTD grid. The Lorentz type medium parameters are chosen as $\omega_{pe}=\omega_{pm}=\omega_s\sqrt{48/25}$, $\omega_{oe}=\omega_{om}=\omega_s/5$ and $\Gamma_e=\Gamma_m=\omega_s/200$, which yields

a refractive index about -1 at the center frequency $(\omega_s = 2\pi f_s)$. FDTD grid parameters are $\Delta x = 0.067$ cm for 1D case and $\Delta x = \Delta y = 0.2$ cm for 2D case with a time step of 0.5 times the Courant limit. Total FDTD domain is chosen as 1000 grid and 400x400 grid for 1D and 2D scenarios, respectively.

Absorbing performance of the proposed formulations are illustrated via reflections from the DNG-Mur boundaries. The reflection coefficient at an observation point is determined by calculating the test and reference field strength versus time using proposed FDTD formulations in two steps [10]. In the first step, the test field E_{test} is calculated at an observation point 2-cells away from the DNG-Mur boundary. In the second step, incident field E_{inc} is obtained by repeating the same calculations, but now considering a larger domain so that boundary reflected fields cannot reach the observation point during the time window of step one. The reflected field can then be obtained as $E_{ref}(t)=E_{test}(t)-E_{inc}(t)$. Then, the reflection coefficient at each frequency is calculated by dividing the discrete Fourier transforms (DFT) of reflected field and incident fields.

In Fig. 1, frequency spectrum of the incident field is shown together with reflection coefficients obtained using DNG-Mur ABCs in 1D and 2D scenarios. For comparison purposes the reflection coefficients obtained using 10-cell thick DNG-UPML ABCs are also plotted. The computation time and memory requirements for both approaches are listed in Table 1. Our numerical results show that 1D and 2D DNG-Mur ABCs reduce reflections to about -60dB and -50dB level over the 7.1−7.9 GHz band under the main lobe and require less memory and computational time than DNG-UPML simulations.

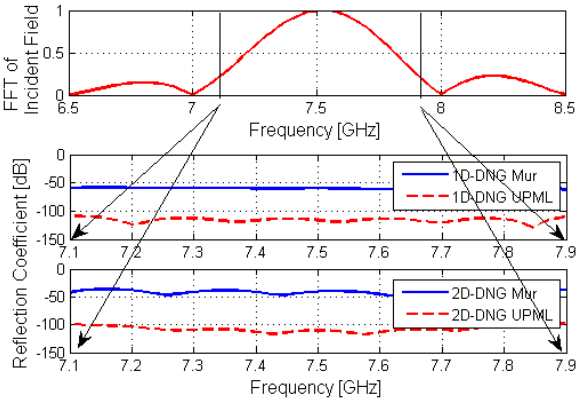

Fig. 1. Frequency spectrum of incident field, and reflection coefficients both for DNG-Mur and DNG-UPML for 1D and 2D scenarios.

We have also calculated the reflection coefficients performance of proposed DNG-Mur ABCs for the case of non-identical Lorentz models using arithmetic mean approach outlined in Sec. IIA. The results obtained with the same parameters for $\chi_e(\omega)$, but $\omega_{pm} = \omega_s$, $\omega_{om} = \omega_s/\sqrt{2}$ and $\Gamma_m = \omega_s/200$ for $\chi_m(\omega)$ are found to differ less than ±3 dB from those shown in Fig. 1, over the entire frequency range.

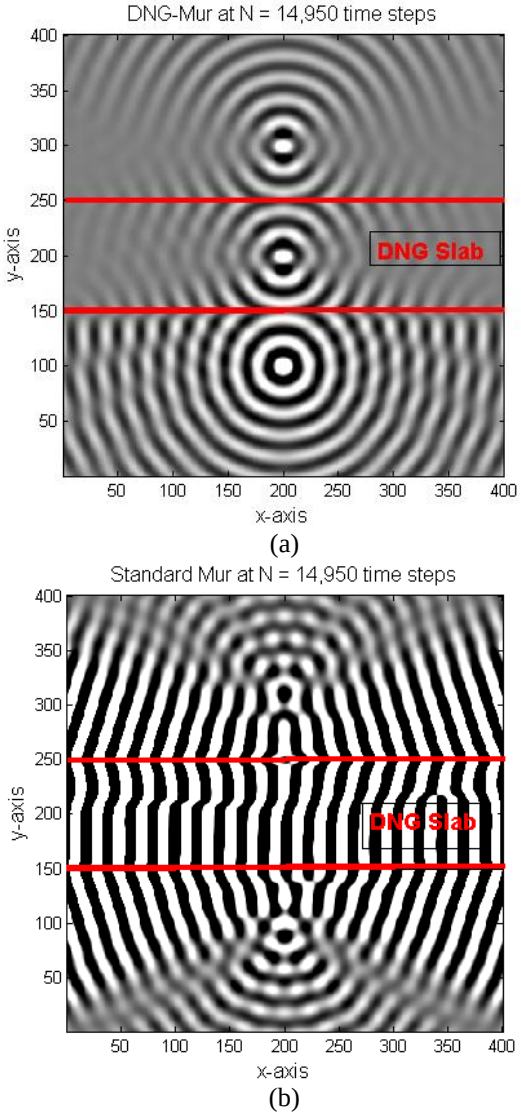

Fig. 2. Snapshot of propagation through DNG slab using: (a) DNG-Mur and (b) standard Mur.

As a second 2D test we consider a DNG slab with a thickness along y-direction about 100Δy imbedded in air, extending infinitely in x, z, and excited by a z-directed line source. We have used 50-1000-50 cycle [15] source at $f_s = 7.5$ GHz. This yields near-perfect match conditions as steady-state conditions set up, and the refractive index of the slab approaches to -1 (-0.9999-

0.0104j). In order to demonstrate the effectiveness of the proposed extension of Mur formalism to DNG media we performed two simulation runs, one using DNG-Mur and the other using Standard-Mur at slab boundaries. For the first simulation, boundaries of the 400x400 grid size computational domain are terminated with standard 2D Mur ABC for air, and with 2D DNG-Mur ABC for the DNG slab boundaries at y-grid points between 150 and 250 (See Fig. 2 (a)). For the second simulation, standard 2D Mur ABC is used at all boundaries (both air and DNG slab, See Fig. 2 (b)). The line source is placed at a point where x=200Δx, y=100Δy, i.e., at a distance 50Δy from the DNG slab for both simulations, and typical outputs are depicted in Fig. 2 (a), Fig. 3 (a), and Fig. 2 (b), Fig. 3 (b), respectively.

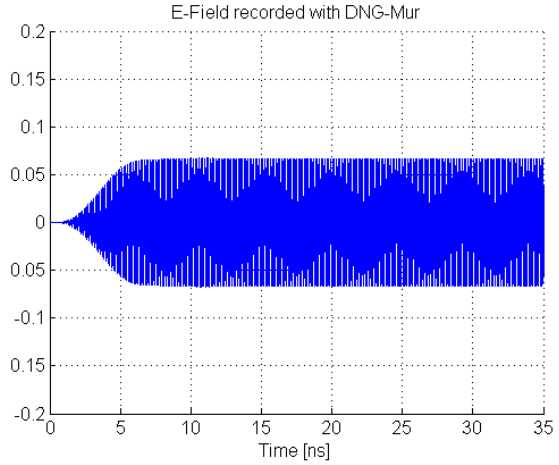

(a)

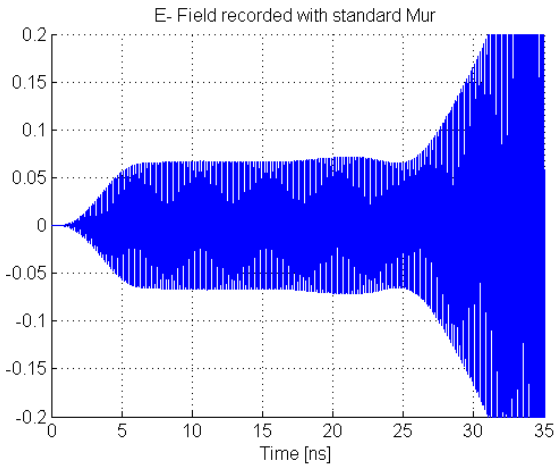

(b)

Fig. 3. Time domain field recorded at an observation point while DNG slab is truncated with a) DNG-Mur and b) Standard Mur.

The snapshot given in Fig. 2 (a) clearly shows the cylindrical wave fronts emanating from the source, as well as from the anticipated image locations [15,16] inside and behind the slab. In Fig. 3 (a) the time history of the E field at an observation point located between source and slab is given which demonstrates the stability of the code when terminating slab boundaries with DNG-Mur. Figure 2 (b) and Fig. 3 (b) correspond to similar outputs obtained when, at slab boundaries, DNG-Mur is replaced with standard Mur. Figure 2 (b) and Fig. 3 (b) show that reflections from improperly terminated boundaries of the DNG slab results in instability after about 10,000 time steps, and completely corrupts field distribution inside the computational domain by 14,950 steps, as shown in Fig. 2 (b).

Table 1: Memory usage and computation time in FDTD simulations for DNG-Mur and DNG-UPML ABCs

FDTD Grid		Time (s)	Memory (MB)
2D Case 1000x1000 cells t=5000Δt	Mur	1693.9	244.45
	UPML	3881.5	516.98
1D Case 1000 cells t=10000Δt	Mur	1.73	0.72
	UPML	2.65	0.87

IV. CONCLUSION

Absorbing boundary conditions based on Mur's approach have been developed for DNG media in 1D and 2D FDTD computational domain. In the presented formulations, DNG slab is modeled with identical Lorentz parameters for $\varepsilon_r(\omega), \mu_r(\omega)$ in frequency dependent one-way wave equations and PLRC method is used to derive FDTD update equations. 1D and 2D simulations demonstrate that the proposed implementations of Mur ABC for terminating DNG media provide stable results and effectively reduce boundary reflections by about 50 dB, which may be acceptable in many applications. Comparison of computational requirements for DNG-Mur and DNG-UPML as listed in Table 1 indicate that the DNG-Mur provides definite advantages both in memory and computation time. The formulations given in this paper are valid for any dispersive media and can be also applied for Drude model.

REFERENCES

[1] G. Mur, "Absorbing boundary conditions for the finite difference approximation of the time-domain electromagnetic-field equations," *IEEE Trans. Electromagn. Compat.*, vol. 23, no. 4, pp.377-382, 1981.

[2] J. P. Berenger, "Three-dimensional perfectly matched layer for the absorption of electromagnetic waves," *J. Computat. Phys.*, vol. 127, pp. 363-379, 1996.

[3] S. D. Gedney, "An anisotropic perfectly matched layer-absorbing medium for the truncation of

FDTD lattices," *IEEE Trans. Antennas Propag*., vol. 44, pp. 1630-1639, Dec. 1996.

[4] M. Kuzuoglu and R. Mittra, "Frequency dependence of the constitutive parameters of causal perfectly matched anisotropic absorbers," *IEEE Microw. Guided Wave Lett*., vol. 6, pp. 447-449, 1996.

[5] J. Roden and S. D. Gedney, "Convolution PML (CPML): An efficient FDTD implementation of the CFS-PML for arbitrary media," *Microw. Opt. Technol. Lett.*, vol. 27, pp. 334-339, 2000.

[6] Y. Mao, A. Z. Elsherbeni, S. Li, and T. Jiang, "Surface impedance absorbing boundary for terminating FDTD simulations," *ACES Journal*, vol. 29, no. 12, pp. 1035-1046, 2014.

[7] Y. Mao, A. Z. Elsherbeni, S. Li, and T. Jiang, "Non-uniform surface impedance absorbing boundary condition for FDTD method," *ACES Express Journal*, vol. 1, no. 7, pp. 197-200, July 2016.

[8] S. D. Gedney, "An anisotropic PML absorbing media for the FDTD simulation of fields in lossy and dispersive media," *Electromagnetics*, vol. 16, no. 4, pp. 399-415, 1996.

[9] S. A. Cummer, "Perfectly matched layer behavior in negative refractive index materials," *IEEE Antennas Wireless Propagat. Lett*., vol. 3, pp. 172-175, 2004.

[10] K. Zheng, W.-Y. Tam, D.-B. Ge, and J.-D. Xu, "Uniaxial PML absorbing boundary condition for truncating the boundary of DNG metamaterials," *PIERL*, vol. 8, 125-134, 2009.

[11] D. Correia and J. M Jin, "3D-FDTD-PML analysis of left-handed metamaterials," *Microw. Opt. Technol. Lett*., vol. 40, no. 3, pp. 201-205, Feb. 2004.

[12] P. Kosmas and C. Rappaport, "A simple absorbing boundary condition for FDTD modeling of lossy, dispersive media based on the one-way wave equation," *IEEE Trans. Antennas Propagat*., vol. 52, no. 9, pp. 2476-2479, Sept. 2004.

[13] D. Kelley and R. J. Luebbers, "Piecewise linear recursive convolution for dispersive media using FDTD," *IEEE Trans. Antennas Propagat.*, vol. 44, no. 6, pp. 792-797, 1996.

[14] A. Pekmezci and L. Sevgi, "FDTD-based metamaterial (MTM) modeling and simulation," *IEEE Antennas and Propagat. Magazine*, vol. 56, no. 5, pp. 289-303, Oct. 2014.

[15] R. W. Ziolkowski and E. Heyman, "Wave propagation in media having negative permittivity and permeability," *Phys. Rev. E*, vol. 64, 056625, 2001.

[16] J. B. Pendry, "Negative refraction makes a perfect lens," *Physical Review Letters*, vol. 85, no. 18, pp. 3966-3969, Oct. 2000.

Aysegul Pekmezci was born in Zonguldak, Turkey, in February 1984. She received a B.S. and an M.S. degree in Electrical and Electronics Engineering from University of Gaziantep, Gaziantep, Turkey in 2007 and 2010. Currently, she is with the Department of Electronics and Communications Engineering, Dogus University at Istanbul, Turkey and pursuing her Ph.D. studies in Institute of Science and Technology of the same university. Her research interests are primarily in the analytical and numerical solutions of electromagnetic wave problems, computational aspects of scattering and interaction with dispersive media.

Ercan Topuz received the M.S. and Ph.D. degrees in Electronics and Communication from Istanbul Technical University, Istanbul, Turkey, in 1965 and 1973, respectively. Currently, he is with the Department of Electronics and Communications Engineering, Dogus University at Istanbul, Turkey. He has authored or co-authored over 70 technical papers in books, journals, and conferences. His research interests include theoretical and computational electromagnetics, microwave/optical devices and systems. Topuz is a Member of the Electromagnetics Academy.

Levent Sevgi has been with Okan University since September 2014. He graduated from Istanbul Technical University (ITU) and completed his Ph.D studies with Prof. Leopold B. Felsen at Weber Research Institute/ New York Polytechnic University. His research study has focused on analytical and numerical methods in electromagnetics. He has published over 170 journal/magazine papers/tutorials and attended nearly 120 international conferences/ symposiums. His two books Complex Electromagnetic Problems and Numerical Simulation Approaches and Electromagnetic Modeling and Simulation were published by the IEEE Press - Wiley in 2003 and 2014, respectively.

Fast Finite-Difference Calculation of Eddy Currents in Thin Metal Sheets

James R. Nagel

Department of Metallurgical Engineering
University of Utah, Salt Lake City, UT 84112, USA
james.nagel@utah.edu

Abstract — Magnetic excitation of eddy currents in a thin metal sheet is a difficult problem that has many useful applications to scrap metal recycling. Using finite-difference approximations on both the curl and divergence of the current density, we develop a numerical algorithm that is simple to implement, quick to solve, and capable of modeling excitation from arbitrary magnetic field distributions. For the special case of a weakly-induced eddy field, the self-inductance terms can be neglected, resulting in a sparse system matrix that is easily inverted. For a strongly-induced eddy field, self-inductance must be included at the cost of a more complex, denser system matrix. The method is validated against the CST EM Studio software suite and produces nearly identical results on a thin-sheet simulation in only a tiny fraction of the time.

Index Terms — Current density, eddy currents, finite-difference method, quasistatics.

I. INTRODUCTION

The excitation of electrical eddy currents in metal objects is a well-known phenomenon with many practical applications. For example, eddy current testing is a form of nondestructive probing that detects the presence of cracks in a metal plate by measuring changes in impedance to a current-carrying coil [1, 2]. Levitation melting is a technology that uses eddy currents to repel particles against gravity to avoid contact contamination with a physical container [3, 4]. Eddy current separation is a popular method for separating nonferrous metal particles from other nonmetallic fluff [5]. Electrodynamic sorting is a recent technology that uses high-frequency electromagnets to separate nonferrous metal particles from other dissimilar metals [6, 7, 8].

For all of its industrial applications, the mathematical theory behind eddy current induction is notoriously complex. Although some canonical problems can be solved analytically [9] (e.g., spheres, cylinders, etc.), many basic geometries are still difficult to model accurately. In particular, the thin metal sheet is especially interesting due to its prevalence among scrap metal particles encountered throughout the recycling industry. Some authors have been able to generate approximate solutions for thin metal rectangles under the assumption of uniform excitation by a magnetic field [10] but only by neglecting the self-inductance of the induced currents. For the purposes of electrodynamic sorting, however, the net force acting on a particle relies on both the nonuniformity of the magnetic field as well as the self-inductance of the induced currents [8, 11].

When analytic solutions are unavailable, the next best alternative is to utilize numerical approximations for the induced eddy currents throughout an object. This is usually accomplished through some variation of the finite-element method (FEM), with many competing formulations to choose from [12, 13]. Generally speaking, however, the majority of such methods tend to fall into one of two distinct categories. The first formalism is commonly referred to as the $\mathbf{A} - \phi$ method because it utilizes on the magnetic vector potential $\mathbf{A}$ and electric scalar potential φ [14]. The second formalism is called the $\mathbf{T} - \Omega$ method because it utilizes the electric vector potential $\mathbf{T}$ and magnetic scalar potential Ω [15].

A key problem with both of these formalisms is the imposition of boundary conditions, which cannot necessarily terminate at the edge of a body of interest [16]. Instead, the simulation must often include a large void of empty space surrounding the particle so that meaningful boundary conditions may be applied far away at near-infinity. As a result, significant computational memory must be devoted to the uninteresting samples of empty space beyond the object of interest. This can be especially wasteful for the case of thin metal sheets, which presumably ought to simplify into much more compact expressions in only two dimensions.

What is needed is a fast, accurate method for calculating the induced eddy current density along a thin metal sheet as it is excited by an arbitrary magnetic field profile. More specifically, we would like a method that only requires sampling along the region of space inside the metal object and that does not waste resources on the empty void of space beyond the particle of interest. To fill that need, this paper reexamines the governing equations of eddy current theory and derives a simplified numerical algorithm accordingly. Rather than invoke the

Submitted On: March 20, 2018
Accepted On: May 19, 2018

use of any specialized potential functions, we may instead solve directly for the desired field components by expressing the problem in terms of divergence and curl. The method shares many similarities with the well-known finite-difference method (FDM), and thus follows a similar derivation to that found in [17]. This makes the algorithm relatively simple to implement by avoiding many of the complex meshing problems typically associated with finite element methods.

II. THEORETICAL BACKGROUND

Figure 1 shows the geometry of interest considered for this work. A rectangular metal sheet with spatially-varying conductivity $\sigma(x,y)$ has length L_x, width L_y, and thickness L_z. The sheet is assumed to be very thin such that $L_z \ll L_x$ and $L_z \ll L_y$. This allows us to consider only the normal component to the magnetic field, since the sheet is too thin to experience any significant excitation by parallel components. We therefore express the impressed magnetic field distribution as $B_i(x,y)\,\hat{\boldsymbol{z}}$, which is assumed to excite the system in a sinusoidal steady state with angular frequency $\omega = 2\pi f$. Our goal is to solve for the eddy current density $\mathbf{J}(x,y)$ induced throughout the plate.

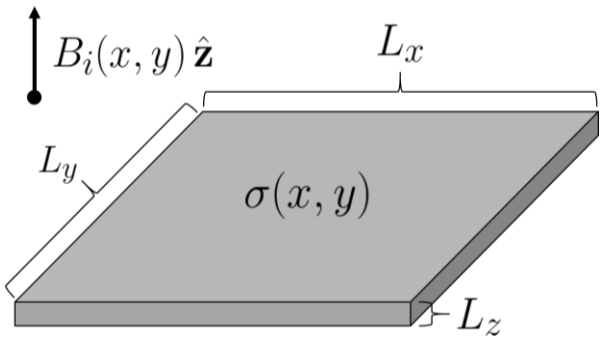

Fig. 1. A thin metal sheet is excited normally by an impressed magnetic field profile $B_i(x,y)\,\hat{\boldsymbol{z}}$.

We begin with Maxwell's curl equations for linear, isotropic, nonmagnetic media in phasor form. Assuming a phasor convention of $Ae^{j\omega t}$, we let $d/dt = j\omega$. Given a magnetic field intensity **B**, electric field intensity **E**, and current density **J**, Ampere's law states that:

$$\nabla \times \mathbf{B} = \mu_0 \mathbf{J} + j\omega\mu_0\epsilon_0 \mathbf{E}\,, \tag{1}$$

where μ_0 is the permeability of free space and ϵ_0 is the permittivity. In the context of eddy current excitation by time-varying magnetic fields, the last term in Ampere's law is assumed to be negligibly small. This condition is commonly known as the quasistatic approximation and allows us to rewrite:

$$\nabla \times \mathbf{B} \approx \mu_0 \mathbf{J}\,. \tag{2}$$

If we now take the divergence of both sides, the curl term vanishes to produce:

$$\nabla \cdot \mathbf{J} = 0\,. \tag{3}$$

What (3) tells us is that no free charges will ever accumulate under quasistatic excitation by a time-varying magnetic field. However, simply knowing the divergence of a vector field does not uniquely define that field. According to the Helmholtz theorem, a unique vector field is only specified if we also know the curl of **J** within a simply connected region, as well as its normal component over the boundary [18].

With such criteria in mind, we now turn our attention to Faraday's law, which states:

$$\nabla \times \mathbf{E} = -j\omega \mathbf{B}\,. \tag{4}$$

Given a conductive material with conductivity σ, Ohm's law further states that $\mathbf{J} = \sigma\mathbf{E}$. Note, however, that it is actually much more convenient to express this law in terms of the resistivity function $\rho = 1/\sigma$ such that $\rho\mathbf{J} = \mathbf{E}$. Substitution back into Faraday's law then reveals:

$$\nabla \times (\rho\mathbf{J}) = -j\omega \mathbf{B}\,. \tag{5}$$

Bear in mind that we are explicitly assuming $\rho(x,y)$ might vary as a function of position and therefore cannot be removed from the curl operation as a constant coefficient.

When taken together, (3) and (5) appear to provide a near-complete description for the divergence and curl of **J**. The only concern is that the curl acts on the quantity $\rho\mathbf{J}$ rather than just **J** alone. Fortunately, this does not present a significant challenge in that ρ can be treated as a sectionally-constant function over the domain of interest, thereby dropping out of the curl operation throughout each region. In practice, however, it will be far more convenient to simply leave (5) in its present form and work accordingly.

III. WEAK-EDDY APPROXIMATION

When modeling the excitation of eddy currents, the magnetic field **B** is expressed as a linear superposition between two distinct contributions,

$$\mathbf{B} = \mathbf{B}_i + \mathbf{B}_e\,. \tag{6}$$

The first contribution is called the impressed magnetic field $\mathbf{B}_i$ and is interpreted as some arbitrary excitation field imposed onto the system by outside forces. The second contribution is called the induced magnetic field $\mathbf{B}_e$, or simply the eddy field, and is created by the presence of moving charges within our domain of interest. While the impressed field $\mathbf{B}_i$ can be treated as a mathematical given, the eddy field $\mathbf{B}_e$ is dependent on the current distribution **J**. This relationship is governed by the Biot-Savart law:

$$\mathbf{B}_e(\mathbf{r}) = \frac{\mu_0}{4\pi}\int_V \frac{\mathbf{J}(\mathbf{r}')\times(\mathbf{r}-\mathbf{r}')}{|\mathbf{r}-\mathbf{r}'|^3}\,dV'\,, \tag{7}$$

where $\mathbf{r}$ is an arbitrary observation point and $\mathbf{r}'$ denotes the set of all points inside the volume V that carry

electrical current. The complication presented by (7) is that we cannot solve for **J** without first solving for $\mathbf{B}_e$. However, we cannot solve for $\mathbf{B}_e$ unless we also possess a solution for **J**. A complete mathematical solution therefore requires **J** and $\mathbf{B}_e$ to be solved together simultaneously.

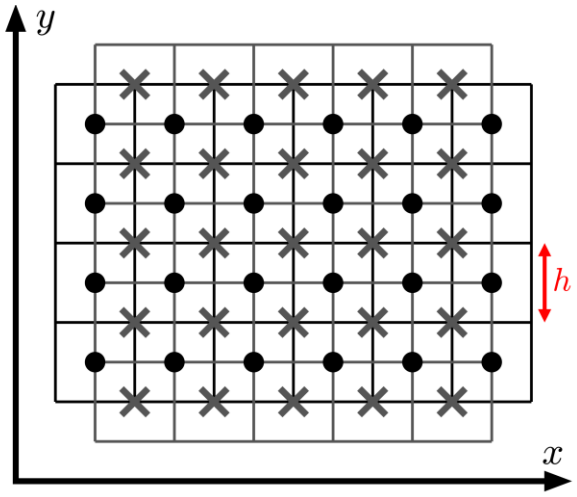

Fig. 2. Staggered mesh positions for sampling vector components of the conduction current density. The Xs denote samples along J_x while dots represent samples along J_y.

Before tackling the simultaneous solution of **J** and $\mathbf{B}_e$, it will first be instructive to consider the special case where $\mathbf{B}_e$ is not a significant factor in relation to $\mathbf{B}_i$. This may occur, for example, when the resistivity ρ is very large, thereby preventing charges from flowing intensely enough to generate any significant self-inductance. A similar situation also occurs when ω is very small, since the changing magnetic fields are too slow to generate significant charge flow. One other scenario occurs when the sheet thickness L_z is very thin, since an infinitely thin sheet of current density technically carries no current. All of these scenarios are mathematically equivalent in that the induced field $\mathbf{B}_e$ is far too weak to compete with the applied magnetic field $\mathbf{B}_i$. In this weak-eddy approximation, the curl equation for **J** may be expressed as:

$$\nabla \times (\rho \mathbf{J}) \approx -j\omega \mathbf{B}_i \quad (|\mathbf{B}_i| \gg |\mathbf{B}_e|)\,. \tag{8}$$

The following sections will first focus exclusively on the weak-eddy approximation by deriving a simultaneous numerical solution to (3) and (8). Doing so will lay the mathematical foundation for discretization of various field components and the subsequent numerical solution that arises. We shall then build on that foundation in later sections by dropping the weak-eddy approximation and deriving a complete numerical solution for **J**.

IV. DISCRETIZATION SCHEME

We begin building our numerical algorithm by establishing a mesh of position coordinates for sampling the vector components J_x and J_y. Figure 2 shows an example of how such a grid might look along a small section of the domain. The Xs denote samples along the J_x function while dots denote samples in J_y. Each sample represents a rectangular block of uniform current density with length and width h but depth L_z. The most important feature of the mesh, however, is the way in which $\mathbf{J}_x$ and $\mathbf{J}_y$ are staggered in space. The significance of this convention will become clear later on when we attempt to calculate the curl and divergence of **J**.

In order to facilitate indexing, it is helpful to define a short-hand notation for each sample along the mesh. We represent the *n*th and *m*th grid samples along *x* and *y* using:

$$x_n = nh \quad (n = 1, 2, 3, \ldots)\,, \tag{9}$$
$$y_m = mh \quad (m = 1, 2, 3, \ldots)\,. \tag{10}$$

Since the grid samples are staggered from each other in space, it helps to note that half-step increments also satisfy:

$$x_{n+1/2} = (n + 1/2)h\,, \tag{11}$$
$$y_{m+1/2} = (m + 1/2)h. \tag{12}$$

We now reference the staggered mesh of current density through a simple indexed notation given by:

$$J_x^{n,m} = J_x\left(x_n, y_{m+1/2}\right)\,, \tag{13}$$
$$J_y^{n,m} = J_y\left(x_{n+1/2}, y_m\right)\,. \tag{14}$$

V. DIVERGENCE STENCIL

With the sample grid formally defined, we are now ready to approximate (3) in terms of a finite-difference stencil. We begin by dividing the domain into a set of primitive volumes, or cells, each of which is defined by a uniform resistivity ρ_{nm}. An example of such a grid is depicted in Figs. 3 and 4 wherein each cell represents a unique volume denoted as Ω_{nm}. The key is to place all J_x samples on the left and right faces of the cell whereas all J_y samples are placed along the top and bottom. It is also important to note how the far-left and far-right boundaries of the metal plate are occupied only by samples in J_y, with the top and bottom boundaries occupied by samples in J_x. This allows us to implicitly force all normal components of the current density to be zero at the boundaries of the domain, thereby satisfying the last requirement of Helmholtz's theorem. Equivalently, one could also think of this as imposing a Dirichlet boundary condition along the edges of the domain for all normal components to the current density.

We now explicitly write out the divergence of **J** in terms of individual vector components. Recalling the thin-sheet approximation to our model, we let $\partial/\partial z = 0$ so that,

$$\nabla \cdot \mathbf{J} = \frac{\partial J_x}{\partial x} + \frac{\partial J_y}{\partial y} = 0\,. \tag{15}$$

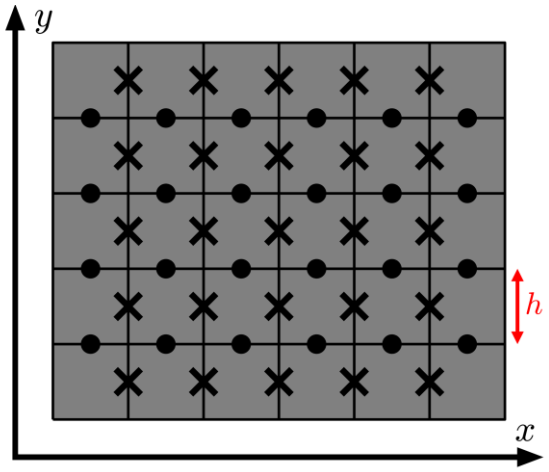

Fig. 3. Divergence mesh with cells of constant resistivity ρ_{nm}.

Applying the central-difference approximation about the $(x_{n+1/2}, y_{n+1/2})$ coordinate then produces:

$$\frac{J_x^{n,m} - J_x^{n-1,m}}{h} + \frac{J_y^{n,m} - J_y^{n,m-1}}{h} = 0\,, \tag{16}$$

or equivalently,

$$J_x^{n,m} - J_x^{n-1,m} + J_y^{n,m} - J_y^{n,m-1} = 0\,. \tag{17}$$

It is interesting to note that we could also obtain an equivalent expression through the use of finite-integration techniques (FIT) [19]. In fact, this is often the preferred method when dealing with variable-coefficient expressions of differential equations [17]. The process begins by calculating the volume integral of (3) over the sub-volume Ω_{nm} to find:

$$\iiint_{\Omega_{nm}} \nabla \cdot \mathbf{J}\, dV = 0\,. \tag{18}$$

By applying the divergence theorem, we can rewrite this expression as the surface integral:

$$\iint_{\partial\Omega_{nm}} \mathbf{J} \cdot d\mathbf{S} = 0\,, \tag{19}$$

where $\partial\Omega_{nm}$ indicates the surface enclosing Ω_{nm} and $d\mathbf{S}$ indicates the outward-pointing differential unit normal to that surface. Since the current density only points along the *x*- and *y*-directions, the contributions to the surface integral along $\pm\hat{\mathbf{z}}$ are zero. Furthermore, since each sample in J_x and J_y is assumed to be constant over its respective region, the complete integral evaluates to the simple expression:

$$J_x^{n,m} - J_x^{n-1,m} + J_y^{n,m} - J_y^{n,m-1} = 0\,. \tag{20}$$

which is identical to (17). This shows how FDM and FIT can actually be viewed as two complementary perspectives on the same mathematical problem.

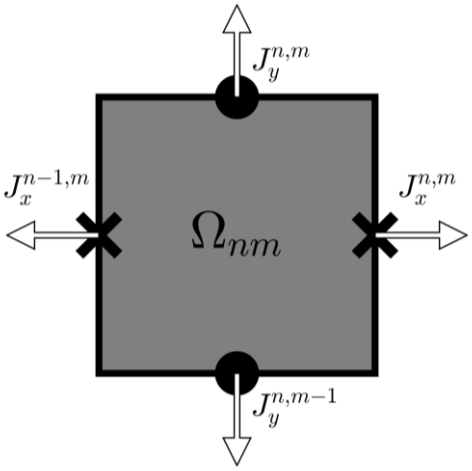

Fig. 4. Individual divergence cell with outward unit normal vectors indicated around the edges.

For the special case of a divergence cell at the far edge of the metal plate, we can implicitly impose boundary conditions by forcing the normal component of the current density to zero. This condition is a direct consequence of (5), which requires that no current be allowed to flow into or out of the edges of the metal plate. For example, at the far-left edge of the metal plate, the $J_x^{n-1,m}$ term contributes nothing and leaves only,

$$J_x^{n,m} + J_y^{n,m} - J_y^{n,m-1} = 0\,. \tag{21}$$

Similar expressions also apply to the top, bottom, and right boundaries of the metal plate as well as the four corner cases.

VI. CURL STENCIL

Looking at the template in Fig. 3, we notice that there are 6×5 divergence cells for a total of 30 divergence equations. However, there are 25 samples in J_x and 24 samples in J_y that need to be calculated. We therefore have only 30 equations with 49 unknowns—an underdetermined system. Speaking more generally, an arbitrary rectangular grid of $N_x \times N_y$ cells will produce $N_d = N_x N_y$ divergence equations. However, the total number of J_x samples is $n_{jx} = (N_x - 1)N_y$, and the total number of J_y samples is $n_{jy} = N_x(N_y - 1)$. The total number of unknown samples N_u is thus:

$$N_u = 2N_xN_y - N_x - N_y\,. \tag{22}$$

This leaves us with a deficit of $N_xN_y - N_x - N_y$ equations before we can arrive at a unique solution.

The reason for our equation deficit is that, as noted earlier, merely specifying the divergence for some vector field does not uniquely define it. It is only when we

specify both the divergence and curl simultaneously (as well as the normal component along the boundary) that we produce a uniquely-defined vector field. To that end, we shall next introduce the curl cells depicted in Fig. 5. Unlike the divergence cells, however, the curl cells are shifted in space so that J_y samples now lie on the left and right edges while J_x samples lie at the top and bottom. We may also assume that the total magnetic field B_{nm} throughout each cell is a constant value. To differentiate between curl cells and divergence cells, the regions of curl are denoted with a prime notation using Ω'_{nm}.

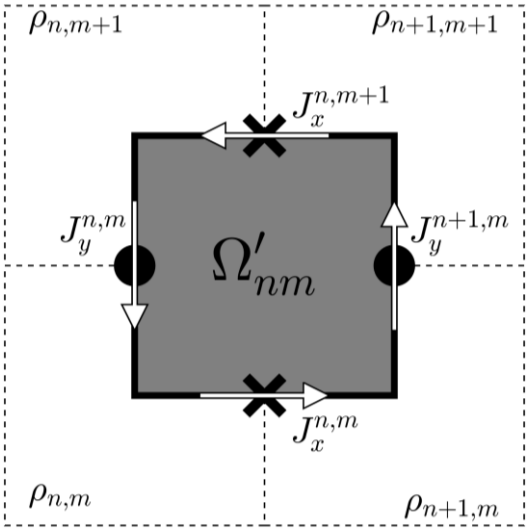

Fig. 5. Individual curl cell with tangential unit vectors indicated. Corresponding resistivity blocks are also indicated.

Unlike the divergence case, a direct finite-difference approximation to (5) is somewhat counter-intuitive due to the product $\rho\mathbf{J}$. This is a classic instance where finite-integration can serve as a more powerful generalization of FDM. Simply begin by calculating the flux integral of (8) across the area within Ω'_{nm} to find:

$$\iint_{\Omega'_{nm}} \nabla \times (\rho\mathbf{J}) \cdot d\mathbf{S} = -j\omega \iint_{\Omega'_{nm}} \mathbf{B}_i \cdot d\mathbf{S}\,, \qquad (23)$$

where $d\mathbf{S} = dxdy\,\hat{\mathbf{z}}$ is the differential unit normal across Ω'_{nm}. By applying Stokes' theorem to the left-hand side, we can convert the surface integral into a contour integral with the form:

$$\oint_{\partial\Omega'_{nm}} (\rho\mathbf{J}) \cdot d\boldsymbol{\ell} = -j\omega \iint_{\Omega'_{nm}} \mathbf{B}_i \cdot d\mathbf{S}\,. \qquad (24)$$

The contour vectors for $d\boldsymbol{\ell}$ are likewise indicated in Fig. 5 and point along the clockwise direction.

Before we can compute the curl integrals, we must first clarify the sampling along resistivity. Since each sample of current density flows across the boundary between two resistivity cells, there is no clear choice for ρ_{nm} to use with (24). We can solve this problem by simply averaging the two resistivities together along each sample. In terms of our grid stencil, this would could be written as:

$$\rho_x^{n,m} = 0.5\left(\rho_{n,m} + \rho_{n+1,m}\right), \qquad (25)$$
$$\rho_y^{n,m} = 0.5\left(\rho_{n,m} + \rho_{n,m+1}\right). \qquad (26)$$

Notice how this naturally lends itself to the introduction of anisotropic materials wherein each sample along J_x and J_y has its own resistivity expressed by ρ_x and ρ_y.

We are now ready to apply (24) to the finite-difference stencil. Assuming that each curl cell is excited by a constant magnetic field intensity B_{nm}, the curl expression evaluates to:

$$\rho_y^{n+1,m} J_y^{n+1,m} - \rho_y^{n,m} J_y^{n,m} + \rho_x^{n,m} J_x^{n,m} - \rho_x^{n,m+1} J_x^{n,m+1} = -j\omega h B_{nm}\,. \qquad (27)$$

Evaluating the above expression over all curl cells will then add $N_c = (N_x - 1)(N_y - 1)$ further equations to our system. When combined with the divergence equations, the total number N_e of equations becomes:

$$N_e = 2N_xN_y - N_x - N_y + 1\,. \qquad (28)$$

It is surprising to note that $N_e = N_u + 1$. This seems to indicate one extra equation more than we need, which might lead one to conclude our system is over-determined. Fortunately, the reality is that we actually have one more divergence equation than necessary. To see why, it helps to consider the two equations $a = b$ and $b = c$. Given such information, we can naturally deduce that $a = c$. From the perspective of a linear system, however, any explicit statement of $a = c$ is technically redundant information. By analogy, the set of all divergence equations likewise possesses the same mathematical redundancy. If $N_d - 1$ expressions of divergence are specified, conservation of charge implicitly tells us the flow of current throughout the last grid cell. This means N_xN_y total divergence equations are possible, but only $N_xN_y - 1$ of them contain unique information. We may therefore discard one divergence equation (any one we like, in fact), and the total number of equations becomes:

$$N_e = 2N_xN_y - N_x - N_y = N_c + N_d - 1. \qquad (29)$$

We now have $N_e = N_u$, and the system is guaranteed a unique solution.

VII. BLOCK MATRIX SOLUTION

To finalize the solution to our eddy current problem, it is necessary to assemble all instances of (17) and (27)

into a complete linear system. We begin by collecting all samples of J_x and J_y into the two vectors $\mathbf{u}_x$ and $\mathbf{u}_y$. Recalling that $n_{jx} = (N_x - 1)N_y$ and $n_{jy} = N_x(N_y - 1)$, we can write these vectors as:

$$\mathbf{u}_x = \left[J_x^1, J_x^2, \ldots, J_x^{n_{jx}} \right]^T, \tag{30}$$

$$\mathbf{u}_y = \left[J_y^1, J_y^2, \ldots, J_y^{n_{jy}} \right]^T. \tag{31}$$

Note that indexing in this context requires a consistent mapping function between every $J_x^{n,m}$ sample on the rectangular grid to a unique J_x^i sample along a linear array. Following the same convention, the forcing vector $\mathbf{b}$ is likewise expressed as:

$$\mathbf{b} = -j\omega h \left[B_1, B_2, \ldots, B_{N_c} \right]^T, \tag{32}$$

where each B_i maps to some unique B_{nm} and denotes the constant magnetic field intensity exciting the ith curl cell.

We are now ready to formulate the $N_d - 1$ divergence equations expressed by (17) as a single matrix equation with the form:

$$\mathbf{D}_x \mathbf{u}_x + \mathbf{D}_y \mathbf{u}_y = \mathbf{0}\,, \tag{33}$$

where $\mathbf{D}_x$ and $\mathbf{D}_y$ are called the divergence matrices with $\mathbf{0}$ representing a vector of all zeros. The $\mathbf{D}_x$ matrix has $N_d - 1$ rows and n_{jx} columns, while $\mathbf{D}_y$ has $N_d - 1$ rows and n_{jy} columns. Both matrices are also highly sparse, with only two nonzero elements at most per row.

Moving on to the curl cells, we can assemble all instances of (27) into a system of N_c linear equations. The outcome can also be written as a matrix-vector equation with the form:

$$\mathbf{C}_x \mathbf{u}_x + \mathbf{C}_y \mathbf{u}_y = \mathbf{0}\,, \tag{34}$$

where $\mathbf{C}_x$ and $\mathbf{C}_y$ are called the curl matrices. Both matrices have exactly N_c, but n_{jx} and n_{jy} columns, respectively. If we then combine (33) and (34) together, the result is a block-matrix equation with the form:

$$\begin{bmatrix} \mathbf{C}_x & \mathbf{C}_y \\ \mathbf{D}_x & \mathbf{D}_y \end{bmatrix} \begin{bmatrix} \mathbf{u}_x \\ \mathbf{u}_y \end{bmatrix} = \begin{bmatrix} \mathbf{b} \\ \mathbf{0} \end{bmatrix}. \tag{35}$$

A complete solution is thus found by inverting (35) and extracting all J_x and J_y samples accordingly.

Although the literature does not yet contain any exact solutions for the eddy current density along a metal rectangle, there does exist an exact solution for the weakly-induced eddy current along a metal disk. Given a disk with radius a and conductivity σ, a uniform magnetic field B_0 exciting the disk at a frequency of f will induce the eddy current **J** satisfying:

$$\mathbf{J}(r) = -\hat{\boldsymbol{\phi}}\, 2j\pi f \sigma B_0 r/2\,, \tag{36}$$

where r is the radial distance from the center of the disk and $\hat{\boldsymbol{\phi}}$ is the unit angular vector. Note that this expression is true for any thickness L_z since there is no self-inductance to account for.

Figure 6 shows a sample calculation of the weakly-induced eddy current density along a metal disk with 2-cm radius. The frequency of excitation was set to $f = 100$ Hz with a uniform magnetic field intensity of $B_0 = 100$ mT. To mimic the geometry of a disk on a rectangular simulation area, the region inside the disk was set to a conductivity of $\sigma = 1.0$ MS/m while the regions beyond the disk were set to a very small value of only $\sigma = 1.0$ S/m. Note that we cannot directly set $\sigma = 0$ in this region without introducing a singularity into the matrix equation. Looking at (27), a point of zero conductivity would introduce infinite resistivity and thus render the matrix non-invertible. Likewise, the resistivity cannot be set to zero, either, or else similar singularities would ensue.

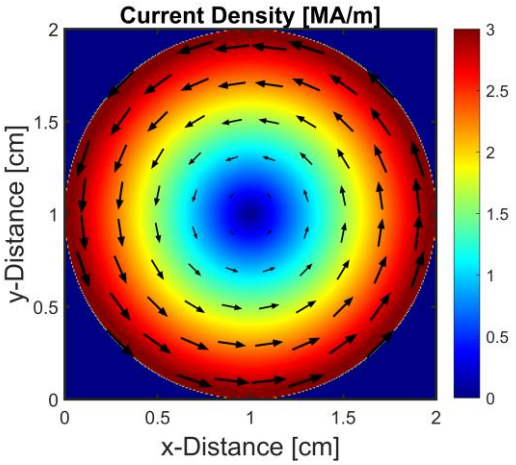

Fig. 6. Induced eddy current density at time $\omega t = \pi/2$ along a metal disk with 2 cm radius and electrical conductivity $\sigma = 1.0$ MS/m. The frequency of excitation is $f = 100$ Hz with a uniform magnetic field intensity of $B_0 = 100$ mT.

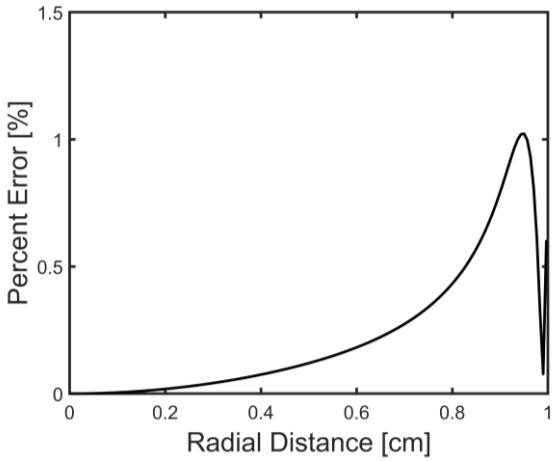

Fig. 7. Percent error between the induced eddy current in Fig. 6 and the analytic expression (36).

For comparison, Fig. 7 plots the percent error as a function of radial distance along the $y = 0$ axis. Since the matrix expression in (35) is highly sparse, the simulation in Fig. 6 could be meshed with an extremely fine resolution of 301×301 cells. The result is very high accuracy in the calculation, with error only reaching 1% near the edge of the disk. This is primarily a result of stair-stepping error that arises from using square cells to approximate a curved boundary, and it is generally unavoidable when utilizing finite-difference schemes that rely on rectangular meshing.

VIII. BLOCK AVERAGING

Once a solution for all J_x and J_y has been obtained, it is often convenient to impose a final post-processing step onto the result. The goal is to adjust the initial placement of samples from a staggered grid onto a consistent grid of positions. Inspired by a similar procedure to that found in [17], one easy way to accomplish this is by simply averaging samples together around the centers of the divergence cells around each Ω_{nm}. The result is a new set of J_x' and J_y' samples that occupy the same position and thus can be plotted meaningfully onto a graphical display. Mathematically, we write this operation as simply,

$$J_x'\left(x_{n+1/2}, y_{m+1/2}\right) = 0.5\left(J_x^{n-1,m} + J_x^{n,m}\right), \quad (37)$$

$$J_y'\left(x_{n+1/2}, y_{m+1/2}\right) = 0.5\left(J_y^{n,m-1} + J_y^{n,m}\right). \quad (38)$$

Note how this places the averaged samples along a new grid at the centers of the divergence blocks. Samples along the edge of the domain (e.g., $J_x^{0,m}$) are simply assumed to be zero.

IX. SELF-INDUCTANCE

Let us now consider the implications of self-inductance by dropping the weak-eddy approximation. We express the eddy field $\mathbf{B}_e$ in terms of a magnetic vector potential vector $\mathbf{A}_e$ where $\mathbf{B}_e = \nabla \times \mathbf{A}_e$. The curl equation (5) then satisfies:

$$\nabla \times (\rho \mathbf{J}) + j\omega \nabla \times \mathbf{A}_e = -j\omega \mathbf{B}_i \,. \quad (39)$$

As we did with (23), we integrate around some arbitrary surface Ω_{nm}' to find:

$$\iint_{\Omega_{nm}'} \nabla \times (\rho \mathbf{J}) \cdot d\mathbf{S} + j\omega \iint_{\Omega_{nm}'} \nabla \times \mathbf{A}_e \cdot d\mathbf{S} = -j\omega \iint_{\Omega_{nm}'} \mathbf{B}_i \cdot d\mathbf{S}. \quad (40)$$

Applying Stokes' theorem to the left-hand side then leads to:

$$\oint_{\partial\Omega_{nm}'} (\rho \mathbf{J} + j\omega \mathbf{A}_e) \cdot d\boldsymbol{\ell} = -j\omega \iint_{\Omega_{nm}'} \mathbf{B}_i \cdot d\mathbf{S} \,. \quad (41)$$

Noting the similarity between (24) and (41), we have only to account for the vector potential field expressed by $\mathbf{A}_e$. This is accomplished by sampling the *x*- and *y*-components of $\mathbf{A}_e$ along the same staggered grid as J_x and J_y. Assuming constant values throughout each cell, we quickly find:

$$\begin{aligned} &+\rho_y^{n+1,m} J_y^{n+1,m} && -\rho_y^{n,m} J_y^{n,m} \\ &+\rho_x^{n,m} J_x^{n,m} && -\rho_x^{n,m} J_x^{n,m+1} \\ &+j\omega A_y^{n+1,m} && -j\omega A_y^{n,m} \\ &+j\omega A_x^{n,m} && -j\omega A_x^{n,m+1} = -j\omega h B_{nm}. \end{aligned} \quad (42)$$

The immediate consequence of accounting for the eddy fields in A_x and A_y is that we have now doubled the number of unknowns in our linear system. We therefore need another N_u equations in order to maintain a unique solution. This is accomplished by expressing the Biot-Savart law in terms of magnetic vector potential using [20]:

$$\mathbf{A}_e(\mathbf{r}) = \frac{\mu_0}{4\pi} \int \frac{\mathbf{J}(\mathbf{r}')}{|\mathbf{r} - \mathbf{r}'|} dV' \,. \quad (43)$$

Splitting the fields into *x*- and *y*-components, we may explicitly write this as:

$$\mathrm{A}_x(\mathbf{r}) = \frac{\mu_0}{4\pi} \int \frac{J_x(\mathbf{r}')}{|\mathbf{r} - \mathbf{r}'|} dV', \quad (44)$$

$$\mathrm{A}_y(\mathbf{r}) = \frac{\mu_0}{4\pi} \int \frac{J_y(\mathbf{r}')}{|\mathbf{r} - \mathbf{r}'|} dV' \,. \quad (45)$$

The importance of (44) and (45) is that we can now derive the necessary information for a unique solution. Using the finite-difference stencil as a guide, we express each integral as a finite sum along each grid cell in the domain. Recalling that each sample in J_x and J_y is represented as a uniform block of length/width h and a thickness L_z, we write out each vector potential sample as:

$$A_x^{n,m} = \frac{\mu_0 h^2 L_z}{4\pi} \sum_{\ell,k} \frac{J_x^{\ell,k}}{\sqrt{(x_\ell - x_n)^2 + (y_\ell - y_k)^2}}, \quad (46)$$

$$A_y^{n,m} = \frac{\mu_0 h^2 L_z}{4\pi} \sum_{\ell,k} \frac{J_y^{\ell,k}}{\sqrt{(x_\ell - x_n)^2 + (y_\ell - y_k)^2}}. \quad (47)$$

A special exception occurs when $\ell = n$ and $k = m$. In this case, we need to evaluate the full integral,

$$\int_{-L_z/2}^{+L_z/2} \int_{-h/2}^{+h/2} \int_{-h/2}^{+h/2} \frac{dxdydz}{\sqrt{x^2 + y^2 + z^2}} \,. \quad (48)$$

It is unfortunate that the above expression has no closed-form solution. It can, however, be evaluated numerically with arbitrary degrees of precision. For this work, we found that the basic midpoint rule provides reasonable accuracy in a short amount of time.

With the addition of (44) and (45), we are now ready to express the complete solution with self-inductance.

Begin by defining the unknown vectors $\mathbf{a}_x$ and $\mathbf{a}_y$ in a similar vein to $\mathbf{u}_x$ and $\mathbf{u}_y$ such that,

$$\mathbf{a}_x = \left[A_x^1, A_x^2, \ldots, A_x^{n_{jx}}\right]^T, \tag{49}$$

$$\mathbf{a}_y = \left[A_y^1, A_y^2, \ldots, A_y^{n_{jy}}\right]^T. \tag{50}$$

This now allows us to simultaneously solve for every A_x and A_y sample alongside the J_x and J_y. Writing out the complete system of equations, we find a block-matrix equation with the form of:

$$\begin{bmatrix} \mathbf{C}_x & \mathbf{C}_y & \mathbf{N}_x & \mathbf{N}_y \\ \mathbf{D}_x & \mathbf{D}_y & \mathbf{0} & \mathbf{0} \\ \mathbf{M}_x & \mathbf{0} & \mathbf{I} & \mathbf{0} \\ \mathbf{0} & \mathbf{M}_y & \mathbf{0} & \mathbf{I} \end{bmatrix} \begin{bmatrix} \mathbf{u}_x \\ \mathbf{u}_y \\ \mathbf{a}_x \\ \mathbf{a}_y \end{bmatrix} = \begin{bmatrix} \mathbf{b} \\ \mathbf{0} \\ \mathbf{0} \\ \mathbf{0} \end{bmatrix}, \tag{51}$$

where $\mathbf{I}$ denotes an identity matrix and $\mathbf{0}$ indicates a matrix (or vector) of all zeros. The matrices $\mathbf{N}_x$ and $\mathbf{N}_y$ can be referred to as the vector-potential matrices, or perhaps the self-inductance matrices, because they arise from the added self-inductance terms in (42). Like the curl matrices $\mathbf{C}_x$ and $\mathbf{C}_y$, these matrices are highly sparse and therefore add little in terms of computational complexity. The last two matrices, $\mathbf{M}_x$ and $\mathbf{M}_y$, are called the Biot-Savart matrices and express the information contained by (46) and (47). Unfortunately, these matrices are completely full and therefore add significant computational cost to the final inversion. The result, however, is a complete expression of eddy current density $\mathbf{J}$ along the metal sheet with full account taken for self-inductance.

An immediate concern with the matrix equation described by (51) is the presence of four scalar fields that need to be solved for simultaneously. Fortunately, we are not really interested in the actual solutions for $\mathbf{a}_x$ and $\mathbf{a}_y$ and can thus remove them through simple substitution. The resulting matrix equation is a far more compact expression given by:

$$\begin{bmatrix} (\mathbf{C}_x - \mathbf{N}_x\mathbf{M}_x) & (\mathbf{C}_y - \mathbf{N}_y\mathbf{M}_y) \\ \mathbf{D}_x & \mathbf{D}_y \end{bmatrix} \begin{bmatrix} \mathbf{u}_x \\ \mathbf{u}_y \end{bmatrix} = \begin{bmatrix} \mathbf{b} \\ \mathbf{0} \end{bmatrix}. \tag{52}$$

A key advantage to (52) is that the system matrix is entirely geometry-dependent. It therefore need only be inverted once, and the resulting eddy currents can be calculated rapidly under any arbitrary forcing function contained within $\mathbf{b}$. This can be especially useful when tracking the trajectory of a metal particle as it passes over an eddy current separator. Each small increment in time requires a fresh calculation of force and torque due to changes in $\mathbf{B}_i$ over position. Fortunately, the system matrix remains identical with each step and thus does not require repeated inversions.

X. VALIDATION

To validate the numerical algorithm presented here, we ran a side-by-side comparison between FDM and the Computer Simulation Technology (CST) EM Studio software suite [21]. The model was comprised of a rectangular metal sheet defined by the physical dimensions $L_x = 2.0$ cm, $L_y = 1.0$ cm, and $L_z = 0.1$ cm with a conductivity of $\sigma = 5.0$ MS/m. The magnetic field exciting the sheet was set to a uniform field profile with amplitude $B_0 = 100$ mT at a frequency of $f = 10$ kHz.

Figure 8 shows the results of the two simulations when sampled at a grid spacing of $h = 0.5$ mm. Since the induced currents are strongly out of phase with the applied field, the results had to be shifted in phase by 90° before rendering the real part of $\mathbf{J}$. For a more precise inspection, Fig. 9 shows both the real and imaginary components of J_y at $t = 0$ along a horizontal cut through the center of the rectangular sheets.

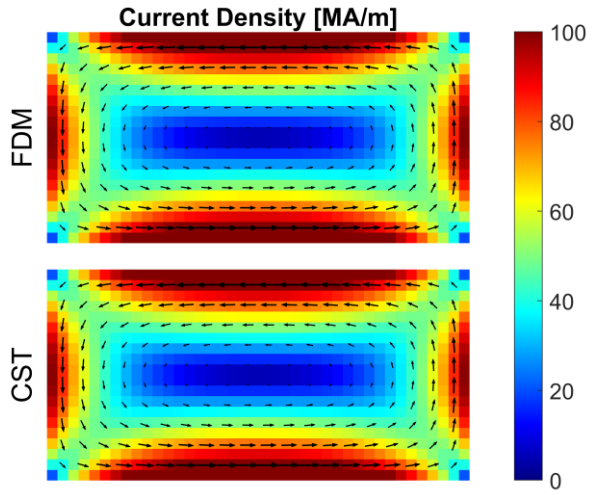

Fig. 8. Induced eddy currents in a thin metal sheet at phase angle $\phi = 90°$. The top solution was calculated using FDM and the bottom solution was calculated using commercial software (CST).

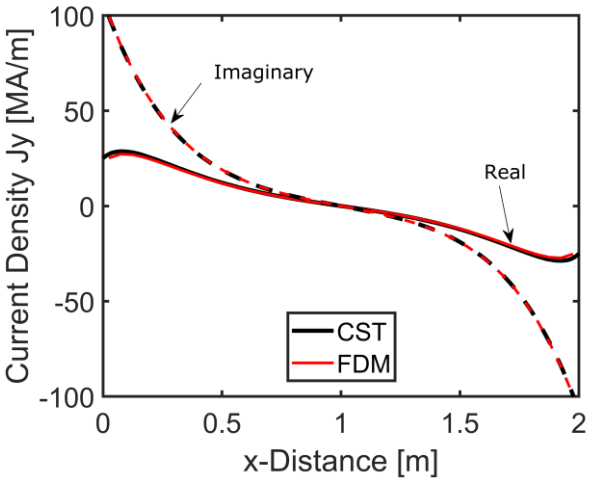

Fig. 9. Real and imaginary components of J_y at $t = 0$ along a horizontal cut down the center of the rectangular metal sheet.

Results from the comparison show very strong agreement, thereby validating the finite-difference approach to eddy current calculations. Any errors in the FDM calculation are primarily the result of using rectangular blocks of constant current density to approximate the true values within. Other errors also accumulate from imperfections in the numerical integration used to solve (44) and (45), as well as the thin-sheet approximation. The key metric of interest, however, is computational time. Since CST is based on the $\mathbf{A} - \varphi$ formalism, a thin metal sheet had to be placed within a three-dimensional void of empty space. As a result, the total number of elements was quite large (31,031 tetrahedrons), and a typical simulation required approximately 60 seconds to complete on a standard laptop computer. In contrast, the FDM model need only sample the metal sheet in isolation and thus required only 800 divergence cells. Consequently, the total time to build the system matrix and solve for the current density was barely 0.5 seconds using standard Matlab sub-routines.

XI. DISCUSSION

Although this work has focused exclusively on the problem of thin metal sheets, there is no reason why it cannot be expanded out to a complete, three-dimensional formalism. Such an algorithm would have a distinct advantage over potential-based formalisms in that the simulation boundary can terminate at the edge of a body of interest. The key trade-off, however, is a forfeiture of the sparse system matrix that must be inverted. Since every sample in the FDM algorithm is dependent on every other sample, the resulting system matrix is necessarily going to be full. This means the computational complexity is necessarily $O(N^3)$ when using Gauss-Jordan elimination to invert an $N \times N$ system matrix. In the future, however, it may be possible to circumvent this limitation through iterative-based inversion methods rather than direct inversion of the full matrix.

ACKNOWLEDGEMENTS

This work was funded by the United States Advanced Research Project Agency-Energy (ARPA-E) METALS Program under cooperative agreement grant DE-AR0000411. The author would also like to thank Professor Raj Rajamani, Jaclyn Ray, and Dawn Sweeney for their insightful edits and proof-reading.

REFERENCES

[1] C. V. Dodd and W. E. Deeds, "Analytical solutions to eddy-current probe-coil problems," *Journal of Applied Physics*, vol. 39, no. 6, pp. 2829-2838, 1968.

[2] J. R. Bowler, "Eddy-current interaction with an ideal crack. 1: The forward problem," *Journal of Applied Physics*, vol. 75, no. 12, pp. 8128-8137, 1994.

[3] E. C. Okress, D. M. Wroughton, G. Comenetz, P. H. Brace, and J. C. R. Kelly, "Electromagnetic levitation of solid and molten metals," *Journal of Applied Physics*, vol. 23, no. 5, pp. 545-552, 1952.

[4] E. Fromm and H. Jehn, "Electromagnetic forces and power absorption in levitation melting," *British Journal of Applied Physics*, vol. 16, no. 5, pp. 653-662, 1965.

[5] F. Maraspin, P. Bevilacqua, and P. Rem, "Modelling the throw of metals and nonmetals in eddy current separations," *International Journal of Mineral Processing*, vol. 73, no. 1, pp. 1-11, 2004.

[6] N. Dholu, J. R. Nagel, D. Cohrs, and R. K. Rajamani, "Eddy current separation of nonferrous metals using a variable-frequency electromagnet," *KONA Powder and Particle Journal*, vol. 34, pp. 241-247, 2017.

[7] Y. R. Smith, J. R. Nagel, and R. K. Rajamani, "Electrodynamic eddy current separation of end-of-life PV materials," in *In: Zhang L. et al. (eds) Energy Technology 2017. The Minerals, Metals & Materials Series.*, Cham, Springer, 2017, pp. 379-386.

[8] J. D. Ray, J. R. Nagel, D. Cohrs, and R. K. Rajamani, "Forces on particles in time-varying magnetic fields," *KONA Powder and Particle Journal*, vol. 35, pp. 251-257, 2018.

[9] J. R. Nagel, "Induced eddy currents in simple conductive geometries," *IEEE Antennas and Propagation Magazine*, vol. 60, no. 1, pp. 81-88, 2018.

[10] G. Sinha and S. S. Prabhu, "Analytical model for estimation of eddy current and power loss in conducting plate and its application," *Physical Review Special Topics: Accelerators and Beams*, vol. 14, no. 6, p. 062401, 2011.

[11] G. Lohofer, "Theory of an electromagnetically levitated metal sphere I: Absorbed power," *SIAM Journal on Applied Mathematics*, vol. 49, no. 2, pp. 567-581, 1989.

[12] T. P. Theodoulidis, N. V. Kantartzis, T. D. Tsiboukis, and E. E. Kriezis, "Analytical and numerical solution of the eddy-current problem in spherical coordinates based on the second-order vector potential formulation," *IEEE Transactions on Magnetics*, vol. 33, no. 4, pp. 2461-2472, 1997.

[13] J. Chen, Z. Chen, C. Tao, and L.-B. Zhang, "An adaptive finite element method for the eddy current model with circuit/field couplings," *SIAM Journal on Scientific Computing*, vol. 32, no. 2, pp. 1020-1042, 2010.

[14] O. Biro and K. Preis, "On the use of the magnetic vector potential in the finite-element analysis of three-dimensional eddy currents," *IEEE Trans-*

actions on Magnetics, vol. 25, no. 4, pp. 3145-3159, 1989.

[15] M. R. Krakowski, "On certain properties of the electric vector potential in eddy-current problems," *IEE Proceedings A - Physical Science, Measurement and Instrumentation, Management and Education - Reviews*, vol. 134, no. 10, pp. 768-772, 1987.

[16] A. Krawczyk and J. A. Tegopoulos, *Numerical Modelling of Eddy Currents*. Oxford: Clarendon Press, 1993.

[17] J. R. Nagel, "Numerical solutions to Poisson equations using the finite-difference method," *IEEE Antennas and Propagation Magazine*, vol. 56, no. 4, pp. 209-224, 2014.

[18] G. B. Arfken and H. J. Weber, *Mathematical Methods for Physicists*. 5th ed., New York: Academic Press, 2001.

[19] M. Clemens and T. Weiland, "Discrete electro-magnetism with the finite integration technique," *Progress In Electromagnetics Research*, vol. 32, pp. 65-87, 2001.

[20] J. D. Jackson, *Classical Electrodynamics*. 3rd ed., Hoboken (NJ): Wiley, 1999.

[21] Computer Simulation Technology, "CST EM Studio," [Online]. Available: www.cst.com. [Accessed 2016].

James R. Nagel studied Electrical Engineering at the University of Utah in Salt Lake City and earned his Ph.D. in 2011. He now works as a Research Associate for the University of Utah where he studies magnetic separation methods for scrap metal recycling.

Accuracy of Finite Element Approximations for Two-dimensional Time-harmonic Electromagnetic Boundary Value Problems Involving Non-conducting Moving Objects with Stationary Boundaries

Praveen K. Ramakrishnan and Mirco Raffetto

Department of Electrical Electronic, Telecommunications Engineering and Naval Architecture
University of Genoa, Via Opera Pia 11a, 16145, Genoa, Italy
pravin.nitc@gmail.com, raffetto@dibe.unige.it

Abstract ─ An analysis of the accuracy of the results computed using a finite element code in the presence of axially moving cylinders is presented. It seems that no result of this type is available in the open literature.

Any material in motion is perceived as a bianisotropic medium. This generates a scattered field having two components: one has the same polarization as the incident field and the other presents the orthogonal polarization. The results on the accuracy of the co-polarized field are new but are similar to those obtained in the presence of motionless media. The outcome on the accuracy of the results related to the orthogonal polarization seems to be more interesting, especially for the information content this component of the field could provide on the axial velocity profile. In particular, using a finite element simulator based on double precision arithmetic, it is shown that the range of axial velocity values over which it is possible to obtain very accurate approximations can span nine or even more decades. This allows the use of the simulator, even when the more difficult components of the field are required to be accurate, for a set of applications ranging from astrophysics to medicine.

Index Terms ─ Bianisotropic media, electromagnetic scattering, error analysis, finite element method, moving media, reconstruction of velocity profiles, time-harmonic electromagnetic fields.

I. INTRODUCTION

The interaction of electromagnetic waves with moving bodies plays a role in many applications [1], [2]. Among these, one can consider many important applications involving only axially moving cylinders. In particular, one can refer to axially moving plasma columns [3], [4], [5], ionized meteor trails [6], jet exhausts [7] or mass flow in pneumatic pipes [8].

In most cases of interest, which could involve multiple cylinders having irregular shapes, inhomogeneous constitutive parameters and non-constant velocity profiles, numerical methods are required to try to approximate the solutions of interest [9].

Notwithstanding the difficulty related to the presence of materials in motion [1], [10], [11], determining the appearance of bianisotropic materials in any reference frame in which the media themselves are not at rest, the first results related to the well-posedness and the finite element approximability for these problems have been deduced [12].

When simulators are exploited, the results related to the convergence of numerical approximations are not the only aspects of practical interest. However, error estimates [13] are important too (particularly, a-priori error estimations), as clearly pointed out in [14] (p. 114). These estimations are not available so far, to the best of authors' knowledge, for two dimensional problems involving moving objects. In particular, results are not available for problems involving axially moving cylinders, like the ones of interest in this paper.

Then, in order to understand what can be expected in practice, we have to perform numerical experiments. Unfortunately, in the presence of axially moving cylinders, no numerical analysis seems to be available. This is the reason why, in this paper, we present a lot of numerical results. They could suggest what can be expected in other cases and could be considered as benchmarks for any error estimate the research community will be able to deduce.

All numerical results which will be presented refer to a simple problem involving a moving cylinder. For such a problem an independent truncated-series solution can be found [4] (see also [15]). In this way, we can evaluate the accuracy of our finite element approximations in terms of absolute and relative errors. The effects of all parameters involved in the definition of the simple problem of reference are studied.

As it has already been pointed out, in the presence of a time-harmonic illumination, the axial motion of cylinders determines, in any reference frame in which the media are not at rest, a bianisotropic effect and this,

Submitted On: September 19, 2017
Accepted On: April 9, 2018

in turn, is responsible for the presence of a scattered field having both polarizations: the same as that of the incident field and the orthogonal one. For the co-polarized component of the field the outcome is absolutely stable. The errors for this component are, in particular, almost independent of the axial velocity and, then, assume almost the same values we get in the presence of motionless media. For the cross-polarized scattered wave the relative errors are very stable, as well, even though it is a-priori known that the previous results cannot be duplicated in this case, due to the fact that this component of the scattered field is known to go uniformly to zero as the axial speed of the scatterers becomes smaller and smaller [16]. Anyway, the errors on this component of the scattered field are indeed stable for a huge range of axial velocity values. By using double precision arithmetic this range can span nine or even more decades, so allowing the use of finite element simulators for velocities varying from a few centimeters per second to many thousands of kilometers per second. That means that the considered finite element method can be reliably used for a set of applications ranging from astrophysics to medicine.

In the paper, we examine the behavior of the error in the co-polarized and cross-polarized components of the field. The results of numerical experiments indicate that the co-polarized component follows quadratic convergence, same as that in the motionless case. On the other hand, the results show that the cross-polarized component has linear convergence. However, at low values of axial speed we expect that the round-off error becomes more and more significant, degrading the accuracy of the cross-polarized component. This is because the co-polarized component remains of the same order of magnitude while the cross-polarized component goes to zero with decreasing velocity. When the ratio of the norm of the cross-polarized component to the co-polarized component becomes too large, the result becomes less reliable. Hence, this number can be used as a general indicator for checking if the results of the simulation are reliable or not.

The results show, in addition to the previously mentioned applications, that the indicated simulator can be exploited as a reliable solver of forward scattering problems in imaging procedures aiming at the reconstruction of axial velocity profiles [16], [17] and this, by the way, was the initial motivation for our study.

The paper is organized as follows. In Section II the mathematical formulation of the problems of interest is recalled together with some of the results available in the open literature. Some new considerations on the properties of the finite element matrices in the presence of moving media are provided in Section III. In order to carry out the error analysis of interest, the definition of a test case is necessary. This is done in Section IV, where, in addition, a complete set of relevant absolute and relative errors is defined. The main section of the manuscript, dealing with the error analysis, is Section V. Finally, before concluding the paper, some considerations on the convergence of two well-known iterative methods are provided.

II. MATHEMATICAL FORMULATION OF THE PROBLEM

The electromagnetic problems of interest in this paper are those in which axially moving cylinders (having parallel axes) are illuminated by a time-harmonic source or field. This class of problems has been studied in [12] and we refer to that paper for the definition of all details. Here we recall just the main points to let the readers understand the developments which will be presented in the next sections.

All our problems will present a cylindrical geometry and we denote by z the axis of such a geometry. The time-harmonic sources and the inhomogeneous admittance boundary conditions involved are assumed to be independent of z, too, so that our problems can be formulated in a two-dimensional domain Ω contained in the (x, y) plane. Γ denotes the boundary of Ω. $\mathbf{n}$ and $\mathbf{l}$ are the unit vectors orthogonal (pointing outward) and tangential to Γ, respectively. We have $\mathbf{n} \times \mathbf{l} = \hat{\mathbf{z}}$.

The media involved in our problems can move in the axial direction with respect to the chosen reference frame. In such a frame a velocity field v_z, assumed to be time-invariant, is naturally defined, even though we will often refer to it in terms of the usual [18] (p. 525) real-valued normalized field $\beta = \frac{v_z}{c_0}$, being c_0 the speed of light in vacuum. Different linear, time-invariant and inhomogeneous materials can be modelled in our problems. Ω_β will denote the subdomain of Ω containing all media in motion.

Under the indicated conditions all fields in all media will be time-harmonic, as the considered sources, and a factor $e^{j\omega t}$, common to all fields of interest, is assumed and suppressed.

Any material involved is isotropic in its rest frame and is there characterized by its relative permittivity ε_r, its relative permeability μ_r and its electric conductivity σ. In the following, any reference to ε_r, μ_r or σ of a moving medium should be interpreted as a reference to the corresponding quantity when the medium is at rest. All moving media will be considered in any case to have $\sigma = 0$ (in order to avoid the difficulties related to the convective currents which could also become surface electric currents and to avoid difficulty related to the no-slip condition which, ultimately, prevents the possibility of using pure two-dimensional models [12]).

By using the subscript "t" to denote the field quantities transverse to the z direction, the constitutive

relations for the media in motion are [12]:

$$\mathbf{D}_t = \frac{1+\mu_r\varepsilon_r-\zeta_1}{c_0^2\mu_0\mu_r}\mathbf{E}_t + \frac{\zeta_2}{c_0\mu_0\mu_r}\ \hat{\mathbf{z}}\times\mathbf{B}_t, \tag{1}$$

$$D_z = \varepsilon_0\varepsilon_r E_z, \tag{2}$$

$$\mathbf{H}_t = \frac{\zeta_1}{\mu_0\mu_r}\mathbf{B}_t + \frac{\zeta_2}{c_0\mu_0\mu_r}\ \hat{\mathbf{z}}\times\mathbf{E}_t, \tag{3}$$

$$H_z = \frac{1}{\mu_0\mu_r}B_z, \tag{4}$$

where

$$\zeta_1 = \frac{1-\mu_r\varepsilon_r\beta^2}{1-\beta^2}, \tag{5}$$

$$\zeta_2 = \frac{\beta(\mu_r\varepsilon_r-1)}{1-\beta^2}. \tag{6}$$

In order to be able to define the problems of interest and to talk of their finite element approximations, it is necessary to introduce some additional notations. $\left(L^2(\Omega)\right)^n$ is the usual Hilbert space of square integrable vector fields on Ω with values in $\mathbb{C}^n$, $n = 2,3$, and with scalar product given by $(\mathbf{u},\mathbf{v})_{0,\Omega} = \int_\Omega \mathbf{v}^*\mathbf{u}\, dS$, where $\mathbf{v}^*$ denotes the conjugate transpose of the column vector $\mathbf{v}$. For a given three-dimensional complex-valued vector field $\mathbf{A} = \left(\mathrm{A_x}, \mathrm{A_y}, \mathrm{A_z}\right) \in (L^2(\Omega))^3$ we consider the operators $\mathrm{curl_{2D}}$ and $\mathrm{grad_{2D}}$, defined according to:

$$\mathrm{curl_{2D}}\ \mathbf{A}_t = \frac{\partial A_y}{\partial x} - \frac{\partial A_x}{\partial y}, \tag{7}$$

$$\mathrm{grad_{2D}}\ A_z = \left(\frac{\partial A_z}{\partial x}, \frac{\partial A_z}{\partial y}\right). \tag{8}$$

The transverse parts of the electric and magnetic fields will be in the Hilbert space:

$$U_{2D} = \left\{ \begin{matrix} \mathbf{A}_t \in \left(L^2(\Omega)\right)^2 \mid \mathrm{curl_{2D}} A_t \in L^2(\Omega) \\ and\ \mathbf{A}_t\cdot\mathbf{l} \in L^2(\Gamma) \end{matrix} \right\}, \tag{9}$$

whose inner product is given by:

$$(\mathbf{u}_t,\mathbf{v}_t)_{U_{2D}} = (\mathbf{u}_t,\mathbf{v}_t)_{0,\Omega} + (\mathrm{curl_{2D}}\mathbf{u}_t, \mathrm{curl_{2D}}\mathbf{v}_t)_{0,\Omega} + (\mathbf{u}_t\cdot\mathbf{l}, \mathbf{v}_t\cdot\mathbf{l})_{0,\Gamma}. \tag{10}$$

The axial components of the same fields are in the Hilbert space:

$$H^1(\Omega) = \left\{ A_z \in L^2(\Omega) \middle|\ \mathrm{grad_{2D}} A_z \in \left(L^2(\Omega)\right)^2 \right\}, \tag{11}$$

whose inner product is:

$$(u_z, v_z)_{1,\Omega} = (u_z, v_z)_{0,\Omega} + (\mathrm{grad_{2D}} u_z, \mathrm{grad_{2D}} v_z)_{0,\Omega}. \tag{12}$$

$\gamma_0 \mathrm{u}_z$ will denote the boundary values of $\mathrm{u}_z \in H^1(\Omega)$ on Γ.

Overall the electric and magnetic fields are in the Hilbert space:

$$U = U_{2D} \times H^1(\Omega), \tag{13}$$

with inner product given by:

$$(\mathbf{u},\mathbf{v})_U = (\mathbf{u}_t,\mathbf{v}_t)_{U_{2D}} + (\mathrm{u}_z,\mathrm{v}_z)_{1,\Omega}. \tag{14}$$

$||\ ||_U$ will denote the corresponding norm. The norms of the different spaces so far introduced will be of particular interest in establishing the accuracy of the results of the finite element simulator considered.

With the indicated notation, the electromagnetic boundary value problem we consider in this paper is: given $\omega > 0$, the electric and magnetic current densities $\mathbf{J_e},\ \mathbf{J_m} \in \left(L^2(\Omega)\right)^3$, the boundary data $f_{Rz}, f_{Rl} \in L^2(\Gamma)$, find $(\mathbf{E},\mathbf{B},\mathbf{H},\mathbf{D}) \in U \times \left(L^2(\Omega)\right)^3 \times U \times \left(L^2(\Omega)\right)^3$ which satisfies:

$$\begin{cases} \mathrm{curl_{2D}}\mathbf{H}_t - j\omega D_z = J_{ez} & in\ \ \Omega, \\ \mathrm{grad_{2D}} H_z \times \hat{\mathbf{z}} - j\omega\mathbf{D}_t = \mathbf{J}_{et} & in\ \ \Omega, \\ \mathrm{curl_{2D}}\mathbf{E}_t + j\omega B_z = -J_{mz} & in\ \ \Omega, \\ \mathrm{grad_{2D}} E_z \times \hat{\mathbf{z}} + j\omega\mathbf{B}_t = -\mathbf{J}_{mt} & in\ \ \Omega, \\ \mathbf{H}_t\cdot\mathbf{l} + Y(\gamma_0 E_z) = -f_{Rz} & on\ \ \Gamma, \\ \gamma_0 H_z - Y(\mathbf{E}_t\cdot\mathbf{l}) = f_{Rl} & on\ \ \Gamma, \end{cases} \tag{15}$$

and the constitutive relations (1), (2), (3) and (4).

After some work [12], one can deduce the equivalent variational formulation: given $\omega > 0$, $\mathbf{J_e},\ \mathbf{J_m} \in \left(L^2(\Omega)\right)^3$, $f_{Rz}, f_{Rl} \in L^2(\Gamma)$, find $\mathbf{E} \in U$ such that:

$$a(\mathbf{E},\mathbf{w}) = l(\mathbf{w}) \qquad \forall \mathbf{w} \in U, \tag{16}$$

where a is the following sesquilinear form:

$$\begin{aligned} a(\mathbf{u},\mathbf{w}) = {} & \left(\frac{\zeta_1}{\mu_r}\mathrm{grad_{2D}} u_z, \mathrm{grad_{2D}} w_z\right)_{0,\Omega} + \\ & + \left(\frac{1}{\mu_r}\mathrm{curl_{2D}}\mathbf{u}_t, \mathrm{curl_{2D}}\mathbf{w}_t\right)_{0,\Omega} + \\ & + j\,\frac{\omega}{c_0}\left(\frac{\zeta_2}{\mu_r}\mathbf{u}_t, \mathrm{grad_{2D}} w_z\right)_{0,\Omega} + \\ & - j\,\frac{\omega}{c_0}\left(\frac{\zeta_2}{\mu_r}\mathrm{grad_{2D}} u_z, \mathbf{w}_t\right)_{0,\Omega} + \\ & - \frac{\omega^2}{c_0^2}(\varepsilon_r u_z, w_z)_{0,\Omega} + \\ & - \frac{\omega^2}{c_0^2}\left(\frac{1+\varepsilon_r\mu_r-\zeta_1}{\mu_r}\mathbf{u}_t, \mathbf{w}_t\right)_{0,\Omega} + \\ & + j\omega\mu_0(Y(\gamma_0 u_z), \gamma_0 w_z)_{0,\Gamma} + \\ & + j\omega\mu_0(Y(\mathbf{u}_t\cdot\mathbf{l}), \mathbf{w}_t\cdot\mathbf{l})_{0,\Gamma}, \end{aligned} \tag{17}$$

for all $\mathbf{u},\mathbf{w} \in U$ and l is the following antilinear form:

$$\begin{aligned} l(\mathbf{w}) = {} & -j\omega\mu_0(J_{ez}, w_z)_{0,\Omega} + \\ & - \left(\frac{\zeta_1}{\mu_r}\hat{\mathbf{z}}\times\mathbf{J}_{mt}, \mathrm{grad_{2D}} w_z\right)_{0,\Omega} + \\ & - j\omega\mu_0(f_{Rz}, \gamma_0 w_z)_{0,\Gamma} + \\ & - \left(\frac{1}{\mu_r}J_{mz}, \mathrm{curl_{2D}}\mathbf{w}_t\right)_{0,\Omega} + \\ & - j\omega\mu_0(\mathbf{J}_{et}, \mathbf{w}_t)_{0,\Omega} + \\ & + j\,\frac{\omega}{c_0}\left(\frac{\zeta_2}{\mu_r}\hat{\mathbf{z}}\times\mathbf{J}_{mt}, \mathbf{w}_t\right)_{0,\Omega} + \\ & - j\omega\mu_0(f_{Rl}, \mathbf{w}_t\cdot\mathbf{l})_{0,\Gamma}, \end{aligned} \tag{18}$$

for all $\mathbf{w} \in U$.

The reader can notice that, whenever $\beta = 0$ everywhere in Ω (which implies $\zeta_2 = 0$ in Ω), the problem splits into two disjoint problems, one for the axial component E_z, the other for the transverse part

$\mathbf{E}_t$. These two disjoint problems are the traditional, two-dimensional variational problems, formulated in terms of E_z or $\mathbf{E}_t$, in the presence of motionless isotropic media.

In [12] we showed that under some non-restrictive hypotheses any electromagnetic problem of the class considered is well posed. In particular, for any problem of interest we can find a unique solution $(\mathbf{E}, \mathbf{B}, \mathbf{H}, \mathbf{D})$ belonging to $U \times \left(L^2(\Omega)\right)^3 \times U \times \left(L^2(\Omega)\right)^3$ and depending continuously on $\mathbf{J_e}$, $\mathbf{J_m} \in \left(L^2(\Omega)\right)^3$ and on $f_{Rz}, f_{Rl} \in L^2(\Gamma)$. It is worth mentioning that, due to the bianisotropic behaviour of the media in motion, all unknown fields will have, in general, all three components, even if the scatterers are illuminated by simple fields.

III. FINITE ELEMENT APPROXIMATION

Under some additional assumptions, in [12] we also found that a finite element method, based on the above variational formulation and exploiting a first-order Lagrangian approximation for the axial component and a first-order edge element approximation for the transverse part, determines $(\mathbf{E}_h, \mathbf{B}_h, \mathbf{H}_h, \mathbf{D}_h) \in U_h \times \left(L^2(\Omega)\right)^3 \times \left(L^2(\Omega)\right)^3 \times \left(L^2(\Omega)\right)^3$ which converges, as h goes to zero, to $(\mathbf{E}, \mathbf{B}, \mathbf{H}, \mathbf{D})$ in $U \times \left(L^2(\Omega)\right)^3 \times \left(L^2(\Omega)\right)^3 \times \left(L^2(\Omega)\right)^3$. In the previous statement U_h is the finite dimensional subspace of U generated by the indicated elements (first-order Lagrangian and first-order edge elements) for a specific triangulation of Ω and h denotes, as usual, the maximum diameter of all elements of the triangulation [14] (p. 131).

In [12] no specific considerations related to the implementation of finite element codes were provided. These considerations could be useful for our next developments and, for this reason, we present here the main points. Suppose that for any mesh adopted, fixing a given U_h, we order the degrees of freedom by placing those related to E_{hz}, $[\mathrm{e}_z] \in \mathbb{C}^{nn}$, in the first part of the vector $[\mathrm{e}] \in \mathbb{C}^{nn+ne}$ of the unknowns while those related to $\mathbf{E}_{ht}$, $[\mathrm{e}_t] \in \mathbb{C}^{ne}$, are in its second and last part. In the previous formulas, nn (respectively, ne) refers to the number of nodes (respectively, edges) of the mesh considered. With this convention, by firstly considering the nn test functions like $\mathbf{w}_h = (0,0,\mathrm{w_{hz}})$ and, then, the ne test functions like $\mathbf{w_h} = \mathbf{w_{ht}}$, one can easily deduce that the general form of the final matrix equation obtained from (16), (17) and (18), with $\mathbf{E}$, $\mathbf{u}$, $\mathbf{w}$ and U replaced, respectively, by $\mathbf{E}_h$, $\mathbf{u}_h$, $\mathbf{w}_h$ and U_h, is:

$$[A][e] = [l], \tag{19}$$

where the entries of $[l] \in \mathbb{C}^{nn+ne}$ are given by $l(\mathbf{w}_h)$, for all test functions considered. The order for its entries is given by the order considered for the test functions and, in analogy to the decomposition of $[e]$ in terms of $[e_z]$ and $[e_t]$, we get $[l_z] \in \mathbb{C}^{nn}$, in the first part of $[l]$ and $[l_t] \in \mathbb{C}^{ne}$ in the second and last one. $[A]$ is given by:

$$[A] = \begin{bmatrix} [A_{zz}] & [A_{zt}] \\ [A_{tz}] & [A_{tt}] \end{bmatrix}. \tag{20}$$

In this formula, $[A_{zz}]$, $[A_{zt}]$, $[A_{tz}]$ and $[A_{tt}]$ are complex matrices whose entries are deduced directly from (17):

$$\begin{aligned}[A_{zz}]_{ij} = &\left(\frac{\zeta_1}{\mu_r} grad_{2D} w_{hzj}, \mathrm{grad_{2D}} w_{hzi}\right)_{0,\Omega} + \\ &-\frac{\omega^2}{c_0^2}\left(\varepsilon_r w_{hzj}, w_{hzi}\right)_{0,\Omega} + \\ &+ j\omega\mu_0 \left(Y\left(\gamma_0 w_{hzj}\right), \gamma_0 w_{hzi}\right)_{0,\Gamma}, \\ &i,j \in 1,\dots,nn, \end{aligned} \tag{21}$$

$$\begin{aligned}[A_{zt}]_{ij} = &\, j\frac{\omega}{c_0}\left(\frac{\zeta_2}{\mu_r}\mathbf{w}_{htj}, \mathrm{grad_{2D}} w_{hzi}\right)_{0,\Omega}, \\ &i \in 1,\dots,nn, \qquad j \in 1,\dots,ne, \end{aligned} \tag{22}$$

$$\begin{aligned}[A_{tz}]_{ij} = &\, -j\frac{\omega}{c_0}\left(\frac{\zeta_2}{\mu_r}\mathrm{grad_{2D}} w_{hzj}, \mathbf{w}_{hti}\right)_{0,\Omega}, \\ &i \in 1,\dots,ne, \qquad j \in 1,\dots,nn, \end{aligned} \tag{23}$$

$$\begin{aligned}[A_{tt}]_{ij} = &\left(\frac{1}{\mu_r}\mathrm{curl_{2D}}\mathbf{w}_{htj}, \mathrm{curl_{2D}}\mathbf{w}_{hti}\right)_{0,\Omega} + \\ &-\frac{\omega^2}{c_0^2}\left(\frac{1+\varepsilon_r\mu_r-\zeta_1}{\mu_r}\mathbf{w}_{htj}, \mathbf{w}_{hti}\right)_{0,\Omega} + \\ &+ j\omega\mu_0\left(Y\left(\mathbf{w}_{htj}\cdot\mathbf{l}\right), \mathbf{w}_{hti}\cdot\mathbf{l}\right)_{0,\Gamma} \\ &i,j \in 1,\dots,ne. \end{aligned} \tag{24}$$

In this case, too, whenever $\beta = 0$ everywhere in Ω, the two matrices $[A_{zt}]$ and $[A_{tz}]$ become trivial and the discrete problem splits into two disjoint parts: one for $[e_z]$, the other for $[e_t]$. These are the classical two-dimensional problems for TM and TE polarized fields, respectively, in the presence of motionless media.

It is important to note that the second and third addends in the right-hand side of (21) are independent of β. The same is true for the first and third addends in the right-hand side of (24). Taking account of (6) one easily deduces that, for small values of the maximum of $|\beta|$, $\zeta_2 \approx \beta(\mu_r\varepsilon_r - 1)$ and all entries of $[A_{zt}]$ and $[A_{tz}]$ have magnitudes which are smaller or equal to numbers proportional to the maximum of $|\beta|$, under the same conditions. Finally, the addends of the right-hand sides of (21) and (24) which depend on β, again for small values of the maximum of $|\beta|$, involve $\zeta_1 \approx 1 + (1-\mu_r\varepsilon_r)\beta^2$ and $1 + \varepsilon_r\mu_r - \zeta_1 \approx \varepsilon_r\mu_r - (1-\mu_r\varepsilon_r)\beta^2$. Thus, the considered quantities are only slightly affected by the motion, if the maximum of $|\beta|$ is small.

In order to solve the algebraic linear system (19) several algorithms can be adopted. Among these, we consider iterative solvers, which are very popular for the solution of linear systems arising in finite element simulations [19] (pp. 382, 383, 396-405), [20] (p. 334). The stopping criteria we adopt in all cases, which defines when the iterative solution has reached convergence, is "criterion 2" of [21] (p. 60). For the reader convenience

we recall that this criterion requires at the beginning the calculation of the Euclidean norm $|||[l]|||$ of $[l]$. At iteration i the approximate solution $[e]_i$ determines an error $|||[A][e]_i - [l]|||$. The iterative process is stopped when the condition $|||[A][e]_i - [l]||| < \delta|||[l]|||$ is satisfied, where δ is the so-called residual. Usually, δ is a small value in the range $[10^{-12}, 10^{-9}]$ when double precision arithmetic is used [21] (pp. 58-60).

If we assume TM polarized plane wave as the incident wave, then as the maximum value of $|\beta|$ goes to zero, the Euclidean norm of components of $[e_t]$ goes to zero whereas that of components of $[e_z]$ goes to the non-zero value of the corresponding motionless problem. Hence the loss of number of significant digits due to round-off errors becomes large for the transverse components. Since for low values of $|\beta|$, $|||[e_t]|||$ becomes proportional to $|\beta|$ and $|||[e_z]|||$ remains almost constant, the ratio $\frac{|||[e_t]|||}{|||[e_z]|||}$ becomes proportional to $|\beta|$ as well. We know that $\frac{||\Delta[e]||}{|||[e]|||} \leq K_A \Delta_{roundoff}$. Here $\Delta[e]$ is the error in the solution due to round-off, K_A the condition number of matrix $[A]$. $\Delta_{roundoff} = (\frac{||\Delta[A]||}{|||[A]|||} + \frac{||\Delta[l]||}{|||[l]|||} + \delta)$, where $\Delta[A]$ and $\Delta[l]$ denote change in $[A]$ and $[l]$ due to round-off. Now assuming that the round-off errors are uniformly distributed across the elements of $[e]$, it is easy to deduce that $\frac{||\Delta[e_t]||}{|||[e_t]|||} \leq \frac{nn+ne}{ne} \frac{|||[e]|||}{|||[e_t]|||} K_A \Delta_{roundoff}$. At low values of $|\beta|$ we can consider $|||[e]||| \approx |||[e_z]|||$ and that $\Delta_{roundoff} \approx \delta$. Thus we can write:

$$\frac{||\Delta[e_t]||}{|||[e_t]|||} \leq \frac{nn + ne}{ne} \frac{|||[e_z]|||}{|||[e_t]|||} K_A \delta. \qquad (25)$$

Thus, it can be seen that the residual error on the transverse component can be magnified by a factor of $\frac{nn+ne}{ne} \frac{|||[e_z]|||}{|||[e_t]|||} K_A$ for small $|\beta|$ values. If the maximum allowable error is δ_{max}, then it needs to be ensured that $\frac{nn+ne}{ne} \frac{|||[e_z]|||}{|||[e_t]|||} \leq \frac{\delta_{max}}{K_A \delta}$.

IV. DEFINITION OF A TEST CASE AND OF THE RELEVANT ERRORS

In order to deduce some results on the accuracy of finite element solutions in the presence of axially moving cylinders we need to consider simple problems which allow the calculation of the fields of interest with other reliable tools. For this reason, we consider single canonical cylinders moving in the axial direction. Analogous studies have been performed under the same type of simplifying assumptions related to the inhomogeneity of the media involved, the particular shapes of the scatterers or the illuminating field (see, for example, [20] (p. 188) or [22]). For this reason, we consider the case of a circular cylinder hosted in vacuum and illuminated by a uniform plane wave. In particular, the cylinder axis is assumed to be the z axis and the cylinder cross-section will have a radius $R \leq 0.2$ m. The medium inside the cylinder is assumed to be homogeneous and, in its rest frame, isotropic and not dispersive. It will be characterized by $\mu_r = 1$. We assume that such a medium is in uniform motion along the z axis. Finally, we will consider a TM-polarized incident plane wave impinging orthogonally on the cylinder and defined by $E_z^{inc} = E_0 e^{j2\pi f \sqrt{\mu_0 \varepsilon_0} y}$, f being the frequency always equal to 1 GHz except for one case when $f = 500$ MHz will be considered. The choice of the simple canonical problem just described was motivated not only by the possibility of finding semi-analytical solutions by using other tools, but also by the possible application of this study to the reconstruction of β profiles, as it will be explained later on. In the following we will consider several different values for the normalized axial speed β of the cylinder, for its relative permittivity ε_r (in its rest frame) and for its radius R.

For problems of this class an efficient semi-analytical procedure, able to compute very good approximations of their solutions was proposed by Yeh [4] (see also Remark 5 of [15]).

The scattering problems just defined are numerically studied by using a finite element simulator based on the considerations reported in the previous section. The domain of numerical investigation we have adopted is, in any case, a polygon approximating a circle in the (x, y) plane, whose center is at the origin and whose radius is equal to 0.4 m. Such a numerical domain is discretized by using several meshes. In particular, all these meshes are obtained by using n concentric circles and, starting from the center, the innermost circle is divided into 6 segments, the next one in 12 and so on. The domain is thus divided almost uniformly into $6n^2$ triangles, with $1 + 3n + 3n^2$ nodes, $3n + 9n^2$ edges and $6n$ boundary edges. An example of one mesh of this type can be found in Fig. 1 of [22] (the reader has to consider just the upper base of the three-dimensional cylinder shown in that figure). In the following n will be equal to 20, 40, 80, 120, 160 or 200. Correspondingly, we will get a mesh characterized, respectively, by h equal to 0.0285874, 0.0143858, 0.00721629, 0.00481608, 0.00361402 or 0.00289216 m, with, respectively, 1261, 4921, 19441, 43561, 77281, 120601 nodes, 2400, 9600, 38400, 86400, 153600, 240000 elements, 3660, 14520, 57840, 129960, 230880, 360600 edges, and 120, 240, 480, 720, 960, 1200 boundary edges. All the indicated values of n can be used to discretize scatterers whose radius R is a multiple of 2 cm (respectively, 1 cm if we avoid using $n = 20$).

It is very important to point out that, in order to keep the analysis as simple as possible, we avoided considering meshes made up of curved triangles. This means, in particular, that, since the scatterer cross-

section is not a polygon, in all our simulations we suffer from a kind of non-conformity [14] (p. 209). As a matter of fact, the scatterer has not the shape of the numerical scatterer and, moreover, the domain of numerical investigation and the numerical scatterer itself change their shapes for different values of n. By the same token, we adopted the semi-analytical procedure defined by Yeh [4] (the series are truncated after the first 60 terms for these calculations) to compute the piecewise constant data f_{Rzh} and f_{Rlh} enforcing the inhomogeneous terms in the admittance boundary conditions considered on Γ for the discretized problem (the admittance Y is set to $Y_0 = \sqrt{\frac{\varepsilon_0}{\mu_0}}$ in any case). In this way, we get another violation of conformity, according to [14] (p. 183). The reader should note that these violations of conformity were not considered in [12] and formally the convergence results we deduced there could not be applied. In the following, however, according to a well-established approach, we neglect this technical problem and assume that our convergence results do apply to the cases considered. The numerical results we will show provide a heuristic proof of this statement.

An evaluation of the numerical errors of the finite element solutions could now be performed. However, we introduce an additional simplification which allows us to find good estimates of the errors by exploiting finite element calculations. In particular, we will call $E_{z,h,analytic}$ and $H_{z,h,analytic}$ the first-order Lagrangian element expansions which are deduced by evaluating their degrees of freedom with the semi-analytical procedure proposed by Yeh [4]. Analogously, $\mathbf{E}_{t,h,analytic}$ will refer to the first-order edge element expansion which is deduced by evaluating its degrees of freedom with Yeh's procedure. In the above three calculations the series involved in Yeh's procedure are truncated after the first 40 terms. The reader should observe that $H_{z,h,analytic}$ is not related to $\mathbf{E}_{t,h,analytic}$ by the usual Maxwell's curl equation (while H_{hz} is, by definition, equal to $-\frac{1}{j\omega\mu_0\mu_r}\mathrm{curl}_{2\mathrm{D}}\mathbf{E}_{ht}$; see equation (3.3) and the considerations below Theorem 5.3 at the end of Section 5 of [12]). As a matter of fact, it is very well known that the curl of a first-order edge element field is piecewise constant while $H_{z,h,analytic}$ is, as it has already been pointed out, a first-order Lagrangian element field. The decision to consider $H_{z,h,analytic}$ and $\mathbf{E}_{t,h,analytic}$ not related by the usual Maxwell's curl equation was made for the possible application of our results to inverse problem techniques aiming at the reconstruction of β profile, as it will be further clarified later on.

The previous definitions allow us to introduce a set of (estimates of) absolute errors on E_z, $\mathbf{E}_t$ and H_z by using different relevant norms or semi-norms. Thus we have:

$$e_{z,a,l2} = ||\, E_{z,h,analytic} - E_{hz} \,||_{0,\Omega}\,, \tag{26}$$

$$e_{z,a,h1} = ||\, E_{z,h,analytic} - E_{hz} \,||_{1,\Omega}\,, \tag{27}$$

$$e_{z,a,semi} = ||\, \mathrm{grad}_{2\mathrm{D}} E_{z,h,analytic} - \mathrm{grad}_{2\mathrm{D}} E_{hz} \,||_{0,\Omega}\,, \tag{28}$$

$$e_{t,a,l2} = ||\, \mathbf{E}_{t,h,analytic} - \mathbf{E}_{ht} \,||_{0,\Omega}, \tag{29}$$

$$e_{t,a,\Gamma} = ||\big(\mathbf{E}_{t,h,analytic} - \mathbf{E}_{ht}\big)\cdot\mathbf{l}\,||_{0,\Gamma}, \tag{30}$$

$$e_{a,hz} = ||\, H_{z,h,analytic} - H_{hz} \,||_{0,\Omega}. \tag{31}$$

In the presence of a constant relative permeability $e_{a,hz}$ can be considered as an estimate of $\frac{1}{\omega\mu_0\mu_r}e_{t,a,semi}$, where,

$$e_{t,a,semi} = ||\mathrm{curl}_{2\mathrm{D}}\mathbf{E}_{t,h,analytic} - \mathrm{curl}_{2\mathrm{D}}\mathbf{E}_{ht}\,||_{0,\Omega}, \tag{32}$$

so that we can also consider:

$$e_{t,a,u2D} = \sqrt{e_{t,a,l2}^2 + e_{t,a,\Gamma}^2 + e_{t,a,semi}^2}, \tag{33}$$

as an estimate of the U_{2D} norm error.

Relative errors are important, too, especially for the problems of interest, due to the huge variation of some of the quantities involved. For this reason, we consider the following relative errors: $e_{z,r,l2}$, $e_{z,r,h1}$, $e_{z,r,semi}$, $e_{t,r,l2}$, $e_{t,r,\Gamma}$ and $e_{r,hz}$, which are defined by dividing the corresponding absolute error by the norm of the "analytic" part involved in the definition of the absolute error itself. Once more, under the indicated condition, $e_{r,hz}$ can be considered as an estimate of $e_{t,r,semi}$.

For the TM-polarized incident field considered, it is important to emphasize that, for a motionless cylinder, the solution presents $\mathbf{E}_t = 0$. Moreover, for small values of $|\beta|$ it is known that $||\mathbf{E}_t||_{U2D}$ is small [16]. Thus, all relative errors related to the transverse part of the electric field (that is, $e_{t,r,l2}$, $e_{t,r,\Gamma}$, $e_{r,hz}$, $e_{t,r,semi}$) are expected to become larger and larger as $|\beta|$ goes to zero. At the same time, it could be important to analyze the behaviours of these errors, especially under the indicated conditions, because, on the one hand, good electromagnetic imagining techniques, able to recover the profile of the axial speed, exploits only, for the indicated incident polarization, data related to $H_z = \frac{j}{\omega\mu_0}\mathrm{curl}_{2\mathrm{D}}\mathbf{E}_t$ [16]. On the other hand, the finite element method we are studying can be exploited to provide approximate values of H_z at the measurement points for any trial solution for the β profile considered by the inverse procedure itself [16].

For this reason, in the next section, a part of our numerical analysis will be devoted to considerations related to the reliability of finite element solutions in terms of H_z and, in particular, of $e_{a,hz}$ and $e_{r,hz}$. This part of the analysis was, actually, the initial motivation for this study.

Remark 1: In many applications the reconstruction of the profiles of ε_r and β are of interest [8]. For the indicated polarization of the incident field, the axial

component of the electric field is the most important quantity for the reconstruction of ε_r while the axial component of the magnetic field is crucial for the reconstruction of β [16]. In particular, under some non-restrictive hypotheses, the reconstruction of ε_r can be carried out neglecting any movement and by using data related to E_z only. The estimated ε_r is then adopted as an input data for the reconstruction of the axial speed profile. For the indicated reasons, a finite element code based on a formulation expressed in terms of $\mathbf{E}$ was considered. In our previous considerations we focused in particular on the generation of reliable data for the second step of the reconstruction process, devoted to the estimate of the β profile, simply because the reconstruction algorithms adopted for determining ε_r have been studied for decades [23] while those adopted to recover β are not so standard in the framework of microwave imaging techniques.

Remark 2: $e_{r,hz}$ could also be referred to a proper subdomain Ω_m of Ω. We could use e_{r,hz,Ω_m} as an alternative symbol in this case. The subdomain can also be of zero measure (e.g., made up of curves or points) because the involved quantities ($H_{z,h,analytic}$ and H_{hz}) are continuous in Ω. However, in this case we have to change the norm in the definition of the error (the $L^2(\Omega)$ norm is not meaningful anymore).

The results provided in [12] can be applied to the problems here considered if some conditions involving ε_r and β are satisfied (see, in particular, Section 7 of [12]). In particular, in order to show some examples, we can say that in the presence of a cylinder having $\varepsilon_r = 2$ the problem is well-posed and the convergence of finite element approximations is guaranteed (neglecting the conformity violations already pointed out) whenever $|\beta| \leq 0.264308$. For other cylinder media, for example when $\varepsilon_r = 1.1$ or $\varepsilon_r = 8$, the upper bounds for $|\beta|$ are 0.777053 or 0.0826784, respectively. The reader should notice that the corresponding upper bounds for the axial speed values are really impressive (equal to $\simeq$ 232954629 m/s when $\varepsilon_r = 1.1$, $\simeq$ 79237545 m/s when $\varepsilon_r = 2.0$ and $\simeq$ 24786361 m/s when $\varepsilon_r = 8.0$) and that they are not much smaller than the values of the normalized speed of light in the media considered (given by $\frac{1}{\sqrt{1.1}} \approx 0.953463$, $\frac{1}{\sqrt{2}} \approx 0.707107$ and $\frac{1}{\sqrt{8}} \approx 0.353355$, respectively).

V. NUMERICAL RESULTS

As was already pointed out, for the defined test case we consider several values of ε_r, β, R and n. The effects of these parameters on the errors related to E_z, $\mathbf{E}_t$ and H_z are studied. In particular, the results related to E_z are shown in the first subsection while in the second one we provide considerations on the errors on $\mathbf{E}_t$ and H_z. From these two sub-sections we establish accuracy of the numerical simulations and the convergence behaviour of the components. In the third subsection, we consider the problematic cases where accuracy of the results related to $\mathbf{E}_t$ and H_z start dropping. This is due to the finite precision of the calculations which start to accumulate round-off errors when the bi-anisotropic effect is too weak to give a significant cross-polarized component.

A. Numerical results related to $\mathbf{E}_z$

The first results on E_z we show are all related to cases involving cylinders characterized by $\varepsilon_r = 2$ and $R = 0.2$ m. In particular, in Fig. 1 we report the absolute errors related to the axial component of the electric field, $e_{z,a,h1}$, $e_{z,a,l2}$ and $e_{z,a,semi}$, versus h for two values of β: $\beta = 0$ and $\beta = 0.25$. As the reader can easily check, it is not possible to distinguish the results of the $\beta = 0$ case from those obtained when $\beta = 0.25$. Many other simulations have been performed, for $\beta = 5\ 10^{-m}$, $m = 1, \ldots, 15$. These additional results are not reported in Fig. 1 because the plots would be the same as those already shown. In the figure two plots proportional to h and h^2 are provided, too, in order to be able to determine the rate of convergence of the results as functions of h.

As it was pointed out in Section III the results for the $\beta = 0$ case can be obtained by using a traditional two-dimensional finite element algorithm based on first-order Lagrangian elements (dealing with isotropic media at rest). There is nothing new in the results shown for this case, as it is very well-known [19]; we can simply observe that the absolute errors related to E_z behave like h^2 and that $e_{z,a,semi}$ is much larger than $e_{z,a,l2}$ so determining almost completely $e_{z,a,h1}$.

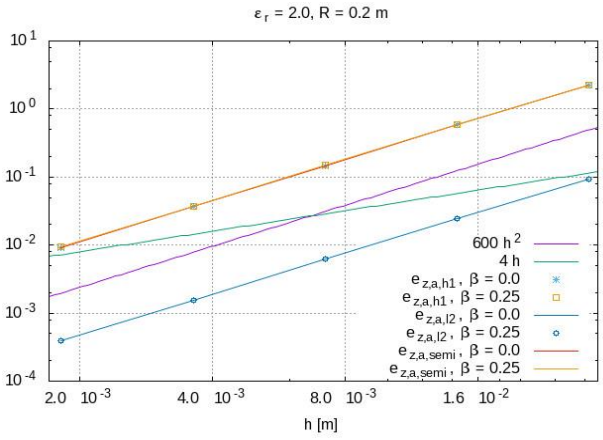

Fig. 1. Behaviour of $e_{z,a,h1}$, $e_{z,a,l2}$ and $e_{z,a,semi}$ versus h, when the cylinder is at rest or moves with $\beta = 0.25$. The cylinder is assumed to have $R = 0.2$ m and to be made up of a material having $\varepsilon_r = 2$ at rest. Two plots proportional to h and h^2 are provided, too.

The results corresponding to $\beta = 0.25$ (determining a huge axial speed of 74948114.5 m/s) show that the finite element capability of approximating the axial

component of the true solution is the same as in the case all media are at rest. In particular, the convergence rate remains quadratic and, taking account of all simulations performed, we can say that this property is completely independent of β. For the same reason, no figure related to the relative errors on E_z is provided.

It could be interesting to observe that $\beta = 0.25$ is close to the upper bound for β reported in Section IV and has a significant effect on E_z. These effects are not shown in a figure for space reasons. We simply observe that, for example, $Re(E_{hz}) = -0.0549$ V/m at the origin in the $\beta = 0$ case while $Re(E_{hz}) = -0.132$ V/m at the same point when $\beta = 0.25$. Both values are obtained by using a mesh with $n = 320$.

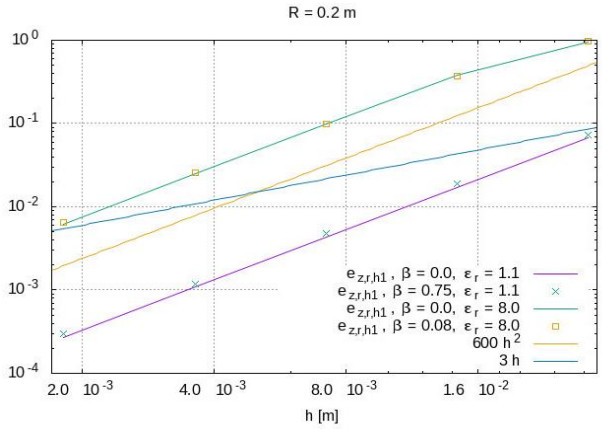

Fig. 2. Behaviour of $e_{z,r,h1}$ versus h for different values of β and ε_r. In particular, for any value of ε_r one of the largest possible normalized axial speed values is considered in addition, for both cases, to $\beta = 0$. The scatterer radius is $R = 0.2$ m.

The previous considerations on the independence of the accuracy of the E_z results from the value of β seem to be correct even when the other parameters are changed. For example, if we consider $\varepsilon_r = 1.1$ or $\varepsilon_r = 8$ we get the relative errors shown in Fig. 2. The reader can easily observe that the error behaviour in both cases does not depend on β and that the convergence rate remains $O(h^2)$. However, for any given mesh, the relative errors on E_z are larger for $\varepsilon_r = 8$ than for $\varepsilon_r = 1.1$, due to the reduction of the wavelength in the scatterer by a factor approximately equal to $2\sqrt{2}$. This effect is very well known and does not require any additional comment [19], [20] (p. 344).

Changes on R are considered, too, but the conclusion for the errors on E_z remains unaltered. When $\varepsilon_r = 2$ and $R = 0.02$ m we get, by using a mesh with $n = 320$, $e_{z,r,h1} = 0.269\ 10^{-3}$ if $\beta = 0$ and $e_{z,r,h1} = 0.270\ 10^{-3}$ if $\beta = 0.25$. The corresponding quantities obtained when $\varepsilon_r = 2$ and $R = 0.2$ m (with the same mesh) are $e_{z,r,h1} = 0.557\ 10^{-3}$ if $\beta = 0$ and $e_{z,r,h1} = 0.563\ 10^{-3}$ if $\beta = 0.25$.

Overall we can say that the finite element approximation of E_z, in the presence of axially moving cylinders illuminated by TM-polarized incident plane waves, is as satisfactory as in the presence of motionless scatterers, independently of all values of the parameters considered.

B. Numerical results related to $\mathbf{E_t}$ and H_z

In this sub-section we examine the errors related to the cross-polarized component $\mathbf{E}_t$ and the related magnetic field component H_z. These quantities are zero in the motionless case, and arises because of the bi-anisotropic effect due to motion. The convergence of these components are examined and the accuracy of the simulation is established for a large range of parameters like β, ε_r and R of the scatterer.

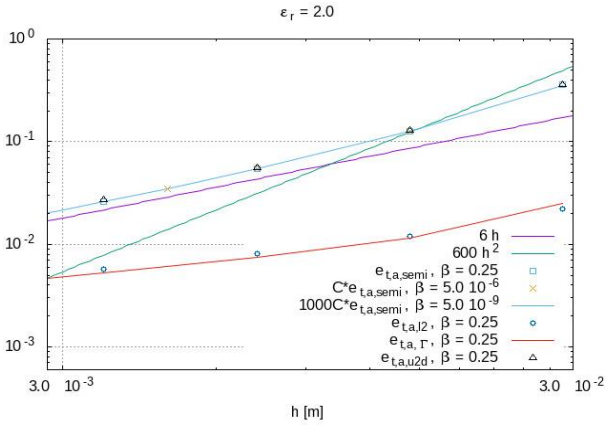

Fig. 3. Behaviour of $e_{t,a,u2d}$, $e_{t,a,l2}$, $e_{t,a,\Gamma}$ and $e_{t,a,semi}$ versus h, when the cylinder moves with $\beta = 0.25$. Plots proportional to $e_{t,a,semi}$ is also reported for $\beta = 5\ 10^{-m}$, $m = 6, 9$. $C = 5\ 10^7$. The cylinder is assumed to have $R = 0.2$ m and to be made up of a material having $\varepsilon_r = 2$ at rest. Two plots proportional to h and h^2 are provided, too.

In Fig. 3 some results related to the absolute errors on $\mathbf{E}_t$ are shown. The case $\beta = 0$ is not meaningful for the present analysis because, for the test case considered, the solution has $\mathbf{E}_t = 0$ in Ω and the finite element method is able to compute $\mathbf{E}_{ht} = 0$ in Ω for any mesh considered. For this reason, the results refer to cases in which $\beta \neq 0$. A complete set of results is shown for $\beta = 0.25$. One can observe that $e_{t,a,semi}$ is much larger than $e_{t,a,l2}$ and $e_{t,a,\Gamma}$ so that $e_{t,a,u2d} \approx e_{t,a,semi}$. Moreover, it can be observed that the convergence rate is $O(h)$ for all errors considered. The values of $e_{t,a,semi}$ for $m = 6$ and $m = 9$ are also shown in the figure. Over this large range of β, the convergence behaviour is not affected.

Now we verify what happens when the cylinder is made up of other materials. As in the previous subsection, we will consider $\varepsilon_r = 1.1$ and $\varepsilon_r = 8$ along with $\varepsilon_r = 2$. Figure 4 shows the relative error in H_z for these cases. The results are analogous to Fig. 2 except for the slower rate of convergence. Again, an increase in ε_r results in an increase in discretization error, due to the reduction in wavelength. The errors remain largely independent of β over a wide range, with β which could be as low as $5\ 10^{-9}$.

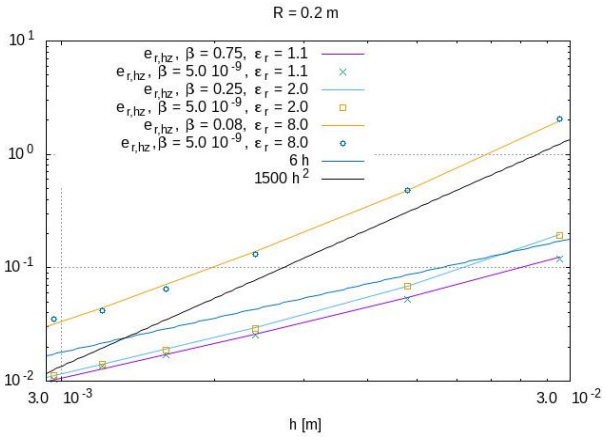

Fig. 4. Behaviour of $e_{r,hz}$ versus h for different values of β and ε_r. In particular, $\varepsilon_r = 1.1$, $\varepsilon_r = 2$ and $\varepsilon_r = 8$ are considered. In each case a value close to the upper bound of β is taken along with $\beta = 5\ 10^{-9}$. Two plots proportional to h and $h^2$are provided, too.

Finally, we study the effect of changing the radius of the scatterer. Along with the $R = 0.2$ m considered for the previous instances, $R = 0.1$ m and $R = 0.05$ m were examined. It is not appropriate to consider too small values of R. This is because of the non-conformity due to polygonal approximation of the circular boundary of the scatterer, as was explained in section IV. Instead the frequency is reduced so that the ratio of R to the wavelength reduces, which is expected to give an equivalent effect on discretization error. Hence, we study $f = 500$ MHz in addition to $f = 1$ GHz considered in the preceding cases. The discretization error is not affected much by the reduction in radius of the scatter. With $n = 120$ and $f = 1$ GHz, for $\beta \leq 5\ 10^{-10}$ the relative errors remain below 4% for all variations of R considered. As for the effect of reducing f, the discretization error drops below 2% which is expected from the increase in wavelength.

The results in this subsection and the last one show as expected [12], that the finite element approximation is converging to the true solution (notwithstanding the two violations of conformity pointed out in Section IV). However, the results related to $\mathbf{E}_t$ and H_z do start becoming worse due to round-off errors when the magnitude of these quantities become small. We consider such cases in the next section.

C. Problematic results related to $\mathbf{E_t}$ and H_z

In this subsection, we consider the cases when the round-off error becomes significant. As indicated by Equation (25), when the cross-polarized component becomes too low, the round-off error becomes more and more significant. Although we get good accuracy for the co-polarized component, the cross-polarized component could be unreliable. This could be the case with very low values of β, ε_r or R. Hence, in these critical cases, one needs to be careful with the simulations.

In Fig. 5 the relative errors pertaining to H_z are shown with respect to h for small β values with $m = 10, \ldots, 15$. For sufficiently small values of h, although the errors remain less than 10% up to $m = 12$, they start increasing for finer discretizations. The results become completely unreliable for smaller values of β. A finer discretization need not produce a decrease in the error in these critical cases, since the increase of round-off error is dominating over the reduction in discretization error. These results suggest that one should be careful in dealing with these delicate cases. One may have to make use of higher precision calculations to accurately solve these problems.

In Fig. 6 we examine the effect of different permittivity values along with small β. Again $\varepsilon_r = 1.1$ and $\varepsilon_r = 8.0$ are taken and we consider $m = 10, 11, 12$. The trend remains similar to that for $\varepsilon_r = 2.0$ in Fig. 5. For $\varepsilon_r = 8.0$, the errors start off large, due to higher discretization error, and goes on becoming worse due to round-off. For $\varepsilon_r = 1.1$, the discretization error is smaller than that for $\varepsilon_r = 2.0$. But once the round-off error becomes significant it can increase very quickly.

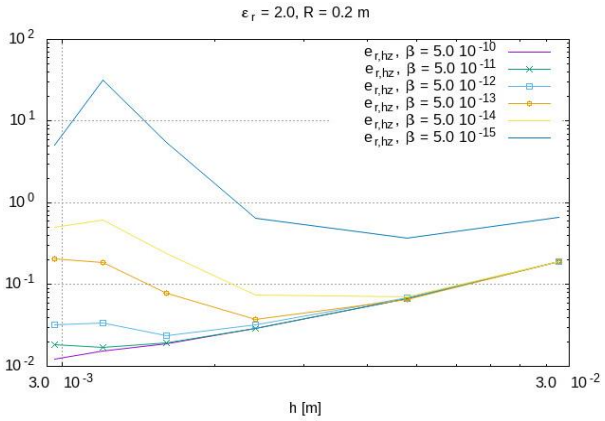

Fig. 5. Behaviour of $e_{r,hz}$ versus h, when the cylinder moves with $\beta = 5\ 10^{-m}$, $m = 10, \ldots, 15$. The cylinder is assumed to have $R = 0.2$ m and to be made up of a material having $\varepsilon_r = 2$ at rest.

In Fig. 7 the relative error on H_z is plotted against β values. Three different values are considered for the radius of scatterer, $R = 0.2, R = 0.1$ and $R = 0.05$ meters. The calculations are done for two frequency values $f = 1$ GHz and $f = 500$ MHz. The bi-anisotropic effect reduces as the scatterer becomes smaller, which might result in a higher round-off error. This could explain why the error starts increasing at $m = 11$ in the case of $f = 1$ GHz whereas for all other cases the error is stable till $m = 12$.

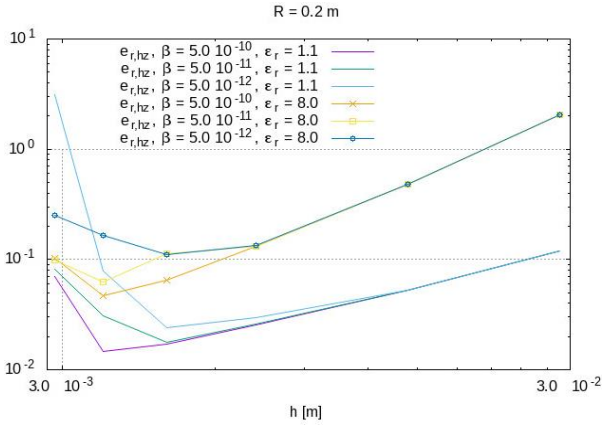

Fig. 6. Behaviour of $e_{r,hz}$ versus h for different values of β and ε_r. We consider $\varepsilon_r = 1.1$ and $\varepsilon_r = 8.0$ with $\beta = 5\ 10^{-m}$ and $m = 10, 11, 12$.

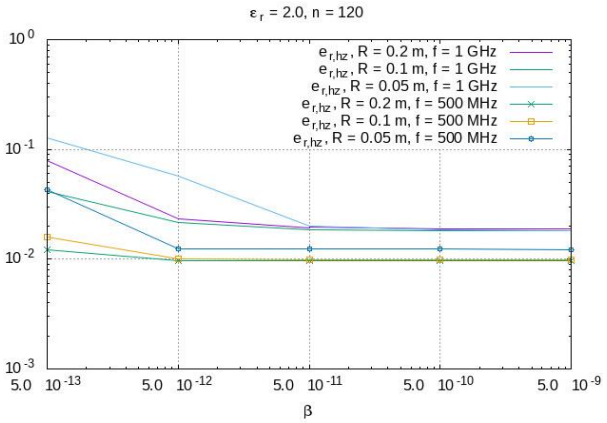

Fig. 7. Behaviour of $e_{r,hz}$ versus β for different values of the scatterer radius R and of the frequency f. The values of β which are particularly critical for $e_{r,hz}$ are considered. The cylinder is assumed to be made up of a material having $\varepsilon_r = 2$ at rest. The numerical solutions are computed by using a mesh with $n = 120$.

In Fig. 8 we plot the values of $\frac{nn+ne}{ne}\frac{|||[e_z]|||}{|||[e_t]|||}$ versus β. As long as the computation of $[e_t]$ is reasonably accurate, the value of $\frac{nn+ne}{ne}\frac{|||[e_z]|||}{|||[e_t]|||}$ is as expected proportional to β^{-1}. For the problem considered here the constant of proportionality is close to 2 in case of $\varepsilon_r = 8$ and $\varepsilon_r = 2$ and close to 20 for $\varepsilon_r = 1.1$. Thus the margin for error steadily decreases in accordance with Equation (25) as β decreases below $5\ 10^{-9}$ which corroborates the observed results.

The results in this subsection suggests that one must be careful with simulations involving weak bianisotropic effects. One needs to keep in mind the possible corruption of the results due to round-off errors. It may be required to use higher precision calculations to get reliable results in such instances. If one has a good estimate of the condition number, then it is possible to gauge the reliability of the result in terms of round-off error as indicated by Equation (25). However, the results that are obtained for the test case considered here reassure that one can obtain reliable solutions for a very wide span of parameters.

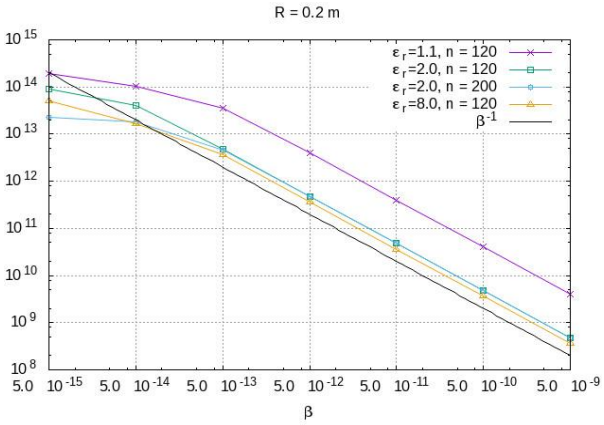

Fig. 8. Values of $\frac{nn+ne}{ne}\frac{|||[e_z]|||}{|||[e_t]|||}$ versus β for different values of ε_r and n. We consider $n = 120$ with $\varepsilon_r = 1.1$, $\varepsilon_r = 2$ and $\varepsilon_r = 8$. In addition, the value corresponding to $n = 200$ with $\varepsilon_r = 2$ is also shown. A plot of β^{-1} provided too.

VI. ISSUES RELATED TO NUMERICAL SOLUTION PROCEDURE

As it was already pointed out, iterative methods are very often exploited to compute the solution of the algebraic linear systems determined by electromagnetic finite element codes [19] (pp. 382, 383, 396-405). In particular, the BiCG (biconjugate gradient method) [19] (pp. 396-405) is known to be particularly efficient for time-harmonic electromagnetic problems [24] (p. 308) involving only traditional media. However, we observed that in our case, this method fails to converge for values of β which are not very small. This is because the structure of the matrix $[A]$ is altered, since its submatrices $[A_{zt}]$ and $[A_{tz}]$ become more significant for higher β values. We may use some alternative iterative methods

in such cases [21], [25]. In particular, CGNE (Conjugate gradient on normal equation) is a simple alternative. However, the condition number is squared in this case resulting in slower convergence and worse round-off errors. Use of preconditioner can help improve the condition number of the system both when BiCG and CGNE are used. Simple Jacobi preconditioner was used for this purpose in the present work and the corresponding methods are denoted as BiCGJP and CGNEJP.

All the results shown in Section V were calculated by using BiCG, BiCGJP, CGNE or CGNEJP. We give a brief discussion of their performance here. If the algebraic linear system to be solved is $[A][e] = [l]$, as reported in Section III, we initially calculate the euclidean norm $||[l]||$ of $[l]$ and do not stop the iterative solver until the approximate solution $[e]_i$ at iteration i satisfies $||[A][e]_i - [l]|| < \delta||[l]||$, with δ always equal to 10^{-p}, $p \in \{10, \dots, 16\}$. One should avoid using larger values of p when double-precision arithmetic is used [21] (p. 58). In order to avoid presenting unreliable results we computed them at least twice, for two consecutive values of p. When the outcomes were different we considered the next larger value of p and did not stop this process until, for two consecutive values of p, we got the same result (with a tolerance equal to 0.1%).

Independently of the reliability of the outcome, we find that the BiCGJP is able to compute the solutions for all values of β and p considered and all $n \leq 80$. For finer meshes the convergence of biconjugate iterative solvers is not guaranteed anymore. Consider, for example, some data for the test cases with $\varepsilon_r = 2$, $R = 0.2$ m and $f = 1$ GHz. When $n = 120$, BiCGJP does not converge for $\beta \geq 5\ 10^{-5}$ (for this specific example the smallest residual value seems to be $\simeq 0.26$ which is by far too large to stop the iterations). BiCG fails to converge, with the same n, for $\beta \geq 5\ 10^{-3}$ (the smallest residual value is $\simeq 0.026$). For a mesh obtained by using $n = 160$ BiCG (respectively, BiCGJP) does not converge for $\beta \geq 5\ 10^{-7}$ (respectively, $\beta \geq 5\ 10^{-5}$). When $\beta = 5\ 10^{-7}$ the smallest residual value is $\simeq 3.2\ 10^{-7}$ (respectively, $\simeq 0.28$ for $\beta = 5\ 10^{-5}$). For the same mesh, by using $p = 13$, BiCGJP converges in 20214 steps (with the indicated mesh we have 308161 unknowns) for $\beta = 5\ 10^{-7}$and in 242643 steps for $\beta = 5\ 10^{-6}$. Finally, when $n = 200$ we have 481201 unknowns and BiCGJP and BiCG fail to converge for $\beta \geq 5\ 10^{-7}$, reaching a minimum residual value, for $\beta = 5\ 10^{-7}$, of $0.45\ 10^{-5}$ and, respectively, 0.5. For this mesh, BiCGJP converges in 22956, 20001, 17834 and 13415 steps for $\beta = 5\ 10^{-m}$, with m respectively equal to 8, 9, 10, 11 for $p = 15$. It is also interesting to point out that it converges in 3556 steps for $\beta = 0$ (and $p = 15$ as before).

From the previous considerations, one can also understand that most of our results were calculated by using CGNE or CGNEJP. The convergence of this type of algebraic solver, however, is by far too slow, independently of the use of the preconditioner. Even though this is not a surprise [24] (p. 308), [21] (p. 18), it is instructive to report some data. For example, CGNE, for $p = 15$ and $n = 200$, requires 536957 steps to converge for $\beta = 5\ 10^{-6}$ and 710410 steps for $\beta = 0.25$ ($\varepsilon_r = 2$, $R = 0.2$ m, $f = 1$ GHz). The results are not much better when the point Jacobi preconditioner is used. For example, with the usual values of ε_r, R and f, for $n = 120$ and $\beta = 0.25$ CGNEJP converges in 220942 steps (173521 unknowns) while CGNE does the same requiring 233866 steps ($p = 13$ in both cases). In terms of CPU time the difference is even lower (equal, more or less, to 4% on the same computer).

Thus, for small values of β BiCG and BiCGJP are suitable for giving fast convergence and lower round-off errors compared to CGNE and CGNEJP. The methods break down for larger values of β and we can use CGNE or CGNEJP which converge but at a much slower rate.

VII. CONCLUSIONS

The accuracy of finite element results in the presence of axially moving cylinders is analyzed for the first time, to the best of authors' knowledge.

The study refers to relative and absolute errors related to two components of the electromagnetic field. The part of the results presented concerning one of the two components is new but the outcome is analogous to the one which is obtained when all media involved are motionless. The second part is related to the field component which is specifically excited by the presence of moving objects. This field component is the most difficult to be approximated. For its information content related to the motion of the objects, it could also be the most important component to be evaluated, at least for some applications.

This study has shown that finite element simulators based on double precision arithmetic could guarantee extraordinary reliability of all their outcomes. These performances suggest that the indicated simulators can be exploited and could become the reference method for astrophysics, engineering and medical applications involving media in motion.

REFERENCES

[1] J. G. Van Bladel, *Electromagnetic Fields*. 2nd ed., Piscataway, NJ, USA: IEEE Press, 2007.

[2] J. H. Alwash and L. J. Qaseer, "Three-dimension finite element analysis of a helical motion induction motor," *Applied Computational Electromagnetics Society Journal*, vol. 25, no. 8, pp. 703-712, 2010.

[3] A. M. Messiaen and P. E. Vandenplas, "High-frequency effect due to the axial drift velocity of a plasma column," *Physical Review*, vol. 149, pp.

131-140, September 1966.

[4] C. Yeh, "Scattering obliquely incident microwaves by a moving plasma column," *Journal of Applied Physics*, vol. 40, no. 13, pp. 5066-5075, December 1969.

[5] T. Shiozawa and S. Seikai, "Scattering of electromagnetic waves from an inhomogeneous magnetoplasma column moving in the axial direction," *IEEE Transactions on Antennas and Propagation*, vol. 20, no. 4, pp. 455-463, July 1972.

[6] J. V. Parker, J. C. Nickel, and R. W. Gould, "Resonance oscillations in a hot nonuniform plasma," *Physics of Fluids*, vol. 7, no. 9, pp. 1489-1500, September 1964.

[7] D. Censor, "Scattering of electromagnetic waves by a cylinder moving along its axis," *IEEE Transactions on Microwave Theory and Techniques*, vol. 17, no. 3, pp. 154-158, March 1969.

[8] Y. Yan, "Mass flow measurement of bulk solids in pneumatic pipelines," *Measurement Science and Technology*, vol. 7, no. 12, pp. 1687-1706, 1996.

[9] A. Freni, C. Mias, and R. L. Ferrari, "Finite element analysis of electromagnetic wave scattering by a cylinder moving along its axis surrounded by a longitudinal corrugated structure," *IEEE Transactions on Magnetics*, vol. 32, no. 3, pp. 874-877, May 1996.

[10] A. Sommerfeld, *Electrodynamics*. ser. Lectures on Theoretical Physics. Academic Press, 1959.

[11] D. K. Cheng and J.-A. Kong, "Covariant descriptions of bianisotropic media," *Proceedings of the IEEE*, vol. 56, no. 3, pp. 248-251, March 1968.

[12] M. Brignone and M. Raffetto, "Well posedness and finite element approximability of two-dimensional time-harmonic electromagnetic problems involveing non-conducting moving objects with stationary boundaries," *ESAIM: Mathematical Modelling and Numerical Analysis*, vol. 49, no. 4, pp. 1157-1192, July-August 2015.

[13] M. M. Botha and D. B. Davidson, "Investigation of an explicit, residual-based, a posteriori error indicator for the adaptive finite element analysis of waveguide structures," *Applied Computational Electromagnetics Society Journal*, vol. 21, no. 1, pp. 63-71, 2006.

[14] P. G. Ciarlet and J. L. Lions (Eds.), *Handbook of Numerical Analysis, vol. II, Finite Element Methods, Part 1*. Amsterdam: North-Holland, 1991.

[15] M. Pastorino and M. Raffetto, "Scattering of electromagnetic waves from a multilayer elliptic cylinder moving in the axial direction," *IEEE Transactions on Antennas and Propagation*, vol. 61, no. 9, pp. 4741-4753, September 2013.

[16] M. Pastorino, M. Raffetto, and A. Randazzo, "Electromagnetic inverse scattering of axially moving cylindrical targets," *IEEE Transactions on Geoscience and Remote Sensing*, vol. 53, no. 3, pp. 1452-1462, March 2015.

[17] M. Brignone, G. L. Gragnani, M. Pastorino, M. Raffetto, and A. Randazzo, "Noise limitations on the recovery of average values of velocity profiles in pipelines by simple imaging systems," *IEEE Geoscience and Remote Sensing Letters*, vol. 13, no. 9, pp. 1340-1344, September 2016.

[18] J. D. Jackson, *Classical Electrodynamics*. 3rd ed., New York: Wiley, 1999.

[19] J. Jin, *The Finite Element Method in Electromagnetics*. New York: John Wiley & Sons, 1993.

[20] P. Monk, *Finite Element Methods for Maxwell's Equations*. Oxford: Oxford Science Publications, 2003.

[21] R. Barrett, M. Berry, T. F. Chan, J. Demmel, J. Donato, J. Dongarra, V. Eijkhout, R. Pozo, C. Romine, and H. Van der Vorst, *Templates for the Solution of Linear Systems: Building Blocks for Iterative Methods*. 2nd Edition. Philadelphia, PA: SIAM, 1994.

[22] G. Cevini, G. Oliveri, and M. Raffetto, "Further comments on the performances of finite element simulators for the solution of electromagnetic problems involving metamaterials," *Microwave and Optical Technology Letters*, vol. 48, no. 12, pp. 2524-2529, December 2006.

[23] M. Pastorino, *Microwave Imaging*. New York: Wiley, 2010.

[24] J. L. Volakis, A. Chatterjee, and L. C. Kempel, *Finite Element Method for Electromagnetics: Antennas, Microwave Circuits, and Scattering Applications*. Piscataway, NJ, USA: IEEE Press, 1998.

[25] Y. F. Jing, T. Z. Huang, B. Carpentieri, and Y. Duan, "Investigating the composite step biconjugate A-orthogonal residual method for non-hermitian dense linear systems in electromagnetics," *Applied Computational Electromagnetics Society Journal*, vol. 27, no. 2, pp. 112-122, 2012.

An Iterative CN-Leapfrog Scheme Based Hybrid Implicit–Explicit Discontinuous Galerkin Finite-Element Time-Domain Method for Analysis of Multiscale Problems

M. Li [1,2], X. D. Ye [3], F. Xu [1], and Y. T. Yang [3]

[1] School of Electronic Science and Engineering
Nanjing University of Posts and Telecommunications, Nanjing, 210003, China

[2] Department of Electronic Information Engineering
Suqian College, Suqian, 223800, China
18800608557@163.com

[3] Department of Communication Engineering
Nanjing University of Science and Technology, Nanjing, 210094, China
yexiaodong@njust.edu.cn

Abstract ─ The discontinuous Galerkin finite-element time-domain (DG-FETD) method with the ability to deal with unstructured meshes is well suited to analyze the multiscale system. However the DG-FETD method with explicit integration schemes is constrained by stability conditions that can be very restrictive upon highly fine meshes. The hybrid implicit–explicit Crank-Nicolson (CN) leapfrog scheme is effective in solving this problem; but because of using CN scheme, the inversion of a large sparse matrix must be calculated at each time step in the fine regions. The hybrid implicit–explicit iterative CN leapfrog scheme is introduced to improve the computational efficiency which can form a block diagonal matrix. The leapfrog scheme is employed for electrically coarse regions and iterative CN scheme for electrically fine ones. The numerical examples have demonstrated the validity and efficiency of the method.

Index Terms ─ Crank-Nicolson, discontinuous Galerkin finite-element time-domain method, multi-scale.

I. INTRODUCTION

When handling the multiscale electromagnetic simulations in transient electromagnetic analysis, such as electromagnetic interference and electromagnetic compatibility problems, traditional methods face great challenges because of small size meshes in the fine regions. The finite-element time-domain (FETD) method is widely used because of its flexibility in geometric modeling, but it must calculate a large sparse matrix inversion at each time step [1]. Then the discontinuous Galerkin method has been proposed and combined with the FETD method called discontinuous Galerkin finite-element time-domain (DG-FETD) method [2]-[4]; Numerical fluxes are introduced to impose the tangential continuity of the electrical and magnetic fields at the interfaces between adjacent elements. Central flux [5, 6] and upwind flux [7, 8] are the commonly used ways. The explicit leapfrog scheme for DG-FETD method can make the mass matrix block-diagonal and it is convenient for matrix inversion and parallel computing rather than solve a huge matrix system as conventional FETD method [9-12]. But the size of the time step of the explicit leapfrog DG-FETD is limited by the spatial discretization of the simulation domain according to the CFL condition which will lead to produce a large number of simulation steps and reduce the computation efficiency. Generally, a discretized multiscale system usually contains both electrically coarse meshes and fine meshes. Because of the constraint of Courant-Friedrichs-Levy (CFL) stability condition [13], the time step increments for electrically fine meshes may be much less than those for electrically coarse meshes when the explicit leapfrog time integration scheme is employed. According to this circumstance, hybrid implicit-explicit Crank-Nicolson (CN) leapfrog scheme have been proposed to get a higher computational efficiency [14]. The implicit CN scheme used in fine regions can make the system unconditionally stable but also require solving large matrices equations which will destroy the original powerful ability of DG-FETD. Therefore, an iterative CN leapfrog scheme DG-FETD is proposed, which can not only make system unconditionally stable but also maintain the advantage of DG-FETD.

In this paper, an iterative CN leapfrog scheme is introduced to analyze multiscale electromagnetic

Submitted On: August 29, 2016
Accepted On: April 21, 2018

problems. The leapfrog scheme is employed for electrically coarse regions and iterative Crank-Nicholson scheme [15] for electrically fine ones. In the paper, an iterative CN leapfrog scheme is first introduced with poor convergence. To solve the poor convergence problem, a modified iterative CN leapfrog scheme is further presented to speed up the convergence.

The paper is organized as follows. The basic theory and formulations of the hybrid implicit–explicit iterative CN leapfrog scheme for DG-FETD is presented in Section II. The numerical results are given to demonstrate the validity of proposed method in Section III, and the conclusion is drawn in Section IV.

II. THEORY AND FORMULATIONS

A. DG-FETD spatial semi-discrete formulation

The implementation steps of the DG-FETD method include choice of the governing equation, grid discretization and imposing the tangential continuity of the electrical and magnetic fields at the interfaces between adjacent elements. In this paper, first order Maxwell's curl equations based on $\boldsymbol{E}$ and $\boldsymbol{H}$ are employed and the model is discretized by tetrahedral meshes, central flux scheme is employed. Considering the time-dependent Maxwell's curl equations for a linear, lossless, isotropic and non-dispersive medium, the electric field $\boldsymbol{E}$ and the magnetic field $\boldsymbol{H}$ can be described as:

$$\varepsilon \frac{\partial \boldsymbol{E}}{\partial t} = \nabla \times \boldsymbol{H} , \tag{1}$$

$$\mu \frac{\partial \boldsymbol{H}}{\partial t} = -\nabla \times \boldsymbol{E} , \tag{2}$$

where ε represents the permittivity and μ denotes the permeability. The electric and magnetic fields can be expanded by Whiney edge elements [16] as:

$$\boldsymbol{E} = \sum\nolimits_j \boldsymbol{W}_{ej} e_j , \quad \boldsymbol{H} = \sum\nolimits_j \boldsymbol{W}_{hj} h_j . \tag{3}$$

The curl-conforming vector basis functions $\boldsymbol{W}_{ej}$ and $\boldsymbol{W}_{hj}$ are chosen to discretize the $\boldsymbol{E}$ field and $\boldsymbol{H}$ field respectively. Then e_j and h_j are the unknown coefficients. The Galerkin's weak forms of Maxwell's equations can be described as:

$$\iiint_V \boldsymbol{W}_{ei} \cdot \varepsilon \frac{\partial \boldsymbol{E}}{\partial t} dV - \iiint_V \nabla \times \boldsymbol{W}_{ei} \cdot \boldsymbol{H} dV = \iint_S \boldsymbol{W}_{ei} \cdot (\mathbf{n} \times \boldsymbol{H}) dS, \tag{4}$$

$$\iiint_V \boldsymbol{W}_{hi} \cdot \mu \frac{\partial \boldsymbol{H}}{\partial t} dV + \iiint_V \nabla \times \boldsymbol{W}_{hi} \cdot \boldsymbol{E} dV = \iint_S \boldsymbol{W}_{hi} \cdot (\mathbf{n} \times \boldsymbol{E}) dS. \tag{5}$$

The central flux is employed for each element to impose the tangential continuity of the electric and magnetic fields at the interfaces between adjacent elements and the expression is:

$$\mathbf{n} \times \boldsymbol{H}\big|_{\partial V} = \frac{1}{2} \mathbf{n} \times (\boldsymbol{H} + \boldsymbol{H}^+)\Big|_{\partial V} , \tag{6}$$

$$\mathbf{n} \times \boldsymbol{E}\big|_{\partial V} = \frac{1}{2} \mathbf{n} \times (\boldsymbol{E} + \boldsymbol{E}^+)\Big|_{\partial V} , \tag{7}$$

where $\boldsymbol{E}$ and $\boldsymbol{H}$ represent the electric and magnetic fields of the elements within sub-domain V, $\boldsymbol{E}^+$ and $\boldsymbol{H}^+$ represent electric and magnetic fields of the adjacent elements within the neighboring sub-domain V+. By substituting (6) and (7) into (4) and (5), the final spatial semi-discrete DG-FETD formulations can be converted into a matrix equation as follows:

$$\mathbf{T}_{ee} \frac{\partial \boldsymbol{e}}{\partial t} = \mathbf{P}_{eh} \boldsymbol{h} + \mathbf{S}^+_{eh} \boldsymbol{h} , \tag{8},$$

$$\mathbf{T}_{hh} \frac{\partial \boldsymbol{h}}{\partial t} = \mathbf{P}_{he} \boldsymbol{e} + \mathbf{S}^+_{he} \boldsymbol{e} , \tag{9}$$

where $\mathbf{T}_{ee}$, $\mathbf{T}_{hh}$, $\mathbf{P}_{eh}$, $\mathbf{P}_{he}$, $\mathbf{S}^+_{eh}$ and $\mathbf{S}^+_{he}$ are the sparse matrices, $\boldsymbol{e}$ and $\boldsymbol{h}$ are the unknown vectors. The matrix elements are defined as:

$$[\mathbf{T}_{ee}]_{ij} = \varepsilon \iiint_V \boldsymbol{W}_{ei} \cdot \boldsymbol{W}_{ej} dV ,$$

$$[\mathbf{T}_{hh}]_{ij} = \mu \iiint_V \boldsymbol{W}_{hi} \cdot \boldsymbol{W}_{hj} dV ,$$

$$[\mathbf{P}_{eh}]_{ij} = \iiint_V \nabla \times \boldsymbol{W}_{ei} \cdot \boldsymbol{W}_{hj} dV + \frac{1}{2} \iint_S \boldsymbol{W}_{ei} \cdot \mathbf{n} \times \boldsymbol{W}_{hj} dS ,$$

$$[\mathbf{P}_{he}]_{ij} = -\iiint_V \nabla \times \boldsymbol{W}_{hi} \cdot \boldsymbol{W}_{ej} dV - \frac{1}{2} \iint_S \boldsymbol{W}_{hi} \cdot \mathbf{n} \times \boldsymbol{W}_{ej} dS ,$$

$$[\mathbf{S}^+_{eh}]_{ij} = \frac{1}{2} \iint_S \boldsymbol{W}_{ei} \cdot \mathbf{n} \times \boldsymbol{W}^+_{hj} dS ,$$

$$[\mathbf{S}^+_{he}]_{ij} = -\frac{1}{2} \iint_S \boldsymbol{W}_{hi} \cdot \mathbf{n} \times \boldsymbol{W}^+_{ej} dS .$$

B. Iterative CN-leapfrog scheme

When dealing with multiscale electromagnetic problems, very small size meshes will appear in fine regions of the model. Though explicit leapfrog scheme of the DG-FETD method makes the mass matrix block-diagonal and it is convenient for matrix inversion and parallel computing. But the size of the time step of the explicit leapfrog DG-FETD is limited by the spatial discretization of the simulation domain according to the CFL condition which lead to produce a large number of simulation steps and reduce the computation efficiency. In contrast, the implicit time step schemes are proved to be unconditionally stable with large time step intervals but require solving large matrix equations. Therefore, hybrid implicit-explicit CN leapfrog scheme can be attractive in multi-scale electromagnetic simulations. However, the implicit-explicit CN leapfrog DG-FETD lost the block diagonal characteristic because of using implicit CN scheme which lead to a mass matrix of DG-FETD. In this section, an iterative CN Leapfrog scheme is proposed to deal with the above problems

which can not only maintain the block diagonal characteristic of the DG-FETD method but also improve the computational efficiency.

The proposed hybrid iterative CN Leapfrog scheme divides the whole computational domain into the coarse region marked by region 1 and the fine region marked by region 2, [1]. In region 1, explicit leapfrog scheme is employed to DG-FETD method and the Eq. (8), Eq. (9) above can be changed into:

$$\mathbf{T}_{hh}\frac{h^{n+\frac{1}{2}}-h^{n-\frac{1}{2}}}{\Delta t}=\mathbf{P}_{he}e^{n}+\frac{1}{2}(\mathbf{S}_{he}e^{n}+\mathbf{S}_{he}^{+}e^{n}), \quad (10)$$

$$\mathbf{T}_{ee}\frac{e^{n+1}-e^{n}}{\Delta t}=\mathbf{P}_{eh}h^{n+\frac{1}{2}}+\frac{1}{2}(\mathbf{S}_{eh}h^{n+\frac{1}{2}}+\mathbf{S}_{eh}^{+}h^{n+\frac{1}{2}}). \quad (11)$$

Where Δt represents the time step size and can be expressed as:

$$\Delta t \le \frac{h_{\min}}{2v_{\max}(\mathrm{p}+1)^{2}},$$

where $h_{\min}$ is the minimum length of the mesh, $v_{\max}$ is the propagation speed of the wave in the object, P is the order of the base function.

In region 2, iterative CN scheme is applied to DG-FETD method and the Eq. (8), Eq. (9) can be expressed as:

$$\mathbf{T_{hh}}\cdot\frac{h^{n+1}-h^{n}}{\Delta t}=\mathbf{P_{he}}\cdot\frac{e^{n+1}+e^{n}}{2}+\mathbf{S_{he}}\cdot\frac{e^{n+1}+e^{n}}{2}+\mathbf{S_{he}}^{+}\cdot\frac{e^{n+1}+e^{n}}{2}, \quad (12)$$

$$\mathbf{T_{ee}}\cdot\frac{e^{n+1}-e^{n}}{\Delta t}=\mathbf{P_{eh}}\cdot\frac{h^{n+1}+h^{n}}{2}+\mathbf{S_{eh}}\cdot\frac{h^{n+1}+h^{n}}{2}+\mathbf{S_{eh}}^{+}\cdot\frac{h^{n+1}+h^{n}}{2}. \quad (13)$$

The proposed scheme can be described by the following steps:

Step 1. Assume that the correct overall distribution of the electromagnetic fields at the time of $n\Delta t$ is known.

Step 2. In region 1, the leapfrog scheme for DG-FETD as Eq. (10) and Eq. (11) calculate the electric and magnetic fields at the time of $(n+\frac{1}{2})\Delta t$:

$$\begin{cases}\mathbf{T_{hh1}}\cdot\dfrac{h_1^{n+\frac{1}{2}}-h_1^{n}}{\Delta t/2}=\mathbf{P_{he1}}\cdot e_1^{n}+\mathbf{S_{he1}}\cdot e_1^{n}+\mathbf{S_{he1}^{+}}\cdot e_1^{n}+\mathbf{S_{he12}^{+}}\cdot e_2^{n}\\ \mathbf{T_{ee1}}\cdot\dfrac{e_1^{n+\frac{1}{2}}-e_1^{n}}{\Delta t/2}=\mathbf{P_{eh1}}\cdot h_1^{n+\frac{1}{2}}+\mathbf{S_{eh1}}\cdot h_1^{n+\frac{1}{2}}+\mathbf{S_{eh1}^{+}}\cdot h_1^{n+\frac{1}{2}}+\mathbf{S_{eh12}^{+}}\cdot h_2^{n}\end{cases}. \quad (14)$$

Step 3. In region 2, CN scheme for DG-FETD as Eq. (12) and Eq. (13) calculate the electric and magnetic fields at the time of $(n+1)\Delta t$:

$$\begin{cases}\mathbf{T_{hh2}}\cdot\dfrac{h_2^{n+1}-h_2^{n}}{\Delta t}\\ =\mathbf{P_{he2}}\cdot\dfrac{e_2^{n+1}+e_2^{n}}{2}+\mathbf{S_{he2}}\cdot\dfrac{e_2^{n+1}+e_2^{n}}{2}+\mathbf{S_{he2}}^{+}\cdot\dfrac{e_2^{n+1}+e_2^{n}}{2}+\mathbf{S_{he21}^{+}}\cdot e_1^{n+\frac{1}{2}}\\ \mathbf{T_{ee2}}\cdot\dfrac{e_2^{n+1}-e_2^{n}}{\Delta t}\\ =\mathbf{P_{eh2}}\cdot\dfrac{h_2^{n+1}+h_2^{n}}{2}+\mathbf{S_{eh2}}\cdot\dfrac{h_2^{n+1}+h_2^{n}}{2}+\mathbf{S_{eh2}}^{+}\cdot\dfrac{h_2^{n+1}+h_2^{n}}{2}+\mathbf{S_{eh21}^{+}}\cdot h_1^{n+\frac{1}{2}}\end{cases}. \quad (15)$$

Equation (15) can be converted into a matrix equation:

$$\begin{aligned}&\begin{bmatrix}\mathbf{T_{ee2}} & -\Delta t\dfrac{\mathbf{P_{eh2}}+\mathbf{S_{eh2}}}{2}\\ -\Delta t\dfrac{\mathbf{P_{he2}}+\mathbf{S_{he2}}}{2} & \mathbf{T_{hh2}}\end{bmatrix}\begin{bmatrix}e_2^{n+1}\\ h_2^{n+1}\end{bmatrix}+\mathbf{S_{eh2}^{+}}\begin{bmatrix}e_2^{n+1}\\ h_2^{n+1}\end{bmatrix}+\mathbf{S_{he2}^{+}}\begin{bmatrix}e_2^{n+1}\\ h_2^{n+1}\end{bmatrix}\\ &=\begin{bmatrix}\mathbf{T_{ee2}} & \Delta t\dfrac{\mathbf{P}_{eh2}+\mathbf{S_{eh2}}+\mathbf{S_{eh2}^{+}}}{2}\\ \Delta t\dfrac{\mathbf{P_{he2}}+\mathbf{S_{he2}}+\mathbf{S_{he2}^{+}}}{2} & \mathbf{T_{hh2}}\end{bmatrix}\begin{bmatrix}e_2^{n}\\ h_2^{n}\end{bmatrix}\\ &+\begin{bmatrix}\Delta t\mathbf{S_{eh21}^{+}}\\ \Delta t\mathbf{S_{he21}^{+}}\end{bmatrix}\begin{bmatrix}e_1^{n+\frac{1}{2}}\\ h_1^{n+\frac{1}{2}}\end{bmatrix},\end{aligned} \quad (16)$$

because $\mathbf{S_{eh2}^{+}}$ and $\mathbf{S_{he2}^{+}}$ present the matrices of the adjacent element in region 2 which destroy the block diagonal characteristic of the mass matrix, $\mathbf{S_{eh2}^{+}}$ and $\mathbf{S_{he2}^{+}}$ are moved to the right-hand side of the equation to ensure the mass matrix of the left-hand side is a block diagonal matrix:

$$\begin{aligned}&\begin{bmatrix}\mathbf{T_{ee2}} & -\Delta t\dfrac{\mathbf{P_{eh2}}+\mathbf{S_{eh2}}}{2}\\ -\Delta t\dfrac{\mathbf{P_{he2}}+\mathbf{S_{he2}}}{2} & \mathbf{T_{hh2}}\end{bmatrix}\begin{bmatrix}e_2^{n+1}\\ h_2^{n+1}\end{bmatrix}\\ &=\begin{bmatrix}\mathbf{T_{ee2}} & \Delta t\dfrac{\mathbf{P}_{eh2}+\mathbf{S_{eh2}}+\mathbf{S_{eh2}^{+}}}{2}\\ \Delta t\dfrac{\mathbf{P_{he2}}+\mathbf{S_{he2}}+\mathbf{S_{he2}^{+}}}{2} & \mathbf{T_{hh2}}\end{bmatrix}\begin{bmatrix}e_2^{n}\\ h_2^{n}\end{bmatrix}\\ &+\begin{bmatrix}\Delta t\mathbf{S_{eh21}^{+}}\\ \Delta t\mathbf{S_{he21}^{+}}\end{bmatrix}\begin{bmatrix}e_1^{n+\frac{1}{2}}\\ h_1^{n+\frac{1}{2}}\end{bmatrix}+\begin{bmatrix}\Delta t\dfrac{\mathbf{S}_{eh2}^{+}}{2}\\ \Delta t\dfrac{\mathbf{S}_{he2}^{+}}{2}\end{bmatrix}\begin{bmatrix}e_2^{n+1}\\ h_2^{n+1}\end{bmatrix}.\end{aligned} \quad (17)$$

The linear system of Eq. (17) will be solved iteratively and can be expressed as:

$$[\mathbf{T}]u_{i,k+1}^{n+1}=[\mathbf{S_1}]u_i^{n}+[\mathbf{S_2}]u_j^{n}+[\mathbf{S_3}]u_{j,k}^{n+1},$$

where subscript i represents the *i*th element, j represents the *j*th adjacent element, subscript k denotes the *k*th iteration. The initial value of $u_{j,0}^{n+1}$ in the right hand side of the equation is set to be the previous time step value u_j^n as $u_{j,0}^{n+1} = u_j^n$. After a few iterations for the solution of the $u_{i,k+1}^{n+1}$, the error can be acceptable and then go to the next step .

Iterative number for convergence determines the speedup effect of the method during the implementation. In this paper, the global iterative method is first proposed. By one-time iteration, all of the unknowns are obtained and compared with the results in the previous step. Root mean square error (RMSE) is calculated to determine whether the iteration is over or not. If the iteration is over, it will go to the next step. However, this method we first proposed with disadvantage of poor convergence performance will lead to increasing the iterative steps and enlarge the time step size. To solve this problem, a modified iterative CN method is further proposed. For this method, electromagnetic fields of each element are calculated by iteration and are updated immediately until all the elements are calculated and updated. Then RMSE is calculated. The procedure of the two proposed methods is given as Fig. 1 below.

Step 4. In region 1, CN scheme is employed in Eq. (6) and Eq. (7) to calculate the electric and magnetic fields at the time of $(n+1)\Delta t$:

$$\begin{cases} \mathbf{T}_{\mathbf{ee1}} \cdot \dfrac{e_1^{n+1} - e_1^{n+\frac{1}{2}}}{\Delta t/2} = \mathbf{P}_{\mathbf{eh1}} \cdot h_1^{n+\frac{1}{2}} + \mathbf{S}_{\mathbf{eh1}} \cdot h_1^{n+\frac{1}{2}} + \mathbf{S}_{\mathbf{eh1}} \cdot h_1^{n+\frac{1}{2}} + \mathbf{S}_{\mathbf{eh12}}^{+} \cdot h_2^{n+1} \\ \mathbf{T}_{\mathbf{hh1}} \cdot \dfrac{h_1^{n+1} - h_1^{n+\frac{1}{2}}}{\Delta t/2} = \mathbf{P}_{\mathbf{he1}} \cdot e_1^{n+1} + \mathbf{S}_{\mathbf{he1}} \cdot e_1^{n+1} + \mathbf{S}_{\mathbf{he1}} \cdot e_1^{n+1} + \mathbf{S}_{\mathbf{he12}}^{+} \cdot e_2^{n+1} \end{cases}.$$

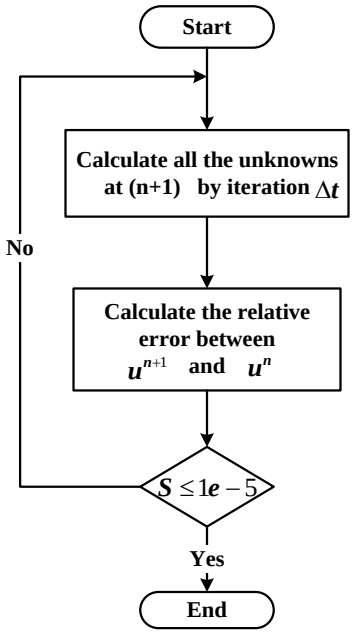

(a)

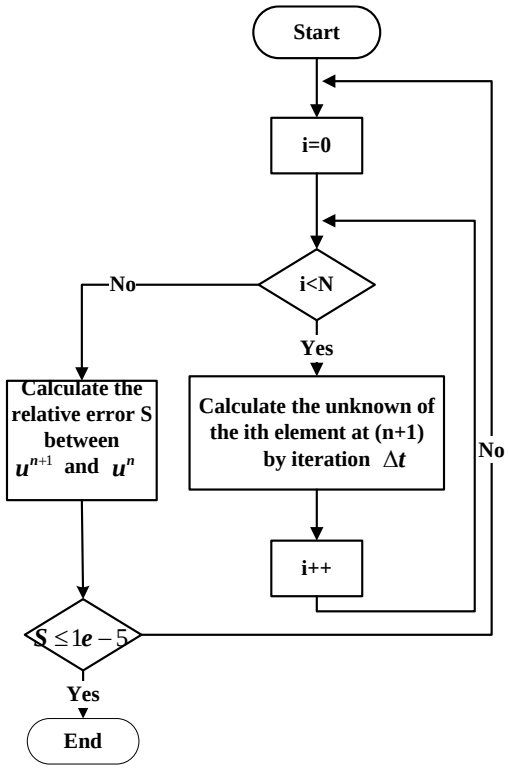

(b)

Fig. 1. (a) Flow chart of the iterative CN scheme, and (b) flow chart of the modified iterative CN scheme.

III. NUMERICAL RESULTS AND DISCUSSION

In order to verify the accuracy and efficiency of the proposed method, two numerical examples are analyzed. The first example is a rectangular cavity with the size of 10*mm*×5*mm*×15*mm*. The number of the discretized tetrahedron is 1771 and the number of unknowns is 19015 and the time step size is 1.17×10^{-13} s which is five times as large as that of the leapfrog scheme. A modulated Gaussian pulse is selected as the excitation and the center frequency is 18GHz. The convergence speed is compared between iterative CN DG-FETD and modified iterative CN DG-FETD when both of the methods require 500 time steps. As shown in Fig. 2, the modified iterative CN DG-FETD can speed up the convergence effectively. The parameters of CN DG-FETD and iterative CN DG-FETD are also compared as shown in Table 1, which further demonstrates that the convergence speed of modified iterative CN method is superior to the iterative CN method and computational time of modified iterative CN method is much less than CN method.

The second example is a metal cylinder cavity loaded with a dielectric cylinder as shown in Fig. 3. The radius of the metal cylinder is 0.5m and the height is 1m .The radius of the dielectric cylinder is 0.05m, the

height is 0.02m and the relative permittivity is 4.0. A modulated Gaussian pulse is selected as the excitation in y direction with the center frequency of 230MHz. The number of the total discretized tetrahedron is 8464. The number of unknowns is 96089 with 14005 unknowns for the fine domain using CN method and 82084 unknowns for coarse domain using leapfrog method. The time step size is 1.33×10^{-11}s which is twice leapfrog time step size, Fig. 4 represents the transient scattering fields with two different method. Good agreement can be shown from the results obtained by the above different ways. Furthermore, Table 2 exhibits computational cost of the above different methods which further demonstrate the efficiency and accuracy of the proposed method.

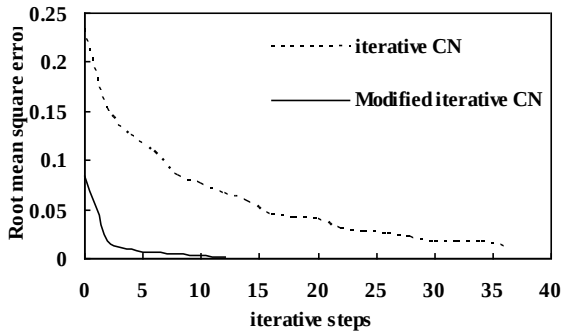

Fig. 2. Comparison of the convergence speed between two methods.

Table 1: Comparison of computational efficiency

Method	Number of Unknowns (CN)	Number of Unknowns (Leapfrog)	Iterative Steps	Iterative Time(s)
CN-leapfrog	14005	82084	5000	1104
Iterative CN-leapfrog	14005	82084	5000	650

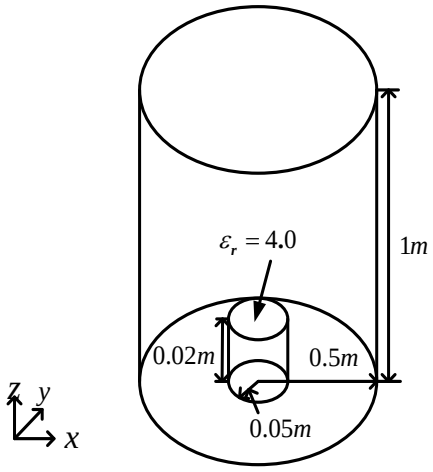

Fig. 3. A metal cylinder cavity loaded with a dielectric cylinder.

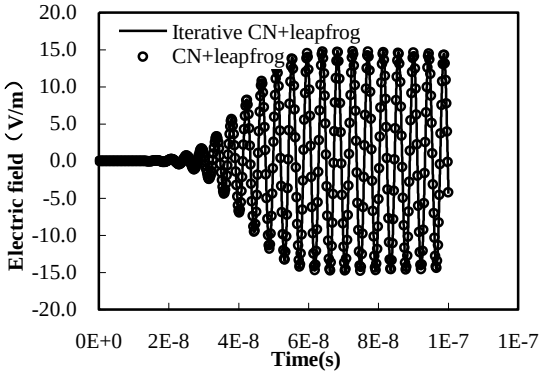

Fig. 4. Electric field in time domain calculated by the two methods.

Table 2: Comparison of computational efficiency

Iterative Method	Amplification of Time Step	Mean Convergence Step	Iterative Time(s)
CN	5	0	600
Iterative CN	5	35	415
Modified Iterative CN	5	13	173

IV. CONCLUSION

In the paper, a hybrid explicit-implicit iterative CN-leapfrog scheme based DG-FETD method is proposed for analysis of multiscale problems. The scheme divides the whole computational domain into two types. The iterative CN scheme is used in the fine regions while the leapfrog scheme is used in the coarse regions. Compared with the existing CN scheme and CN-leapfrog scheme, our scheme can not only enlarge the time step size but also ensure the mass matrix with the block diagonal characteristic. Numerical results show the accuracy and efficiency of the proposed iterative CN-leapfrog scheme DG-FETD.

ACKNOWLEDGMENT

We would like to thank the support of the major project fund of natural science research in colleges and universities of Jiangsu province under grant No. 16KJA510003.

REFERENCES

[1] T. Wan, R. S. Chen, and Z. D. Ding, "An efficient finite-element time-domain method via hier-archical matrix algorithm for electromagnetic simulation," *Appl. Comput. Electromag. Society J.*, vol. 26, no. 7, pp. 584-595, July 2011.

[2] B. Cockburn, F. Li, and C. W. Shu, "Locally divergence-free discontinuous Galerkin methods for the Maxwell equations," *J. Comput. Phys.*, vol. 194, no. 2, pp. 588-610, Mar. 2004.

[3] T. Lu, P. Zhang, and W. Cai, "Discontinuous Galerkin methods for dispersive and lossy Maxwell's equations and PML boundary conditions," *J. Comput. Phys*., vol. 200, no. 2, pp. 549-580, Nov. 2004.

[4] J. Chen and Q. H. Liu, "Discontinuous Galerkin time domain methods for multiscale electromagnetic simulations: A review," *Proc. IEEE*, vol. 101, no. 2, pp. 242-254, Feb. 2013.

[5] S. D. Gedney, C. Luo, J. A. Roden, R. D. Crawford, B. Guernsey, J. A. Miller, T. Kramer, and E. W. Lucas, "The discontinuous Galerkin finite-element time-domain method solution of Maxwell's equations," *Appl. Comput. Electromag. Society J*., vol. 24, no. 2, pp. 129-142, Apr. 2009.

[6] S. Dosopoulos and J. F. Lee, "Interconnect and lumped elements modeling in interior penalty discontinuous Galerkin time-domain methods," *J. Comput. Phys*., vol. 229, no. 2, pp. 8521-8536, Nov. 2010.

[7] J. H. Lee, J. Chen, and Q. H. Liu, "A 3-D discontinuous spectral element time-domain method for Maxwell's equations," *IEEE Trans. Antennas Propag*., vol. 57, no. 9, pp. 2666-2674, Sep. 2009.

[8] S. Dosopoulos and J. F. Lee, "Interior penalty discontinuous Galerkin finite element method for the time-dependent first order Maxwell's equations," *IEEE Trans. Antennas Propag*., vol. 58, no. 12, pp. 4085-4090, Dec. 2010.

[9] S. Dosopoulos, B. Zhao, and J. F. Lee, "Nonconformal and parallel discontinuous Galerkin time domain method for Maxwell's equations: EM analysis of IC packages," *J. Comput. Phys*., vol. 238, pp. 48-70, Dec. 2012.

[10] S. Dosopoulos, J. D. Gardiner, and J. F. Lee, "An MPI/GPU parallelization of an interior penalty discontinuous Galerkin time domain method for Maxwell's equations," *Radio Science*, 46, pp. RS0M05, 2011.

[11] C. Potratz, H.-W. Glock, and U. Van Rienen, "Time-domain field and scattering parameter computation in waveguide structures by GPU-accelerated discontinuous-Galerkin method," *IEEE Trans. Microw. Theory Tech*., vol. 59, no. 11, pp. 2788-2797, Nov. 2011.

[12] S. Gedney, C. Luo, B. Guernsey, J. A. Roden, R. Crawford, and J. A. Miller, "The discontinuous Galerkin finite-element time-domain method (DGFETD): A high order, globally-explicit method for parallel computation," *IEEE Int. Symp. on Electromagnetic Compatibility*, Honolulu, 2007.

[13] R. Courant, K. Friedrichs, and H. Lewy, "On the partial difference equations of mathematical physics," *IBM J*., vol. 11, no. 2, pp. 215-234, Mar. 1967.

[14] V. Dolean, H. Fahs, L. Fezoui, and S. Lanteri, "Hybrid explicit-implicit time integration for grid-induced stiffness in a DGTD method for time domain electromagnetics," *Spectral and High Order Methods for Partial Differential Equations*, Berlin, Germany: Springer-Verlag, pp. 163-170, 2011, ser. Lecture Notes in Computational Science and Engineering.

[15] H. Xu, D. Z. Ding, and R. S.Chen. "A hybrid explicit-implicit scheme for spectral-element time-domain analysis of multiscale simulation," *[J]. Journal of ACES*, vol. 31, no. 4, pp. 77-82, Apr. 2016.

[16] J. M. Jin, *The Finite Element Method in Electromagnetics*. 2nd ed., New York: Wiley, 2002.

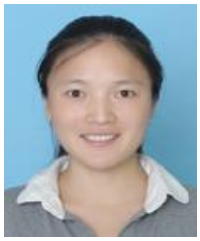

Min li received the M.S. degree in Electromagnetic Field and Microwave Technology from the School of Electrical Engineering and Optical Technique, Nanjing University of Science and Technology in 2012 and is currently working toward the Ph.D. degree in Nanjing University of Posts and Telecommunications. Her research interests include semiconductor simulation, RF-integrated circuits and computational electromagnetic.

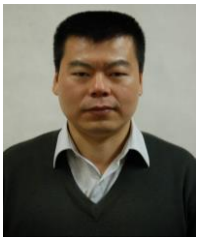

Xiaodong Ye was born in Jiangsu, China. He is currently an Associate Professor with the Electronic Engineering of NJUST. His current research interests include computational electromagnetics, electromagnetic scattering and radiation.

Tunable Band-Notched UWB Antenna from WLAN to WiMAX with Open Loop Resonators using Lumped Capacitors

Wael A. E. Ali [1] and Ahmed A. Ibrahim [2]

[1] Department of Electronics & Communications Engineering, College of Engineering and Technology
Arab Academy for Science, Technology and Maritime Transport (AASTMT), Alexandria, Egypt
wael.ali@aast.edu

[2] Department of Electrical Engineering
Faculty of Engineering, Minia University, Minia, Egypt
ahmedabdel_monem@mu.edu.eg

Abstract ─ The proposed antenna in this paper is compact UWB monopole antenna with a rectangular patch consists of stepped cuts and triangular slot. A two open loop resonators are designed and added near microstrip feed line to achieve sufficient band rejection from 5.1 GHz to 6.5 GHz for avoiding interference with WLAN frequency bands. The proposed antenna has low profile and compact size, its size equals 3.2 x 3.2 cm^2. It has bandwidth from 3.1 GHz to 19.3 GHz with voltage standing wave ratio (VSWR) < 2, except the undesired band of 5.1–6.5 GHz. Two-lumped capacitors are inserted in order to investigate the ability of tuning the resonance frequency of the band-notched structures from 5.6 GHz to 3.5 GHz. Finally, the layout of the proposed UWB monopole antenna with the notched band is experimentally fabricated and measured to verify the simulation results. Furthermore, the return loss and far-field measurements of the fabricated antenna exhibit good match with simulation predictions.

Index Terms ─ Lumped capacitors, notched characteristic, open loop resonator, UWB monopole antenna.

I. INTRODUCTION

The congestion of the frequency spectrum and the interference of various communication systems are considered the most important problems due to the advancement of wireless systems and the sustainable demand for improving the operation bandwidth [1]. Commercially, the development of the ultra-wideband systems is evident after the allocation of frequency band 3.1–10.6 GHz by the Federal Communications Commission (FCC) for that purpose [2-8].

There are many wireless communication systems operating in the UWB frequency range (3.1-10.6) GHz such as at 5.15-5.85 GHz and 3.3-3.8 GHz for Wireless Local Area Network (WLAN) and Worldwide Interoperability for Microwave Access (WiMAX) respectively. The previous systems cause interference with the UWB systems and degrade the overall performance. Hence, an UWB antenna with band rejection characteristic is desired [9-17].

In order to eliminate the interference, the UWB antenna should be integrated with external band-stop filters, which in turn will increase size, cost, and complexity of the system. Consequently, the demand for compact antenna with band-notched characteristics became necessary [18]. Furthermore, the theory behind creating the band-notched characteristics with UWB antennas is like using resonators in multiband antennas to increase the number of frequency bands [19]. Different methods such as etching slots with various shapes in the microstrip feed-line [20, 21], loading resonators etched on the radiator [19, 21-24] or on the ground plane [25], loading parasitic elements of different shapes behind the truncated ground plane [26], and utilizing EBG structures [27] have been addressed to obtain UWB operation with the capability of band rejection.

In this paper, a single band-notched monopole antenna for UWB operation is introduced. The UWB monopole antenna with stepped cuts and partial slotted ground plane is designed firstly, which exhibits radiating characteristics in the frequency range 3-19 GHz. Two open loop resonators are mounted on the substrate behind the microstrip feed line and the radiator to achieve the band-notched functionality at the operating band of WLAN applications. The proposed UWB antenna with stop band behavior is fabricated on low cost substrate and then measured in order to verify the simulation results. To tune the resonance frequency of band-notched structure from the operating band of WLAN to the operating band of WiMAX, two lumped capacitors are used. Commercial software HFSS 13 is employed to simulate the proposed antenna.

Submitted On: August 8, 2017
Accepted On: April 21, 2018

II. DESIGN PROCEDURES

A. UWB antenna configuration

The designed UWB monopole antenna is fed by 50 Ω microstrip line and is printed on epoxy FR4 substrate with 4.4 relative permittivity, 0.02 loss tangent and 1.5 mm thickness 'h'.

The antenna is designed to achieve the desired UWB performance. Subsequently, different procedures are introduced in order to achieve the desired design. First of all, monopole antennas with partial ground plane and triangle slot in the radiator patch are designed (case I and case II) to produce UWB behavior as shown in Fig. 1. However, this design has frequency band from 3 GHz to 10 GHz with VSWR lower than 2 as shown in Fig. 2. In order to extend the frequency band from 3 GHz to 13 GHz, the case III with triangle slot in the patch radiator and simple U slot in the ground plane are utilized. Also the matching bandwidth of the UWB antenna can be improved by using three steps in the radiator patch as shown in case IV. The bandwidth of case IV is extended to operate at frequency band from 3 GHz to 19 GHz as illustrated in Fig. 2. Finally, the proposed antenna (with/without triangle slot) is integrated with two open loop resonators to achieve a single notch frequency for interference mitigation with the WLAN applications (case V & VI). It can be noticed from Fig. 2 that the behaviour of case V is the same as case VI except the frequency range from 14.6 to 16.3 GHz. So, case VI is chosen as the proposed model for band-notched UWB antenna.

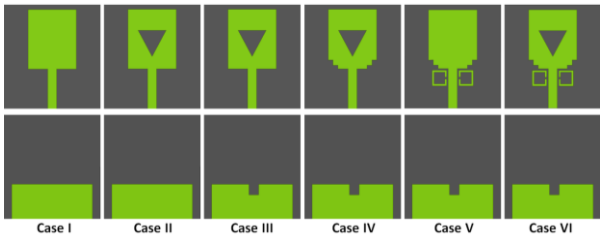

Fig. 1. Design procedures of the proposed UWB antenna.

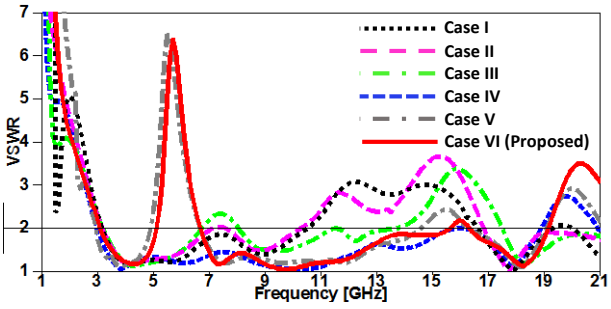

Fig. 2. VSWR of the UWB antenna at different cases.

The total length of the utilized resonator to be resonating at the WLAN frequency band should be half the guided wavelength of the rejection frequency [28, 29] as the following equations:

$$L_{total} \approx \frac{\lambda_g}{2} = \frac{c}{2 f_{notch} \sqrt{\varepsilon_{eff}}}, \quad (1)$$

$$\varepsilon_{eff} \approx \frac{\varepsilon_r + 1}{2}. \quad (2)$$

The VSWR which is shown in Fig. 2 for case VI illustrates the UWB behavior of the proposed antenna with band-notch from 5 GHz to 6.5 GHz.

B. Parametric study of band-notched UWB antenna

The layout of the proposed UWB antenna is demonstrated in Fig. 3. The optimized dimensions of antenna are tabulated in Table 1. The antenna is composed of monopole antenna with three steps stepped cut, triangle slot in the radiating patch and two open loop resonators near the microstrip feed line. Also, the ground plane has simple slot as shown in Fig. 3. To understand the effects of the resonator gap (g), width (W_5) and length (L_7) on the impedance matching characteristics, parametric studies are carried out.

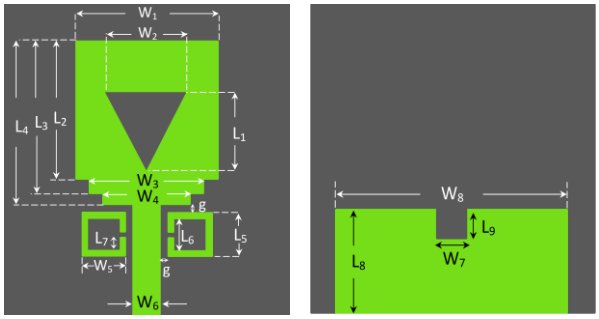

(a) (b)

Fig. 3. 2-D layout of WLAN band-notched UWB antenna: (a) top and (b) bottom view.

Table 1: Design parameters of the proposed band-notched UWB antenna

Parameter	L_1	L_2	L_3	L_4	L_5	L_6
Value (mm)	7.5	14.5	16	17	4.5	3.4
Parameter	L_7	L_8	L_9	W_1	W_2	W_3
Value (mm)	1.4	10	3	15	8.66	12
Parameter	W_4	W_5	W_6	W_7	W_8	g
Value (mm)	9	4.5	2.76	3	25	0.5

Figure 4 shows the VSWR at different gaps (g) of the band-notched resonator. It is clear that the gap (g) affects the position of the band-notched frequency. The position of the center frequency is shifted from 3.5 GHz to 5.6 GHz when the gap (g) is changed from 0.1 mm to 0.7 mm and we chose the gap (g) of 0.5 mm to achieve the desired band-notched characteristics. Figure 5 and

Fig. 6 illustrate the VSWR at different width (W_5) and length (L_7). It is obvious that the open loop resonator consists of parallel inductance (the overall length of the resonator) and capacitor (the gap between the resonator arms), so when the length and the width of the resonator are increased, the inductance of the resonator is increased. Consequently, the center frequency of the notched band is shifted down as shown in Fig. 5 and Fig. 6.

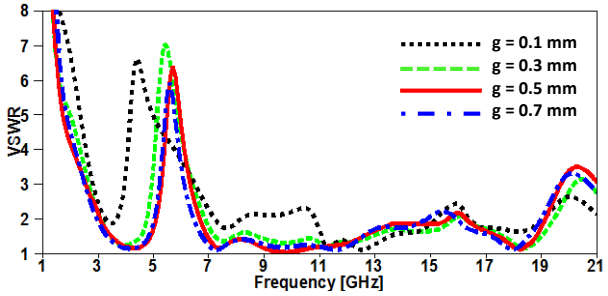

Fig. 4. Simulated VSWR at different gaps (g).

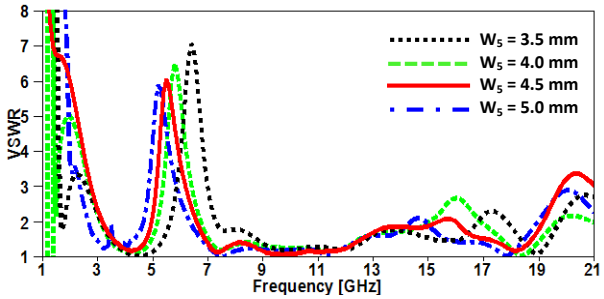

Fig. 5. Simulated VSWR at different widths of the open loop resonator.

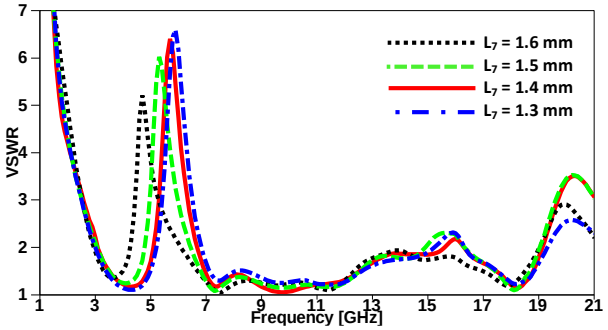

Fig. 6. Simulated VSWR at different lengths of the open loop resonator.

C. Results and discussions

A photograph of the fabricated UWB antenna is shown in Fig. 7. The antenna was tested for its VSWR characteristics using Agilent N9918A vector network analyzer (VNA), whereas the radiation pattern and gain were measured in an anechoic chamber. Figure 8 shows a comparison between the simulated and measured VSWR results of the band-notched UWB monopole antenna, where the practical results coincide with the simulation results over the whole bandwidth. It can be noticed that the two curves are all below 2 from 3.2 to 19.3 GHz except a rejection in the band from 5.1 to 6.5 GHz, which makes the presented antenna suitable for UWB applications without interfering WLAN applications.

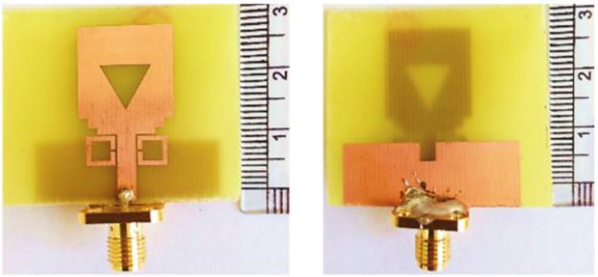

(a) (b)

Fig. 7. Photographs of fabricated UWB antenna: (a) front view and (b) back view.

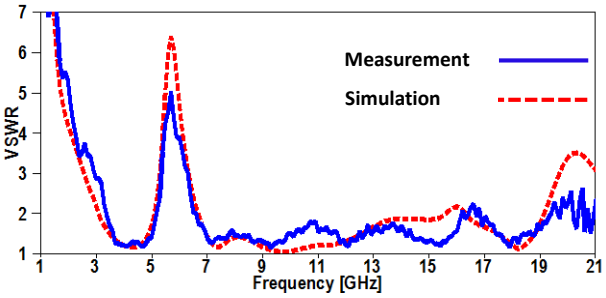

Fig. 8. The simulated and measured VSWR of the optimized structure against frequency.

III. PROPOSED TUNABLE UWB ANTENNA DESIGN

As discussed in the previous section, the center frequency of the notch can be controlled by changing both the inductance and the capacitance of the open loop resonator. By studying the electric field distribution at 5.6 GHz on the open loop resonator, it can be observed that the electric filed is concentrated around the open loop gap as shown in Fig. 9. By inserting lumped capacitor in the gap of the open loop resonator as shown in Fig. 10 (a), the center frequency of the notch can be tuned and controlled. In order to study the effect of the values of lumped capacitor on the proposed antenna response, a parametric study is carried out as illustrated in Fig. 11. It can be noticed from Fig. 11 that the central frequency of the notch is shifted from 5.6 GHz (without capacitor) to 2.9 GHz when lumped capacitors of 0.4 pF are used.

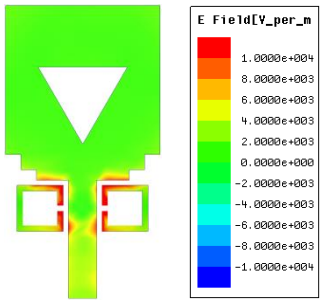

Fig. 9. Simulated electric filed distribution of antenna at 5.6 GHz.

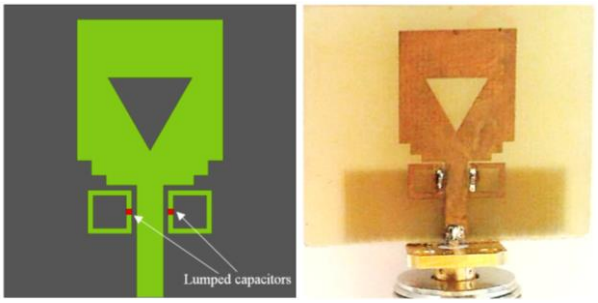

(a) (b)

Fig. 10. The geometry of the proposed UWB antenna: (a) 2 D layout and (b) fabricated photograph.

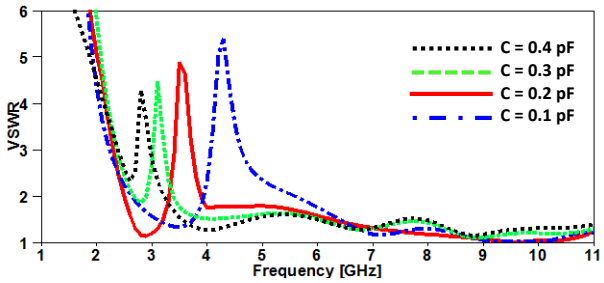

Fig. 11. The VSWR of the proposed antenna at different values of lumped capacitors.

The proposed UWB antenna has been simulated, fabricated, and tested using Agilent N9918A vector network analyzer (VNA). The fabricated photograph of the proposed antenna is illustrated in Fig. 10 (b). The VSWR of the antenna was measured and compared with the simulated one with lumped capacitors of 0.2 pF as demonstrated in Fig. 12. As depicted from the Fig. 12, there is a good consistency between simulated and measured VSWR but with small frequency shift due to the fabrication tolerance and misalignment of the welding process. Finally, it is concluded that the lumped capacitor can tune the center frequency of the notch from the WLAN operating band to WIMAX operating band.

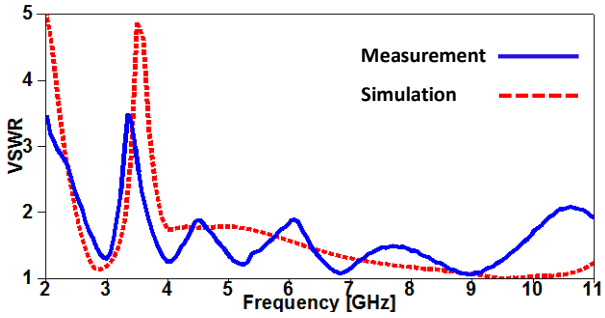

Fig. 12. The simulated and measured VSWR of the optimized structure against frequency with capacitor of 0.2 pF.

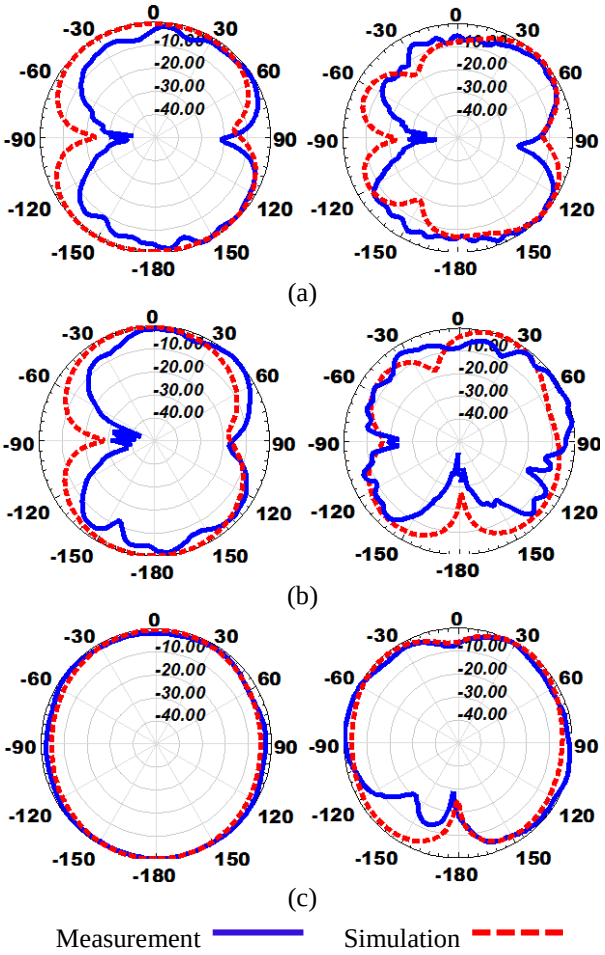

Fig. 13. The simulated normalized radiation patterns at f = 4 GHz (left) and f = 9.3 GHz (right): (a) x-y plane, (b) y-z plane, and (c) x-z plane.

The normalized simulated and measured radiation patterns in x-z, y-z and x-y planes of the proposed antenna are shown in Fig. 13. It follows from Fig. 13 that the UWB monopole antenna has nearly omnidirectional

patterns in x-z plane and almost bi-directional patterns in y-z and x-y planes. From the previous results, it is clear that the proposed antenna is convenient for UWB application.

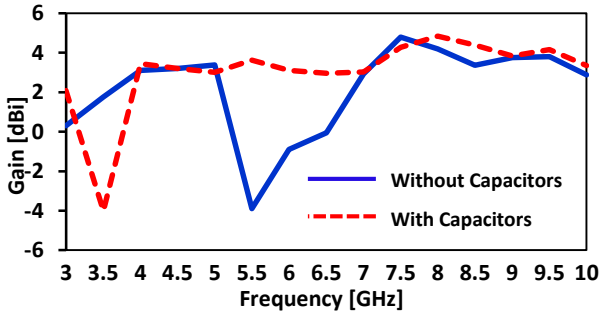

Fig. 14. The measured realized gain of the band-notched UWB antenna.

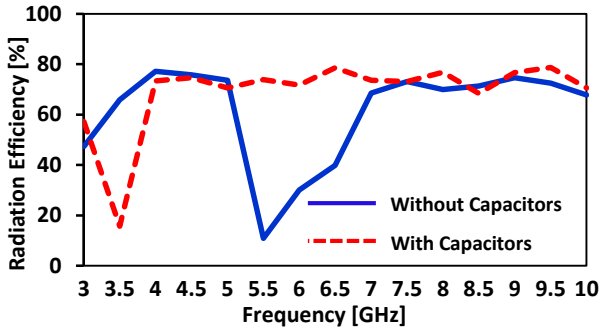

Fig. 15. The measured efficiency of the band-notched UWB antenna

Table 2: Comparison between different band-notched UWB antenna designs

Ref.	Size [mm^2]	Freq. Range [GHz]	Notch Frequencies [GHz]	Realized Gain [dBi]
[9]	58 × 65.5	3.1-11	–	–
[10]	24 × 32	2.9-12.5	5.5	-4.9
			7	-3.9
[11]	12.3 × 28	3-12.8	3.5	-3.3
			8.2	-2.5
[12]	30 × 32	3.1-14	5.5	-2
			6.8	-0.9
			11.5	-0.7
[13]	24 × 32	2.7-12	3.5	-4.3
			8	-2.1
This work	32 × 32	3-19.3	5.6/3.5	-4

A comparison between measured realized gains of the proposed UWB monopole antenna with/without lumped capacitors is demonstrated in Fig. 14. The average measured realized gain of the UWB antenna is nearly constant around 3 dBi, except the notched frequency bands with values equal -4 dBi at 5.6 GHz and 3.5 GHz for the two cases of without and with using lumped capacitors respectively. Figure 15 shows a comparison between measured radiation efficiencies of the proposed band-notched UWB antenna with/without lumped capacitors. The average measured efficiency over the entire frequency band is 74% except the notched frequencies with values 15.7% and 10.8% at 3.5 GHz and 5.5 GHz, respectively.

A comparison between the proposed antenna and other reported UWB antennas is illustrated in Table 2. It can be concluded from this comparison that the proposed antenna has compact size and higher bandwidth. The gain at the center frequency of the notched band is comparable, or somewhat higher.

IV. CONCLUSION

A compact band-notched monopole antenna printed on 3.2×3.2 cm^2 low cost FR4 substrate has been proposed for UWB systems. A frequency band rejection has been investigated by embedding open loop resonators in the antenna structure to avoid the interference of UWB systems with WLAN applications. The experimental results confirm that the fabricated antenna is suitable for UWB systems by covering frequency range 3.1–19.3 GHz with the band-notched characteristic at 5.1–6.5 GHz. Moreover, good omnidirectional radiation characteristics and gain have been achieved throughout the UWB frequency band except the undesired notched band. The tunablility of the notched band has been investigated by embedding two lumped capacitors. The proposed tunable band-notched UWB monopole antenna provides very interesting specifications to be presented for various wireless communication systems.

REFERENCES

[1] B. Badamchi, J. Nourinia, C. Ghobadi, and A. Valizade Shahmirzadi, "Design of compact reconfigurable ultra-wideband slot antenna with switchable single/dual band notch functions," in *Microwaves, Antennas & Propagation, IET*, vol. 8, no. 8, pp. 541-548, June 4, 2014.

[2] First Report and order, "Revision of part 15 of the Commission's Rule Regarding Ultra-Wideband Transmission System FCC 02-48," Federal Communications Commission, 2002.

[3] A. Abdelreheem and M. Abdalla, "Compact curved half circular disc-monopole UWB antenna," *International Journal of Microwave and Wireless Technologies*, pp. 1-8, 2015.

[4] J. Pourahmadazar, "Broadband CPW-fed circularly polarized square slot antenna with inverted-L strips for UWB applications," *IEEE Antennas and Wireless Propagation Letters*, vol. 10, pp. 369-372,

2011

[5] W. A. Ali, A. I. Zaki, and M. H. Abdou, "Design and fabrication of rectangular ring monopole array with parasitic elements for UWB applications," *Microw. Opt. Technol. Lett.*, 58: 2268-2273, 2016.

[6] W. A. Ali, A. M. Mansour, and D. A. Mohamed, "Compact UWB wearable planar antenna mounted on different phantoms and human body," *Microw. Opt. Technol. Lett.*, 58: 2531-2536, 2016.

[7] N. Ojaroudi, M. Ojaroudi, and S. Amiri, "Enhanced bandwidth of small square monopole antenna by using inverted U-shaped slot and conductor-backed plane," *ACES*, vol. 27, no. 8, pp. 685-690, 2012.

[8] M. Majidzadeh and C. Ghobadi, "Compact microstrip-fed monopole antenna with modified slot ground plane for UWB applications," *ACES*, vol. 27, no. 10, pp. 801-807, 2012.

[9] Y. Tawk and C. G. Christodoulou, "A new reconfigurable antenna design for cognitive radio," *IEEE Antennas and Wireless Propagation Letters*, vol. 8, pp. 1378-1381, 2009.

[10] Y. Li, W. Li, and Q. Ye, "A reconfigurable wide slot antenna integrated with sirs for UWB/ multiband communication applications," *Microw. Opt. Technol. Lett.*, vol. 55, pp. 52-55.

[11] Y. Li, W. Li, and Q. Ye, "Miniaturization of asymmetric coplanar strip-fed staircase ultra-wideband antenna with reconfigurable notch band," *Microw. Opt. Technol. Lett.*, vol. 55, pp. 1467-1470.

[12] Y. Li, W. Li, and Q. Ye, "A reconfigurable triple-notch-band antenna integrated with defected microstrip structure band-stop filter for ultra-wideband cognitive radio applications," *International Journal of Antennas and Propagation*, vol. 2013, Article ID 472645, 13 pages, 2013.

[13] Y. Li, W. Li, and R. Mittra, "A compact CPW-fed circular slot antenna with reconfigurable dual band-notch characteristics for UWB communication applications," *Microwave and Optical Technology Letters*, vol. 56, no. 2, pp.465-468, 2014.

[14] M. Abdollahvand, G. Dadashzadeh, and D. Mostafa, "Compact dual band-notched printed monopole antenna for UWB application," in *IEEE Antennas and Wireless Propagation Letters*, vol. 9, pp. 1148-1151, 2010.

[15] J. Xu, D. Shen, X. Zhang, and K. Wu, "A compact disc ultrawideband (UWB) antenna with quintuple band rejections," in *IEEE Antennas and Wireless Propagation Letters*, vol. 11, pp. 1517-1520, 2012.

[16] Y. Sung, "Triple band-notched UWB planar monopole antenna using a modified H-shaped resonator," *IEEE Transactions on Antennas and Propagation*, vol. 61, no. 2, pp. 953-957, 2013.

[17] A. A. Ibrahim, M. A. Abdalla, and A. Boutejdar, "Resonator switching techniques for notched UWB antenna in wireless applications," *IET Microwaves, Antennas & Propagation*, 2015

[18] J. Wang, Y. Yin, and X. Liu, "A novel compact planar ultra-wideband antenna with dual band-notched characteristics," *Int. J. RF and Microwave Comp. Aid. Eng.*, vol. 25, pp. 48-55, 2015.

[19] K. D. Xu, Y. H. Zhang, R. J. Spiegel, Y. Fan, W. T. Joines, and Q. H. Liu, "Design of a stub-loaded ring-resonator slot for antenna applications," *IEEE Transactions on Antennas and Propagation*, vol. 16, no. 2, pp. 517-524, 2015.

[20] Y. Cai, H. Yang, and L. Cai, "Wideband monopole antenna with three band-notched characteristics," *IEEE Antennas and Wireless Propagation Letters*, vol. 13, pp. 607-610, 2014.

[21] W. Ali, A. A. Ibrahim, and J. Machac, "Compact size UWB monopole antenna with triple band-notches," *Radioengineering*, vol. 26, no. 2, pp. 57-63, 2017.

[22] S. Das, D. Mitra, and S. R. B. Chaudhuri, "Design of UWB planar monopole antennas with etched spiral slot on the patch for multiple band-notched characteristics," *International Journal of Microwave Science and Technology*, vol. 2015, Article ID 303215, 9 pages, 2015.

[23] A. Nemati and B. A. Ganji, "UWB monopole antenna with switchable band-notch characteristic using a novel MEMS afloat," *ACES*, vol. 30, no. 12, pp. 1306-1312, 2015.

[24] S. Naser and N. Dib, "Printed UWB pacman-shaped antenna with two frequency rejection bands," *ACES*, vol. 32, no. 3, pp. 186-192, 2017.

[25] H. Liu, Z. Xu, B. Wu, and J. Liao, "Compact UWB antenna with dual band-notches for WLAN and WiMAX applications," *IEICE Electronics Express*, vol. 10, no. 17, pp. 1-6, 2013.

[26] A. Boutejdar, A. A. Ibrahim, and E. Burte, "A compact multiple band-notched planer antenna with enhanced bandwidth using parasitic strip lumped capacitors and DGS-technique," *TELKOMNIKA Indonesian Journal of Electrical Engineering*, vol. 13, no. 2, pp. 203-208, 2015.

[27] G. K. Pandey, H. S. Singh, B. Wu, P. K. Bharti, and M. K. Meshram "Design and analysis of multiband notched pitcher-shaped UWB antenna," *Int. J. RF and Microwave CAE*, vol. 25, no. 17, pp. 795-806, 2015.

[28] Y. Jin and J. Choi, UWB antenna with quintuple notch bands," *2015 IEEE International Symposium on Antennas and Propagation & USNC/URSI National Radio Science Meeting*, Vancouver, BC, pp. 1950-1951, 2015.

[29] D. Sarkar, K. V. Srivastava, and K. Saurav, "A compact microstrip-fed triple band-notched UWB monopole antenna," in *IEEE Antennas and Wireless Propagation Letters*, vol. 13, pp. 396-399, 2014.

Wael A. E. Ali was born in 1982. He received his B.Sc. and M.Sc. in Electronics and Communications Engineering from Arab Academy for Science, Technology and Maritime Transport (AASTMT), Alexandria, Egypt in 2004 & 2007, respectively. He obtained his Ph.D. in Electronics and Communications Engineering from Alexandria University, Alexandria, Egypt in 2012. He is currently an Associate Professor at Arab Academy for Science, Technology and Maritime Transport (AASTMT), Alexandria, Egypt. His research interests include smart antennas, microstrip antennas, microwave filters, metamaterials, and MIMO antennas and its applications in wireless communications.

Ahmed A. Ibrahim was born in 1986. He received the B.Sc. degree, with grade of very good, in Electrical Engineering from the Electronic and Communication Engineering Department, Elminia University, Elminia, Egypt in 2007. He was awarded the M.Sc. degree in Electronic and Communication Engineering from Elminia University in 2011 and the Ph.D. degree from Electronic and Communication Engineering from Minia University in 2014. He is Lecturer in Electronic and Communication Engineering Department. His research focused on the design and analysis of microstrip antennas, microstrip filters, and its application in wireless communications. Also metamaterial MIMO antenna and different metamaterial applications in microwave bands.

A Differential CPW-fed Ultra-wideband Antenna with Dual Notched Bands

Jinhai Liu, Zhao-Yang Tang, and Ying-Zeng Yin

National Laboratory of Science and Technology on Antennas and Microwaves
Xidian University, Xi'an 710071, China
liujinhai568@126.com, zhaoyangt@126.com, yyzeng@mail.xidian.edu.cn

Abstract ─ In this letter, a differential coplanar waveguide (CPW)-fed ultra-wideband (UWB) antenna with dual notched bands is presented. The proposed antenna is mainly composed of two C-shaped radiating elements and a polygon slot ground plane. To alleviate the electromagnetic signal interference, two pairs of open-ended slots etched on the ground plane are adopted to reject 3.5 GHz WiMAX band while a pair of Y-shaped slots embedded in the C-shaped radiating elements is used to filter 5.5 GHz WLAN band. Measured results demonstrate that a 10-dB impedance bandwidth implemented is 131% (from 2.57 to 12.31 GHz), along with dual notched bands of 3.29-3.95 GHz and 4.73-6.55 GHz. Furthermore, the low cross-polarization is obtained because of differential feeding structure. Finally, the antenna expresses good radiation patterns in the whole operating band.

Index Terms ─ Differential-fed, notched bands, open-ended slot, UWB antenna, Y-shaped slot.

I. INTRODUCTION

Currently, the ultra-wideband (UWB) wireless communication technology operating in the frequency of 3.1-10.6 GHz has gained much attention due to its inherently attractive advantages of wide bandwidth, low power consumption, high data rate and so on. UWB antennas play an important role in the wireless communication systems. In the open literatures, UWB antennas with excellent performances have been presented [1-8]. As is well known, the operating band of UWB communication technology overlaps that of some other existing narrowband services like WiMAX (3.4-3.69 GHz) and WLAN (5.15-5.825 GHz) which may cause electromagnetic signal interference. To alleviate this problem, a band-rejection filter is always adopted to filter the bands of the existing narrowband services. However, the system complexity is increased due to the additional filter. Therefore, the UWB antennas with band-notched characteristics are desirable. In [9], an open loop resonator is introduced to obtain a notch band at 5.15 GHz. The proposed antenna achieves good notched band characteristics by optimizing the position and dimension of the open-loop resonator. In [10], by using an inverted π-shaped parasitic structure in the ground plane, a frequency notch band of 5.11-6.02 GHz is achieved. In the design of [11], a compact UWB slot antenna with band-notched characteristics is proposed. Combining a short-ended split-ring slot and an open-ended slot, a notched band ranging from 5.15-5.9 GHz with sharp selectivity is achieved. However, the mentioned designs [9-11] have a single notched band, and they cannot filter the 3.5 GHz WiMAX band. In [12], a microstrip line-fed planar antenna with dual notched bands is designed by etching a single tri-arm resonator below the patch. It has a wide bandwidth (return loss ≤ -10 dB) ranging from 2.98 to 10.76 GHz with two notched bands operating at 3.56 and 5.5 GHz. In [13], a dual-notched characteristic is presented by utilizing the semi-circular and annular circular slot etched on the circular ring radiator. However, the cross polarization problem in these antennas is needed to be improved. To enhance the purity of polarization, a differential feeding technology has been widely applied in the RF system. Normally, a balun is adopted to transform differential signals into single-ended signals, leading to cause additional losses and shrink the impedance bandwidth. The single-ended antenna is hard to be directly integrated with the differential circuit. Hence, a differential-fed antenna excited by two signals with uniform amplitude but 180° phase difference is needed. In [14], a differential-fed magneto-electric (ME) dipole antenna is designed for UWB communication system. However, the antenna has a bulky volume and cannot reject the operating bands of narrowband communication systems. In [15], a differential-fed UWB antenna with good radiation patterns is presented. It is clear that the radiation patterns are greatly improved by using differential feeding structure. Nevertheless, the antenna does not have the function of filtering undesired band. A differential-fed tapered-slot UWB antenna with band-rejected characteristics is designed [16], but it just has a single notched band of 5.2-6.0 GHz which cannot reject the 3.5 GHz WiMAX operating band. In the design of [17], a planar differential-fed antenna with dual band-notched characteristics is presented for UWB applications.

Submitted On: December 26, 2017
Accepted On: May 19, 2018

Nevertheless, the planar feeding structure is not preferred because it cannot offer easy integration with the existing fabrication facilities.

However, CPW feed lines have several useful characteristics, low radiation losses, less dissipation, and uniplanar configurations. For RF applications, they can be easily mounted and they have good compatibility with other active devices, which is very important for Miniature Hybrid Microwave Integrated Circuits and Monolithic Microwave Integrated Circuits technologies.

In this letter, a differential CPW-fed UWB antenna with dual notched bands is presented. A wide impedance bandwidth of 131% (from 2.57 to 12.31 GHz) for differential reflection coefficient less than -10 dB is obtained. By introducing the open-ended slots and the Y-shaped slots, two notched bands are implemented to reject the 3.5 GHz WiMAX band and the 5.5 GHz WLAN band, respectively. In addition, the antenna has low cross polarization because of differential feeding mechanism. Based on the design parameters, the antenna is fabricated and tested.

II. ANTENNA DESIGN

Figure 1 shows the geometry of the proposed antenna. The proposed antenna is composed of two parts: two C-shaped radiating elements placed face to face and a polygon slot ground plane. Each C-shaped radiating element has a Y-shaped slot and the ground plane has two pairs of open-ended slots. Both the radiating elements and the ground plane are etched on FR-4 substrate with a thickness of 1 mm, relative dielectric constant of 4.4 and loss tangent of 0.02. The simulation and analysis for the proposed antenna are performed using the electromagnetic simulator ANSYS HFSS. The optimized design parameters of the antenna are shown in Table 1.

Table 1: Optimized parameters of the proposed antenna

Parameters	W	g	Lt	Ws	L1
Values/mm	28	0.4	2	0.2	5.6
Parameters	Wg	R1	Ls	W2	Wf
Values/mm	3.8	6	12.8	1.7	2.2
Parameters	R2	ds	L2	s	Wt
Values/mm	5.5	1.4	2.2	0.3	8
Parameters	W1	ts	L	Lg	dr
Values/mm	1.4	0.2	30	5	3

As is known, the two-port s-parameter matrix [18] is shown in (1):

$$S = \begin{bmatrix} S_{11} & S_{12} \\ S_{21} & S_{22} \end{bmatrix}. \quad (1)$$

For the convenience in analyzing differential signals, the s-parameter matrix S^{mm} is presented, which is employed to describe the transmission characteristic of differential circuits. Usually, a differential-fed antenna can be regarded as a two-port network. Then, the s-parameter matrix can be simplified as (2):

$$S^{mm} = \begin{bmatrix} S_{dd} & S_{dc} \\ S_{cd} & S_{cc} \end{bmatrix}. \quad (2)$$

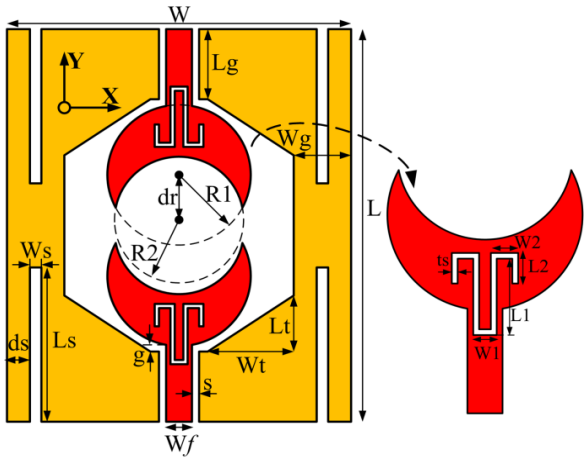

Fig. 1. Geometry of the proposed antenna.

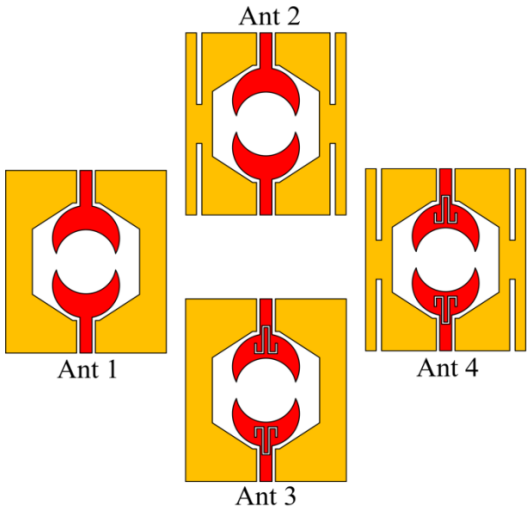

Fig. 2. Evolution of the proposed antenna.

Each of the s-parameters is as follows:

$$S_{dd} = \frac{1}{2}(S_{11} - S_{12} - S_{21} + S_{22}), \quad (3)$$

$$S_{dc} = \frac{1}{2}(S_{11} + S_{12} - S_{21} - S_{22}), \quad (4)$$

$$S_{cd} = \frac{1}{2}(S_{11} - S_{12} + S_{21} - S_{22}), \quad (5)$$

$$S_{cc} = \frac{1}{2}(S_{11} + S_{12} + S_{21} + S_{22}). \quad (6)$$

S_{dd}: Differential-mode of the s-parameters;
S_{dc}: Common-mode to differential-mode;
S_{cd}: Differential-mode to common-mode;

S_{cc}: Common-mode of the s-parameters.

The differential reflection coefficient of the antenna can be calculated by Equation (7):

$$\Gamma_{odd} = S_{dd} = \frac{(S_{11} - S_{12} - S_{21} + S_{22})}{2}. \quad (7)$$

Thus, the results of two port simulations and measurements can be used to calculate the reflection coefficients that the will be seen by the source in an odd mode excitation. An Agilent N5230A vector network analyzer is used to measure the S-parameter, S_{11}, S_{22}, S_{12} and S_{21}, for the proposed antenna. The odd mode return loss in dB is defined as $20\log_{10}|\Gamma_{odd}|$.

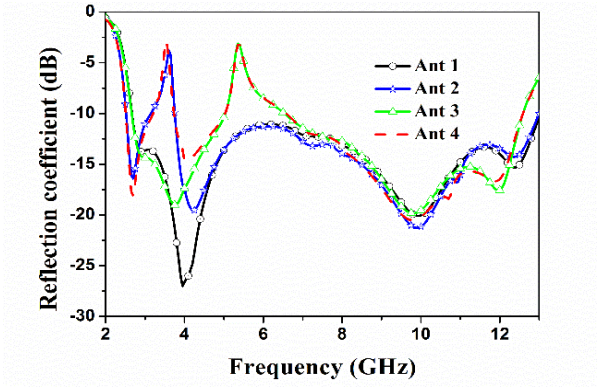

Fig. 3. Simulated reflection coefficients of various antennas mentioned.

Figure 2 shows the evolution of the proposed antenna, and the corresponding simulated differential reflection coefficient for each antenna is exhibited in Fig. 3. As shown in Fig. 2, the original antenna named as Ant 1 consists of two C-shaped radiating elements and a polygon slot ground plane. Meanwhile, a wide impedance bandwidth is obtained from 2.67 to 13 GHz when C-shaped radiating elements excite the polygon slot using differential feeding mechanism in Fig. 3. Nevertheless, the operating band of the UWB communication technology overlaps that of some other existing narrowband services like WiMAX (3.4-3.69 GHz) and WLAN (5.15-5.825 GHz) which may cause electromagnetic signal interference. To eliminate the adverse effects, two different methods are adopted to filter the operating bands of WiMAX and WLAN communication systems.

First, two pairs of open-ended slots etched on the ground plane are introduced into Ant 1, and the new antenna named Ant 2 is formed. Therefore, it can be seen that a rejected band is obtained covering the band of 3.5 GHz WiMAX, as shown in Fig. 3. The bandwidth and resonant frequency of the rejected band can be easily controlled by adjusting the dimension and position of the open-ended slots. Additionally, each open-ended slot is approximately equal to a quarter guided wavelength λg at 3.6 GHz. The guided wavelength λg can be calculated by Equation (8) as follows:

$$\lambda_g = \frac{c}{\sqrt{\varepsilon_{eff}} f}, \quad (8)$$

where c is the velocity of light in free space, f is the resonant frequency of notched band, and ε_{eff} is the effective relative permittivity.

Second, two identical Y-shaped slots are embedded in Ant 1, and Ant 3 with a notched band to filter 5.5 GHz WLAN band is implemented. The corresponding reflection coefficient depicted in Fig. 3 demonstrates the good operation of Y-shaped slots, and the resonant frequency of the notched band is 5.4 GHz. Meanwhile, the length of Y-shaped slot is about half of one guided wavelength at 5.4 GHz. Finally, the proposed UWB antenna with dual notched bands (Ant 4) is obtained by a subtle combination of open-ended slots and Y-shaped slots, and the relevant reflection coefficient is illustrated in Fig. 3.

To further demonstrate the operation mechanism of open-ended slots and Y-shaped slots, the simulated surface current distributions on the proposed antenna at the rejected bands are shown in Fig. 4. It is clear that the simulated current has various distributions on the proposed antenna. The surface current distributions focus mainly on the edge of the open-ended slots at the frequency of 3.6 GHZ. In addition, the surface current distributions mainly concentrate along the edge of the Y-shaped slots at the frequency of 5.4GHz. Because the open-ended slots and the Y-shaped slots work as resonators in the notched bands and the impedance mismatching of the proposed antenna is serious, the antenna cannot radiate outside in the notched bands.

To better show the performances of the proposed antenna, the figures of merit (including the size, operating bandwidth and notched band) of the previously reported dual-band notched UWB antennas are compared in Table 2. Note that the antenna size in [19], [20] and [21] is not compact and there is incomplete rejection in the bands 3.30-3.80 GHz and 5.15-5.85 GHz. The designed antenna has a compact size of 28×30mm^2. Meanwhile, two frequency bands 3.29-3.95 GHz and 4.73-6.55 GHz for WiMAX and WLAN are sharply notched in the operating band of the proposed antenna.

Table 2: Comparison between the reported antennas with the proposed dual band-notched UWB antennas

Reference	Antenna Size (mm)	Operating Bandwidth (GHz)	Notched Band
[19]	40.4×44	3.1-11.0	5.2-5.3 5.65-5.85
[20]	50×50	2.6-10.8	4.65-4.85 7.4-7.6
[21]	28×18	3.2-11.7	5.1-6.0 7.83-8.47
Proposed antenna	28×30	2.57-12.31	3.29-3.95 4.73-6.55

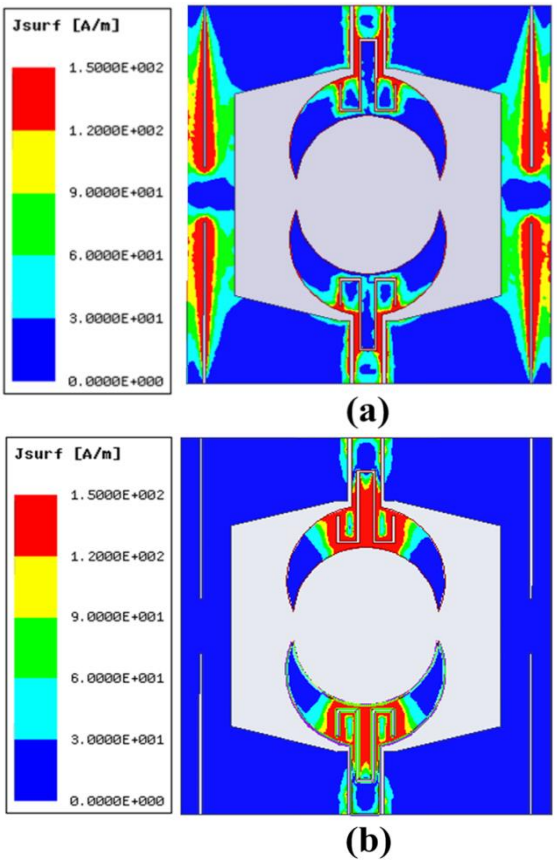

Fig. 4. Simulated current distributions on the proposed antenna at: (a) 3.6 GHz and (b) 5.4 GHz.

III. RESULTS AND DISCUSION

Based on the optimized design parameters mentioned in Table 1, the fabricated antenna and a 180° power-divider which can be used to excite the proposed antenna are shown in Fig. 5. The simulated and measured reflection coefficients of the proposed antenna are illustrated in Fig. 6. It is shown that the proposed UWB antenna achieves a wide bandwidth of 131% (2.57-12.31 GHz), along with dual notched bands of 3.29-3.95 GHz and 4.73-6.55 GHz covering the operating bands of 3.5 GHz WiMAX and 5.5 GHz WLAN. Additionally, the difference between the simulated and measured results may be attributed to the testing circumstance and the error of fabrication.

Figure 7 depicts the simulated and measured radiation patterns at 3.1, 4.5 and 8.5GHz. It can be seen that the quasi-omnidirectional radiation patterns in the *H*-plane and dipole-like radiation patterns in the *E*-plane are obtained. Meanwhile, the polarization purity of the proposed antenna is greatly improved. In Fig. 8, the measured and simulated results agree well with each other. It can be seen that the measured gain is flat in all operating bands, and it declines rapidly in the notched bands.

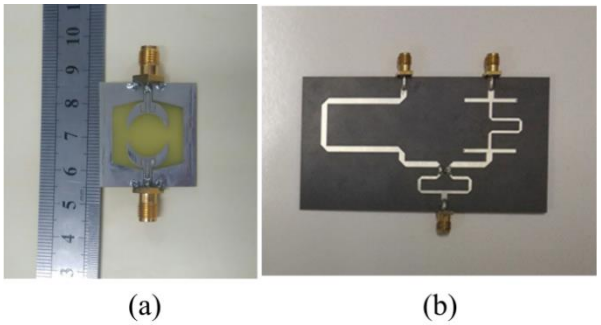

Fig. 5. (a) Photograph of the fabricated antenna, and (b) 180° power divider.

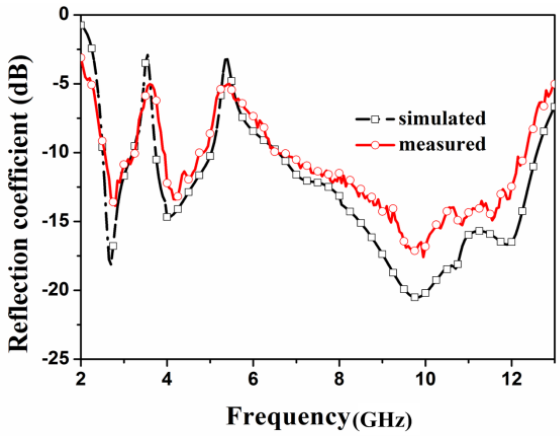

Fig. 6. Simulated and measured reflection coefficients of the proposed antenna.

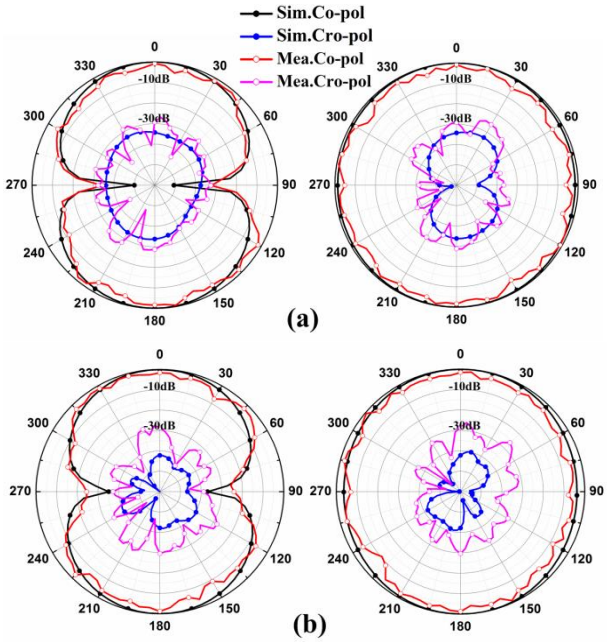

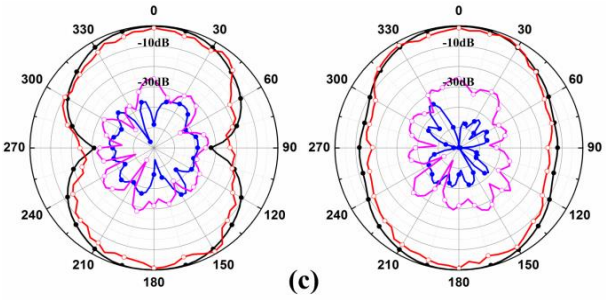

Fig. 7. Simulated and measured E-plane (left) and H-plane (right) radiation patterns of the proposed antenna at: (a) 3.1 GHz, (b) 4.5 GHz, and (c) 8.5 GHz.

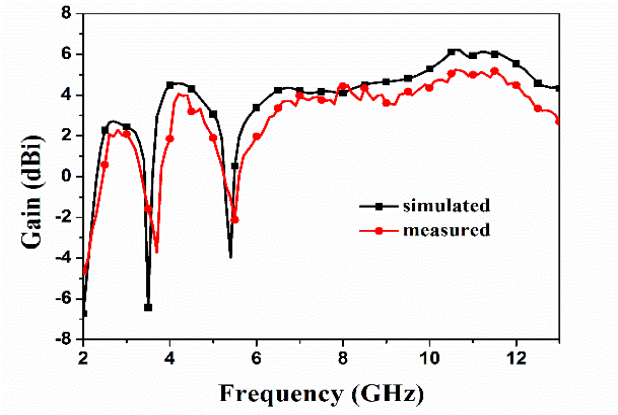

Fig. 8. Simulated and measured gains of the proposed antenna.

IV. CONCLUSION

A differential CPW-fed UWB antenna with dual band-notched characteristics is proposed. To generate filtering behavior, the open-ended slots and the Y-shaped slots are introduced into the antenna design, and two notched bands of 3.29-3.95 GHz and 4.73-6.55 GHz are obtained to filter the 3.5 GHz WiMAX and 5.5 GHz WLAN bands. Then the antenna achieves good radiation patterns and stable gain. In addition, the antenna also has low cross polarization because of differential feeding mechanism. Finally, the measured results demonstrate that the proposed antenna is a good candidate for the UWB applications.

REFERENCES

[1] Q. Wu, R. H. Jin, J. P. Geng, and M. Ding, "Printed omni-directional UWB monopole antenna with very compact size," *IEEE Trans. Antennas Propag.*, vol. 56, no. 3, pp. 896-9, 2008.

[2] M. Ojaroudi, N. Ojaroudi, and N. Ghadimi, "A novel design of dual band-notched slot antenna using a pair of Γ-shaped protruded strips for UWB applications," *ACES Journal*, vol. 28, no. 4, April 2013.

[3] A. Abdollahvand, A. Pirhadi, M. Rasoul Hosseinnezhad, and H. Ebrahimian, "A compact UWB printed monopole antenna with triple-band notched characteristics," *ACES Journal*, vol. 30, no. 4, April 2015.

[4] S. R. Emadian and J. Ahmadi-Shokouh. "Modified ground circle like-slot antenna with dual band-notched characteristics for super UWB applications," *ACES Journal*, vol. 30, no. 4, April 2015.

[5] A. K. Gautam, S. Yadav, and B. K. Kanaujia, "A CPW-fed compact UWB microstrip antenna," *IEEE Antennas Wirel. Propag. Lett.*, vol. 12, pp. 151-4, 2013.

[6] M. D. Cengizhan, C. Sibel, and C. Gonca, "Planar octagonal-shaped UWB antenna with reduced radar cross section," *IEEE Trans. Antennas Propag.*, vol. 62, no. 6, pp. 2946-53, 2014.

[7] G. P. Gao, B. Hu, and J. S. Zhang, "Design of a miniaturization printed circular-slot UWB antenna by the half-cutting method," *IEEE Antennas Wirel. Propag. Lett.*, vol. 12, pp. 567-70, 2013.

[8] Z. Ma, F. Dong, Z. Han, S. Han, and Q. Xue, "Compact UWB antenna with triple band-notches using C-shaped and S-shaped structures," *ACES Journal*, vol. 31, no. 4, April 2016.

[9] J. R. Kelly, P. S. Hall, and P. Gardner, "Band-notched UWB antenna incorporating a microstrip open-loop resonator," *IEEE Trans. Antennas Propag.*, vol. 59, no. 8, pp. 3045-48, 2011.

[10] N. Ojaroudi, M. Ojaroudi, and N. Ghadimi, "Square monopole antenna with band-notched characteristic for UWB communications," *ACES Journal*, vol. 28, no. 8, August 2013.

[11] Q. X. Chu, C. X. Mao, and H. Zhu, "A compact notched band UWB slot antenna with sharp selectivity and controllable bandwidth," *IEEE Trans. Antennas Propag.*, vol. 61, no. 8, pp. 3961-6, 2013.

[12] R. Azim, M. T. Islam, and A. T. Mobashsher, "Dual band-notch UWB antenna with single tri-arm resonator," *IEEE Antennas Wirel. Propag. Lett.*, vol. 13, pp. 670-673, 2014.

[13] S. A. Hassan, Md. Samsuzzaman, M. J. Hossain, Md. Akhtaruzzaman, and T. Islam, "Compact planar UWB antenna with 3.5/5.8 GHz dual band-notched characteristics for IoT application," *2017 IEEE International Conference on Telecommunications and Photonics (ICTP)*, Dhaka, Bangladesh, pp. 195-199, 26-28 December, 2017.

[14] M. J. Li and K. M. Luk, "A differential-fed magneto-electric dipole antenna for UWB applications," *IEEE Trans. Antennas Propag.*, vol. 61, no. 1, pp. 92-9, 2013.

[15] J. H. Wang, and Y. Z. Yin, "Differential-fed UWB microstrip antenna with improved radiation patterns," *IET Electron Lett.*, vol. 50, no. 20, pp.

1412-4, 2014.

[16] Z. H. Tu, W. A. Li, and Q. X. Chu, "Single-layer differential CPW-fed notch-band tapered-slot UWB antenna," *IEEE Antennas Wirel. Propag. Lett.*, vol. 13, pp. 1296-1299, 2014.

[17] W. Hu, Z. Tang, L. Zhou, and Y. Yin, "Design of planar differential-fed antenna with dual band-notched characteristics for UWB applications," *ACES Journal*, vol. 32, no. 3, April 2017.

[18] W. R. Eisenstadt, B. Stengel, and B. M. Thompson, *Microwave Differential Circuit Design Using Mixed-Mode S-Parameters*. Boston, MA: Artech House, vol. 42, no. 45, pp. 1-25, 2006.

[19] A. A. Gheethan and D. E. Anagnostou, "Dual band-reject UWB antenna with sharp rejection of narrow and closely-spaced bands," *IEEE Trans. Antennas Propag.*, vol. 60, no. 4, pp. 2071-2076, 2012.

[20] C. Saha, J. Y. Siddiqui, and Y. M. M. Antar, "Multilayered stacked square SRR coupled UWB monopole antenna with dual notch function," *Antennas and Propagation Society International Symposium (APSURSI), 2014 IEEE*, 2014.

[21] W.-A. Li, Z.-H. Tu, Q.-X. Chu, and X.-H. Wu, "Differential stepped-slot UWB antenna with common-mode suppression and dual sharp-selectivity notched bands," *IEEE Antennas Wirel. Propag. Lett.*, vol. 15, pp. 1120-1123, 2016.

Jinhai Liu received the M.S. degrees from Xidian University, Xi'an, China, in 2010. He is currently pursuing the Ph.D. degree in Electromagnetic Field and Microwave Technology from the National Laboratory of Science and Technology on Antennas and Microwaves, Xidian University, Xi'an, China.

His research interests include multiband antennas, UWB antennas, and antennas for base stations.

Zhaoyang Tang received the B.S. and M.S. degrees from Xidian University, Xi'an, China, in 2013 and 2016, respectively. He is currently pursuing the Ph.D. degree in Electromagnetic Field and Microwave Technology from the National Laboratory of Science and Technology on Antennas and Microwaves, Xidian University, Xi'an, China.

His research interests include multiband antennas, UWB antennas, and antennas for base stations.

Yingzeng Yin received the B.S. degree and the M.S. degree and Ph.D. degree in Electromagnetic Wave and Microwave Technology from Xidian University, Xi'an, P. R. China, in 1987, 1990 and 2002, respectively.

From March 1990 to June 1992, he was a Research Assistant and an Instructor at the Institute of Antennas and Electromagnetic Scattering, Xidian University. From July 1992 to June 1996, he was an Associate Professor in the Department of Electromagnetic Engineering, Xidian University. Since June 2004, he has been a Professor at the University. His research interest includes the areas of design of antennas, feeds for parabolic reflectors, microstrip antennas, artificial magnetic conductors, phased array antennas, and computer aided design for antennas.

Analysis and Synthesis of Equilateral Triangular Ring Microstrip Antenna using Support Vector Machine

Ahmet Kayabasi

Department of Electrical and Electronics Engineering
Engineering Faculty, Karamanoglu Mehmetbey University, Karaman, 70100, Turkey
ahmetkayabasi@kmu.edu.tr

Abstract ─ A support vector machine (SVM) based analysis and synthesis models are presented for the equilateral triangular ring microstrip antennas (ETRMAs) that operate at ultrahigh band applications. The analysis and synthesis of irregularly shaped microstrip antennas (MAs) require complex, lengthy and time consuming mathematical procedures and artificial intelligence techniques such as SVM eliminate great effort and time. In this paper, two models based on SVM are constructed for analysis and synthesis of ETRMAs. The number of 100 ETRMAs with various geometrical and electrical parameters (L, l, h and ε_r) are simulated in terms of resonant frequency (f_r) with the aid of an electromagnetic simulator program to obtain the data set. Two different SVM models are designed to obtain the resonant frequency and slot dimension of ETRMAs by using the simulation data set. The obtaining the resonant frequency and slot size are analysis and synthesis processes, respectively. The SVM models are trained with the simulated data set of 75 ETRMAs and tested with remainders 25 ETRMAs. A prototype of ETRMA is then fabricated to verify the proposed models in this paper. The testing results of the SVM are compared with the simulation/measurement results and the models are found to be successful. Antenna designers can use the proposed models quickly and simply in analysis and synthesis process of ETRMAs without the need for complex processes.

Index Terms ─ Analysis, microstrip antenna, synthesis, support vector machine, triangular ring microstrip antenna.

I. INTRODUCTION

Microstrip antennas (MAs) have significant advantages such as low size, lightness, robustness, ease of production, low production cost and physical compatibility with the surfaces. Because of these advantages, MAs are widely used in portable/non-portable wireless communication applications that require miniaturized geometry [1]. The smaller size antennas can be produced by using the substrate having high dielectric constant but this leads to a reduction of performance efficiency and bandwidth parameters [1]. Therefore, performing the requirements of mobile communication devices is difficult by using the traditional patch geometries of MAs such as rectangular, triangular, circular, square. The miniaturized MAs are produced by applying some modification such as shorting pins, slits or slots on the traditional geometry structures [1]. Equilateral triangular ring microstrip antennas (ETRMAs) are constructed by triangular slot loading in the center of triangular patch. According to the same size triangular microstrip antenna, the resonant frequency is reduced due to slot loading into the triangular patch. For the same resonant frequency, the size of ETRMA reduces compared to the equilateral triangular microstrip antenna (ETMA).

Antenna analysis involves the process of calculating performance parameters such as resonance frequency, gain, bandwidth, radiation patterns, etc. On the other hand, antenna synthesis is the process of deriving physical structure for the given performance parameters reverse of antenna analysis. Several analytical and numerical methods having some disadvantages are generally used for analysis process [2]. The numerical methods give good results by using mixed mathematical operations. The numerical methods such as finite difference time domain method, finite element method and method of moment require much more time in solving Maxwell's equations including integral and/or differential computations. So, it becomes time consuming since it repeats the same mathematical procedure even if a minor change in geometry is carried out. Moreover, the analytical methods such as the cavity model and the transmission line model are accurate but they are based on physical assumptions. These methods are more suitable for conventional MAs because of their regular shapes. In addition, these approaches require a new solution for every small change in the patch geometry [3]. Antenna designers need the synthesize to find the best antenna solution. Simulator tool packs such as HyperLynx® 3D EM [4], Ansoft HFSS [5], CST microwave studio [6], Agilent ADS [7] are commonly

Submitted On: March 28, 2018
Accepted On: May 10, 2018

used to simplify the synthesis process. These simulation packages do not themselves produce a synthesized antenna, but they only analyze the antenna structure and provide calculated performance results for a synthesized antenna. Hence, artificial intelligence techniques are widely preferred as a faster and accurate alternative methods to accomplish these challenges associated with the traditional techniques in analysis and synthesis processes of MAs [3, 8]. Artificial intelligence models such as artificial neural network (ANN) [9], support vector machine (SVM) [10] and adaptive neuro fuzzy inference system (ANFIS) [11] eliminate the complex mathematical procedures and time consuming for processes of antenna design. These models have been widely used for analysis and synthesis of various MAs in the literature [12-25]. In [12-18], analysis studies were carried out to determine some performance parameters of MAs having various shapes with artificial intelligence techniques such as ANN, SVM and ANFIS. Also, synthesis models were proposed for MAs and microwave devices in [19-25]. In this study, SVM is preferred because of the following advantages: SVM often converges on global minimum rather than local minimum in high nonlinear problem. The overfitting problem and calculation procedures are less in the SVM method according to ANN and ANFIS. SVM requires less memory than other modeling methods.

In this work, SVM-based analysis and synthesis models is proposed as a tool for the design of ETRMAs. Using SVM technique, the resonant frequency (f_r) and slot size (l) of the ETRMAs are obtained as a function of input variables. For this purpose, ETRMA is designed and a two SVM models are constructed with a 100 ETRMAs simulation data set. The simulations are performed with the aid of a 3D full wave simulator using the method of moment (MoM) [26]. The data set of 75 ETRMAs are used to train the SVM models and remainders 25 ETRMAs are utilized to test the accuracy of models. The testing data set is not included in training process. The SVM models are then verified through the measured data set of a prototyped ETRMA in this study.

II. ETRMA STRUCTURE AND SIMULATION PROCESS

ETRMA is formed by loading an equilateral triangular slot with size "l" on an equilateral triangular patch of size "L" as shown Fig. 1. The constituted ETRMA patch is placed on a substrate with h thickness and ε_r dielectric constant, all over on the ground layer. The ETRMA is fed at the point of x and y. The equilateral triangular slot causes to a reduction in resonant frequency compared to an ETMA of the same size. Also, the size of ETRMA is smaller than the size of ETMA in the same resonant frequency. These situations are seen in the simulation results given in Table 1 and Fig. 2.

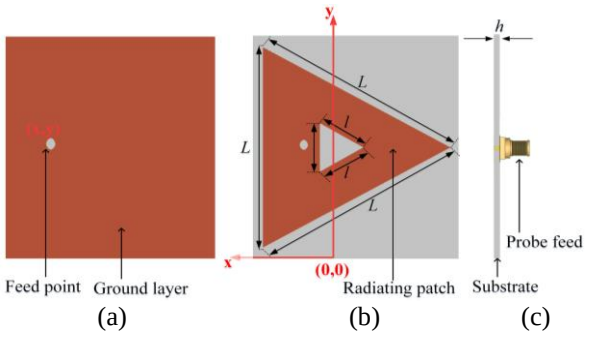

Fig. 1. Geometry of the ETRMA: (a) back view, (b) front view, and (c) side view.

Table 1: Comparative simulation results for ETMA and ETRMA

Antenna	*Patch Dimension (mm)*			ε_r	f_r
	L	***l***	***h***		
ETMA	52	0	1.6	2.33	2.432
ETRMA	52	17.2	1.6	2.33	2.226
ETRMA	43.3	25.8	1.6	2.33	2.432

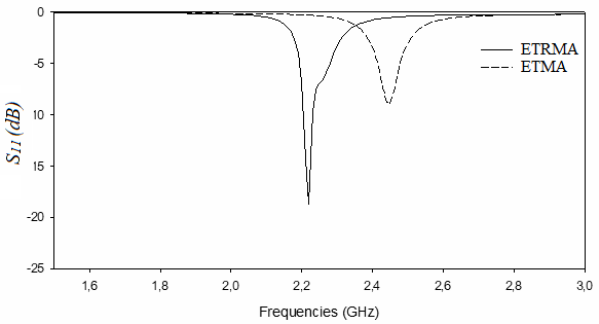

Fig. 2. The compared S_{11} parameters of simulated ETMA and ETRMA for the same size

The 100 ETRMA with 4 parameters (L, l, h and ε_r) are simulated to determine the resonant frequency (f_r). A total of 100 data set are generated, 75 of which are used for training the SVM models. The remaining 25 are used for testing the performance of the trained SVM models on inputs. From the data set, 75 and 25 ETRMAs are uniformly selected to train and test the accuracy of the models according to 75% and 25% of ETRMA data, respectively. These ratios used for training and testing data are widely preferred in the literature. The 25 testing data are not used in the training process. For this purpose, simulations of 100 ETRMAs are performed with the respect to the resonant frequency according to parameters given in Table 2. The "h" and "ε_r" values given in Table 2 belong to the substrate materials commonly used in the literature. Because the proposed analysis and synthesis models cover ETRMAs operating in the ultrahigh band, the patch dimensions are determined accordingly.

Table 2: Geometrical and electrical parameters of simulated ETRMAs

Number of Simulations	Patch Dimensions (mm)			Dielectric Constant (ε_r)
	L	***l***	***h***	
20	26	3.44, 6.88, 10.32, 13.76, 17.2	1.6, 2.5	2.33, 4.4
20	34	5.16, 10.32, 15.48, 20.64, 25.8		
20	52	8.6, 17.2, 25.8, 34.4, 43		
20	69	17.2, 25.8, 34.4, 43, 51.6		
20	86	25.8, 34.4, 43, 51.6, 60.2		

The ETRMA structures are modelled/simulated according to topology in Fig. 3 by means of computational electromagnetic software HyperLynx® 3D EM [4] using method of moment (MoM) [26]. In the simulations, 1 Volt wave source with coaxial fed is used for the ETRMAs. The antenna models are meshed with lines per wavelength ratio of 40 and maximum frequency of 5 GHz. It is simulated between the frequency of 0 GHz and 5 GHz. The HyperLynx® 3D EM's built-in optimization module was used to determine the feed point with the objective function S_{11} (dB) < −10 for the resonant frequencies.

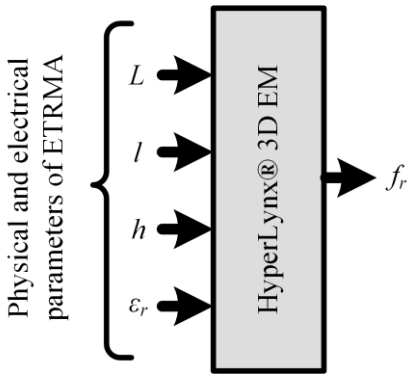

Fig. 3. The topology of the simulation process by HyperLynx® 3D EM software.

III. PROCESS OF SVM MODELS CONSTRUCTION

The process of SVM models construction is outlined in Fig. 4 for analysis and synthesis of ETRMAs. The resonant frequency and slot dimension of ETRMAs are obtained in the analysis and synthesis process, respectively. The SVM models are trained with 75 antenna data so that fitting the models's outputs to results of simulation in the objective of minimizing MAPE calculating the mean absolute percentage error between the targets and outputs.

A. SVM modelling

Analysis and synthesis models based on SVM are proposed for the design of ETRMAs according to the topology shown in Figs. 5 (a) and 5 (b). Machine learning methods are used for classification, regression and clustering problems. SVM is a new generation supervised learning model which used for regression analysis in machine learning [10]. In the nonlinear problems such as analysis and synthesis of antennas, SVM depends on the principle which is separation of two data groups by N-dimension optimum hyperplane by using the Kernel functions. The key point in SVM is linear discriminant function called hyperplane reflecting the characteristics of data-set. SVM effectively establishes an optimum hyperplane having equidistant from both of the data in a high or infinite dimensional space. [27].

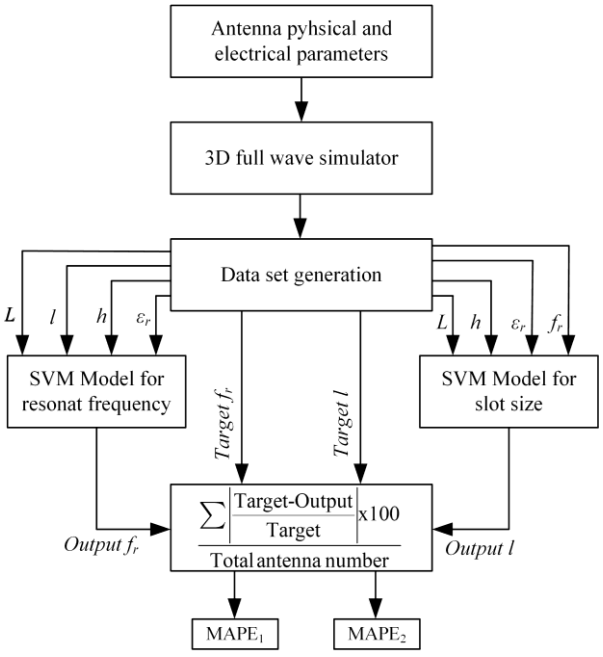

Fig. 4. The working principle of the SVM models.

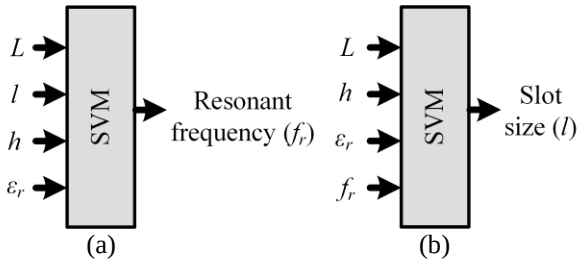

Fig. 5. The topology of SVM models: (a) for analysis, and (b) for synthesis.

B. Training the SVM models

The SVM models are trained through 75 of total 100 ETRMA data set according to flow chart given in Fig. 6. They are constructed using parameters in Table 3 for obtaining the resonant frequency and slot size of ETRMAS as shown in Figs. 7 (a) and 7 (b). The SVM models are codded in MATLAB® software. In this work, the used gaussian kernel function is given as

$$K(x, x_i) = \exp\left(-\frac{\|x - x_i\|^2}{2\sigma^2}\right). \quad (1)$$

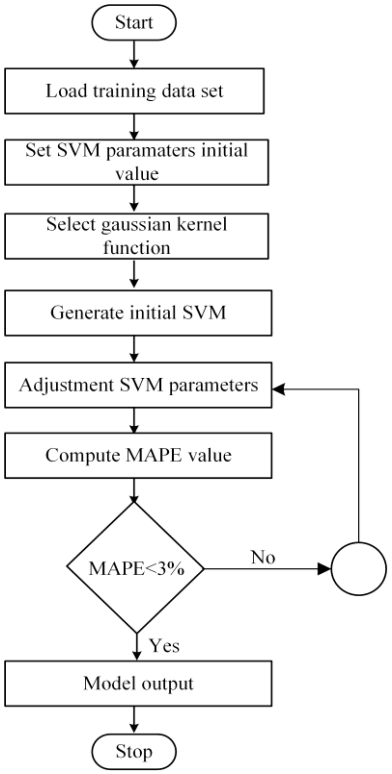

Fig. 6. Flow chart of the SVM models in the training phase.

As it is seen from the Fig. 8, that the results of proposed SVM models and obtained from simulations are in a good harmony and MAPEs are achieved as 0.312% and 2.741% respectively for analysis (f_r) and synthesis (l) in the training process. The synthesis problem is more nonlinear than the analysis problem, therefore the MAPE calculated as a result of analysis is lower than the MAPE of synthesis.

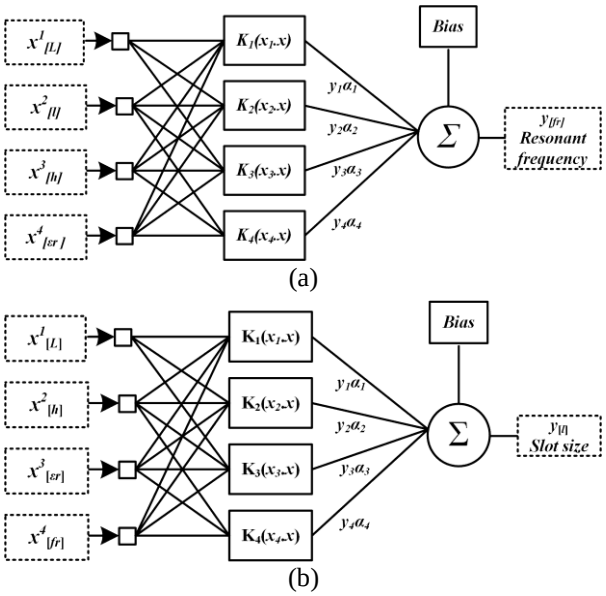

Fig. 7. The proposed SVM models: (a) for resonant frequency, and (b) for slot size.

Table 3: The used SVM parameters for analysis and synthesis of ETRMA

Models	Parameters	Set Type/Value
Analysis model	Kernel function	Gaussian
	Kernel function coefficient (σ)	28
	Penalty weight (C)	1000000
	Slack variables (epsilon-ξ)	0.001
	Number of input	4
	Number of output	1
Synthesis model	Kernel function	Gaussian
	Kernel function coefficient (σ)	13
	Penalty weight (C)	1000000
	Slack variables (epsilon-ξ)	0.0025
	Number of input	4
	Number of output	1

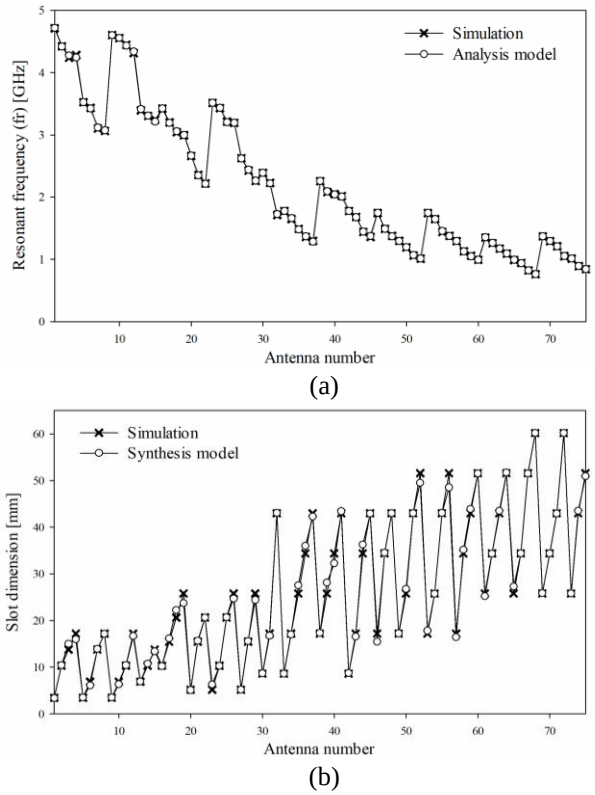

Fig. 8. Comparative results of the simulation and SVM models: (a) for analysis and (b) for synthesis.

IV. TESTING RESULTS OF ANALYSIS AND SYTNHESIS PROCESS FOR ETRMA

In the last section, SVM models are constructed and trained with properly parameters. The accuracies the SVM models are now tested through 25 ETRMAs data set not included in the training phase. As shown Figs. 9 (a) and 9 (b), graphical user interfaces (GUIs) are designed in MATLAB® software to use the SVM models for the antenna designer. Antenna designers be able to use this GUIs practically in ETRMA analysis and synthesis process.

A. Testing results of analysis process

The accuracy of the SVM-based analysis model for obtaining the resonant frequency is tested through 25 ETRMAs data that is not utilized in training the model. The parameters of 25 simulated antennas with respective resonant frequency values and results of analysis model are given in Table 4. It is seen from the results; model successfully obtains the resonant frequency with MAPE of 1.109%. Also the harmony of simulation and SVM model results is seen in Fig. 10.

B. Results of synthesis process

The validity of the synthesis model based on SVM for obtaining the slot dimension is tested through 25 ETRMAs. The testing data set for the synthesis model are not included in the training process. The parameters of 25 simulated antennas and testing results of synthesis model are given in Table 5. Although the problem of obtaining slot dimension is a high nonlinearity problem, the results of the SVM-based synthesis model are harmony with the simulation results as shown in Table 5 and Fig. 11. The slot dimension with MAPE of 5.507% is obtained by the proposed model.

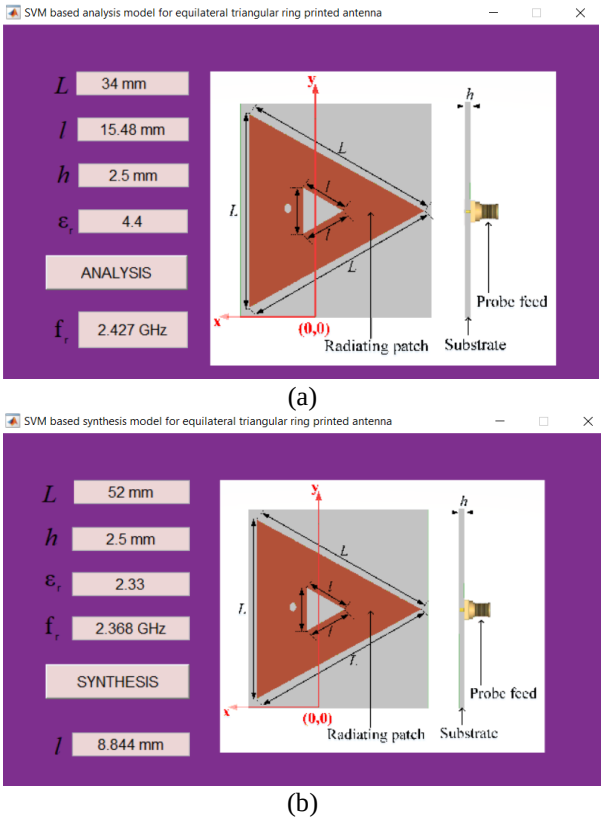

Fig. 9. The screenshots for GUI of the SVM models: (a) for analysis and (b) for synthesis.

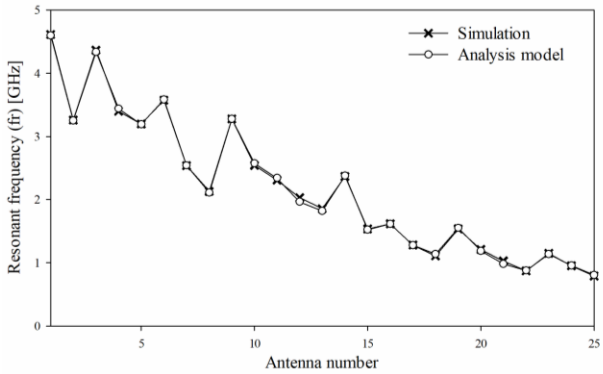

Fig. 10. Comparative results of the simulation and analysis model in the testing process.

C. Fabrication of ETRMA

The accuracy and validity of SVM analysis/ synthesis models are verified on the fabricated ETRMA. ETRMA illustrated in Fig. 12 is printed on FR4 PCB substrate of which dielectric permittivity, tangent loss and thickness are 2.22, 0.02 and 1.6 mm, respectively. All parameters related to the antenna are given in Table 6. The prototyped antenna is measured by using Keysight Technologies N5224A PNA network analyzer. The measured S_{11} parameter is shown in Fig. 13 in comparison with the simulated one. The results of measured and the analysis/synthesis models are listed in Tables 6 and 7 in order to evaluate the testing process in detail.

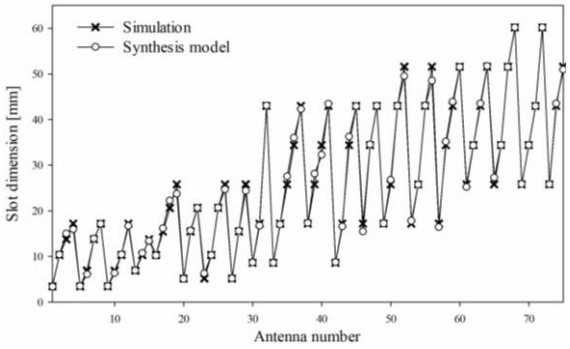

Fig. 11. Comparative results of the simulation and synthesis model in the testing process.

Table 4: Data set of testing for resonant frequencies and obtained results

Antenna Number	Inputs				Outputs of Simulation [GHz]	Outputs of SVM [GHz]	Absolute Percentage Error (APE)
	L [mm]	l [mm]	h [mm]	ε_r	$f_{r\_simulation}$	f_{r_SVM}	
1	26	6.88	1.6	2.33	4.614	4.599	0.325
2	26	10.32	1.6	4.4	3.261	3.254	0.227
3	26	13.76	2.5	2.33	4.365	4.338	0.625
4	26	3.44	2.5	4.4	3.401	3.441	1.179
5	26	17.2	2.5	4.4	3.198	3.195	0.102
6	34	5.16	1.6	2.33	3.576	3.585	0.253
7	34	10.32	1.6	4.4	2.538	2.543	0.188
8	34	25.8	1.6	4.4	2.130	2.114	0.773
9	34	15.48	2.5	2.33	3.278	3.279	0.031
10	34	10.32	2.5	4.4	2.544	2.575	1.223
11	34	20.64	2.5	4.4	2.309	2.342	1.446
12	52	25.8	1.6	2.33	2.030	1.964	3.245
13	52	34.4	1.6	2.33	1.856	1.821	1.874
14	52	8.6	2.5	2.33	2.368	2.378	0.430
15	52	25.8	2.5	4.4	1.536	1.524	0.784
16	69	25.8	1.6	2.33	1.616	1.614	0.114
17	69	51.6	1.6	2.33	1.280	1.277	0.209
18	69	34.4	1.6	4.4	1.110	1.139	2.589
19	69	34.4	2.5	2.33	1.536	1.552	1.035
20	69	25.8	2.5	4.4	1.210	1.189	1.734
21	86	60.2	1.6	2.33	1.030	0.981	4.709
22	86	43	1.6	4.4	0.870	0.878	0.936
23	86	51.6	2.5	2.33	1.150	1.136	1.208
24	86	34.4	2.5	4.4	0.950	0.957	0.789
25	86	60.2	2.5	4.4	0.790	0.803	1.685
Mean absolute percentage error (MAPE)							1.109

Table 5: Data set of testing for slot sizes and obtained results

Antenna Number	Inputs				Outputs [mm]		Absolute Percentage Error (APE)
	L [mm]	h [mm]	ε_r	f_r [GHz]	$l_{simulation}$	l_{SVM}	
1	26	1.6	2.33	4.614	6.88	5.731	16.702
2	26	1.6	4.4	3.261	10.32	11.18	8.291
3	26	2.5	2.33	4.365	13.76	13.60	1.184
4	26	2.5	4.4	3.401	3.44	3.64	5.718
5	26	2.5	4.4	3.198	17.20	15.34	10.820
6	34	1.6	2.33	3.576	5.16	5.56	7.700
7	34	1.6	4.4	2.538	10.32	9.35	9.339
8	34	1.6	4.4	2.130	25.80	23.81	7.686
9	34	2.5	2.33	3.278	15.48	17.62	13.817
10	34	2.5	4.4	2.544	10.32	9.473	8.208
11	34	2.5	4.4	2.309	20.64	21.79	5.597
12	52	1.6	2.33	2.030	25.80	26.69	3.463
13	52	1.6	2.33	1.856	34.40	35.61	3.544
14	52	2.5	2.33	2.368	8.60	8.844	2.839
15	52	2.5	4.4	1.536	25.80	28.37	9.971
16	69	1.6	2.33	1.616	25.80	24.89	3.504
17	69	1.6	2.33	1.280	51.60	50.39	2.341
18	69	1.6	4.4	1.110	34.40	35.48	3.160
19	69	2.5	2.33	1.536	34.40	35.02	1.807
20	69	2.5	4.4	1.210	25.80	25.74	0.205
21	86	1.6	2.33	1.030	60.20	59.87	0.544
22	86	1.6	4.4	0.870	43.00	44.37	3.208
23	86	2.5	2.33	1.150	51.60	49.38	4.294
24	86	2.5	4.4	0.950	34.40	34.64	0.718
25	86	2.5	4.4	0.790	60.20	58.37	3.035
Mean absolute percentage error (MAPE)							5.507

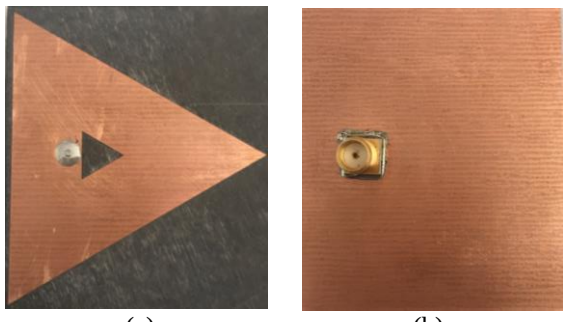

(a) (b)

Fig. 12. The photograph of prototyped ETRPA: (a) front view and (b) back view.

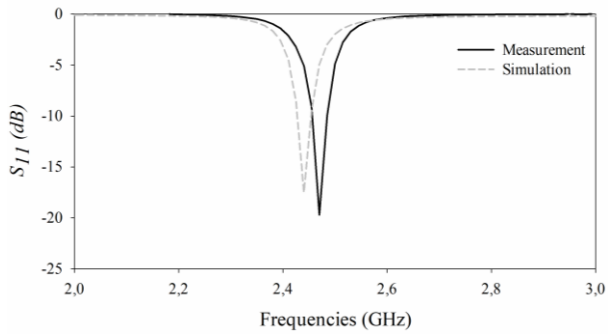

Fig. 13. S_{11} parameters of simulated and measured prototyped ETRMA.

Table 6: The comparative results for resonant frequency

Inputs				Resonant Frequency [GHz]		
L [mm]	l [mm]	h [mm]	ε_r	$f_{sim.}$	$f_{mea.}$	f_{SVM}
52	8.6	1.6	2.22	2.438	2.468	2.391

Table 7: The comparative results for slot size

Inputs				Outputs [mm]	
L [mm]	h [mm]	ε_r	f_r [GHz]	$l_{mea.}$	l_{SVM}
52	1.6	2.22	2.468	8.600	8.427

From Tables 6 and 7, the results of SVM models are much close to the simulated/measured results. Therefore, the SVM models can be successfully used to obtain the resonant frequency (f_r) and slot size (l) of the ETRMAs without handling sophisticated mathematical functions and transformations. Moreover, the proposed models can be modified or improved to use similar tasks of nonlinear electromagnetic problems. The antenna designers can use practically the proposed models for analysis and synthesis of ETRMA.

V. CONCLUSION

In this work, two SVM models are implemented for analysis and synthesis of the ETRMAs. A data set of 75 ETRMAs are used for training and the remainders 25 data set are utilized for testing the SVM models. The four antenna parameters are input the model to obtain the resonant frequency of ETRMA in the analysis process. In this design process, synthesis is defined as the forward side and then analysis as the reverse side of the problem. At the output of the synthesis model, slot dimension of ETRMA is also obtained by inputting length of antenna, height/dielectric constants of the chosen substrate and resonant frequency. The results achieved in this study show that proposed SVM models can be successfully used to obtain the resonant frequency and slot size of ETRMAs with high accuracy. The SVM technique may be preferred as a faster and accurate alternative methods according to the traditional techniques in analysis and synthesis processes of MAs.

REFERENCES

[1] K. Wong, *Compact and Broadband Microstrip Antennas*. John Wiley & Sons, Inc., 2002.

[2] J. R. James, P. S. Hall, and C. Wood, *Microstrip Antenna Theory and Design*. IEE. Peter Peregrinus, 1981.

[3] Q. J. Zhang and K. C. Gupta, *Neural Networks for RF and Microwave Design*. Artech House Publishers, 2000.

[4] HyperLynx® 3D EM, Version 15, Mentor Graphics Corporation, 8005 SW Boeckman Road, Wilsonville, OR 97070.

[5] Ansoft Corporation, HFSS v. 10.1.1 user manual, July 2006. http://www.ansoft. com

[6] CST GmbH-Computer Simulation Technology, CST Microwave Studio 2006 user manual, 2006. http://www.cst.com

[7] Agilent Technologies, EEsof EDA, Momentum. http://eesof.Tm. Agilent.com/products/momentum main. html

[8] C. G. Christodoulou and M. Georgiopoulos, *Applications of Neural Networks in Electromagnetics*. Artech House, Boston, 2001.

[9] S. Haykin, *Neural Networks: A Comprehensive Foundation*. Macmillan College Publishing Company, New York, ABD, 1994.

[10] N. V. Vapnik and A. Y. Chervonenkis, "The Necessary and Sufficient Conditions for Consistency in the Empirical Risk Minimization Method," Lect. Notes, Comput. Sc., vol. 1, no. 3, pp. 283-305, 1991.

[11] J. S. R. Jang, "ANFIS: Adaptive-network-based fuzzy inference system," *IEEE TSyst. Man. Cy.*, vol. 23, pp. 665-685, 1993.

[12] A. Akdagli, A. Kayabasi, and I Develi, "Computing resonant frequency of C-shaped compact microstrip antennas by using ANFIS," *Int. J. Elec.*, vol. 102, pp. 407-417, 2015.

[13] A. Kayabasi and A. Akdagli, "Predicting the resonant frequency of E-shaped compact microstrip antennas by using ANFIS and SVM," *Wireless Pers. Commun*., vol. 82 pp. 1893-1906, 2015.

[14] A. Kayabasi, A. Toktas, A. Akdagli, M. B. Bicer, and D. Ustun, "Applications of ANN and ANFIS to predict the resonant frequency of L-shaped compact microstrip antennas," *Appl. Comput. Electrom.*, vol. 29, pp. 460-469, 2014.

[15] K. Guney and N. Sarikaya, "Adaptive neuro-fuzzy inference system for computing the resonant frequency of circular microstrip antennas," *Appl. Comput. Electrom.*, vol. 19, pp. 188-197, 2004.

[16] F. Güneş, N. T. Tokan, and F. Gürgen, "A consensual modeling of the expert systems applied to microwave devices," *Int. J. RF Microw. Comput.-aided Eng.*, vol. 20, pp. 430-440, 2010.

[17] Y. Tighilt, F. Bouttout, and A. Khellaf, "Modeling and design of printed antennas using neural networks," *Int. J. RF Microw. Comput.-aided Eng.*, vol. 21, pp. 228-233, 2011.

[18] A. R. Venmathi and L. Vanitha, "Support vector machine for bandwidth analysis of slotted microstrip antenna," *Int. J. Comput. Inf. Sci.*, vol. 4, no. 1, pp. 67-61, 2011.

[19] W. Zhongbao and S. Fang, "ANN synthesis model of single-feed corner-truncated circularly polarized microstrip antenna with an air gap for wideband applications," *Int. J. Antennas Propag.*, 2014.

[20] H. J. Delgado, M. H. Thursby, and F. M. Ham, "A novel neural network for the synthesis of antennas

and microwave devices," *IEEE Trans. Neural Netw. Learn. Syst. NN*, vol. 16, no. 6, pp. 1590-1600, 2005.

[21] Z. Wang, S. Fang, Q. Wang, and H. Liu, "An ANN-based synthesis model for the single-feed circularly-polarized square microstrip antenna with truncated corners," *IEEE Trans. Neural Netw. Learn. Syst. NN*, vol. 60, no. 12, pp. 5989-5992, 2012.

[22] T. Khan, A. De, and M. Uddin, "Prediction of slot-size and inserted air-gap for improving the performance of rectangular microstrip antennas using artificial neural networks," *IEEE Antennas Wireless Propag. Lett*., vol. 12, pp. 1367-1371, 2013.

[23] E. Demircioglu, M. H. Sazlı, S. T. İmeci, and O. Sengul, "Soft computing techniques on multi-resonant antenna synthesis and analysis," *Microw. Opt. Technol. Lett*., vol. 55, no. 11, pp. 2643-2648, 2013.

[24] L. Merad, F. T. Bendimerad, and S. M. Meriah, "Design and resonant frequency calculation of rectangular microstrip antennas," *Int. J. Numer. Model El*, vol. 24, no. 2, pp. 144-153, 2011.

[25] N. K. Saxena, M. Khan, P. K. S. Pourush, and N. Kumar, "Neural network analysis of switchability of microstrip rectangular patch antenna printed on ferrite material," *Int. J. RF Microw. Comput.-aided Eng.*, vol. 20, no. 1, pp. 1-5, 2010.

[26] R. F. Harrington, *Field Computation by Moment Methods*. IEEE Press, Piscataway, NJ, 1993.

[27] N. T. Tokan and F. Gunes, "Support vector characterization of the microstrip antennas based on measurements," *Prog. Electromagn. Res. B*, vol. 5, pp. 49-61, 2008.

Ahmet Kayabasi was born in 1980. He received his B.S. and M.S. degrees in EEE from Selcuk University, Turkey, in 2001, 2005 respectively. In 2015, he received his Ph.D. degree in Electrical and Electronics Engineering from Mersin University, Turkey. From 2001 to 2015, he was a Lecturer in the Electronics and Automation Department of Selcuk University. He has been working as Assistant Professor in the Department of Electrical and Electronics Engineering at Karamanoglu Mehmetbey University. His current research interests include antennas, microstrip antennas, computational electromagnetic, artificial intelligent.

Design and Analysis of Ring-Focus Reflector Antenna using Method of Moments Solution of Electric Field Integral Equation

I. Ismatullah [1], Ghulam Ahmad [1,2], and Shafaat A. K. M. Ali [1]

[1] Geo-Sat Payload Division
Satellite Research and Development Center, Lahore/Karachi, 54000, Pakistan
ismatullah@gmail.com

[2] Faculty of Engineering and Physical Sciences
University of Surrey, Guildford, GU2 7XH, United Kingdom
g.ahmad@surrey.ac.uk

Abstract ─ Ring-focus dual reflector antennas have been employed in various satellite communication applications because of their higher gain and geometrical compactness as compared to the conventional Cassegrain or Gregorian counterparts. In this contribution the geometrical design, full-wave analysis and testing of a ring-focus dual reflector antenna based on axially displaced ellipse (ADE) configuration are reported. The geometrical design of this dual reflector system is conceived through conic section formulations. An analytical methodology based on multilevel fast multipole method (MLFMM) accelerated method of moments (MoM) solution of surface integral equations for open perfect electrically conducting objects was developed for its RF performance prediction. The distinctive nature of surface current distributions of a ring-focus subreflector is investigated and compared with that of a Cassegrain counterpart. Finally, the developed procedure was applied to predict the performance of a 35 wavelength ADE ring focus antenna. A close agreement of predicted and measured performance was observed which proves the validity of our fast analytical procedure.

Index Terms ─ Axially displaced ellipse, EFIE, MLFMM, MoM, ring focus antenna, SATCOM.

I. INTRODUCTION

Design methods for efficiency enhancement and sidelobes reduction in high gain antennas have always been a topic of keen interest among antenna design engineers. Increasing the gain of a communication antenna directly increases signal to noise ratio and hence the communication link can support increased data rates [1]. However, since the antenna gain is proportional to its effective area [2]; the trend towards compactness may pose conflicting requirements. Consequently, the demand for compact yet efficient aperture antennas is on the rise.

A ring-focus reflector antenna is an excellent candidate for high gain compact antennas. It has proved its effectiveness in recent years particularly in SATCOM on the move applications [1,3,4]. A ring focus subreflector can be made several times smaller in comparison to that of classical Cassegrain/Gregorian antennas. Similarly, the feed horn can be placed closer to a ring focus subreflector without experiencing detrimental blockage effects [1]. The aperture efficiency of a ring-focus antenna can exceed 80% due to its ray inversion features [5,6]. In other reflector antenna configurations the aperture efficiency is relatively less than that of a ring focus design. Although, there exist few exotic designs, e.g., top hat fed reflector antennas [7,8] which can achieve a comparable efficiency. However, it takes significant efforts to meet such a target. In such designs the antenna bandwidth and its cross polarization discrimination (XPD) become potential design concerns.

The geometrical design of a ring-focus reflector antenna can be accomplished by using the necessary design equations for a given set of known parameters and can be found in literature [6,9,10]. However, in the work presented here, a more fundamental approach has been adopted to enable a better design insight and its direct implementation in the GiD pre and postprocessor software [11]. In this approach, primary conic section definitions have been used to obtain the profiles of main- and sub-reflectors. A macro was written to get the complete surface model of a ring-focus reflector in a single run.

When the multilevel fast multipole method (MLFMM) accelerated method of moments (MoM) solution of electric field integral equations (EFIE) [12-19] is solved through an efficient MoM direct method [20], the resulting solution is computationally efficient. Our developed EM solver combines the above two methods to achieve a computationally faster solution of the presented ring focus antenna. This EM solver takes as input the surface mesh which can be generated in GiD

Submitted On: March 4, 2016
Accepted On: January 3, 2018

software. Using our EM solver we investigated the distinctive nature of the surface current density on the presented ring-focus subreflector for its effects on the overall radiation performance.

In Section II the geometrical design of a ring-focus reflector from the basic conic section formulations is presented. Section III provides an overview of the formulation followed in the full-wave analysis of the designed reflector antenna. The developed EM solver was used to predict the performance of a 35 wavelength diameter ring focus antenna which is compared with the measured radiation patterns in Section IV. Section V concludes the work being presented in this paper.

II. GEOMETRICAL DESIGN OF A RING-FOCUS REFLECTOR

A ring-focus dual reflector antenna system based on axially displaced ellipse (ADE) configuration [5,10] is shown in Fig. 1. Due to geometrical optics (GO) an axial ray originating from the feed horn travels towards the main reflector's outer rim after a reflection from a ring focus subreflector. Whereas a ray arriving at subreflector's outer rim travels towards the central portion of the main reflector which is contrary to classical Cassegrain/Gregorian designs. This is known as the ray inversion phenomena of a ring-focus antenna. The whole geometry presented in Fig. 1 is rotationally symmetric about the axis of symmetry (z-axis here). Geometries of main and sub-reflectors can be generated by using the following mathematical treatment.

It is usual to start the antenna design by knowing certain parameters [10]. The gain requirement of an antenna determines its aperture, where the diameter of a subreflector is selected a few percentage of the main reflector's diameter. Focal length is mainly decided by the accommodation space available for the antenna, although longer focal lengths lead to a better XPD. In the work presented here, it is assumed that the diameter of main reflector (D_m), diameter of subreflector (D_s), focal length of the main reflector (F_m) and the location of feed phase center (F_S) as shown in Fig. 1 are already known. It is to be noted that an elliptical subreflector possesses two foci. One of these coincides with the main reflector's focal point. Whereas the second focus is made coincident with the feed phase center for an optimum performance. In the equations given below, P_s (say) represents a point on the main/subreflector and (x_{P_S}, z_{P_S}) represent it's x and z coordinates respectively.

The profile of a parabolic main reflector can be generated by the basic equation of a conic section:

$$z = \frac{\left(x - {D_s}/{2}\right)^2}{4F_m}, \quad \frac{D_s}{2} \le x \le \frac{D_m}{2}. \tag{1}$$

Keeping in view the ray inversion phenomenon, where ray $\overrightarrow{F_{S1}S_1}$ will travel along $\overrightarrow{S_1F_{S2}M_2}$ after reflection at S_1, the point S_1 can be determined from equation of a straight line. Thus, knowing $x_{S1} = 0$; the z-coordinate of S_1 can be written as:

$$z_{S1} = z_{F_{S2}} + \frac{z_{M2} - z_{F_{S2}}}{x_{M2} - x_{F_{S2}}}\left(x_{S1} - x_{F_{S2}}\right). \tag{2}$$

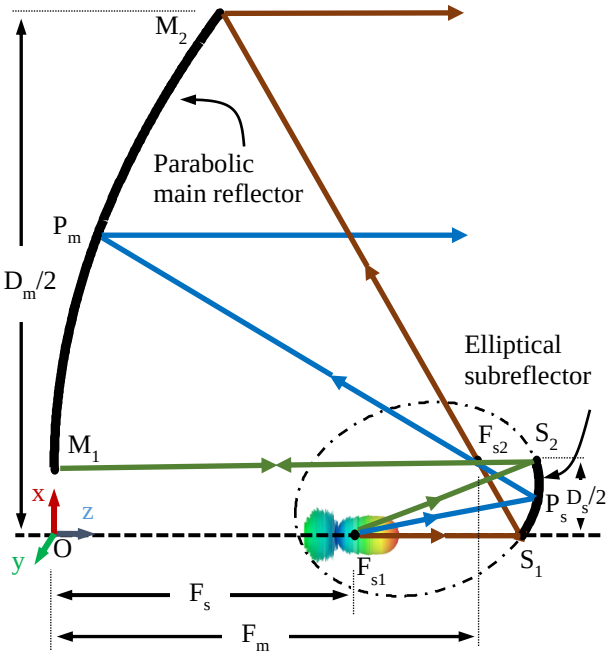

Fig. 1. Geometry of a ring-focus dual reflector antenna.

The semi-major axis "a" of an ellipse can be calculated from its basic property:

$$a = \frac{|\overline{F_{s1}S_1}| + |\overline{F_{s2}S_1}|}{2}. \tag{3}$$

Once "a" is determined, the set of points representing a subreflector can be constructed using quadratic equation's solution of an ellipse:

$$|\overline{F_{s1}P_s}| + |\overline{F_{s2}P_s}| = 2a \; 0 \le x_{P_S} \le \frac{D_s}{2}. \tag{4}$$

Therefore, the solution of (4) for z_{P_S} can be expressed as:

$$z_{P_S} = \frac{-\beta \pm \sqrt{\beta^2 - 4\alpha\gamma}}{2\alpha}, \tag{5}$$

where

$$\alpha = 4\left[(2a)^2 - \left(z_{F_{S2}} - z_{F_{S1}}\right)^2\right], \tag{5a}$$

$$\beta = 4\left[\delta\left(z_{F_{S2}} - z_{F_{S1}}\right) - 8a^2 z_{F_{S2}}\right], \tag{5b}$$

$$\gamma = 16a^2\left[\left(z_{F_{s2}}\right)^2 + \left(x_{P_S} - x_{F_{s2}}\right)^2\right] - \delta^2, \tag{5c}$$

where $\delta = 4a^2 + \left(z_{F_{S2}}\right)^2 - \left(z_{F_{S1}}\right)^2 + \left(x_{P_S} - x_{F_{S2}}\right)^2 - \left(x_{P_S} - x_{F_{S1}}\right)^2$. (5d)

Corresponding to each x_{P_S}, Equation (5) generates two values of z_{P_S}, and ADE geometry can be obtained by using positive discriminant in Equation (5) which corresponds to right-sided (solid) curve of the ellipse as

shown in Fig. 1. Once the 2-dimensional profiles of main and sub-reflectors are obtained, the 3D surface model can be obtained by rotating these profiles around the z-coordinate (see Fig. 1). The locus of the main reflector's focal point (and its coincident subreflector focal point) traces a ring in 3D due to this rotation and hence the name ring-focus.

III. ANALYSIS OF RING-FOCUS REFLECTOR ANTENNA USING MLFMM ACCELARATED MOM SOLUTION OF EFIE

The MoM solution of surface integral equations is a well-known powerful numerical tool for solving electromagnetic problems [12-13]. For the analysis of our ring-focus reflector antenna, electric field integral equations (EFIE) which couples the incident electric field to induced current density on an arbitrary shaped surface has been taken into consideration. In this formulation, the surface S of the ring-focus reflector antenna is replaced by equivalent surface electric current density $\overrightarrow{J_S}$ which radiates the electric and magnetic fields $(\vec{E}, \vec{H})$ in free space. $\overrightarrow{J_S}$ can be obtained by solving [12-16]:

$$\hat{n} \times \left[\hat{n} \times \left\{\iint_S \left[\bar{\bar{G}}_J^E(\vec{r},\vec{r}').\vec{J}_S(\vec{r}')\right]ds' + \vec{E}^{inc}(\vec{r})\right\}\right] = 0, \quad (6)$$

where $\vec{E}^{inc}(\vec{r})$ is the incident electric field, $\hat{n}$ is the outward directed unit surface normal and $\bar{\bar{G}}_J^E(\vec{r},\vec{r}')$ represents the free space dyadic Green's function. To solve the integral equation (6), $\vec{J}_S(\vec{r}')$ (unknown surface current densities) is expanded using a set of basis functions as:

$$\vec{J}_S = \sum_{n=1}^{N} I_n \vec{f}_n. \quad (6a)$$

In this work, the Rao-Wilton-Glisson (RWG) [17] functions associated with the common edge $\overrightarrow{12}$ of the triangle pair shown in Fig. 2 were chosen as the basis functions which are expressed as:

$$\vec{f}_n = \hat{n} \times (\lambda_1 \nabla\lambda_2 - \lambda_2 \nabla\lambda_1). \quad (6b)$$

A graphical representation of RWG basis functions is reproduced from [16] in Fig. 2. Interested readers may refer to [13,16,17] for the nomenclature of symbols used and further details on the integral equation. Application of Galerkin's procedure [13-16] with same basis and weighting functions transforms the surface integral Equation (6) into a system of linear equation of the form [12-16]:

$$[Z]\{x\} = \{b\}, \quad (7)$$

where $\{x\}$ is the unknown surface current density, $\{b\}$ is the excitation vector and $[Z]$ is the coupling matrix. The mn^{th} element of $[Z]$ is given by [14,16]:

$$Z_{mn} = -j\frac{\omega\mu}{4\pi}\sum_{p=0}^{P}\sum_{q=-p}^{p}\left(\vec{f}_{pq}^{\,m}\right)^{*}.\vec{g}_{pq}^{\,n}, \quad (8)$$

where

$$\begin{Bmatrix} \vec{f}_{pq}^{\,m} \\ \vec{g}_{pq}^{\,n} \end{Bmatrix} = \oiint \begin{Bmatrix} \vec{\bar{f}}_m(\theta,\phi) \\ \vec{\bar{g}}_m(\theta,\phi) \end{Bmatrix} Y_{pq}^{*}(\theta,\phi)d\hat{k}^2, \quad (9)$$

$\vec{\bar{f}}_m$ and $\vec{\bar{g}}_m$ are the $\hat{k}$-space basis and weighting functions respectively and Y_{pq} are the orthonormalized spherical harmonics. In the above equations X^* represents the complex conjugate of X. The coupling matrix $[Z]$ is fully populated and system of linear Equation (7) becomes computationally complex for electrically large problems. A use of numerical acceleration techniques (e.g., MLFMM) can reduce the computational complexity of Equation (7) from $O(N^3)$ for traditional MoM down to $\mathrm{O(N^{1.5}\log N)}$ for single level FMM and $\mathrm{O(N\log N)}$ for MLFMM [13,19]. Moreover, as reported in [14,16] the abovementioned spherical harmonics expansion based multilevel fast multipole method (SE-MLFMM) accelerated solution of Equation (7) provides considerable amount of memory saving without compromising accuracy and the numerical speed.

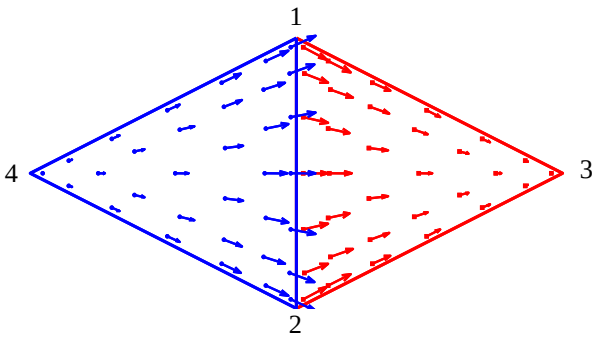

Fig. 2. WG vector basis/weighting functions for domain discretization of the electric field integral Equation (6).

In the multilevel fast multipole algorithm, the domain under consideration is enclosed in a large box, which is divided into eight smaller boxes. Each sub-box is then recursively subdivided into further smaller boxes until the side length of the smallest box is around one-half wavelength [13]. The interaction among the transmitting and receiving basis vectors residing in same or nearby smallest boxes is computed using conventional MoM. However, coupling contribution among those vectors residing in far apart boxes is calculated using MLFMM. During MLFMM, the fields radiated by different basis functions (shown with solid black arrows in the boxes on the right side of Fig. 3) within a box are first 'aggregated' into a single center. This box center then acts as the radiation center. The contribution of all radiation centers is recursively aggregated to another radiation center at the higher level. These radiated fields are then received firstly by the centers of the other boxes and then redistributed to the weighting functions (shown

with solid black arrows in the boxes on the left side of Fig. 3) belonging to the same box –so called 'disaggregation' process. Figure 3 demonstrates MLFMM process in a pictorial form. For more details on the numerical solution to EFIE, interested readers may refer to [13-19].

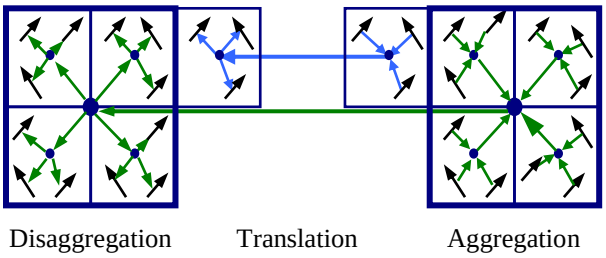

Fig. 3. Pictorial overview of MLFMM.

IV. RESULTS AND DISCUSSION

The EM solver software realized through this research was used to predict the RF performance of a Ku band ring-focus antenna system with main and sub-reflector diameters of 760 mm and 110 mm respectively. Two foci of elliptical subreflector were located at $F_{S1}(x = 0, z = 226.6)$ mm and $F_{S2}(x = 55, z = 280)$ mm in accordance with Fig. 1. A corrugated feed horn was used to illuminate the subreflector with -18 dB edge taper. GiD was used to obtain the planer triangular surface mesh of the whole structure including feed horn and subreflector supports. On average the linear dimensions of the triangular domain were of the order of λ/8 which generated around 1.4 million unknowns. The resulting matrix-vector product took around 3 hours and 40 minutes on a HP Z800 Intel® Zeon® X5690 @ 3.47 GHz dual processor with 32 GB of RAM to converge to a residual error of 8×10^{-4} which is extensively faster in comparison to general purpose commercially available 3D EM solvers.

EM solver predicted results are shown in Fig. 4 at an operating frequency of 13.75 GHz. These numerically computed results took into account the feed interaction and strut losses. A peak directivity of 38.1 dBi, around -12 dB down sidelobes and slant plane on-axis XPD better than 50 dB were predicted by our EM solver as listed in Table 1.

A prototype model of the designed ring focus antenna was manufactured and measurement results are compared with EM solver predictions in Fig. 5, where the developed reflector antenna can be seen in the inset. The measured results are in excellent agreement with EM solver predicted results in the main lobe and up to around 20 dB below the peak value. A close agreement between simulated and measured performance parameters of interest is evident from Table 1. Particularly in sidelobe regions the disagreement in predicted and measured results is mainly due to a big metallic antenna support structure used to hold the antenna on the test positioner in the anechoic chamber. This structure was not modelled in the EM solver.

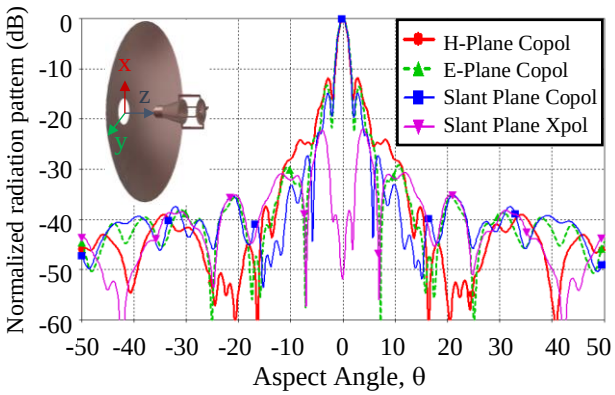

Fig. 4. Predicted performance of a 35 wavelength aperture diameter ring focus reflector antenna.

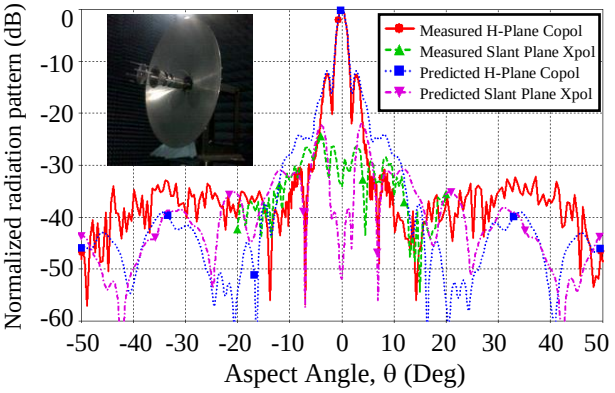

Fig. 5. Comparison of simulated and measured radiation patterns of the ring focus reflector. Inset shows the developed ring focus reflector antenna under test in an anechoic chamber.

Table 1: Summary of simulated vs. measured performance parameters

Parameter	Simulated Value	Measured Value
Peak gain	38.1 dBi	37.9 dBi
1st Sidelobe level	- 12.1 dB	- 12.6 dB
Slant plane on-axis XPD	- 50 dB	< - 30 dB

Additionally, during measurement process this metallic support structure was not covered with absorbers which resulted in higher far sidelobe levels. The difference in predicted and measured cross polarization levels is mainly due to the measurement accuracy of the anechoic chamber. It is also worth mentioning here that the feed horn used in this research was a multimode feed horn supporting TE_{11} and TE_{21} modes for communication and tracking respectively.

There was also a coupling of TE_{21} degenerate modes observed in the feed assembly design which further lowered the cross polarization. Measurements using a pure mode feed horn provided a better XPD of around 35 dB.

The equivalent surface current densities $\vec{J}_S$ on the ring-focus subreflector as well as on an exemplary Cassegrain subreflector were computed using the method described in Section III. Resulting current densities in both cases are shown in Fig. 6. For Cassegrain subreflector the central region exhibits higher amplitudes of the equivalent surface current density. In contrast, in the central region of a ring-focus subreflector very weak amplitudes of current density are observed. Weak surface current density in the central region of a ring focus subreflector may be attributed to the apex geometry along the axis.

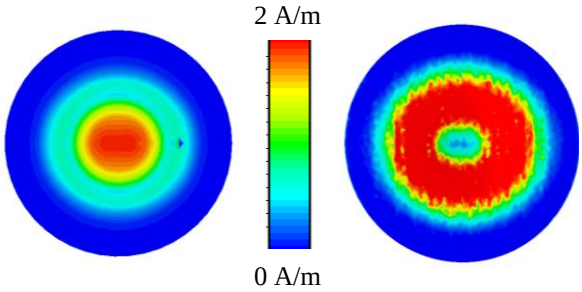

Fig. 6. Numerically computed surface current densities on Cassegrain and ring focus sub-reflectors.

It is to note that intense current densities in the central regions of a Cassegrain subreflector cause radiations towards the feed horn. These reflected radiations in the feed horn can degrade its reflection performance therefore, resulting in an overall gain degradation.

It was found through numerical simulations as well as measurements that a hole in the center of a ring focus subreflector has no significant impact on the overall antenna performance. This distinctive attribute of weak surface current density in the central region of a ring focus subreflector can be exploited to cancel radiations in certain directions e.g. to reduce the antenna sidelobe levels [21]. The inactive part of a subreflector can be removed and replaced by a dielectric lens antenna with a hyperbolic profile such that the waves passing through the lens antenna become 180˚ out of phase with those reflected by the main reflector in that particular direction.

V. CONCLUSION

A new formulation for the design of a ring-focus reflector antenna based on conic section definitions was conceived through research presented in this paper. This enabled a significant design insight and a direct CAD model creation using GiD. A fast EM solver package was developed through this research based on SE-MLFMM accelerated MoM solution of the electric field integral equation. The developed EM solver was validated through a comparison with measurements of a 35λ ring focus antenna. The distinctive feature of a ring focus sub reflector's surface current density was investigated. This will open new research areas for antenna radiation cancellation in certain directions.

ACKNOWLEDGMENT

Authors are grateful to International Center for Numerical Methods in Engineering (CIMNE) [11] for providing free license of GiD software ver. 12 which was used for domain discretization and surface current visualization.

REFERENCES

[1] A. Prata, Jr., F. J. S. Moreira, and L. R. Amaro, "Displaced-axis-ellipse reflector antenna for space-craft communications," *Microwave and Opto-electronics Conference*, vol. 1, pp. 391-395, 2003.

[2] C. A. Balanis, *Antenna Theory Analysis and Design*. New York, John Wiley & Sons, 1982.

[3] I. M. Davis, J. S. Kot, C. Granet, G. Pope, and K. Verran, "Compact shaped dual-reflector system for military Ka-band SATCOM on the move," *Proc. EuCAP2011*, pp. 3518-3521, Apr. 2011.

[4] C. Kumar, V. V. Srinivasan, V. K. Lakshmeesha, and S. Pal, "Performance of an electrically small aperture, axially displaced ellipse reflector antenna," *IEEE Antennas and Wireless Propagation Letters*, vol. 8, pp. 903-904, 2009.

[5] A. P. Popov and T. Milligan, "Amplitude aperture-distribution control in displaced axis two reflector antennas," *IEEE Antennas and Propagation Magazine*, 39, pp. 58-63, 6, Dec. 1997.

[6] F. J. S. Moreira, "Design and rigorous analysis of generalized axially symmetric dual reflector antennas," Ph.D. dissertation, *Univ. of Southern California*, Los Angeles, CA, Aug. 1997.

[7] E. G. Geterud, J. Yang, T. Ostling, and P. Bergmark, "Design and optimization of a compact wideband hat-fed reflector antenna for satellite communications," *IEEE Transactions on Antennas and Propagation*, vol. 61, pp. 125-133, 2013.

[8] A. Motevasselian and T. Ostling, "A self-supported hat-fed reflector antenna for 60 GHz frequency band," in *9th European Conference on Antennas and Propagation (EuCAP)*, pp. 1-4, 2015.

[9] F. J. S. Moreira and A. Prata, Jr., "Generalized classical axially symmetric dual-reflector antennas," *IEEE Transactions on Antennas and Propagation*, vol. 49, no. 4, pp. 547-554, Apr. 2001.

[10] C. Granet, "A simple procedure for the design of

classical displaced-axis dual reflector antennas using a set of geometric parameters," *IEEE Antennas Propag. Mag.*, vol. 41, pp. 64-72, Dec. 1999.

[11] International Center for Numerical Methods in Engineering (CIMNE). http://www.gidhome.com/

[12] R. F.Harrington, *Time Harmonis Electromagnetic Fields*. New York: McGraw-Hill, 1961.

[13] W. C. Chew, J. M. Jin, and E. Michielssen, *Fast and Efficient Algorithms in Computational Electromagnetics*. Boston: Artech House, 2001.

[14] T. F. Eibert, "A diagonalizied multilevel fast multipole method with spherical harmonics expansion of the k-space integrals," *IEEE Trans. Antenna Propagat.*, vol. 53, no. 2, pp. 814-817, Feb. 2005.

[15] A. Tzoulis and T. F. Eibert, "A hybrib FEBI-MLFMM-UTD method for numerical solutions of electromagnetic problems including arbitrarily shaped and electrically large objects," *IEEE Trans. Antenna Propagat.*, vol. 53, pp. 3358-3366, Oct. 2005.

[16] Ismatullah and T. F. Eibert, "Surface integral equation solutions by hierarchical vector basis functions and spherical harmonics based multilevel fast multipole method," *IEEE Trans. Antenna Propagat.*, vol. 57, no. 7, pp. 2084-2093, July 2009.

[17] S. M. Rao, D. R. Wilton, and A. W. Glisson, "Electromagnetic scattering by surfaces of arbitrary shape," *IEEE Trans. Antennas Propagat.*, vol. 30, no. 3, pp. 409-418, May 1982.

[18] R. Coifman, V. Rokhlin, and S. Wandzura, "The fast multipole mathod: A pedestrian prescription," *IEEE Antenna and Propagation Magazine*, vol. 35, pp. 7-12, 1993.

[19] J. M. Song and W. C. Chew, "Multilevel fast multipole algorithim for solving combined field integral equations of electromagnetic scattering," *Microwave Opt. Technology Letters*, vol. 10, no. 1, pp. 14-19, Sep. 1995.

[20] T. Wan, R. Chen, X. Hu, Y. Chen, and Y. Sheng, "Efficient direct solution of EFIE for electrically large scattering problems using H-LDLT and PE basis function," *ACES Journal*, vol. 26, no. 7, pp. 561-571, July 2011.

[21] S. Karimkashi and J. Rashed-Mohassel, "Sidelobe reduction in symmetric dual-reflector antennas using a small lens antenna," *Intl. Symp. of Microwave, Antenna, Propagation and EMC Technologies for Wireless Communications*, pp. 703-705, Aug. 2007.

Ismatullah received M.Sc. in Physics from the University of the Punjab, Lahore, Pakistan in 1999 and Dr.-Ing. from Technische Universität München,Munich, Germany in 2010. He is employed as a Scientist in SUPARCO. Together with Prof. T. F. Eibert he also received the "Best Antennas Paper Prize" of the EuCAP'2007 Conference. Numerical techniques in computational electromagnetics, antenna design, analysis and measurement are his major areas of interest.

Ghulam Ahmad is currently working towards his Ph.D. degree in mm-Wave High Gain Smart Antennas at Surrey Space Center, University of Surrey. He is the recipient of SSC-NPL mm-Waves Research Grant. In the past he was working as Communication Satellite Payload Engineer at the National Space Agency of Pakistan for more than a decade where he held various technical and management roles including Antenna Design Engineer, Antenna System Engineer, Payload System Engineer, and Deputy Project Manager. Ahmad is interested in electromagnetic theory, EM modelling, numerical techniques, antennas, antenna arrays, satellite antennas, satellites payloads, flight hardware qualification, and teaching.

Shafaat A.K.M. Ali received his M.Sc. degree from Delft University of Technology, Netherlands in 2007 and presently pursuing his Ph.D. from NED University of Engineering & Technology, Pakistan in the field of 'Metamaterial and Meta-surface Antenna'.

He joined SUPARCO (National Space Agency of Pakistan) in 2003 and is presently leading the 'Antenna & Passive Microwave' Research Laboratory. He is responsible for the design, development and testing of space borne and airborne antenna. He is also in charge of the Anechoic Chamber Test Facility. His current research work includes characterization of synthetic polymers that can be used as a meta-surface.

Compact Zeroth-order Resonance Loaded Microstrip Antenna with Enhanced Bandwidth for Wireless Body Area Networks/Brain Activity Detection

Kai Sun [1], Lin Peng [1,2,*], Quan Li [1], Xiaoming Li [1], and Xing Jiang [1]

[1] Guangxi Key Laboratory of Wireless Wideband Communication and Signal Processing
Guilin University of Electronic Technology, Guilin, Guangxi, 541004, China
[*]penglin528@hotmail.com, jiang_x@guet.edu.cn

[2] Guangxi Experiment Center of Information Science, Guilin, 541004, Guangxi, China
penglin528@hotmail.com

Abstract ― A novel bandwidth enhanced compact microstrip antenna for wireless body area networks (WBANs) applications is designed by loading zeroth-order resonator (ZOR) structure. The broadband was realized by combining the ZOR resonant frequency with the microstrip patch resonant frequency. The patch dimensions of the antenna are $0.212\lambda c \times 0.310\lambda c \times 0.027\lambda c$, where λc is the wavelength of the lower cutoff frequency. By using the ZOR, the bandwidth of the proposed antenna increased by 150% compared to the reference microstrip antenna. The proposed antenna was fabricated. The measured and simulated the -10 dB $|S_{11}|$ bandwidth are 5.5% (2.352-2.485 GHz) and 6.7% (2.320-2.481 GHz), respectively. Thus, the antenna covers the medical BAN (MBAN) band (2.36-2.4 GHz) and the 2.4–2.48 GHz Industrial, Scientific and Medical (ISM) band. From the simulated and measured results, both the microstrip patch mode and the ZOR mode of the proposed antenna radiate uni-directionally. The gains of the antenna are 2.56 dBi and 4.54 dBi at the ZOR mode and microstrip patch mode, respectively. The off-body characteristics of the antenna were investigated and compared with the free-space characteristics. As the antenna was mounted as off-body, the simulated and measured impedance bandwidths of the antenna are 5.5% (2.352-2.484 GHz) and 4.7% (2.35-2.465 GHz), respectively. Although the bandwidths are reduced, the ISM band and the MBAN band are still covered. Though the antenna with tissue backing has increased back radiation, good uni-directionally radiation patterns are also observed. The robust off-body performances reveal that the proposed antenna is a good candidate for WBAN applications. In addition, to evaluate its safety for brain activity detection, the electromagnetic radiation energy of antennas was considered and the safety performance of the antenna is studied by measuring the value of specific absorption rate (SAR).

Index Terms ― Band-width, brain activity detection, compact, off-body performance, SAR, wireless body-area network (WBAN), ZOR.

I. INTRODUCTION

In recent years, tremendous advancements have been developed in the field of body area network (BAN) electromagnetics, and revolutionary functionalities were achieved for the health monitoring, patient tracking, physiotherapy, wearable computing, battlefield survival, the Internet of Things (IoT), and so on. Thereby, BAN technology holds great promising for the revolutionizing of many aspects of the daily life of human beings [1-4], such as real-time online healthcare, patients can be tracked and monitored in normal or emergency conditions at their homes, hospital rooms, and in Intensive Care Units (ICUs). Typically, the type of communication within a WBAN can be classified into three modes, including on-body, in-body (or sometimes called through-body), and off-body communications [5]. Thus, the antennas applied on the WBAN require radiation pattern normal to the body surface and a smaller size. The frequency bands for BAN communication systems mainly include the 402–405 MHz Medical Implant Communication Services (MICS) band [5-6] that are primarily used for on-body and through-body communications, the 2.4–2.48 GHz Industrial, Scientific, and Medical (ISM) band [5, 7] as well as the 3.1–10.76 GHz Ultra-Wide Band (UWB) range [5, 8] that are primary used for off-body communication, and the medical BAN (MBAN) band that operates from 2.36 GHz to 2.4 GHz [5, 9]. As a vital component of WBAN, the antenna is very close to the human body, and it is required with the characteristics of lightweight, low profile and small size [3]. However, the performances of an antenna could be impaired by the loading effect of the loss of the tissue. Many antennas have been studied for WBAN applications, including monopole antennas [10], inverted-F antennas [11-12], microstrip patch antennas [13], artificial magnetic conducting surface

Submitted On: November 21, 2017
Accepted On: April 21, 2018

backed antennas [14] and so on. In [10], the vertical monopole antennas with narrow band and high-profile are studied for on-body communications. Reference [11] presents a broadband textile planar inverted-F antenna (PIFA), and [12] presents a dual-band Sierpinski fractal PIFA, and the antennas require complex 3-dimensional and thicker structures. Reference [13] utilizes microstrip patch antenna to statistical analyze the performance of on-body radio propagation, and the antenna is narrow bandwidth. In [14], a dual-band coplanar patch antenna integrated with an electromagnetic band gap substrate is described. The electromagnetic band-gap (EBG) substrate provides a high isolation between the antenna and human tissue, and the antenna covers the 2.45 GHz and 5.8 GHz wireless bands. However, the antenna still suffered from low front-to-back ratio (FBR). To obtain further compact antenna size, a novel zeroth-order resonance (ZOR) antenna with a spiral slotted ground plane was proposed in [15]. Though, the antenna in [15] is miniaturized, its bandwidth is very narrow. Moreover, multiband and broadband antennas are preferable options for multiple functions [16-17]. In [17], a miniaturized omnidirectional antenna has two bands, the 403.5 MHz for medical implant communication services (MICS) and the 2.45 GHz for industrial, scientific, and medical (ISM) applications. However, the antenna has complicated structure and increased profile as it consists of two-stacked center-fed circular patch over a circular ground plane. In recent years, the wearable technology has been developed rapidly [18], then, the public is paying more and more attention to the electromagnetic radiation problems of wireless terminals. Under the action of electromagnetic field, the body will produce induction electromagnetic fields as various organs are lossy medium, which lead to electromagnetic energy absorption and dissipation, and then, it is necessary to study the specific absorption rate (SAR) value to evaluate the security performance of the wireless device [19].

The traditional microstrip antennas were widely used because they have many advantages of other antennas, such as low profile, light weight, low cost and easy construction [20]. However, the microstrip antennas have a shortage of narrow bandwidth (typically 2%), and the narrow bandwidth could be a limitation for its applications in WBAN. In order to overcome the shortcoming of narrow bandwidth, bandwidth broadening microstrip antenna technologies had been studied. The most common methods for increasing the bandwidth of the microstrip antenna are shown as follows. The technique of low Q value by low permittivity (air gap), thick substrate and capacitive feeding are used to enhance bandwidth [21], [22]. Multi-layer structure technology and fold structure technology in [23] and [24] lead to high profile and complex structure. Metamaterials in [25] greatly increase the bandwidth of the antenna. In [26], new zeroth-order resonators (ZORs) were utilized as parasitic elements to enhance bandwidth of the microstrip antenna. By utilizing one, two and three resonators, extra corresponding numbers of resonances were generated, by merging the resonances of the resonators with that of the microstrip antenna, the measured impedance bandwidth can be increased from 56 MHz of the reference microstrip antenna to 101, 120, and 133 MHz of the ZORs loaded antennas. However, the parasitic elements lead to antenna size enlargement.

In this article, a novel ZOR-loaded compact microstrip antenna with enhanced bandwidth was proposed for the ISM/MBAN bands and for the brain activity detection in this paper. The wideband performance is achieved by combining the ZOR resonance with the microstrip patch resonance. As the ZOR structure is placed in the interior of the microstrip patch, the antenna size is unchanged with operational frequency decreasing, and the microstrip patch mode still operates good performances. The proposed antenna was measured both in free space and with pork, and reliable off-body performance is achieved. The ZOR antenna has a 150% increasing in the bandwidth compared to the microstrip antenna. In free-space, the simulated and measured -10 dB $|S_{11}|$ bandwidths are 6.7% (2.320-2.481GHz) and 5.5% (2.352-2.487GHz), respectively. As the antenna was mounted as off-body, the simulated and measured impedance bandwidths of the antenna are 5.5% (2.352-2.484 GHz) and 4.7% (2.35-2.465 GHz), respectively. Thus, the antenna meets the MBAN band and the ISM band. The gains at the ZOR mode and microstrip patch mode of the proposed antenna were 2.56 dBi and 4.54 dBi, respectively. In our previous researches for the brain activity detection, antennas were required to radiate face to the head [27-29], and electromagnetic safety would be an issue. Then, (SAR) values of the antenna were calculated by installing the antenna around a human head. Research found that, the antenna radiation meets the health and safety requirements with very small SAR as its backside face the head. While the antenna is installed with its front side face to the brain, 28 mm distance between the brain and the antenna is required.

II. ANTENNA DESIGN AND ANALYSIS

The configurations of the proposed antenna as well as its equivalent circuit were shown in Fig. 1. The proposed antenna consists of two components, a microstrip patch fed by coaxial probe and a ZOR structure embedded in the microstrip patch. The antenna has a substrate dimensions 50mm × 60mm × 1.6mm ($0.384\lambda c \times 0.461\lambda c \times 0.027\lambda c$) and the size of the patch is 28mm × 40mm × 1.6mm ($0.212\lambda c \times 0.310\lambda c \times 0.027\lambda c$). The ZOR's size is only 9mm × 10mm ($0.069\lambda c \times 0.076\lambda c$). Owing to the zero phase constant (β=0) feature of the ZOR, its size can be very small. Then, the ZOR was embedded in the patch, which makes the size and

profile of the proposed antenna is not increased with bandwidth increasing. In this configuration, the bend line acts as a series inductance L_R and the gaps between bend line and the patch generates series capacitance C_L. Since the Q-factor of the resonator is determined by the series inductance and capacitance, the resonant frequency of the ZOR is related to the bending line and the gaps. The proposed antenna was fabricated on a FR4 substrate with a permittivity of 4.4 and thickness of 1.6 mm. The parameters of the antenna are shown below: L_0=50mm, W_0=60, L=28, W=40, a=9, b=10, T=4.5, m=3.3, H_t=2, d=0.6, L_d=0.6, S=4 (unit: mm).

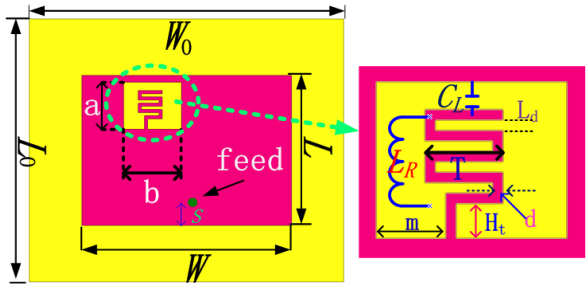

Fig. 1. Configurations of the antenna and its equivalent circuit.

The impedance matching characteristics of the proposed antenna and the reference microstrip antenna (RMA) were compared as shown in Fig. 2. It can be clearly seen that the proposed antenna has an extra ZOR resonance compared to the RMA. Then, the bandwidth of the proposed antenna is increased by 150% compared to the RMA, which completely covers the MBAN and band the ISM band.

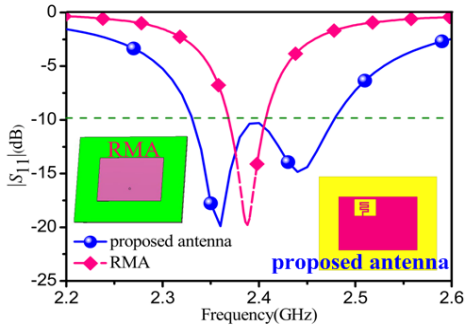

Fig. 2. The simulated $|S_{11}|$ of the proposed antenna and RMA.

ZOR resonances include mu-zero resonator (MZR) and epsilon-zero resonator (EZR) that related to the series and shunt tanks of a composite left and right hand transmission line (CRLH-TL) as shown in Fig. 3 [30-32]. Equations (1) and (2) are the resonant frequencies of the series and shunt tanks, respectively:

$$\omega_{se} = \frac{1}{\sqrt{L_R C_L}}, \tag{1}$$

$$\omega_{sh} = \frac{1}{\sqrt{L_L C_R}}. \tag{2}$$

And the constitutive parameters of the CRLH TL are calculated by Equations (3) and (4):

$$\mu(\omega) = \frac{2Z_B}{j\omega} \bullet \frac{1}{d} = \frac{\left(\frac{\omega}{\omega_{se}}\right)^2 - 1}{\omega^2 C_L} = L_R - \frac{1}{\omega^2 C_L}, \tag{3}$$

$$\varepsilon(\omega) = \frac{Y_B}{j\omega} \bullet \frac{1}{d} = \frac{\left(\frac{\omega}{\omega_{sh}}\right)^2 - 1}{\omega^2 L_L} = C_R - \frac{1}{\omega^2 L_L}. \tag{4}$$

It is found from Equation (3) that the permeability μ is determined by the series tank and it equals zero at the resonance ω_{se}. From the Equation (4), the permittivity ε equals zero at the resonance ω_{sh}. That mean MZR is corresponded to μ = 0, and EZR is related to ε = 0.

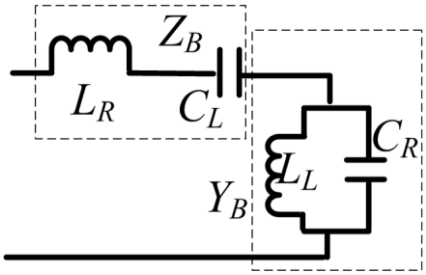

Fig. 3. The equivalent circuit of CRLH-TL.

To verify the ZOR feature of the embedded resonator, the constitutive parameters of the resonator were retrieved by a Kramers-Kroning relationship based metamaterial parameters extraction method [33]. The retrieved method requires the calculation of S parameters. Then, an appropriate simulation model is required to explore the ZOR. As demonstrated in the inset of the Fig. 4, a microstrip line based model was built. A microstrip line has similar field distributions to a microstrip antenna, then, microstrip line based model imitates the operational environment of the ZOR in the microstrip antenna. The microstrip line model used the same substrate as the designed antennas. Figure 4 exhibits the constitutive parameters curves of the ZOR. As shown in the figure, resonance is occurred for the ZOR as large mutations is happened for the effective permittivity (ε_{reff}) and effective permeability (μ_{reff}) curves. For the ZOR, the ε_{reff} is positive in the whole operating band. While the μ_{reff} obtains zero value around 2.35. It can be judged that the embedded structure is a ZOR (MZR) resonator.

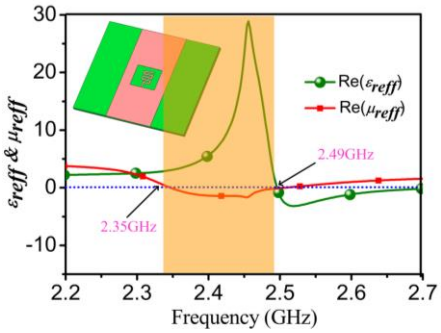

Fig. 4. The simulated dielectric constant and permeability of ZOR structure.

To further reveal the resonances, the impedance curves and the electric field intensity distributions of the proposed antenna were plotted in Fig. 5. From Fig. 5, the antenna has two resonant points. The lower one is the ZOR resonance and the higher one is the microstrip patch resonance. The two resonant points merge with each other wand imply a wide impedance bandwidth. The electric field intensity distributions for the two resonances of the antenna were demonstrated as insets in Fig. 5. At the lower resonance, the electric field is mainly concentrated on the bending line (ZOR structure). At the higher resonance, the electric field is mainly focused on the microstrip patch.

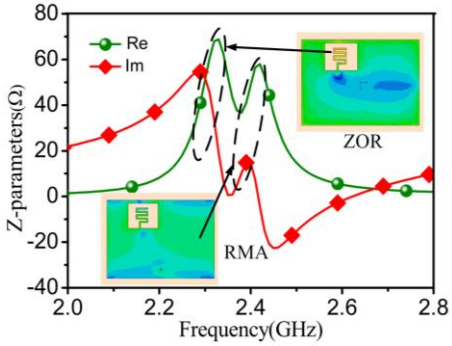

Fig. 5. The electric field intensity distributions and impedance curves of the proposed antenna.

The antenna was fabricated on a 1.6-mm-thick FR4 substrate with a dielectric constant of 4.4 and loss tangent of 0.02. A photograph of the fabricated antenna is shown in Fig. 6 (a). The simulated and measured $|S_{11}|$ of the proposed antenna is shown in Fig. 6 (b). It can be clearly seen that the simulated result is in good agreement with the measured one. Both the measured and simulated -10 dB $|S_{11}|$ bandwidth cover the MBAN band (2.36-2.4 GHz) and the ISM (2.4-2.48 GHz) band completely. In free space, the measured and simulated bandwidths are 133 MHz (2.352-2.485 GHz) and 161 MHz (2.320-2.481 GHz), respectively.

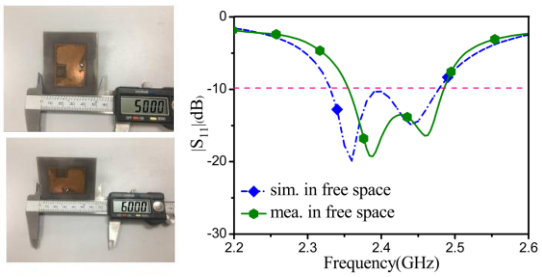

Fig. 6. Photograph of: (a) the fabricated antenna, and (b) the simulated and measured $|S_{11}|$ in free space.

To further investigate the characteristics of the proposed antenna and reveal the independently adjustment of the resonant frequencies, parametric studies were conducted. As shown in Fig. 7, the parameters T and H_t were swept. From Fig. 7 (a), by increasing the parameter T from 4mm to 5.5mm with a step of 0.5mm, the resonance point of ZOR reduce from 2.50 GHz, to 2.35 GHz, 2.25GHz and 2.15 GHz, while microstrip antenna resonant point (MPR) is almost unchanged. Similarly, from Fig. 7 (b), as the height H_t of the ZOR structure increased from 2mm to 3mm with a step of 0.5mm, the ZOR resonant point of the antenna decreased from 2.35 GHz, to 2.30 GHZ and 2.26 GHz, while the MPR was little affected. Thus, it is confirmed that the ZOR resonant point is affected by the parameters of ZOR structure, and the resonant frequencies can be adjusted independently.

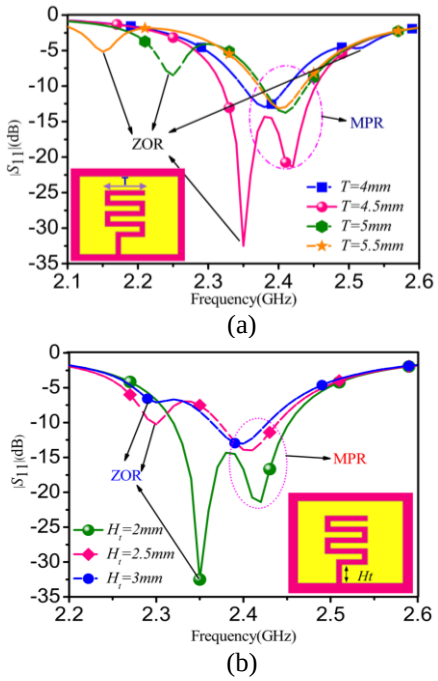

Fig. 7. The simulated $|S_{11}|$ for antenna parameters: (a) T and (b) H_t.

III. ANTENNA OFF-BODY PERFORMANCE

The off-body performances of the antenna was analyzed and compared to the free space performances. In particular, the antenna was simulated under the human equivalent tissue and measured with human arm and pork.

To analyze the off-body performance of the proposed antenna with simulation, the equivalent environment of human tissues should be used. The physical electrical parameters of the human body (tissue) were shown in Table 1 [34-35]. The relative dielectric constant ε_r and loss tangent of human tissue decreased with the frequency increasing. However, the relative conductivity σ increased as the frequency increasing [35]. As the proposed antenna is working at 2.36-2.4 GHz (MABN) and 2.40-2.48 GHz (ISM) bands, the equivalent physical electrical parameters of the tissue in 2.38 GHz and 2.45 GHz were presented in Table 1.

Table 1: Physical electrical parameters of the tissue [34, 35]

Target Frequency (MHz)	Muscle		
	Conductivity [S/m]	Relative Permittivity	Loss Tangent
402-405 (MICS)	0.797	57.106	0.622
600	0.850	55.960	0.455
2360-2400 (MBAN)	1.689	52.820	0.242
2400-2480 (ISM)	1.722	52.760	0.241

In this research, the electrical parameters of the equivalent arm muscles were selected. The equivalent human muscle tissue size is 100mm × 150mm × 50mm. The proposed antenna has a 5mm distance from the tissue to imitate the off-body environment [36]. As the tissue parameters are different for the MBAN and the ISM bands, two equivalent models were established as shown in Fig. 8. In Fig. 8 (a), the equivalent electrical parameters are ε_r=52.820, σ=1.689s/m, tan δ=0.242 for the MBAN band. While in Fig. 7 (b), the physical electrical parameters of the tissue are ε_r=52.760, σ=1.722s/m, tan δ=0.241 for the ISM band.

The results of the simulation and measurement of the fabricated antenna on the free-space and off-body were plotted in Fig. 9. As shown in the figure, in free-space, the simulated and measured $|S_{11}|$ are 2.320-2.481 GHz and 2.352-2.485 GHz, respectively. As the antenna was mounted as off-body, the simulated -10 dB $|S_{11}|$ band is 2.325-2.475 GHz with tissue parameters set at the MBAN band as shown in Fig. 8 (a), while the simulated -10 dB $|S_{11}|$ band for tissue parameters set at the ISM band as shown in Fig. 8 (b) is 2.352-2.484 GHz. Then, both the simulated -10 dB $|S_{11}|$ bands for the tissue parameters settings almost cover the MBAN and the ISM bands. The measured -10 dB $|S_{11}|$ band with the antenna above an arm is 2.35-2.465 GHz. It is found that two resonances were observed for both the free-space and off-body environments.

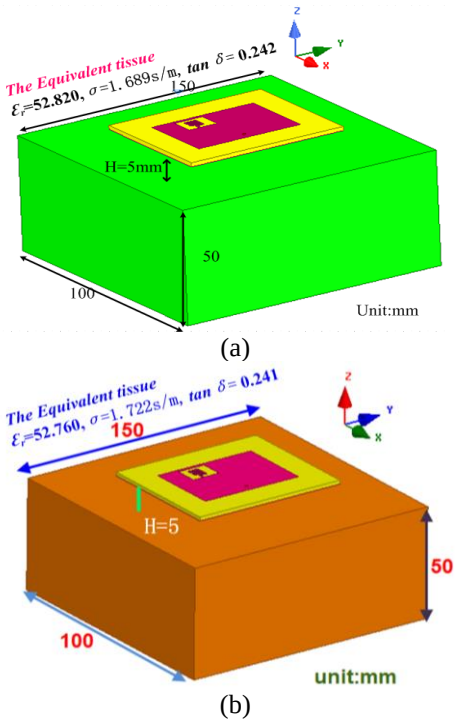

Fig. 8. The model of the proposed antenna and equivalent muscle tissue: (a) at the MABN, and (b) at the ISM.

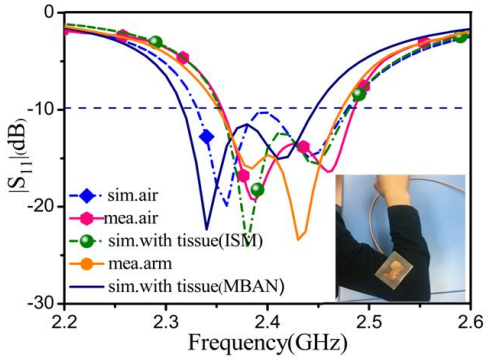

Fig. 9. Simulation and measured $|S_{11}|$ in free-space and the equivalent tissue.

The radiation patterns of the proposed antenna were measured by the NSI2000 system in a microwave anechoic chamber as shown in Fig. 10 (a). Both the patterns in free-space (air) and off-body (pork) were measured [37]. Only half space was measured due to the limitation of the NSI2000 system, and it is enough to verify the simulated results. Radiation patterns of the fabricated antenna were measured at the resonant

frequencies of 2.38 GHz (ZOR) and 2.45 GHz (MPR) as shown in Figs. 10 (b) and (c). The simulated results were also plotted in the figures for comparison. The simulated and measured results show reasonable agreement. As shown in Fig. 10 (b), at 2.38 GHz, the simulated and measured E-plane (xoz-plane φ=0) and H-plane (yoz-plane φ=90°) have good uni-directionally radiation patterns for both the free-space and off-body environments, though the back radiation for off-body environment is larger. At 2.45 GHz, the radiation patterns are similar to 2.38 GHz as shown in Fig. 10 (c). As the size of the ZOR structure is very small, its antenna gain is 2.56 dBi at 2.38 GHz, while the antenna gain for the MPR frequency (2.45 GHz) is 4.54 dBi. In Fig. 10 (d), the antenna efficiency of the RMA is larger than 80%, and the antenna efficiency of the proposed antenna is not bad in the band, such as 70%, though the efficiency drops a few near the ZOR mode. It is clear from Fig. 10 that the proposed antenna maintains good radiation performance both in free-space and off-body. The proposed antenna has relatively stable uni-directional radiation patterns under different environments. The robust off-body performances reveal that the proposed antenna is a good candidate for WBAN applications.

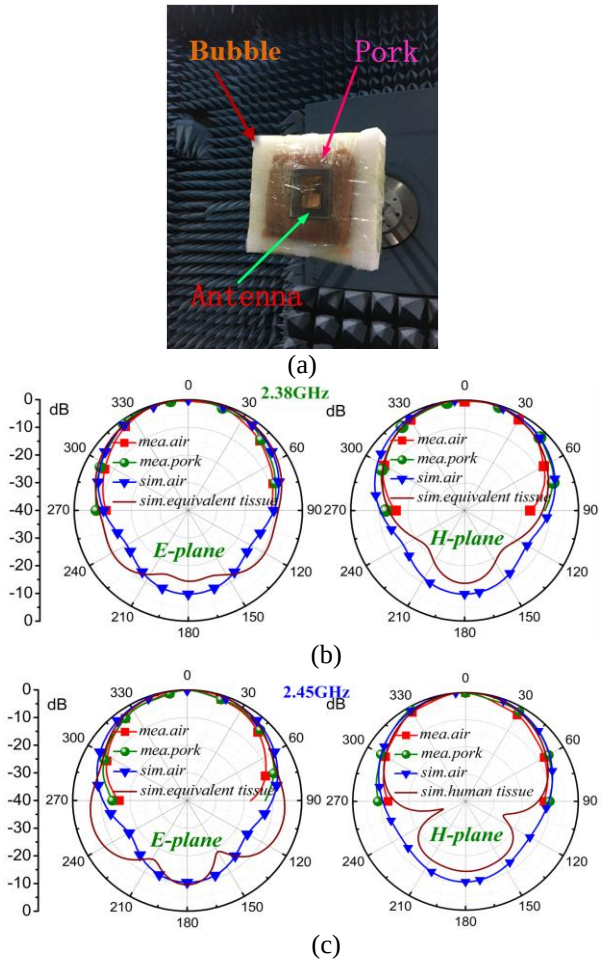

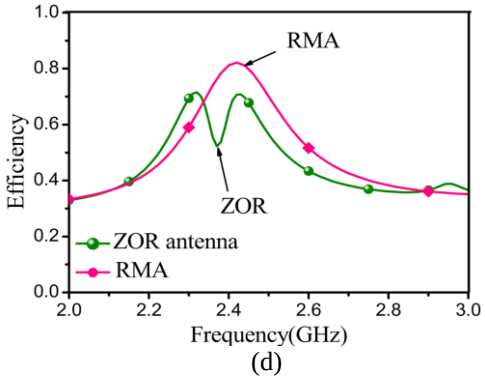

Fig. 10. Simulated/measured radiation patterns in the E-plane and H-plane in free-space and off-body: (a) measurement environment, (b) 2.38 GHz, (c) 2.45 GHz, and (d) efficiencies.

In recent years, there are many studies aiming at abnormal tissue detection such as early breast cancer detection and stroke detection [38, 39] and brain activity detection [27, 28, 29]. For these applications, the SAR level of the antenna needs to be analyzed in the design stage to ensure that the safety limit is obeyed. According to the guidelines of the FCC and the CNIRP, the SAR must not be larger than 2 W/kg averaged over 10g and not greater than 1.6W/kg averaged over 1g of human tissues [40, 41]. The calculated equation for SAR is:

$$SAR = \frac{d}{dt}\left(\frac{dW}{dm}\right) = \frac{d}{dt}\left(\frac{dW}{\rho dV}\right), \quad (5)$$

where W is radiative energy, m is r mass, V is volume and ρ denotes density.

SAR is divided into local SAR and mean SAR. In general, we focus on local SAR, and local SAR values can be obtained by:

$$SAR = \frac{\sigma E}{\rho}, \quad (6)$$

σ is the conductivity, E is the electric field intensity, ρ denotes density.

The input power of 1W is selected as a benchmark to calculate the SAR. The calculation of the SAR and electric field intensity were conducted by the HFSS software. Figures 11 (a) and (b) describe the distribution of electric field intensity for the antenna back size and front size to the antenna, respectively. The SARs with the back size and front size of the antenna to the head were plotted in Figs. 12 (a) and (b), respectively. As shown in Fig. 11 (a) and Fig. 12 (a), when the antenna was back to the brain, the SAR values of the antenna are much smaller than the safety requirement. As shown in Fig. 11 (b), more electromagnetic energy radiates into the brain when the antenna front size to the brain. As shown in Fig. 12 (b), the distance between the antenna and the brain should be larger than 28mm to meet the SAR safety standard.

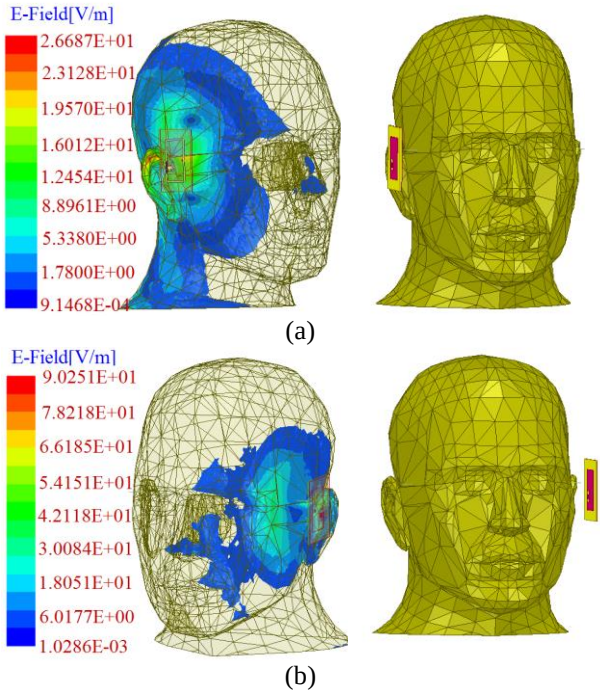

Fig. 11. The distribution of electric field intensities in different situations of the simulation: (a) back and (b) face.

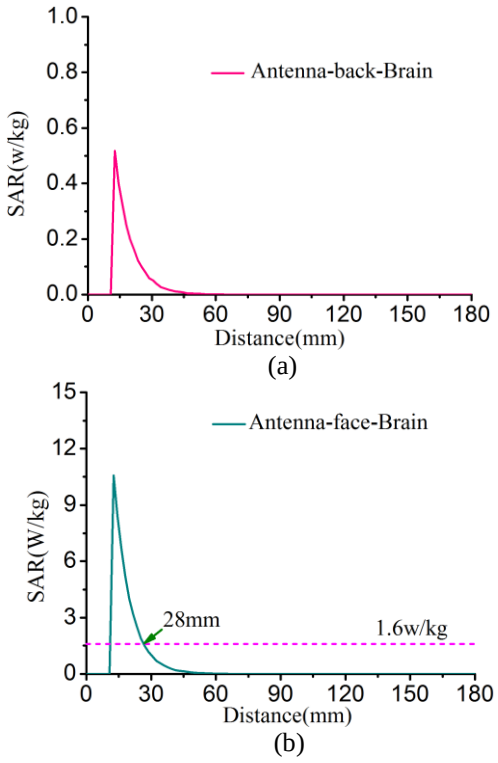

Fig. 12. The antenna of SAR in different situations of the simulation: (a) back and (b) face.

IV. CONCLUSION

In this paper, a novel compact bandwidth enhanced microstrip antenna is designed by loading zeroth-order resonator. The ZOR structure was embedded in the microstrip patch, and the bandwidth of the antenna increased as the adding ZOR resonance. The bandwidth of the antenna increased by 150% compared to the RMA, and it is wide enough to meet the MBAN band and the ISM band. The proposed antenna performances such as reflection characteristic and radiation patterns are examined both in free-space and off-body environments. Robust measured off-body performances were achieved and agree well with the simulation results. The gains of 2.56 dBi and 4.54 dBi were obtained at ZOR frequency and MPR frequency, respectively. The broadband, uni-directional and miniaturization are major advantages that make the proposed antenna can be well applied to WBAN systems. The SAR characteristics of the antenna were also discussed for brain activity detection.

ACKNOWLEDGMENT

This work was supported in part by National Natural Science Foundation of China under Grant Nos. 61661011, 61401110 & 61761012, in part by Natural Science Foundation of Guangxi under Grant No. 2015GXNSFBA139244, in part by Innovation Project of GUET Graduate Education under Grant No. 2017YJCX30, and in part by the project of the basic ability enhancement of Guangxi young teachers under Grant No. 2017KY0204.

REFERENCES

[1] P. S. Hall and Y. Hao, *Antennas and Propagation for Body-Centric Wireless Communications*. Norwood MA, USA: Artech House, 2006. ISBN: 9781608073764.

[2] S. Park and S. Jayaraman, "Enhancing the quality of life through wearable technology," *IEEE Eng. Biol. Mag.*, vol. 22, no. 3, pp. 41-48, 2003.

[3] P. S. Hall, Y. Hao, Y. I. Nechayev, and A. Alomainy, "Antennas and propagation for on-body communication systems," *IEEE Antennas Propag. Mag*., vol. 49, pp. 41-58, 2007.

[4] Y. Peng, X. Wang, L. Guo, Y. Wang, and Q. Deng, "An efficient network coding-based fault-tolerant mechanism in WBAN for smart health-care monitoring systems," *Applied Sciences*, vol. 7, no. 8, pp. 817-835, 2017.

[5] Z. H. Jiang, T. W. Yue, and H. Douglas, *Meta-material-Enabled and Microwave Circuit Integrated Wearable Antennas for Off-body Communications*. in Electromagnetics of Body Area Networks: Antennas, Propagation, and RF Systems, by *Wiley-IEEE Press*, pp. 27-59. 2016.

[6] Federal Communications Commission (FCC): The Medical Implant Communication Services (MICS). Available at: http://wireless.fcc.gov/services/personal/medicalimplant/

[7] IEEE 802.11 Wireless LAN Working Group. Available at: http://www.ieee802.org/11/

[8] FCC, "Federal Communications Commission Revision of Part 15 of the Commission's Rules Regarding Ultra-Wideband Transmission Systems," FCC First Report and Order FCC, April 2002.

[9] Low-Rate Wireless Personal Area Networks (LR-WPANs) Amendment 4, IEEE Standard 802.15.4j-2013.

[10] Y. I. Nechayev, P. S. Hall, and Z. H. Hu, "Characterization of narrowband communication channels on the human body at 2.45 GHz," *IET Microw. Antennas Propag.*, vol. 4, no. 6, pp. 722-732, 2010.

[11] P. J. Soh, G. A. E. Vandenbosch, S. L. Ooi, and N. M. A. Rais, "Design of a broadband all-textile slotted PIFA," *IEEE Trans. Antennas Propag.*, vol. 60, no. 1, pp. 379-384, 2012.

[12] P. J. Soh, G. A. E. Vandenbosch, S. L. Ooi, and M. R. N. Husna, "Wearable dual-band Sierpinski fractal PIFA using conductive fabric," *Electron. Lett.*, vol. 47, no. 6, pp. 365-367, 2011.

[13] A. Alomainy, Y. Hao, A. Owadally, C. G. Parnini, Y. Nechayev, C. C. Constantinou, and P. S. Hall, "Statistical analysis and performance evaluation for on-body radio propagation with microstrip patch antennas," *IEEE Trans. Antennas Propag*., vol. 55, no. 1, pp. 245-248, 2007.

[14] S. Zhu and R. Langley, "Dual-band wearable textile antenna on an EBG substrate," *IEEE Trans. Antennas Propag*., vol. 57, no. 4, pp. 926-935, 2009.

[15] S. Baek and S Lim, "Miniaturised Zeroth-order antenna on spiral slotted ground plane," *Electron. Lett*., vol. 45, no. 20, pp. 1012-1014, 2009.

[16] Z. G. Liu and Y. X. Guo, "Dual band low profile antenna for body centric communications," *IEEE Trans. Antennas. Propag*., vol. 61, no. 4, pp. 2282-2285, 2013.

[17] S. Chamaani and A. Akbarpour, "Miniaturized dual-band omnidirectional antenna for body area network basestations," *IEEE Antennas and Wireless Propagation Letters*, vol. 14, pp. 1722-1725, 2015.

[18] B. W. An, J. H. Shin, S. Y. Kim, J. Kim, S. Ji, J. Park, et al., "Smart sensor systems for wearable electronic devices," *Polymers*, vol. 9, no. 8, pp. 303-344, 2017.

[19] A. Y. I. Ashyap, Z. Z. Abidin, S. H. Dahlan, H. A. Majid, S. M. Shah, M. R. Kamarudin, et al., "Compact and low-profile textile EBG-based antenna for wearable medical applications," *IEEE Antennas & Wireless Propagation Letters*, pp. 99-102, 2017.

[20] A. Sabban, "New wideband printed antennas for medical applications," *IEEE Trans. Antennas Propag*., vol. 61, pp. 84-91, 2013.

[21] A. K. Verma and Nasimuddin, "Resonance frequency of rectangular microstrip antenna on thick substrate," *Electronics Letters*, vol. 37, no. 2, pp. 1373-1374, 2001.

[22] L. Peng, C. L. Ruan, and X. H. Wu, "Design and operation of dual/triple-band asymmetric M-shaped microstrip patch antennas," *IEEE Antennas Wireless Propag. Lett*., vol. 9, no. 1, pp. 1069-1072, 2010.

[23] L. Peng, J. Y. Xie, and S. M. Li, "Wideband microstrip antenna loaded by elliptical rings," *Journal of Electromagn. Waves Appl.*, vol. 30, no. 2, pp. 154-166, 2016.

[24] D. Guha, C. Sarkar, S. Dey, and C. Kuma, "Wide-band high gain antenna realized from simple unloaded single patch," *IEEE Trans. Antennas Propag*., vol. 63, no. 10, pp. 4562-4566, 2015.

[25] Md. Mahmud, M. Islam, N. Misran, M. Singh, K. Mat, "A negative index metamaterial to enhance the performance of miniaturized UWB antenna for microwave imaging applications," *Applied Sciences*, vol. 7, pp. 1149-1165, 2017.

[26] L. Peng, J. Y. Mao, X. F. Li, X. Jiang, and C. L. Ruan, "Bandwidth of microstrip antenna loaded by parasitic zeroth-order resonators," *Microwave and Optical Technology Letters*, vol. 59, no. 5, pp. 1096-1100, 2017.

[27] X. Jiang, B. Kang, X. M. Li, and L. Peng, "Microwave technology for brain activities detection of rats," *International Symposium on Antennas, Propagation and EM Theory IEEE*, pp. 918-920, 2017.

[28] X. Jiang, X. B. Jiang, L. Peng, and X. M. Li, "Microwave transmission approach for human neuronal activities detection," *IEEE International Conference on Microwave and Millimeter Wave Technology IEEE*, pp. 485-487, 2016.

[29] X. Jiang, Z. Geng, X. M. Li, L. Peng, B. Kang, and C. J. Zheng. "Microwave transmission approach for dynamic dielectric detection at brain functional site," *IEEE/mtt-S International Microwave Symposium - IMS IEEE*, pp. 1235-1238, 2017.

[30] A. Lai, K. M. K. H. Leong, and T. Itoh, "Infinite wavelength resonant antennas with monopolar radiation pattern based on periodic structures," *IEEE Trans. Antennas Propag*., pp. 868-876, 2007.

[31] J. H. Park, B. C. Park, Y. H. Ryu, et al., "Modified mu-zero resonator for efficient wireless power transfer," *IET Microwaves, Antennas & Propag.*, no. 8, pp. 912-920, 2014.

[32] L. Peng, J. Y. Xie, X. Jiang, and C. L. Ruan, "Design and analysis of a new ZOR antenna with wide half power beam width (HPBW) characteristic," *Frequenz*, vol. 71, no. 1-2, pp. 41-50, 2017.

[33] Z. Szabo, G. H. Park, R. Hedge, and E. P. Li, "A unique extraction of metamaterial parameters based on Kramers–Kronig relationship," *IEEE Transactions on Microwave Theory and Techniques*, vol. 58, no. 10, pp. 2646-2653, 2010.
[34] K. Chan, R. F. Cleveland, and D. L. Means, "Evaluating compliance with FCC guidelines for human exposure to radiofrequency electromagnetic fields," *Current Reviews in Musculoskeletal Medicine*, vol. 1, no. 2, pp. 88-91, 2001.
[35] IFAC, "Dielectric Properties of Body Tissues," [Online]. Available: http://niremf.ifac.cnr.it/tissprop/htmlclie/htmlclie.php
[36] J. Baek, Y. Lee, and J. Choi, "A wideband Zeroth-order resonance antenna for wireless body area network applications," *IEICE Transactions on Communications*, vol. 10, pp. 2348-235, 2013.
[37] X. Q. Zhu, Y. X. Guo, and W. Wu, "A compact dual-band antenna for wireless body-area network applications," *IEEE Antennas and Wireless Propagation Letters*, vol. 15, pp. 98-101, 2016.
[38] S. Luo, Z. Ji, S. Yang, and D. Xing, "Near-field transmission-type microwave imaging for non-invasive evaluation of electromagnetic characteristics: Towards early breast tumor detection," *IEEE Photonics Journal*, pp. 99, 2017.
[39] Md. D. Hossain and A. S. Mohan, "Cancer detection in highly dense breasts using coherently focused time reversal microwave imaging," *IEEE Trans. on Computational Imaging*, pp. 9, 2017.
[40] A. Ahlbom, U. Bergqvist, J. H. Bernhardt, J. P. Cesarini, M. Grandolfo, M. Hietanen, A. F. Mckinlay, M. H. Repacholi, D. H. Sliney, A. J. Stolwijk, "Guidelines for limiting exposure to time-varying electric, magnetic, and electromagnetic fields (up to 300 GHz)," *International Commission on Non-Ionizing Radiation Protection, Heal. Phys*., vol. 74, pp. 494-522, 1998.
[41] IEEE Recommended Practice for Measurements and Computations of Radio Frequency Electromagnetic Fields with Respect to Human Exposure to Such Fields, 100 kHz–300 GHz, IEEE Std. C95.3-2002, (Revision of IEEE Std. C95.3-1991), pp. i-126.

Kai Sun was born in Zhejiang Province, China, in 1992. He received the B.E. degree in Electronic Information from Hangzhou Dianzi University, Hangzhou, Zhejiang, China, in 2015, and he is currently pursuing a Master's degree in Electronic and Communication Engineering from Guilin University of Electronic Technology (GUET), Guangxi, China. His research interests include antennas and metamaterials.

Lin Peng was born in Guangxi Province, China, in 1981. He received the B.E. degree in Science and Technology of Electronic Information, Master and Doctor's degree in Radio Physics from University of Electronic Science and Technology of China (UESTC), Chengdu, China, in 2005, 2008 and 2013, respectively. From 2011 to 2013, he was sponsored by the China Scholarship Council (CSC) to study at the University of Houston (UH) as joint Ph.D. student. From 2013, he joint Guilin University of Electronic Technology (GUET), and became an Associate Professor from Jan. 2016.

Peng has published over 20 papers as first and corresponding author. He is also co-author with over 20 papers. In recent years, he is sponsored by several funds, such as Fundamental Research Funds for the Central Universities, National Natural Science Foundation of China, Program for Innovative Research Team of Guilin University of Electronic Technology, and Guangxi Wireless Broadband Communication and Signal Processing Key Laboratory, etc. Peng serves as Reviewer for *IEEE TMTT*, *IEEE MWCL*, *IEEE AWPL*, *ACES*, *EL*, *Wireless Personal Communications*, *Progress in Electromagnetics Research*, *IET Microwave, Antennas & Propagation*, and *Journal of Electromagnetic Waves and Applications*.

Peng's research interests include antenna/filter design (for example: communication antennas, Zeroth-Order Resonator (ZOR) antenna, circular-polarized antenna, UWB antenna, microstrip antenna and WLAN antenna), Electromagnetic Bandgap (EBG) structure design and its application in antenna, Composite Right/Left-Handed (CRLH) transmission line and its applications, and conformal antenna array.

Quan Li was born in Shanxi Province, China, in 1991. He received the B.E. degree in Electronic Information College of Electronic Information major of Shaanxi University of Technology, Hanzhong, Shanxi, China, in 2014, and the Master's degree in Electronic and Communication Engineering from Guilin University of Electronic Technology (GUET), Guangxi, China. He is currently a student at the GUET. His research interests include active antenna and dielectric resonant antenna.

Xing Jiang received the Master's degree in Electromagnetic Field and Microwave Technology from Beijing Institute of Technology (BIT), in 1986. From 2000, she joint Guilin University of Electronic Technology (GUET) as Professor. Jiang has published over 30 papers. She also sponsored by National Natural Science Foundation of China and Natural Science Foundation of Guangxi. Jiang is a Senior Member of China Communications Society, a Member of Chinese Institute of Electronics (CIE). Jiang's research interests include smart communication system design, conformal antenna array, and bio-electromagnetics.

Electromagnetic Shielding Effectiveness Calculation for Cascaded Wire-Mesh Screens with Glass Substrate

Hany M. El-Maghrabi

Institute of Electromechanical Research
Housing and Building National Research Center, Cairo, Egypt
helmaghrabi@hbrc.edu.eg

Abstract ─ In this paper, a model is presented to calculate the electromagnetic shielding effectiveness of two cascaded wire-mesh sheets with glass substrate. The model is based on transmission line theory for calculating the equivalent sheet impedance of each wire-mesh screen. The total shielding effectiveness for the sheets is obtained based on transmission matrix method. The wire-mesh screen is numerically simulated as a unit cell with periodic boundary conditions in order to verify the analytical results. It is shown that the shielding effectiveness is decreased by increasing the operating frequency. Also, it is shown that the total shielding effectiveness of the double wire-mesh layers is satisfactory high compared with single sheet shielding. The proposed structure is highly attractive for different shielding applications due to its lower cost, reduced weight and optical transparency compared to metallic sheets. The model results are compared with measurements. Good agreement between the analytical model and the measurements results is obtained.

Index Terms ─ Electromagnetic shielding, transmission line theory, wire-mesh screens.

I. INTRODUCTION

The increased usage and wide spreading of electronic equipment in communications, broadcasting and other purposes have led to a lot of Electromagnetic Interference (EMI) problems [1-12]. The cause of the EMI can be due to telecommunications towers, radar stations with high radiated power and wireless systems which emit electromagnetic waves [10-11]. One of the main concerns which should be considered for protection from EMI is the threat of Intentional Electromagnetic Interference (IEMI) [12-13]. IEMI is the intentional usage of high electromagnetic energy to cause damage to the electronic systems and is considered a big threat to critical infrastructure [14]. Another concern for people who need to work at a certain frequency band is likely to experience severe electromagnetic interference from external sources which is difficult to suppress it [15]. Also, people who are living in the vicinity of telecommunication mobile stations are exposed to high electromagnetic power which can cause dangerous health problems [6-9]. To ensure that electronics devices operate well in the presence of external electromagnetic interference, shielding is required especially for such areas with devices which are highly sensitive to external interference such as military systems, radar stations, and hospital medical electronic devices [16-17]. Electromagnetic shielding can be defined as a barrier to decrease or eliminate the transmission of the electromagnetic wave between two areas [18].

Practically, there are a lot of efforts which have been taken for different shielding techniques, starting from improving the sensitivity of the receiving electronic devices and enhancing the antenna systems till suppressing interference by use of a variety of filters and different shielding materials while all of the above could not get an ideal result because of the technical limitations or high cost [19-20]. A low-cost with high shielding effectiveness technique is required. One such type of good enough shield with the low-cost is the wire-mesh screens [1-4, 21-26]. Due to their physical flexibility and less weight compared to metal sheets, they are appropriate for shielding of large structures [26]. Another advantage of the wire-mesh screen windows over metal coated windows is its optical transparency [27-30]. However, they suffer from lower Shielding Effectiveness (SE) compared with metallic sheets. The objective of the present work is to discuss the shielding effectiveness of a double-sided coated glass window where both sides of the glass window are coated with wire-mesh sheets. It is shown that the proposed structure is highly attractive for different shielding applications due to its high electromagnetic shielding, lower cost, reduced weight and optical transparency compared to metallic sheets.

This article presents the shielding effectiveness calculation method for single wire-mesh screen based on transmission line theory as discussed in [22]. In Section III, the shielding effectiveness for two cascaded wire-mesh screens with a glass substrate is obtained. Finally, measurements are conducted in order to verify the

Submitted On: January20, 2018
Accepted On: May 26, 2018

analytical analysis.

II. ANALYTICAL AND NUMERICAL ANALYSIS OF SINGLE WIRE-MESH SCREEN

Electromagnetic shielding refers to decrease or suppress electromagnetic wave propagation from one interface to another one. Electromagnetic shielding effectiveness is defined as the ratio of the received power before and after shielding. It can be expressed as [23]:

$$SE\ (dB) = 10log_{10}\left(\frac{P_0}{P_s}\right), \quad (1)$$

where P_0 is the received power without shielding, and P_s is the power measured after shielding the area. The same concept is applied to the electric and magnetic fields shielding.

A. Analytical analysis of wire-mesh screen

The simple structure of wire-mesh screens is constructed by parallel metal wires with equal space. For such a case, the shielding effectiveness of the wire mesh is depending on the spacing between the wires and the thickness of the wires as well as the angle of incidence of the wave [20]. To increase the shielding effectiveness for such mesh, we can add additional wires orthogonal to the first set.

The electromagnetic shielding effectiveness of wire-mesh screens is considered where the mesh apertures are of a small size compared to the operating wavelength. It is described by the equivalent sheet-impedance of the wire-mesh screen [22]. Because of the mesh aperture periodicity and the mesh aperture is electrically small compared to the wavelength, a mesh under the incidence of an electromagnetic wave carries a reactive field that is confined to the vicinity of the mesh surface where the reactive field decays away from the screen surface as an exponential factor [20, 30].

The shielding effectiveness of a mesh with square aperture of length a_s and wire radius r_w as shown in Fig. 1 can be described as [22]:

$$SE(\omega,\theta) = -10log_{10}\left[\frac{1}{2}|T_1(\omega,\theta)|^2 + \frac{1}{2}|T_2(\omega,\theta)|^2\right], \quad (2)$$

where $T_1(\omega,\theta)$ and $T_2(\omega,\theta)$ are the transmission coefficients for the polarization of Transverse Electric (TE) and Transverse Magnetic (TM) modes, respectively and given by [20]:

$$T_1(\omega,\theta) = \frac{\left(\frac{2Z_{s1}(\omega)}{Z_0}\right)cos\,\theta}{1+\left(\frac{2Z_{s1}(\omega)}{Z_0}\right)cos\,\theta}, \quad (3)$$

$$T_2(\omega,\theta) = \frac{\left(\frac{2Z_{s2}(\omega)}{Z_0}\right)}{cos\,\theta+\left(\frac{2Z_{s2}(\omega)}{Z_0}\right)}, \quad (4)$$

where θ is the angle of incidence and calculated from the normal of the planar sheet and Z_0 is the free-space impedance. Z_{s1} and Z_{s2} are the eigenvalues of the mesh impedance operator corresponding to the TE and TM modes, respectively [20, 30]:

$$Z_{s1}(\omega) = Z_w\, a_s + j\omega L_s, \quad (5)$$

$$Z_{s2}(\omega) = Z_{s1} - \frac{j\omega L_s}{2}sin^2\theta, \quad (6)$$

where the sheet inductance LS and the wire impedance per unit length Z_w are given by [20, 30]:

$$L_s = \frac{\mu_0}{2\pi}ln\left\{\left(1 - e^{\frac{-2\pi r_w}{a_s}}\right)^{-1}\right\}, \quad (7)$$

$$Z_w = (\pi r_w^2\sigma)^{-1}, \quad (8)$$

where μ_0 is the free space permeability and σ is the wire conductivity.

It is important to note that the above analysis for mesh with square apertures [22]. If the apertures of the mesh are not square as for hexagonal aperture, an equivalent square area can be calculated as discussed in [20].

B. Numerical simulation of wire-mesh screen

The transmission of electromagnetic wave through the wire-mesh screen was numerically simulated by using HFSS (High Frequency Structural Simulator) [31]. HFSS is a commercial computational electromagnetics software package which uses the finite element method to solve the electromagnetic problems including antennas and microwave filters design [31]. The numerical simulation is used to verify the proposed analytical results. The mesh screen is approximated in the simulation analysis as an infinite periodic structure [20, 32]. Typically, the wire mesh screen is constructed of periodic small square apertures. In case of an incident plane wave, the structure can be approximated by a single unit cell with periodic boundary conditions [33]. The fields on both sides of the screen are identical with a phase shift that depends on the angle of incidence of the planar wave [21].

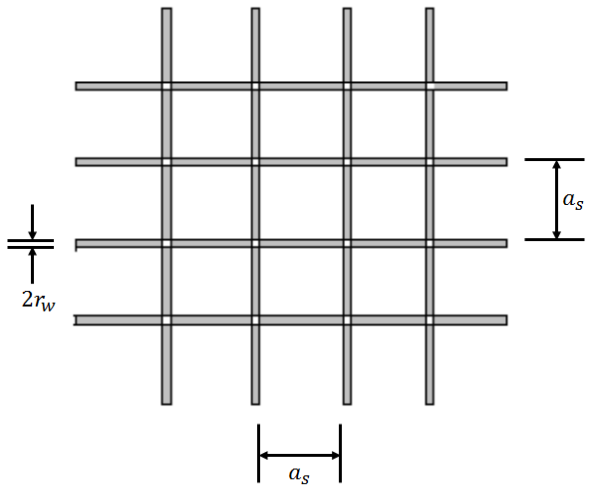

Fig. 1. Wire-mesh screen with square apertures [22].

In order to check the validity of the model, the shielding effectiveness is calculated analytically using the presented model and numerically simulated using HFSS for wire-mesh screen with square aperture of width is 2 mm and radius is 0.05 mm. The frequency band is 200-900 MHz which covers multi-bands including lower GSM band. The sheet is made of aluminum material with conductivity is 3.7×10^7 s/m. The excitation is assumed to be plane wave with normal incidence. Figure 2 shows the comparisons between analytical and simulation results with good agreement is obtained. The calculated mean error between the analytical model and simulation results is about 3%.

It can be noted that the shielding effectiveness is quite high at low frequency band while by increasing the operating frequency, the shielding effectiveness decreases. This can be explained as by increasing the frequency, the sheet impedance increases and the shielding effectiveness decreases [24]. From the plane wave theory, when a radio wave propagates from a free space with high intrinsic impedance into a wire-mesh sheet with low impedance, the reflection coefficient is high and the total shielding effectiveness increases while by increasing the frequency, the sheet resistance increases and the total shielding effectiveness decreases [24].

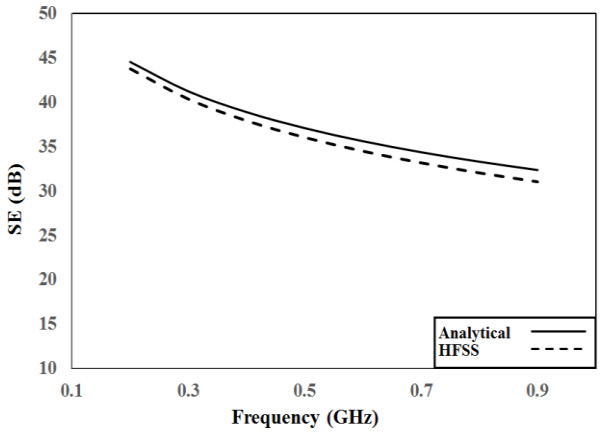

Fig. 2. SE of aluminum wire-mesh screen with square aperture, the aperture is width=2 mm and radius=0.05 mm.

Using the analytical model, shielding effectiveness for a mesh with square aperture is calculated for different angle of incidence and operating frequencies. The mesh aperture dimensions is kept constants with width of 2 mm and wire radius is 0.05 mm. Figure 3 shows the shielding effectiveness as a function of the frequency and incidence angle. It worth noting that the effect of the angle of incidence on the shielding effectiveness is limited to large incidence angles, also it can be shown that higher frequencies leads to lower shielding effectiveness. The same analysis is repeated to calculate the effect of the mesh aperture width a_s and wire radius r_w on the total the shielding effectiveness. The operating frequency is kept constant for 0.5 GHz and normal wave incidence is assumed. Figure 4 shows the shielding effectiveness as a function of the aperture width and wire radius. It can be shown that increasing the aperture width leads to low SE while the opposite is true for wire radius. The best SE can obtained by using an optimization techniques to determine the optimum aperture width and wire radius for desired operating frequency.

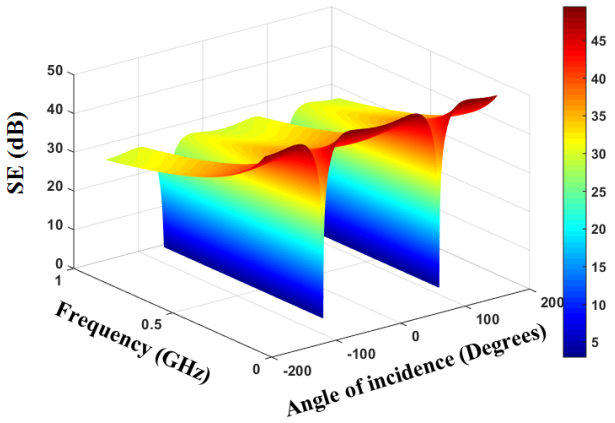

Fig. 3. SE as a function of frequency and angle of incidence for single layer of aluminum wire-mesh screen with square aperture, the aperture is width=2 mm and radius=0.05 mm.

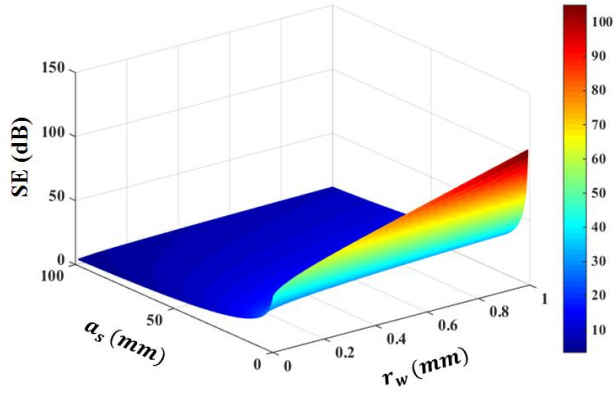

Fig. 4. SE as a function of mesh aperture length and wire radius for single layer of aluminum wire-mesh screen with square aperture, the operating frequency is 0.5 GHz with normal wave incidence.

III. SHEILDING EFFECTIVNESS OF DOUBLE-SIDED COATED GLASS WINDOW

In this section, the total shielding effectiveness of the double-sided coated glass window is obtained. The coating sheets can be of same material as to increase the total SE. Also, the sheets can be of different materials for

wide frequency band shielding or it can be used for different shielding applications, as one layer can be used for electromagnetic shielding of radio wave of specific band, e.g., GSM band, and the other one can be used for magnetic shielding by using the second sheet with high permeability material [34-35] in which, the structure shielding will server for different types of applications.

Ciddor and Whitbourn [36] presented an equivalent film model for single wire-mesh sheet based on transmission line lumped circuit and gave a transfer matrix M_{mesh} for wire-mesh with a normalized equivalent admittance Y_{mesh} [36]:

$$M_{mesh} = \begin{bmatrix} 1 & 0 \\ Y_{mesh} & 1 \end{bmatrix}, \quad (9)$$

where the normalized admittance Y_{mesh} is the reciprocal of the sheet impedance Z_{mesh} of transparent conductive wire-mesh screen,

$$Y_{mesh} = \frac{1}{Z_{mesh}}, \quad (10)$$

the normalized impedance Z_{mesh} can be given by (5) and (6).

The transfer matrixes of glass window substrate M_{win} can be obtained using a transfer matrix theory of optical thin films [36]:

$$M_{win} = \begin{bmatrix} \cos\varphi & iY_{win}\sin\varphi \\ \left(\frac{i}{Y_{win}}\right)\sin\varphi & \cos\varphi \end{bmatrix}, \quad (11)$$

where φ is the optical path difference and Y_{win} is the optical admittance of the film [36]:

$$\varphi = \frac{2\pi n t_{win}}{\lambda}, \quad (12)$$

where n is the complex refractive index of the film and t_{win} is the film thickness. The optical admittance Y_{win} is obtained by [36]:

$$Y_{win} = nY_0, \quad (13)$$

where Y_0 is the free space admittance.

For double mesh coting with glass substrate as shown in Fig. 5, the transfer matrix for each wire screen is calculated using (9). According to transmission matrix method, the transfer matrix M_{total} of the structure can be calculated by:

$$M_{total} = M_{mesh1}\, M_{win}\, M_{mesh2} = \begin{bmatrix} A & B \\ C & D \end{bmatrix}. \quad (14)$$

The total transmittance coefficient T_{total} of the structure is obtained from the transfer matrix M_{total} [24]:

$$T_{total} = \frac{2}{A+B/Z_0+C\,Z_0+D}, \quad (15)$$

and the total shielding effectiveness can be obtained by [24]:

$$SE_{total}(dB) = -20log_{10}(T_{total}). \quad (16)$$

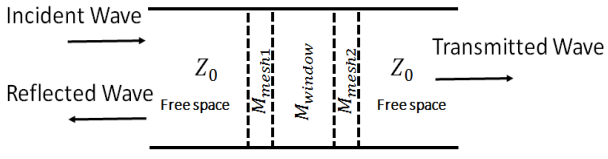

Fig. 5. Cascaded wire-mesh screens layout.

The total shielding effectiveness of two aluminum sheets with glass substrate is calculated analytically using the presented model and numerically simulated using HFSS. The sheets are constructed of square wire-mesh with aperture width is 2 mm and wire radius is 0.05 mm. The frequency band is 200-900 MHz. The glass substrate relative permittivity is 5.2 and thickness is 6 mm. Figure 6 shows the comparisons between analytical results and HFSS simulation with a good agreement is obtained. It can be noted that the shielding effectiveness of the structure is increased by about 50% with introducing additional coating layer of wire-mesh. The calculated mean error between the model and simulation results is about 4.1%.

The same HFSS setup is used while one of the sheets is kept aluminum and the other one is replaced with iron material of conductivity is 1.01×10^7 s/m using the same dimensions. Figure 7 shows SE as a function of frequency based on HFSS simulation for two scenarios. In the first scenario, the two sheets are made of aluminum while the other scenario, one of the sheets is kept aluminum and the other sheet is replaced with iron sheet. It can be shown that changing the wire mesh material with different conductors has less effect on the total SE of the structure.

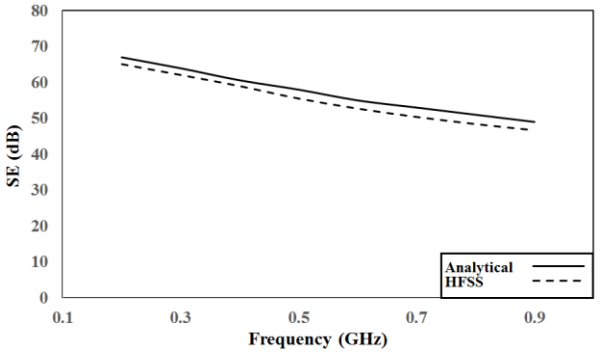

Fig. 6. SE of double coating wire-mesh screens with square aperture, the aperture is width=2 mm and radius=0.05 mm. The two sheets are made of aluminum.

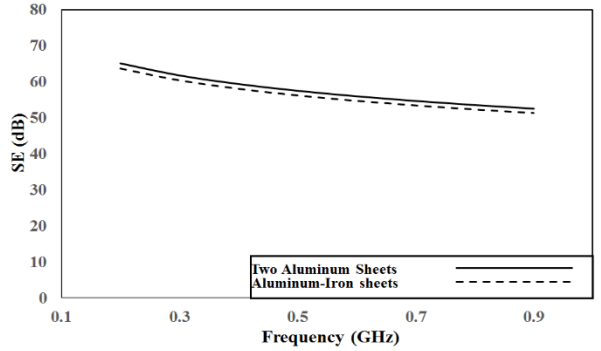

Fig. 7. SE of two coating wire-mesh screens with different materials based on HFSS simulation.

IV. MEASUREMENTS

In this section, sample results are presented to verify the accuracy of the proposed model for two scenarios, single and double-sided coated glass window.

The experimental setup consists of Handheld RF Signal Generator (RFEGEN 1.12) with dipole antenna with gain of 2.2 dBi which is used as a transmitter while the receiver is RF Viewer wireless USB dongle and data is collected using computer software package RF spectrum analyzer (TOUCHSTONE PRO) as shown in Fig. 8. The transmitting and receiving antennas are kept vertically polarized as shown in Fig. 8. In the first scenario, single aluminum wire-mesh screen is fixed in the front face of shielded box with dimensions 50 cm × 50 cm × 30 cm and the transmitter is fixed on wood table at 1 m away from the receiver as shown in Fig. 8. The mesh aperture width is 2 mm and wire radius is 0.05 mm. The operating frequency band is 200-900 MHz which covers multi-bands including lower GSM band. The received power is measured where no sheets are installed in the front face of the box while the other faces as fully shielded then the measured data is collected after shielding with single layer of aluminum wire-mesh sheet. The shielding effectiveness is calculated as the ratio between the received power with and without shielding. Figure 9 shows a comparison between the shielding effectiveness which is calculated from the measured data and the one which is calculated by using the analytical model. Good agreement between the measured and analytical results is obtained. The slight differences can be explained due to errors in the manual positioning of the receiving antenna, differences due to the boundary conditions of the actual setup and slight interference from external sources. The mean calculated error between the model and measured results is about 5.9%.

The same setup is used while by fixing two layers of aluminum wire-mesh sheets on both sides of a commercial glass window with thickness of 6 mm and relative permittivity is 5.2. The structure is installed in the front face of the box while the other faces are kept fully shielded. Figure 10 shows a comparison between measured SE in dB and the calculated one by using the proposed model for cascaded wire-mesh screens. Good agreement between the measured and calculated results is obtained. It should be noted that two mesh layer on both side of the glass window can increase the total SE by about 50% compared with single wire-mesh screen. The total SE of the structure is satisfactory high while the total cost is quite low with good optical transparency compared to metallic sheets. The proposed structure is highly attractive for wide band of shielding applications. The mean calculated error between the model and measured results is about 2.8%.

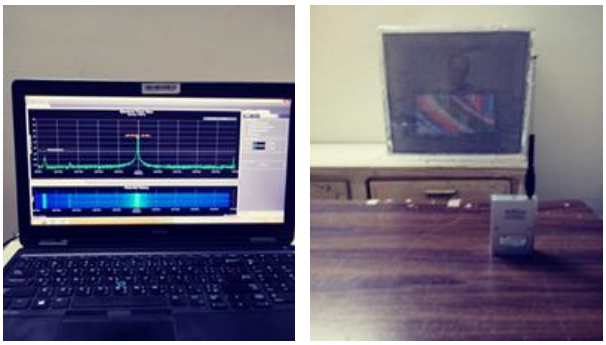

(a) (b)

Fig. 8. Measurement setup: (a) TOUCHSTONE PRO RF spectrum analyzer software package. (b) Transmitter (RF Signal Generator) and receiver antenna are installed in shielded box with single aluminum wire-mesh screen in the front face with glass window.

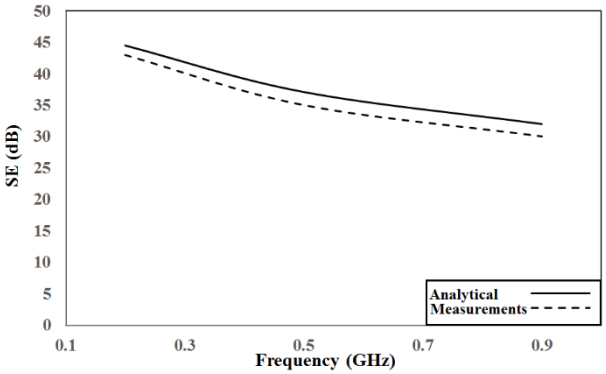

Fig. 9. Shielding effectiveness for single layer wire-mesh screen with aluminum material, $a_s = 2\ mm$ and $r_w = 0.05\ mm$.

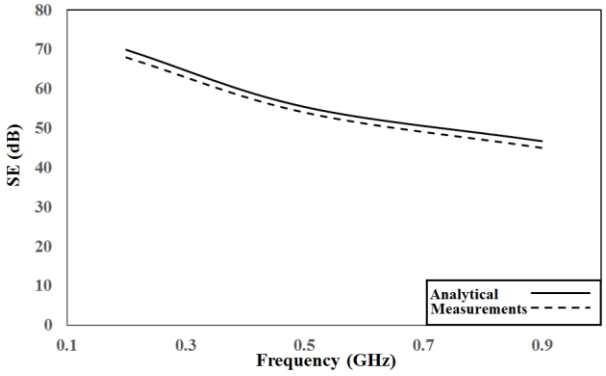

Fig. 10. Shielding effectiveness for double layers of aluminum wire-mesh screens with glass substrate, $a_s = 2\ mm$, $r_w = 0.05\ mm$ and glass thickness = 6 mm.

V. CONCLUSION

An approach is proposed to calculate the shielding

effectiveness of wire-mesh screens for single and double wire-mesh layers with glass substrate. The model is based on transmission line theory. It is shown that the wire-mesh screen is providing high shielding effectiveness in low frequency range and by increasing the frequency the shielding effectiveness is decreased. Also, it is shown that the structure shielding effectiveness is satisfactory increased by introducing additional wire mesh layer. The proposed structure is highly attractive for wide band of shielding applications due to its lower cost, reduced weight and optical transparency compared to metallic sheets. The proposed model is verified by comparison with experimental results. Good agreements are obtained from these comparisons.

REFERENCES

[1] Z. Kazerouni and H. Aliakbarian, "Wideband full wave shielding effectiveness simulation of structures with wire grid meshes," *International Symposium on Electromagnetic Compatibility-EMC EUROPE*, Nov. 2017.

[2] F. Bulut, H. S. Efendıoğlu, V. Solak, M. Yabuloğlu, and H. Özer, "Electromagnetic shielding behavior of different metallic wire-meshes and thin metal plate," *International Electromagnetic Compatibility Conference (EMC Turkiye)*, Nov. 2017.

[3] G. Rosu, N. Druta, and O. Baltag, "The study of the microwave shielding properties of various screen configurations," *International Conference on Comm-unications (COMM)*, Aug. 2016.

[4] S. Hyun, I. Jung, I. Hong, C. Jung, E. Kim, and J. G. Yook, "Modified sheet inductance of wire mesh using effective wire spacing," *IEEE Transactions on Electromagnetic Compatibility*, vol. 58, no. 3, June 2016.

[5] Bio-initiative Report, *A Rationale for a Biologically-based Public Exposure Standard for Electromagnetic Fields (ELF and RF)*, Mobile Telecommunications and Health Research Program (MTHR) Report 2007.

[6] B. Levitt and H. Lai, "Biological effects from exposure to electromagnetic radiation emitted by cell tower base stations and other antenna arrays," *Environ. Rev*., vol. 18, pp. 369-395, Nov. 2010.

[7] N. Kumar and G. Kumar, "Biological effects of cell tower radiation on human body," *ISMOT*, Delhi, India, pp. 678-679, Dec. 2009.

[8] R. Santini, P. Santini, J. Danze, P. L. Ruz, and M. Seigne, "Study of the health of people living in the vicinity of mobile phone base stations: Incidence according to distance and sex," *Pathology Biology*, pp. 369-73, 2002.

[9] Z. Lai, *Electromagnetic Interference and Electromagnetic Compatibility [M]*. *Atomic Energy Press*, 1993.

[10] American National Standard Dictionary of Electromagnetic Compatibility (EMC) including Electromagnetic Environmental Effects (E3), *ANSI C63.14-2014*, 2014.

[11] IEC Standard, 61000-1-5, "Electromagnetic compatibility (EMC) - Part 1-5: General | High Power Electromagnetic (HPEM) Effects on Civil Systems," Nov. 2004.

[12] W. Radasky, C. E. Baum, and M. W. Wik, "Introduction to the special issue on high-power electromagnetics (HPEM) and intentional electromagnetic interference (IEMI)," *IEEE Trans. on Electromagnetic Compatibility*, vol. 46, no. 3, pp. 314-321, Aug. 2004.

[13] F. Sabath, "System oriented view on high-power electromagnetic (HPEM) effects and intentional electromagnetic iInterference (IEMI)", *General Assembly of the URSI*, vol. 29, Aug. 2008.

[14] D. Nitsch and F. Sabath, *Electromagnetic Effects on Systems and Components.* Book of Abstracts AMEREM, July 2006.

[15] S. Seker, A. Morgul, and T. M. Tulgar, "Electromagnetic pollution survey in a typical Turkish residence, plant and hospital," *9th Mediterranean Electrotechnical Conference*, May 1998.

[16] D. Alonso, J. Rulf, Ferran Silva, M. Pous, J. Coves, and R. Oriol, "Measuring, modelling and correction actions for EMC assessment between high speed railway and medical equipment," *Electrical Systems for Aircraft, Railway and Ship Propulsion (ESARS)*, Dec. 2010

[17] F. E. Vance, "Shielding and grounding topology for interference control," *Air Force Weapons Laboratory*, Note 306, Apr. 1977.

[18] D. Markham, "Shielding: Quantifying the shielding requirements for portable electronic design providing new solutions by using of combination of materials and design," *Materials and Design*, vol. 21, Dec. 2000.

[19] T. Shinn and F. Chang, "EMI shielding effectiveness of metal-coated carbon fiber-reinforced ABS composites," *Materials Science and Engineering A*, Apr. 2001.

[20] D. Mansson and A. Ellgardt, "Comparing analytical and numerical calculations of shielding effectiveness of planar metallic meshes with measurements in cascaded reverberation chambers," *Progress In Electromagnetics Research C*, vol. 31, July 2012.

[21] Y. Duan and S. Liu, "Effect of metal wire mesh with slits on shielding effectiveness," *Shielding Technology & Shielding Material*, 2004.

[22] K. F. Casey, "Electromagnetic shielding behavior of wire-mesh screens," *IEEE Trans. on Electromagnetic Compatibility*, vol. 30, no. 3, Aug. 1988.

[23] L. Liu and Q. Zhang, "Analysis of electromagnetic

shielding effectiveness of metal material," *Advanced Materials Research*, pp. 655-659, June 2012.

[24] Y. Liu and J. Tan, "Frequency dependent model of sheet resistance and effect analysis on shielding effectiveness of transparent conductive mesh coatings," *Progress In Electromagnetics Research*, vol. 140, pp. 353-368, May 2013.

[25] J. Halman, K. Ramsey, M. Thomas, and A. Griffan, "Predicted and measured transmission and diffraction by a metallic mesh coating," *Proc. SPIE*, May 2009.

[26] L. B. Wang, K. Y. See, and W. Y. Chang, "Electromagnetic shielding analysis of printed flexible meshed screens," *Asia-Pacific International Symposium on Electromagnetic Compatibility*, Apr. 2010.

[27] M. Y. Koledintseva, A. G. Razmadze, A. Y. Gafarov, V. V. Khilkevich, J. L. Drewniak, and T. Tsutaoka, "Attenuation in extended structures coated with thin magneto dielectric absorber layer," *Progress In Electromagnetics Research*, vol. 118, pp. 441-459, July 2011.

[28] M. Kohin, S. J. Wein, J. D. Traylor, R. C. Chase, and J. E. Chapman, "Analysis and design of transparent conductive coatings and filters," *Opt. Eng*., vol. 32, no. 5, pp. 911-925, May 1993.

[29] C. I. Bright, "Electromagnetic shielding for electro-optical windows and domes," *Proc. SPIE*, pp. 388-396, Sep. 1994.

[30] A. Avinash, B. Mritunjay, and K. Ravindra "Characterization of shielding effectiveness of general metallized structure," *I. J. Wireless and Microwave Technologies*, Nov. 2014.

[31] Ansoft High Frequency Structure Simulation (HFSS), ver. 15, Ansoft Corporation, Pittsburgh, PA, 2013.

[32] B. A. Munk, *Frequency Selective Surfaces: Theory and Design*. John-Wiley, New York, 2000.

[33] A. Chatterjee and S. Parui, "A dual layer frequency selective surface reflector for wideband applications," *Radioengineering*, vol. 25, no. 1, Apr. 2016.

[34] K. Yeon, D. Son, E. Park, J. Lee, K. Do, and J. Park, "Magnetic shielding effectiveness measurement of magnetic steel sheets in ELF range," *Journal of Magnetics*, Jan. 2008.

[35] L. B. Whitbourn and R. C. Compton, "Equivalent-circuit formulas for metal grid reflectors at a dielectric boundary," *Appl. Opt*., vol. 24, no. 2, pp. 217-220, 1985.

[36] P. E. Ciddor and L. B. Whitbourn, "Equivalent thin film of a periodic metal grid," *Appl. Opt*., vol. 28, no. 6, pp. 1228-1230, Mar. 1989.

Hany M. El-Maghrabi M.Sc. and Ph.D. Electronics and Electrical Communications, Faculty of Engineering, Cairo University at 2011 and 2017, respectively. El-Maghrabi has got a position of Research Assistant in Housing and Building National Research Center (HBNRC), Institute of Electromechanical, Department of Communication (Egypt) at 2005. He became Assistant Researcher at HBNRC at 2011 and Researcher at 2017. He has co-authored technical journal article and conference papers. El-Maghrabi has an experience in electromagnetics, antennas, microstrip structures, numerical methods, wave propgation and their applications in microwave. El-Maghrabi has been awarded The Best Paper in NRSC 2015.

A General Equivalent Model for Multi-Coil Wireless Power Transfer System Analysis and its Application on Compensation Network Design

Yanjie Guo [1,2], Lifang Wang [*1,2], and Chenglin Liao [1,2]

[1] Key Laboratory of Power Electronics and Electric Drives, Institute of Electrical Engineering
Chinese Academy of Sciences, No.6 Beiertiao, Zhongguancun, Beijing, 100190, China
yjguo@mail.iee.ac.cn, *wlf@mail.iee.ac.cn, liaocl@mail.iee.ac.cn

[2] Collaborative Innovation Center for Electric Vehicles in Beijing, Beijing 100081, China

Abstract — This paper presents a novel general equivalent model of multi-coil coupled wireless power transfer (WPT) system and its application on compensation network design. The proposed equivalent model has the advantages of concise expressions, good accuracy, and fast calculation speed. Firstly, the general equivalent model is established to get the concise expressions of system efficiency and output power. Then, based on the proposed model, compensation network design method is discussed, considering several system performance indicators. Furthermore, the proposed model and method are verified by a developed WPT prototype. Meanwhile, the equivalent characteristics and the mutual-resistance effect are analyzed. Also, numerical simulations are conducted to study the magnetic flux distribution, the magnetic field exposure issue, and the current distribution in coil Litz wire. Finally, a varied capacitor compensation method is presented to improve system efficiency on the conditions of coil misalignments.

Index Terms — Compensation network design, efficiency improvement, general equivalent model, Wireless power transfer.

I. INTRODUCTION

Wireless power transfer (WPT) can make people free from connecting wires and bring convenience to consumers. So, it has attracted much attention and has been used in implanted devices, sensors, mobile phone and electric vehicle (EV) charging, etc. [1,2].

Coupling coils are a key part of WPT system. They can be described by coupled-mode theory [3], circuit model [4], or some electromagnetic descriptions [5]. WPT system works through the electromagnetic coupling among the coils. So, it is an electromagnetic problem essentially, affected by coil sharp, size, position, and so on [5,6]. However, the coils can be considered to be electrically small, because their sizes and lengths are much smaller than the wavelength of WPT operating frequency [5]. Moreover, distance between the coils is much smaller than the wavelength of WPT operating frequency. So, we can think the energy is stored in the near-field and not radiated into space. Hence, the radiation loss can be neglected. Based on the above two points, WPT system can be approximately equivalent to a lumped parameter circuit.

Lumped parameter circuit model of WPT system can be obtained from voltage-current equations based on impedance matrix [7,8]. But for the multi-coil WPT system, the circuit models usually contain too many parameters, and cannot get a concise expression of system efficiency or output power [4,7]. So, several methods are proposed to solve this problem, including making the coils and compensation networks working in the resonance states [9], assuming the coils are identical [10], adopting S-parameters to describe the WPT system [1], and reducing the order of the multi-coil WPT model [11]. The most common way is considering only the mutual-inductances between adjacent coils to simplify the model [12,13]. This simplified model could give concise expressions, but will lead to inaccurate results in some applications.

The other key part of WPT system is compensation networks, which include series capacitor, paralleled capacitor, LCC compensation network and so on [14,15]. They can be designed in the resonance state, which has the advantages that the resonant frequency is irrelevant with the coupling coefficient and is also independent of the load condition [15]. But in some close range applications, the optimal system does not work in the completely resonance state [4]. So, the compensation networks need to be optimized considering features of both the coils and the load [16], in order to adjust system output power and keep system efficiency in a high value.

Based on the research above, a novel general equivalent model of multi-coil coupled WPT system is proposed in this paper. This model contains complete information of the multi-coil WPT system, so it has good accuracy. At the same time, concise efficiency and output power expressions can be obtained, which are

Submitted On: March 15, 2017
Accepted On: April 21, 2018

more convenient for system analysis and design. Also, the proposed model can achieve faster calculation speed, because the *n*-order impedance matrix has been transferred to a two-order one, so the calculation time of the reverse operation will be significantly reduced. This paper is organized as follows. Section II presents the general equivalent model. Section III shows the compensation network design method. Section IV gives an example of a four-coil system, corresponding experimental verifications and analysis.

II. GENERAL EQUIVALENT MODEL

The electromagnetic coupling problem of WPT system can be analyzed through the lumped parameter circuit model, since it meets the requirements of electrically small. Circuit model of a typical multi-coil WPT system is shown in Fig. 1. Where, compensation networks with series capacitors are adopted, since they have simple structures and been widely used in multi-coil system; U_S is equivalent voltage source; R_L is equivalent load resistance, I_1, I_2, I_3, … I_{n-1}, I_n are currents in the coils; L_1, L_2, L_3, … L_{n-1}, L_n are self-inductances of the coils; R_1, R_2, R_3, … R_{n-1}, R_n are stray resistances of the coils' loops; C_1, C_2, C_2, … C_{n-1}, C_n are series compensation capacitances; M_{12}, M_{13}, M_{23}, … $M_{2(n-1)}$, $M_{3(n-1)}$, M_{3n} , … $M_{n(n-1)}$ are mutual-inductances among the coils.

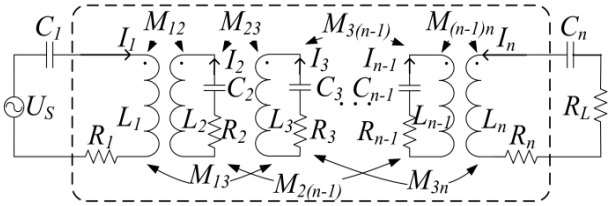

Fig. 1. Circuit model of the multi-coil coupled WPT system with series compensation capacitors.

According to Kirchhoff's law and mesh current analysis method, the voltage-current equation of the circuit model in Fig. 1 is given by Equation (1a):

$$\begin{bmatrix} Z_{11}' & Z_{12} & Z_{13} & \cdots & Z_{1(n-1)} & Z_{1n} \\ Z_{12} & Z_{22} & Z_{23} & \cdots & Z_{2(n-1)} & Z_{2n} \\ Z_{13} & Z_{23} & Z_{33} & \cdots & Z_{3(n-1)} & Z_{3n} \\ \vdots & \vdots & \vdots & \ddots & \vdots & \vdots \\ Z_{1(n-1)} & Z_{2(n-1)} & Z_{3(n-1)} & \cdots & Z_{(n-1)(n-1)} & Z_{(n-1)n} \\ Z_{1n} & Z_{2n} & Z_{3n} & \cdots & Z_{(n-1)n} & Z_{nn}' \end{bmatrix} \begin{bmatrix} I_1 \\ I_2 \\ I_3 \\ \vdots \\ I_{n-1} \\ I_n \end{bmatrix} = \begin{bmatrix} U_S \\ 0 \\ 0 \\ \vdots \\ 0 \\ 0 \end{bmatrix}. \tag{1a}$$

Where, system impedances are defined by Equation (1b), and ω is the angle frequency:

$$\begin{aligned} Z_{11}' &= Z_{11} + 1/j\omega C_1 = R_1 + j\omega L_1 + 1/j\omega C_1; \\ Z_{nn}' &= Z_{nn} + R_L + 1/j\omega C_n = R_n + j\omega L_n + R_L + 1/j\omega C_n; \\ Z_{pp} &= R_p + j(\omega L_p - 1/\omega C_p);\ p = 2,3\ldots n-1; \\ Z_{pq} &= j\omega M_{pq};\quad p,q = 1,2,3\ldots n-1,n,\ and\ p \neq q. \end{aligned} \tag{1b}$$

Equations (1a) and (1b) indicate that the inverse matrix of the *n*-order impedance matrix has to be solved to get the results. This inverse operation will lead to lots of calculations and complex final expressions. For the sake of solving this problem, we consider to reduce the order of the impedance matrix by making an equivalent with a two-coil system like shown in Fig. 2. In the equivalent process, U_S, R_L, I_1, I_n, C_1 and C_n are kept at the same. We build an equivalent relationship between the part in dashed box in Fig. 1 and the one in dashed box in Fig. 2. This conversion will change the *n*-order impedance matrix to a two-order one, so the corresponding calculations of the inverse operation will be significantly reduced, and it is possible to obtain concise equation solutions.

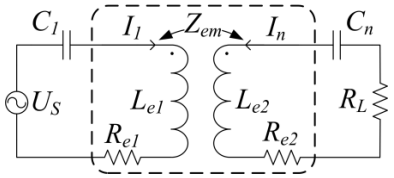

Fig. 2. Equivalent two-coil model used to express the multi-coil WPT system.

In Fig. 2, L_{e1} and L_{e2} are the self-inductances, and R_{e1} and R_{e2} are the resistances of the two equivalent coils' loops, respectively. Also, primary side impedance Z_{e1}, secondary side impedance Z_{e2}, and mutual-impedance Z_{em} are defined as follows: $Z_{e1}=R_{e1}+j\omega L_{e1}$, $Z_{e2}=R_{e2}+j\omega L_{e2}$, $Z_{em}=R_{em}+j\omega M_e$. Where, R_{em} and M_e are mutual-resistance and mutual-inductance between the two equivalent coils. It should be noticed that mutual-impedance between the two equivalent coils contains resistance component R_{em}, which is different from the expressions of the traditional two-coil WPT system.

Using the general equivalent model, expressions of system efficiency and output power can be got according to the following steps. Firstly, the *n*-coil coupled circuit in Fig. 1 is transferred to the equivalent two-coil model in Fig. 2, to the aim of reducing the impedance matrix order. Specifically, we find the relationships between impedances of the *n*-coil coupled circuit model (Z_{pp} and Z_{pq}) and impedances of the equivalent two-coil model (Z_{e1}, Z_{e2}, and Z_{em}), as the functions shown in Equation (2):

$$\begin{aligned} Z_{e1} &= f_{e1}(Z_{pp}, Z_{pq});\quad Z_{e2} = f_{e2}(Z_{pp}, Z_{pq}), \\ Z_{em} &= f_{em}(Z_{pp}, Z_{pq});\quad p,q = 1,2,3\ldots n-1,n,\ and\ p \neq q. \end{aligned} \tag{2}$$

Then, based on the transfer relationships in Equation (2), the voltage-current equation of the equivalent two-coil model in Fig. 2 is given by Equation (3):

$$\begin{bmatrix} Z_{e1}+1/\ j\omega C_1 & Z_{em} \\ Z_{em} & Z_{e2}+R_L+1/\ j\omega C_n \end{bmatrix}\begin{bmatrix} I_1 \\ I_n \end{bmatrix}=\begin{bmatrix} U_S \\ 0 \end{bmatrix}. \quad (3)$$

At last, system efficiency and output power expressions can be calculated and given by Equations (4) and (5). Where, $R_{sec}=R_{e2}+R_L$, $X_{e1}=\omega L_{e1}-1/\omega C_1$, $X_{e2}=\omega L_{e2}-1/\omega C_n$, $Z_{eq}=R_{e1}\ R_{sec}-R_{em}{}^2+\omega^2 M_e{}^2$.

$$\eta=\frac{(\omega^2 M_e{}^2+R_{em}{}^2)R_L}{R_{\sec}(\omega^2 M_e{}^2-R_{em}{}^2)+R_{e1}(R_{\sec}{}^2+X_{e2}{}^2)-2\omega M_e R_{em}X_{e2}}. \quad (4)$$

$$P_o=\frac{(\omega^2 M_e{}^2+R_{em}{}^2)R_L U^2}{(Z_{eq}-X_{e1}X_{e2})^2+(R_{e1}X_{e2}+R_{\sec}X_{e1}-2\omega M_e R_{em})^2}. \quad (5)$$

Equations (4) and (5) suggest that concise solutions can be obtained from the proposed equivalent model. They will be helpful for system analysis and design.

Furthermore, Equations (4) and (5) can be used to get optimal system states, such as maximum efficiency and so on. According to the traditional two-coil WPT model, system can achieve maximum efficiency, when the secondary side is in resonance state, which means $X_{e2}=0$. However, the situation in the proposed equivalent two-coil model is different, because of the introduction of R_{em}. The optimal X_{e2} to achieve maximum efficiency is calculated and given by Equation (6):

$$X_{e2\_opt}=\omega M_e R_{em}/R_{e1}. \quad (6)$$

Through Equation (6), the maximum system efficiency η_{max} can be solved, as well as system output power P_{om} when having maximum efficiency. Their expressions are given in Equations (7) and (8). Based on these equations, compensation capacitors can be designed to achieve high system performance:

$$\eta_{\max}=\frac{(\omega^2 M_e{}^2+R_{em}{}^2)R_L R_{e1}}{R_{e1}R_{\sec}(\omega^2 M_e{}^2-R_{em}{}^2)+R_{e1}{}^2R_{\sec}{}^2-\omega^2 M_e{}^2R_{em}{}^2}. \quad (7)$$

$$P_{om}=\frac{(\omega^2 M_e{}^2+R_{em}{}^2)R_L U^2}{(Z_{eq}-X_{e1}\omega M_e R_{em}/R_{e1})^2+(R_{\sec}X_{e1}-\omega M_e R_{em})^2}. \quad (8)$$

Besides, the proposed equivalent model can also be achieved and investigated through electromagnetic theory, but the circuit model is more suitable and has higher accuracy on the specific condition in this paper.

III. COMPENSATION NETWORK DESIGN

Compensation networks are designed to make the WPT system achieve high performance, such as maximum efficiency, rated output power, high coil misalignment tolerance, etc. Since every coil has a corresponding compensation capacitor as shown in Fig. 1, the system will have *n* degrees of freedom, which can be used for design. This means *n* equations can be simultaneously solved to reach several design targets at the same time.

Firstly, efficiency and output power targets are most important. So, Equation (6) should be included in the target equations to reach the maximum system efficiency. Also, $P_{om}=P_{ref}$ should be solved based on Equation (8) to make the system output rated power. Where, P_{ref} is rated system output power.

Then, system input impedance characteristics need to be adjusted to match the power source. For example, sometimes system input resistance should be 50Ω to match the radio frequency (RF) source. Moreover, if the source is an inverter, system input reactance should be adjusted to control the inverter load reactive power, in order to reduce electric stress of power electrics devices. Equation (9) shows the expression of system input reactance. In order to adjust the reactive power, $X_{inv}=X_{req}$ needs to be added in the target equations. Where, X_{req} is the reference reactance:

$$X_{inv}=\frac{R_{\sec}(R_{\sec}X_{e1}-2\omega M_e R_{em})+X_{e2}(R_{em}{}^2-\omega^2 M_e{}^2+X_{e1}X_{e2})}{R_{\sec}{}^2+X_{e2}{}^2}. \quad (9)$$

Furthermore, coil misalignment tolerance could be considered, if there still have design degrees of freedom. For example, making the WPT system reach maximum efficiency or achieve reference efficiency, when the coils have a certain misalignment distance. Equation (10) gives the target equation which make the system reach maximum efficiency when misalignment. Where, subscripts '*_d*' represent the corresponding equivalent model parameters in the coil misalignment distance *d*:

$$X_{e2\_opt\_d}=\omega L_{e2\_d}-1/\omega C_n=\omega M_{e\_d}R_{em\_d}/R_{e1\_d}. \quad (10)$$

Solving process of the target equation is a little complex, if we want WPT system to achieve reference efficiency η_d in the coil misalignment distance *d*. This is caused by the efficiency expression is a two-order function of X_{e2}, as shown in Equation (4). So, firstly, Equation (11a) is used to determine whether the efficiency equation is solvable. If there is a solution, the target equation can be given by Equation (11b):

$$\Delta=4\omega^2 M_{e\_d}{}^2R_{em\_d}{}^2-4R_{e1\_d}(R_{e1\_d}R_{sec\_d}{}^2+R_{sec\_d}{}^2 \times(\omega^2 M_{e\_d}{}^2-R_{em\_d}{}^2)-\frac{(\omega^2 M_{e\_d}{}^2+R_{em\_d}{}^2)R_L}{\eta_d})\geq 0. \quad (11a)$$

$$X_{e2\_opt\_d}=\frac{2\omega M_{e\_d}R_{em\_d}+\sqrt{\Delta}}{2R_{e1\_d}}. \quad (11b)$$

Through simultaneously solving the above target equations, values of the compensation capacitors can be obtained by considering several system performance indicators. It should be noticed that sometimes there is no analytical solution for these equations. Numerical solution methods need to be used on this condition. Also, calculated values of the compensation capacitors require fine tuning in practice to get better results.

IV. EXAMPLE OF A FOUR-COIL SYSTEM

A. Equivalent model of four-coil system

Circuit model of a typical four-coil WPT system is shown in Fig. 3. Where, the four coupled coils are named as drive coil, transmit coil, receive coil, and load coil, in the order from source to load; the variables have the same meaning with the ones shown in Fig. 1.

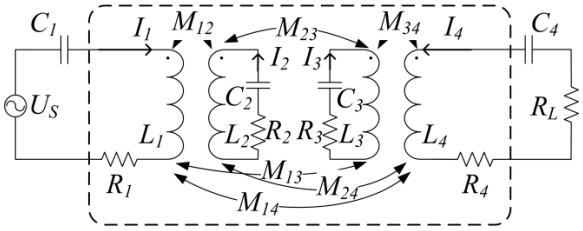

Fig. 3. Circuit model of the four-coil coupled WPT system with series compensation capacitors.

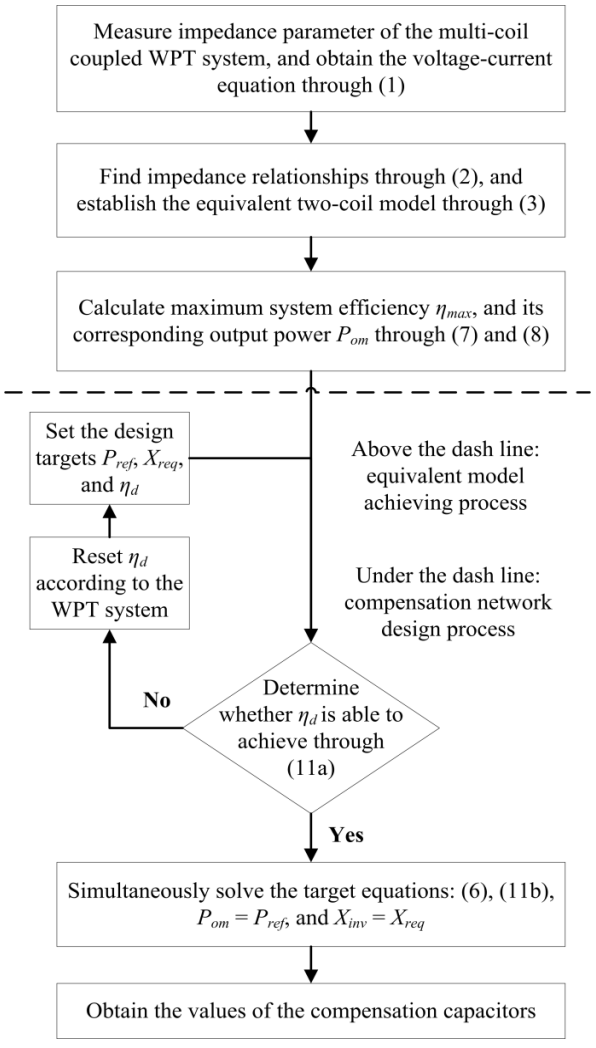

Fig. 4. Flow chart of the proposed equivalent model achievement and compensation network design method.

The solution procedure based on the proposed equivalent model and the compensation network design method are shown in Fig. 4. According to the equivalent model achieving process shown in Fig. 4, we can build an equivalent relationship between the part in dashed box in Fig. 3 and the one in dashed box in Fig. 2. This conversion will change the four-order impedance matrix to a two-order one. Through operations of the impedance matrixes and their elements, the relationships are obtained and given by Equation (12):

$$Z_{e1} = Z_{11} - \frac{Z_{12}^2 Z_{33} + Z_{13}^2 Z_{22} - 2Z_{12}Z_{13}Z_{23}}{Z_{22}Z_{33} - Z_{23}^2},$$

$$Z_{e2} = Z_{44} - \frac{Z_{24}^2 Z_{33} + Z_{34}^2 Z_{22} - 2Z_{23}Z_{24}Z_{34}}{Z_{22}Z_{33} - Z_{23}^2},$$

$$Z_{em} = Z_{14} - \frac{Z_{12}Z_{24}Z_{33} + Z_{13}Z_{34}Z_{22} - Z_{23}(Z_{12}Z_{34} + Z_{13}Z_{24})}{Z_{22}Z_{33} - Z_{23}^2}. \quad (12)$$

Equation (12) suggests that primary side impedance Z_{e1} of the equivalent two-coil model is decided by the self-impedances of drive coil, transmit coil, receive coil, and the mutual-impedances among them. But it does not have a relationship with the load coil. Similarly, secondary side impedance Z_{e2} has no relationship with the drive coil. Mutual-impedance Z_{em} is independent of self-impedances of drive coil and load coil. It should be noticed mutual-impedance between the two equivalent coils contains resistance component R_{em}, because self-impedance Z_{22} and Z_{33} are included in the transfer relationship of the last equation in Equation (12).

B. Compensation capacitor design and experimental verifications

In order to verify the proposed general equivalent model and the compensation network design method, a WPT prototype for EV charging is developed. Where, a full bridge inverter is used as the power source, and the system load is a diode rectifier with resistor. The drive coil and transmit coil are set up together in the ground side, wound by Litz wires. Also, ferromagnetic materials are adopted to constraint electromagnetic field. The load coil and receive coil share the same structure in the vehicle side. The size of the coils is 40cm × 40cm, and the vertical distance between ground side and vehicle side coils is 20cm.

The prototype is designed with rated output power 3.3kW on the input DC voltage 300V. However, we are worried that the electric stress may be too large to harm the system or devices in large misalignment distances, if the prototype works in the rated power. Therefore, the input voltage is reduced to 100V with the output power 366.7W for most of the following experiments and analysis. The equivalent load resistance R_L is 23.2Ω, and system operation frequency is 100kHz. Values of other parameters are shown as follows: L_1=13.7uH, L_2=53.1uH,

L_3=44.2uH, L_4=12.1uH, M_{12}=21.6uH, M_{34}=19.1uH. Also, measured results of M_{13}, M_{14}, M_{23}, and M_{24} are given in Fig. 5, which all change with the lateral misalignment distance.

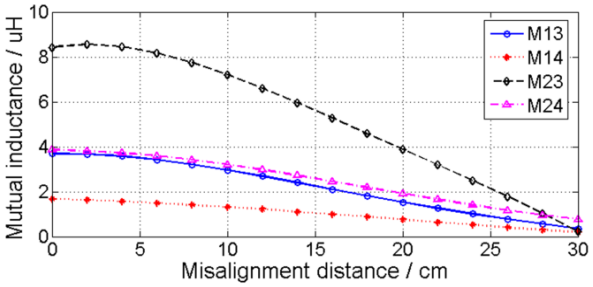

Fig. 5. Measured values of coil mutual-inductances on conditions of lateral misalignments.

Based on the parameter values in the prototype, the compensation capacitors have been designed, according to the design process shown in Fig. 4. Since there are four compensation capacitors in the four-coil WPT system, we can set four target equations. The first one is the target equation to get maximum efficiency, based on Equation (6); the second is P_{om} = 366.7W to make the system output rated power, based on Equation (8); the third is the target equation to adjust the inverter load reactive power, based on Equation (9); the last one is the target equation to keep system efficiency at 85% in the misalignment distance 20cm, to improve system misalignment tolerance, based on Equation (11). Simultaneously solving these four target equations and then fine tuning in practice, finally the values of the compensation capacitors can be obtained as follows: C_1=41.2nF, C_2=39.6nF, C_3=49.5nF, C_4=39.2nF.

On the basis of the designed compensation capacitors, the prototype has been completed, and the experimental waveforms are given in Fig. 6. It suggests the prototype works well on the conditions of both coil alignment and misalignment. Further tests show that the measured system efficiency (DC source to load resistor) is 92.5% on the condition of coil alignment, which meets the requirement of the first target equation. System output power is 367.8W, which approximately meets the requirement of the second target equation. System input reactance is very small on the condition of coil alignment, which has minimized the inverter load reactive power, and reduced electric stress of the power electrics devices. Measured system efficiency is 84.3% on the condition of misalignment distance 20cm, which is a little lower than the requirement of the last target equation. This is caused by some ignored factors, such as cable stray resistances, device on-off losses, etc.

To sum up, these experimental results have proved the effectiveness of the proposed general equivalent model and the compensation network design method.

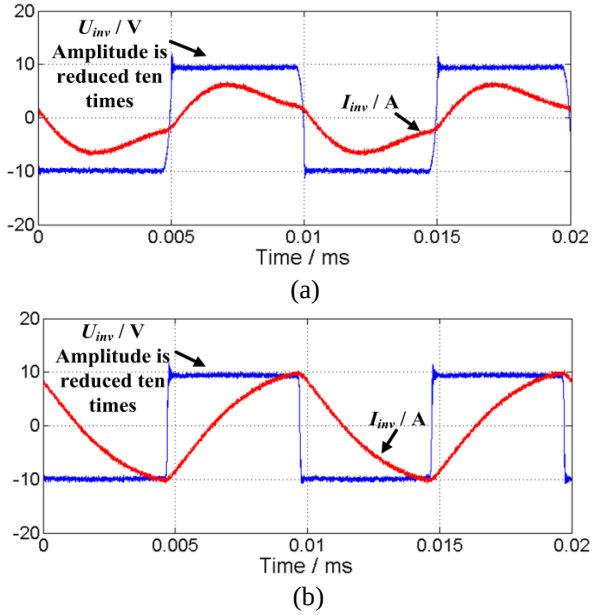

Fig. 6. Experimental waveforms of the inverter output voltages and currents. (a) On the condition of coil alignment; (b) on the condition of coil misalignment distance 20cm.

C. Equivalent characteristic analysis

Based on the parameter values of the developed WPT prototype, we can discuss the equivalent characteristics between the original multi-coil coupled model and the proposed equivalent model. In this section, system efficiency, input and output variables are used to analyze the equivalent features. Only power losses of the coils and compensation networks are considered. So, system efficiency shown in this section will be a little higher than the experimental results.

Calculated efficiencies according to the original four-coil coupled model and the proposed equivalent two-coil model are given in Fig. 7. Additionally, the result of existing simplified four-coil model [13], which ignores the mutual-inductances M_{13}, M_{14}, and M_{24}, is also given in Fig. 7 for comparison.

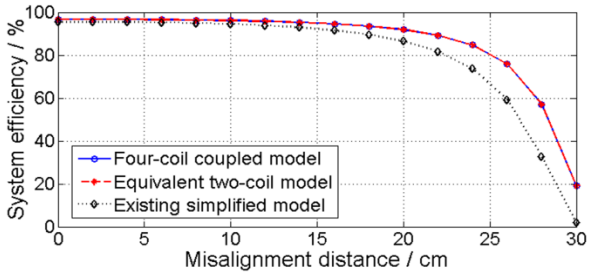

Fig. 7. Comparison of system efficiency calculation results among the original four-coil coupled model, the proposed equivalent two-coil model and the existing simplified four-coil model.

Figure 7 shows that the proposed equivalent two-coil model can get the same accurate system efficiencies as the original four-coil coupled model. This has been verified on the conditions of both coil alignment and misalignment. Because all the parameters in the four-coil coupled model are considered during the equivalent process, the equivalent two-coil model contains all information of the original model. Figure 7 also indicates that all system efficiency calculation results reduce with the misalignment distance, while the result of existing simplified model reduces faster. The existing simplified four-coil model has an acceptable deviation on the condition of coil alignment, only about 3%. However, with the increasing of misalignment distance, the deviation becomes bigger significantly, even reaches to more than 24% in the misalignment distance 28cm.

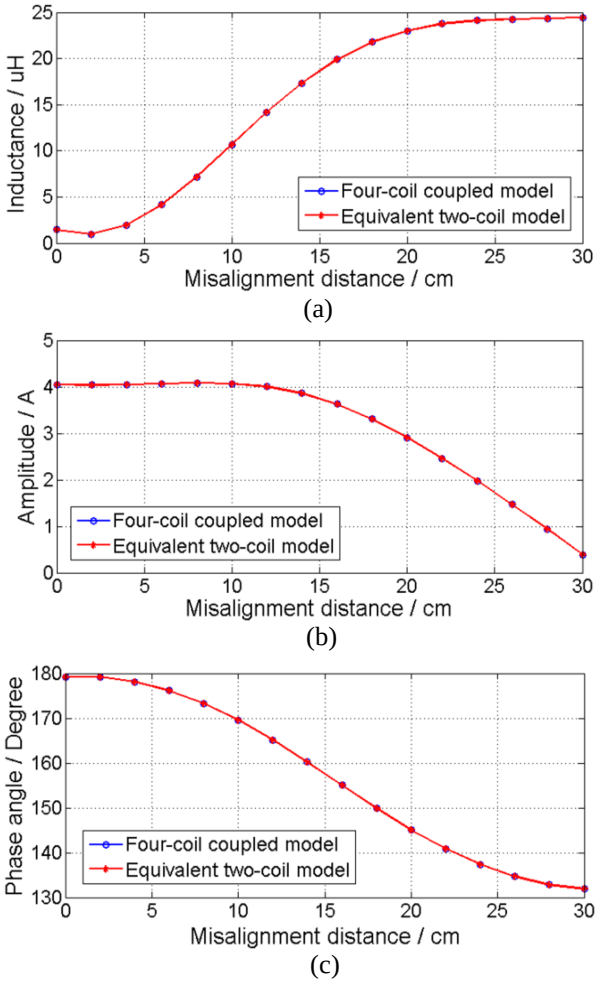

Fig. 8. Comparison of calculation results between the original four-coil coupled model and the proposed equivalent two-coil model. (a) Inverter load inductance L_{inv}; (b) amplitude of load current I_4; (c) phase angle of load current I_4.

Meanwhile, the calculation time based on the four-coil coupled model is 0.798ms, while the one with the proposed equivalent two-coil model is 0.058ms, according to the counting function in the software MATLAB. This result suggests the calculation time based on the proposed equivalent two-coil model is ten times less than the one based on the four-coil model. Its advantage on the calculation speed is very obvious, and will make it more effective in actual applications.

Moreover, other comparisons between the original four-coil coupled model and the proposed equivalent two-coil model are given in Fig. 8, including the calculation results of inverter load inductance L_{inv}, amplitude and phase angle of load current I_4. They suggest that the proposed equivalent two-coil model can get the same accurate input and output variables as the original four-coil coupled model. This has further proved its effectiveness.

Finally, the effect of mutual-resistance R_{em}, which is an obvious difference between the proposed model and the traditional two-coil WPT system model, is analyzed on the conditions of both coil alignment and misalignment. The efficiency calculation results with and without R_{em} are both shown in Fig. 9 for comparison.

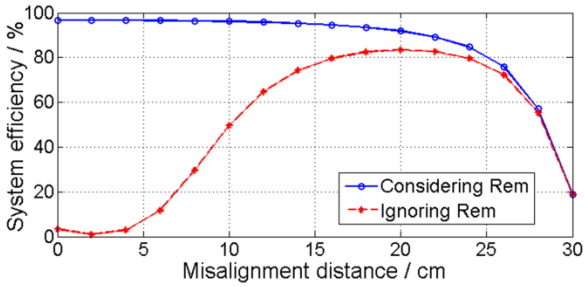

Fig. 9. Comparisons between calculated system efficiencies considering and ignoring R_{em}.

Figure 9 suggests that if ignoring R_{em}, the calculation results will have deviations, especially on conditions of coil alignment and small misalignment. So, R_{em} is an important parameter which affects the accuracy of efficiency calculation. Essentially, R_{em} is a parameter indicating the coupling degree between ground side and vehicle side coils. The stronger the coupling degree is, the greater its effect will be. When lateral misalignment distance increases, the coupling degree becomes weaker, and the effect of R_{em} becomes smaller. Hence, when ignoring R_{em}, the calculation deviation will decrease with the misalignment distance as shown in Fig. 9.

D. Numerical simulation analysis

Some issues arising with the proposed model and method are discussed based on numerical simulations. Firstly, a numerical simulation model is established

through the finite element analysis software COMSOL, according to the developed WPT prototype. The schematic of the 2D numerical simulation is shown in Fig. 10.

Then, the magnetic flux distribution is analyzed based on the 2D numerical simulation. Here, the rated output power 3.3kW is considered for this simulation, and the result is shown in Fig. 11. It suggests the major magnetic flux is confined within the air-gap between the coils, because of the ferromagnetic materials. The maximum magnetic flux density can be larger than 2mT, and the magnetic flux density in most of the space between the coils is larger than 1mT. However, the magnetic flux density will decrease fast in the space out of the air-gap between the coils. After a short distance away, it will reduce to less than 100uT.

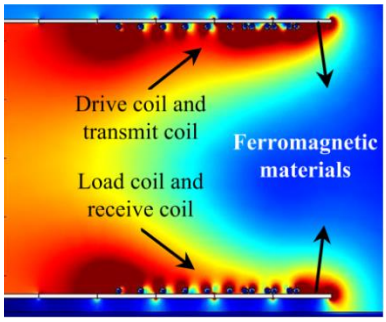

Fig. 10. 2D numerical simulation schematic of the developed WPT prototype.

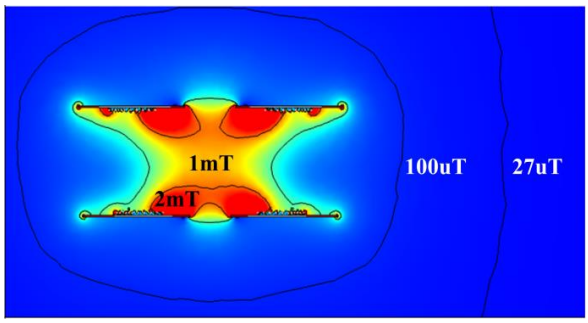

Fig. 11. Magnetic flux distribution simulation result of the developed WPT prototype.

Furthermore, the magnetic field exposure issue of WPT system is discussed for human safety concern, according to the International Commission on Non-Ionizing Radiation Protection (ICNIRP) guidelines [17]. The magnetic field exposure level should be under 27uT, at the frequency of 100kHz. As shown in the simulation result, the 27uT threshold line shifts outward from 573cm. Considering the scenario of EV wireless charging, most passage cars are more than 1500mm wide, which naturally keeps people around at least 700mm away. So, the ICNIRP guidelines can be met if the WPT prototype is set on the symmetrical centerline of the vehicular chassis.

Finally, the current distribution in the Litz wire used for the coils is analyzed, as well as the frequency effect. Here, a usually used frequency tuning range of 90kHz - 110kHz is adopted to show the frequency influence, considering system operation frequency 100kHz as the central frequency. Current distributions in Litz wire at different frequencies can be obtained from numerical simulation conducted by the software COMSOL. The simulation results are shown in Fig. 12, on the conditions of different frequencies.

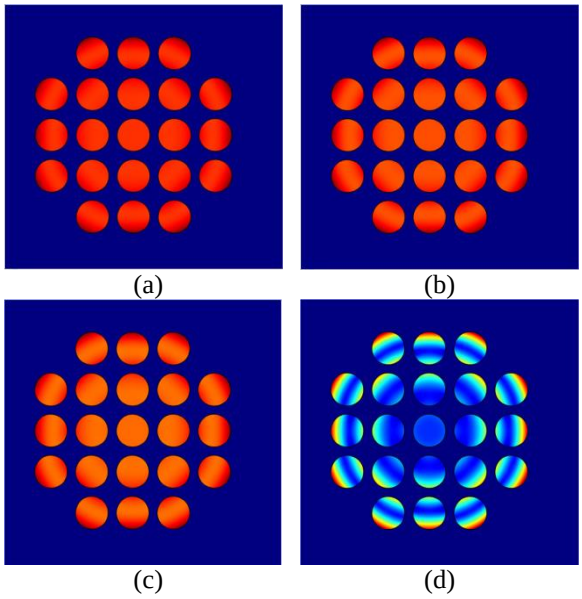

Fig. 12. Simulation results of frequency influence on the Litz wire current distribution. (a) Frequency: 90kHz; (b) frequency: 100kHz; (c) frequency: 110kHz; (d) frequency: 1MHz.

Figure 12 suggests the current distribution in Litz wire becomes more and more inhomogeneous, when frequency increases from 90kHz to 110kHz. But this inhomogeneity and the change of current distribution are both not very obvious in the frequency range of 90kHz - 110kHz. So, the numerical simulation results indicate that skin effect and proximity effect only have small effects on current distribution in the range usually used for frequency tuning. However, if the frequency continues increasing, the influence of skin effect and proximity effect will be significant as shown in Fig. 12 (d). In this case, AC resistance of the Litz wire will greatly increase and lead to substantial power losses.

E. Efficiency improvement

On the basis of the above analysis, a varied capacitor compensation method is presented to improve system efficiency on conditions of coil misalignments. As in Section IV.C, only the power losses of coils and compensation networks are considered.

Parameter values of the equivalent two-coil model will change with coil misalignment distance, and lead to efficiency reduction. If the load coil compensation capacitor C_4 is adjusted according to different misalignment distances, the influence of misalignment could be partly compensated. The optimal values of C_4 can be calculated through Equation (10), and the results are shown in Fig. 13. It suggests that the optimal compensation capacitor $C_{4\ opt}$ decreases with coil misalignment distance and has a large change range.

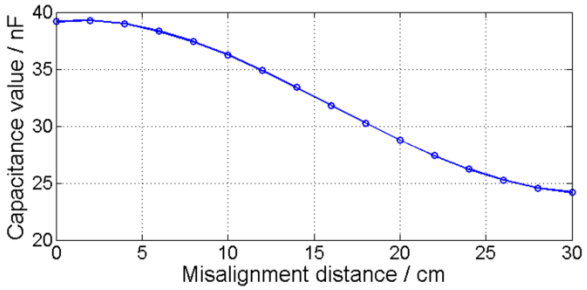

Fig. 13. Calculation results of the optimal load coil compensation capacitor $C_{4\ opt}$.

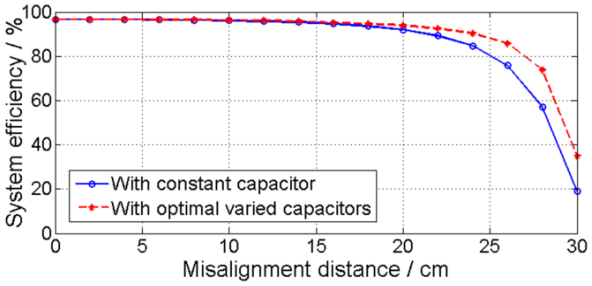

Fig. 14. Efficiency comparisons between adopting the constant capacitor and the optimal varied capacitors.

The varied capacitor compensation method is used in WPT system, and the results are shown in Fig. 14. It suggests system efficiency can be improved through this method, especially in the misalignment distances larger than 20cm. Further calculation indicates that the maximum efficiency improvement can reach up to 16%. These results have proved the effectiveness of the proposed efficiency improvement method.

V. CONCLUSION

This paper presents a novel general equivalent model for multi-coil WPT system analysis and its application on compensation network design. The proposed model has good accuracy because it contains complete information of the multi-coil WPT system. Also, it can lead to concise results, and fast calculation speed. These advantages make the compensation network design easier to be conducted, and has been verified by a developed WPT prototype on the conditions of both coil alignment and misalignment. The results show that the proposed equivalent model can get the same accurate efficiencies, input and output variables as the original multi-coil model; meanwhile, the compensation network design method works well. Based on the actual parameter values, the equivalent characteristics are analyzed, as well as the magnetic flux distribution, the magnetic field exposure issue, and the current distribution in coil Litz wire. Finally, a varied capacitor compensation method is presented to improve system efficiency. The proposed model and methods in this paper will be helpful for multi-coil WPT system analysis and design.

ACKNOWLEDGMENT

This work was supported by National Natural Science Foundation of China (51507168), and International Science & Technology Cooperation Program of China (2016YFE0102200).

REFERENCES

[1] X. Shi, C. Qi, M. Qu, *et al.*, "Effects of coil locations on wireless power transfer via magnetic resonance coupling," *Appl. Comput. Electromagn. Soc. J.*, vol. 31, no. 3, pp. 270-278, Mar. 2016.

[2] X. H. Jin, J. M. Caicedo, and M. Ali, "Near-field wireless power transfer to embedded smart sensor antennas in concrete," *Appl. Comput. Electromagn. Soc. J.*, vol. 30, no. 3, pp. 261-269, Mar. 2015.

[3] A. Kurs, A. Karalis, R. Moffatt, *et al.*, "Wireless power transfer via strongly coupled magnetic resonances," *Science*, vol. 317, no. 83, pp. 83-86, July 2007.

[4] Q. W. Zhu, L. F. Wang, and C. L. Liao, "Compensate capacitor optimization for kilowatt-level magnetically resonant wireless charging system," *IEEE Trans. Ind. Electron.*, vol. 61, no. 12, pp. 6758-6768, Dec. 2014.

[5] K. Fotopoulou and B. W. Flynn, "Wireless power transfer in loosely coupled links: coil misalignment model," *IEEE Trans. Magn.*, vol. 47, no. 2, pp. 416-430, Feb. 2011.

[6] J. H. Wang, S. L. Ho, W. N. Fu, *et al.*, "Analytical design study of a novel Witricity charger with lateral and angular misalignments for efficient wireless energy transmission," *IEEE Trans. Magn.*, vol. 47, no. 10, pp. 2616-2619, Oct. 2011.

[7] J. Yin, D. Y. Lin, C. K. Lee, *et al.*, "A systematic approach for load monitoring and power control in wireless power transfer systems without any direct output measurement," *IEEE Trans. Power Electron.*, vol. 30, no. 3, pp. 1657-1667, Mar. 2015.

[8] C. Zhang, W. X. Zhong, X. Liu, *et al.*, "A fast method for generating time-varying magnetic field patterns of mid-range wireless power transfer

systems," *IEEE Trans. Power Electron.*, vol. 30, no. 3, pp. 1513-1520, Mar. 2015.
[9] S. J. Zhou and C. C. Mi, "Multi-paralleled LCC reactive power compensation networks and their tuning method for electric vehicle dynamic wireless charging," *IEEE Trans. Ind. Electron.*, vol. 63, no. 10, pp. 6546-6556, Oct. 2016.
[10] J. Zhou, Y. Q. Gao, X. Y. Huang, *et al.*, "Voltage transfer ratio analysis for multi-receiver resonant power transfer systems," *IET Power Electron.*, vol. 9, no. 15, pp. 2795-2802, Aug. 2016.
[11] A. Junussov, M. Bagheri, and M. Lu, "Analysis of magnetically coupled resonator and four-coil wireless charging systems for EV," in *Proc. 2017 Int. Conf. Sustain. Energy Eng. and Appl.*, pp. 1-7, 2017.
[12] A. K. RamRakhyani and G. Lazzi, "On the design of efficient multi-coil telemetry system for bio-medical implants," *IEEE Trans. Biomed. Circuits Syst.*, vol. 7, no. 1, pp. 11-23, Feb. 2013.
[13] T. P. Duong and J. W. Lee, "Experimental results of high-efficiency resonant coupling wireless power transfer using a variable coupling method," *IEEE Microw. Wireless Compon. Lett.*, vol. 21, no. 8, pp. 442-444, Aug. 2011.
[14] J. W. Kim, D. H. Kim, and Y. J. Park, "Analysis of capacitive impedance matching networks for simultaneous wireless power transfer to multiple devices," *IEEE Trans. Ind. Electron.*, vol. 62, no. 5, pp. 2807-2813, May 2015.
[15] S. Q. Li, W. H. Li, J. J. Deng, *et al.*, "A double-sided LCC compensation network and its tuning method for wireless power transfer," *IEEE Trans. Veh. Technol.*, vol. 64, no. 6, pp. 2261-2273, June 2015.
[16] M. F. Fu, H. Yin, X. N. Zhu, *et al.*, "Analysis and tracking of optimal load in wireless power transfer systems," *IEEE Trans. Power Electron.*, vol. 30, no. 7, pp. 3952-3963, July 2015.
[17] International Commission on Non-Ionizing Radiation Protection, "ICNIRP Statement - Guidelines for Limiting Exposure to Time-varying Electric and Magnetic Fields," *Health Phys.*, vol. 99, no. 6, pp. 818-836, Dec. 2010.

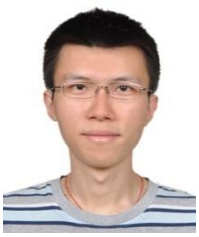

Yanjie Guo received the Ph.D degree in 2013 from the Institute of Electrical Engineering, Chinese Academy of Sciences (IEECAS).

Now he is an Associate Professor at the Department of Vehicle Energy System and Control Technology, IEECAS, and also at the Key Laboratory of Power Electronics and Electric Drives, Chinese Academy of Sciences. His research interests include wireless power transfer modeling and design, stationary wireless EV charging system, dynamic wireless EV charging system, electromagnetic compatibility (EMC), power electronics applications, and electromagnetic field analysis.

Lifang Wang got her Ph.D degree in 1997 from Jilin University. After that she joined the Institute of Electrical Engineering, Chinese Academy of Sciences (IEECAS). During the Chinese tenth-five year plan (2001-2005), she was a Member of the National Specialist Group of Key Special Electric Vehicle Project of the National 863 Program, and she was the head of the 863 Special EV Project Office.

She is currently the Director of Department of Vehicle Energy System and Control Technology at IEECAS. She is also the Vice Director of Key Laboratory of Power Electronics and Electric Drives, Chinese Academy of Sciences. Her research interests include wireless charging system for EV, electric vehicle control system, EV battery management system, electromagnetic compatibility and smart electricity use. She has directed more than 15 projects in these fields and has published more than 90 papers and 30 patents.

Chenglin Liao received the Ph.D. degree in Power Machinery and Engineering from Beijing Institute of Technology, Beijing, China, in 2001. After that he had spent 2 years as a Postdoctoral Researcher at the Tsinghua University.

He is now the Deputy Director of Department of Vehicle Energy System and Control Technology, Institute of Electrical Engineering, Chinese Academy of Sciences (IEECAS). His currently research is mainly on wireless charging system for electric vehicles.

LF Sky Wave Propagation Excited by a Horizontal Electric Dipole Towards Understanding of Its Radiation Mechanism

Honglei Xu, Tingting Gu, Juan Zheng, and Kai Li

Department of Information Science and Electronic Engineering
Zhejiang University, Hangzhou, 310012, China
hongleixu@zju.edu.cn, ttgu@zju.edu.cn, juanzheng@zju.edu.cn, kaili@zju.edu.cn

Abstract ─ In this paper, the electromagnetic pulses have been investigated based on the theory of wave-hop propagation. The approximate formulas are obtained for the electromagnetic field of a vertical magnetic dipole in the presence of an Earth-ionosphere waveguide. Based on the results obtained, the approximate formulas are derived readily for the ground wave and sky waves due to horizontal electric dipole excitation by using a reciprocity theorem. The corresponding computations and discussions are carried out specifically by analogy with those generated by a vertical electric dipole with the formulas in CCIR's recommendation. It is shown that the sky wave pulses would interfere at certain distances and occur by different time-delays.

Index Terms ─ Horizontal electric dipole, LF wave, wave-hop theory.

I. INTRODUCTION

Theoretical investigations of the electromagnetic wave propagation have led to a clearer understanding of radiation mechanism. During the last decades, the electromagnetic fields of vertical and horizontal electric dipoles in the Earth-ionosphere waveguide have been investigated for applications [1,2].

Early in the 1960's, the analytical formulas were derived for the ground wave and sky waves generated by horizontal and vertical electric dipoles in the Earth-ionosphere cavity. The details of the research findings are well summarized in a classic book [3]. It was demonstrated that the total field is a summation of ground wave and sky waves.

In the last decades, many researchers had revisited the problem and some new progresses had been made [4]. Recently, the ELF wave generated by a horizontal electric dipole was treated analytically in the Earth to anisotropic ionosphere cavity in former research by Li et al. [5]. The details of the study and ELF wave propagation in the presence of Earth-ionosphere cavity were summarized in the book by Pan and Li [6].

Based on these investigations, the LF (Low Frequency: from 30Hz to 300Hz) wave propagation is to be investigated in the present study for evaluations caused by a horizontal electric dipole source [7,8].

Despite calculations and measurements of the magnetic induction signal due to electromagnetic pulse had been presented earlier being utilized on radio detection of the radiation [9], it is necessary to investigate the radiation mechanism by analytical approximations. In the treatment of this problem, the transient field is also analyzed by the inverse Fourier transformation where an electric dipole moment is adopted here to represent the radiating source.

According to CCIR's recommendation, it is known that the total field on or near the spherical surface of the Earth is determined primarily by sky wave at long distances [10]. However, the explicit formulas have not been recorded in literature for ground wave and sky waves by horizontal electric dipole excitation. Therefore, the LF wave propagation due to horizontal electric dipole excitation is addressed in the present study.

In what follows, the computational scheme is developed when both the observation point and the transmitting antennas are located on the ground due to a horizontal electric dipole excitation. The influence of radiation mechanism radiation is investigated in time-domain for each ground pulse and sky pulses, respectively. When the observation point and the radiating source are located above the ground, the LF waves in variant of propagating paths are considered by the changes of the height factor.

II. FORMULATIONS

The geometry under consideration is shown in Fig. 1. The horizontal electric dipole representing for the radiating source is located on the upward-directed *z*-axis at a distance z_s from the origin of coordinates above the spherical Earth.

A. The electromagnetic field excited by a vertical magnetic dipole

Following the same manner in [6], we started by using ' $\boldsymbol{V}$ ' as the magnetic type potential function to represent LF waves which is generated by a vertical

Submitted On: November 1, 2017
Accepted On: January 9, 2018

magnetic dipole. They are:

$$\left.\begin{aligned} E_{\varphi} &= \frac{-\mathrm{i}\omega\varepsilon_0}{r}\frac{\partial(rV)}{r\partial\theta} \\ H_r &= -\frac{\frac{\partial}{\partial\theta}\sin\theta\frac{\partial V}{\partial\theta}}{r\sin\theta} \\ H_{\theta} &= \frac{1}{r}\frac{\partial^2}{\partial r\partial\theta}(rV) \end{aligned}\right\}, \tag{1}$$

where the wave equation is written as:

$$\nabla^2 V + k^2 V = 0\,. \tag{2}$$

By the method of separation of variables [11], we can derive the electromagnetic wave vectors in the earth-ionosphere waveguide in air as follows:

$$E_{\varphi} = E_0'\sqrt{\pi x}\mathrm{e}^{\mathrm{i}\frac{\pi}{4}}\sum \Lambda_m' G_m(z_s)G_m(z_r)\mathrm{e}^{\mathrm{i}t_m' x}\,, \tag{3}$$

$$\eta H_r = E_0'\sqrt{\pi x}\mathrm{e}^{\mathrm{i}\frac{\pi}{4}}\sum \Lambda_m' G_m(z_s)G_m(z_r)\mathrm{e}^{\mathrm{i}t_m' x}\,, \tag{4}$$

$$\eta H_{\theta} = iE_0'\sqrt{\pi x}\mathrm{e}^{\mathrm{i}\frac{\pi}{4}}\sum \Lambda_m' G_m(z_s)\frac{\partial G_m(z_r)}{k\partial z}\mathrm{e}^{\mathrm{i}t_m' x}\,, \tag{5}$$

where $x = (ka/2)^{1/3}\theta$, and

$$E_0' = \frac{\omega\mu_0 \mathrm{I}\mathrm{d}a}{\lambda a}\frac{\mathrm{e}^{\mathrm{i}ka\theta}}{\sqrt{\theta\sin\theta}} \qquad (\mathrm{V}\cdot\mathrm{m}^{-1})\,. \tag{6}$$

Unlike the traditional WKB approximation [12] Airy function is employed here in order to guarantee the higher accuracy of solution at the higher frequencies in LF band. The coefficients are derived correspondingly with the excitation factor expressed by:

$$\Lambda_m' = \left[t_m - (q^{he})^2 - (t_m - (q_i^{he})^2 - y_0) \times\left(\frac{W_1'(t_m) - q^{he}W_1(t_m)}{W_1'(t_m - y_0) + q_i^{he}W_1(t_m - y_0)}\right)^2\right]^{-1}, \tag{7}$$

and the height gain factor defined by:

$$G_t(r) = AW_1(t-y) + BW_2(t-y)\,, \tag{8}$$

where

$$A(t_m) = -\frac{W_2'(t_m - y_0) + q_i^h W_2(t_m - y_0)}{W_1'(t_m - y_0) + q_i^h W_1(t_m - y_0)}\,, \tag{9}$$

$$B(t_m) = -\frac{W_1'(t_m) - q^h W_1(t_m)}{W_2'(t_m) - q^h W_2(t_m)}\,, \tag{10}$$

and t_{m} are the roots of modal equation of magnetic type $A(t_m)B(t_m)=1$. Airy functions $W_1(t-y)$ and $W_2(t-y)$ are defined by:

$$W_{1,2}'(x) = \frac{1}{\sqrt{\pi}}\int_{\Gamma_{1,2}} \mathrm{e}^{ux-\frac{u^3}{3}}\mathrm{d}u\,. \tag{11}$$

B. Approximate formulas for ground wave and sky waves excited by a horizontal electric dipole

Based on the results derived, the electromagnetic components of LF wave are readily derived by using a reciprocity theorem. The six wave components are summarized as:

$$E_r^{he} = -\frac{iIds^{he}\eta}{\lambda a}\frac{e^{ika\theta}}{\sqrt{\theta\sin\theta}}\sqrt{\pi x}e^{i\frac{\pi}{4}}\cos\varphi \times i\sum \Lambda_n' Z_n(z_s)\left.\frac{\partial Z_n(z)}{k_0\partial z}\right|_{z=z_r}\left[1+\left(\frac{k_0 a}{2}\right)^{2/3}\frac{\mathrm{t}_n}{2}\right]^{-1} e^{it_n x}\,, \tag{12}$$

$$E_{\theta}^{he} = -\frac{Ids^{he}\eta}{\lambda a}\frac{e^{ika\theta}}{\sqrt{\theta\sin\theta}}\sqrt{\pi x}e^{i\frac{\pi}{4}}\cos\varphi \times\left\{-i\sum \Lambda_n'\left.\frac{\partial Z_n(z)}{k_0\partial z}\right|_{z=z_r}\left.\frac{\partial Z_n(z)}{k_0\partial z}\right|_{z=z_s} e^{it_n x} + \frac{1}{k_0 a\sin\theta}\sum \Lambda_m'\left.\frac{\partial G_m(z)}{k_0\partial z}\right|_{z=z_r}\left.\frac{\partial G_m(z)}{k_0\partial z}\right|_{z=z_s} e^{it_m x}\right\}\,, \tag{13}$$

$$E_{\varphi}^{he} = \frac{iIds^{he}\eta}{\lambda a}\frac{e^{ika\theta}}{\sqrt{\theta\sin\theta}}\sqrt{\pi x}e^{i\frac{\pi}{4}}\sin\varphi \times\left\{\frac{i}{k_0 a\sin\theta}\sum \Lambda_n'\left.\frac{\partial Z_n(z)}{k_0\partial z}\right|_{z=z_r}\left.\frac{\partial Z_n(z)}{k_0\partial z}\right|_{z=z_s} \times\left[1+\left(\frac{k_0 a}{2}\right)^{2/3}\frac{\mathrm{t}_n}{2}\right]^{-1} e^{it_n x} + \sum \Lambda_m'\left.\frac{\partial G_m(z)}{k_0\partial z}\right|_{z=z_r}\left.\frac{\partial G_m(z)}{k_0\partial z}\right|_{z=z_s} e^{it_m x}\right\}\,, \tag{14}$$

$$H_{\theta}^{he} = \frac{Ids^{he}}{\lambda a}\frac{e^{ika\theta}}{\sqrt{\theta\sin\theta}}\sqrt{\pi x}e^{i\frac{\pi}{4}}\sin\varphi \times\left\{\frac{i}{k_0 a\sin\theta}\sum \Lambda_n' Z_n(z_r)\left.\frac{\partial Z_n(z)}{k_0\partial z}\right|_{z=z_s} \times\left[1+\left(\frac{k_0 a}{2}\right)^{2/3}\frac{\mathrm{t}_n}{2}\right]^{-1} e^{it_n x} - \sum \Lambda_m'\left.\frac{\partial G_m(z)}{k_0\partial z}\right|_{z=z_r} G_m(z_s)e^{it_m x}\right\}\,, \tag{15}$$

$$H_{\varphi}^{he} = -\frac{iIds^{he}}{\lambda a}\frac{e^{ika\theta}}{\sqrt{\theta\sin\theta}}\sqrt{\pi x}e^{i\frac{\pi}{4}}\cos\varphi \times\left\{i\sum \Lambda_n' Z_n(z_r)\left.\frac{\partial Z_n(z)}{k_0\partial z}\right|_{z=z_s} e^{it_n x} + \frac{1}{k_0 a\sin\theta}\sum \Lambda_m'\left.\frac{\partial G_m(z)}{k_0\partial z}\right|_{z=z_r} G_m(z_s)e^{it_m x}\right\}\,, \tag{16}$$

$$H_r^{he} = -\frac{iIds^h}{\lambda a}\frac{e^{ika\theta}}{\sqrt{\theta\sin\theta}}\sqrt{\pi x}e^{i\frac{\pi}{4}}\cdot\sin\varphi\sum \Lambda_m' G_m(z)G_m(z_0)e^{it_m x}, \tag{17}$$

where the superscript '*he*' designates the horizontal electric dipole for the radiating source.

Therefore, the approximate formulas for the ground

wave and sky waves are correspondingly obtained by invoking of Equations (12)-(17) due to a horizontal electric dipole excitation. For simplicity, we take the radial electric field as an example. The ground wave is approximated by the fundamental term in Equation (12) expressed by:

$$E_r = E_0 V^{he}, \tag{18}$$

where

$$E_0 = -\frac{iIds^{he}\eta}{\lambda a}\frac{e^{ika\theta}}{\sqrt{\theta\sin\theta}} \quad (\mathrm{V/m}), \tag{19}$$

$$V^{he} = \sqrt{\pi x}e^{i\frac{\pi}{4}}\cos\varphi i\sum \Lambda_n' Z_n(z_s)\left.\frac{\partial Z_n(z)}{k_0\partial z}\right|_{z=z_r} \times\left[1+\left(\frac{k_0 a}{2}\right)^{2/3}\frac{t_s}{2}\right]^{-1}, \tag{20}$$

in which $t_s (s = 1, 2, 3, ...)$ are the sequential roots of modal equation defined by:

$$W_2'(t_s) - qW_2(t_s) = 0. \tag{21}$$

In the meanwhile, the first two sky waves are expressed by:

$$E_1^{he} = \frac{Ids^{he}\eta}{\lambda}\cos\varphi 2\mathrm{e}^{ik_0 L_1}\cos^2\psi_1 {}_{//}R_{//} DF_t F_r / L_1, \tag{22}$$

in which L_1 is the total ray length of the first-hop sky wave; ψ_1 is the arriving angle on the ground of the first-hop sky wave; D is the convergence coefficient due to the spherical curvature of the ionosphere; F_t and F_r represent for the antenna background factors of the launch point and observation point, respectively, caused by the earth curvature and the finite conductivity; ${}_{//}R_{//}$ is the ionospheric reflection coefficient where the subscript // indicates that the electric vectors of the incident wave and the reflected wave are parallel to the incident plane, respectively;

$$E_2^h = \frac{Ids^{he}\eta}{\lambda}\cos\varphi 2\mathrm{e}^{ik_0 L_2}\left(\cos\psi_2\right)^2 D^2 D_g F_t F_r \times\left({}_{//}R_{//}\cdot R_{g//}\cdot {}_{//}R_{//} + {}_{//}R_{\perp}\cdot R_{g\perp}\cdot {}_{\perp}R_{//}\right)/L_2, \tag{23}$$

in which L_2 is the total ray lengths of second-hop sky wave; ψ_2 is the arriving angle on the ground of the second-hop sky wave; D_g is the convergence coefficient due to the spherical curvature of the ground; ${}_{//}R_{\perp}$, ${}_{\perp}R_{//}$ are also the ionospheric reflection coefficients where the pre-subscripts indicate that the electric vector of the incident wave is parallel or perpendicular to the incident plane while the subscripts indicate that of the reflected wave is perpendicular or parallel to the incident plane, respectively.

The computational scheme of the above parameters in this paper is not developed in detail for simplicity which is similar to the case excited by a vertical electric dipole. The related calculation methods are found in the literature [10].

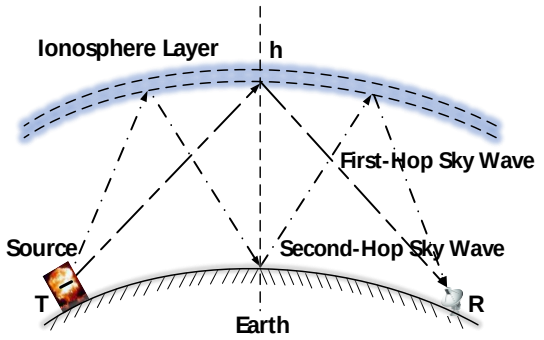

Fig. 1. The geometry of wave propagation routines due to a horizontal electric dipole excitation.

III. COMPUTATIONS AND DISCUSSIONS

Based on Equations (12)-(17), the evaluations are carried out for LF waves generated by the radiating source by horizontal electric dipole excitation in time-domain and frequency-domain, where z_s and z_r represent for the heights of radiating source and receiving point, respectively.

A. Radiation source located on the ground

To illustrate the general formulas for the field components obtained by horizontal electric dipole excitation, the computations are carried out at f = 200 KHz and f = 300 KHz in Fig. 2 for summer daytime where the ionosphere parameters taken as follows: the equivalent height of the ionosphere assumed to be h = 70 km, electron density $N = 10^9$ m^{-3}, electron collision frequency $\nu = 10^7$ s^{-1}, the ground which is characterized by the relative dielectric constant $\varepsilon_r = 80$, electrical conductivity $\sigma = 5$ S·m^{-1} and $z_r = z_s = 0$ km.

It is seen that when the receiving point and the radiating source are placed on the surface of the Earth, the ground wave decays along the propagation path, but for each sky wave the maximum value occurs after a certain propagation distance.

B. Radiation source located above the ground

Assuming the receiving point is on the ground and the radiating source is located at a certain distance from the origin of coordinates above the Earth, the computation for the ground wave is similar to that excited by a horizontal electric dipole on the ground except for the enhanced gain factor. But for the sky waves, corrections of angular distances should be additionally taken into consideration by the change of propagation paths.

(1) For the first-hop sky wave, the routine from the radiating source T to the receiving point R in Fig. 3 (a) experiences a reflex by path $\overline{TAP}$ before the hop path $\overline{APR}$. This can be equivalent by the contribution of the image source B which is identical to the source B on the ground in Fig. 3 (b)

with the equivalent Earth radius |OC|. Considering the equivalent Earth radius |OC| ≈ a, the propagation path is approximated in Fig. 3 (b) with the equivalent angular distance θ. By the triangle similarity of $\overline{PBA}$ and $\overline{PBC}$,

$$\frac{h}{h+d}=\frac{\rho-a\theta_1}{(a-d)(\rho/a+\theta_1)}, \tag{24}$$

$$\theta_1=\frac{\rho d+\rho hd/a}{2ah+ad-hd}. \tag{25}$$

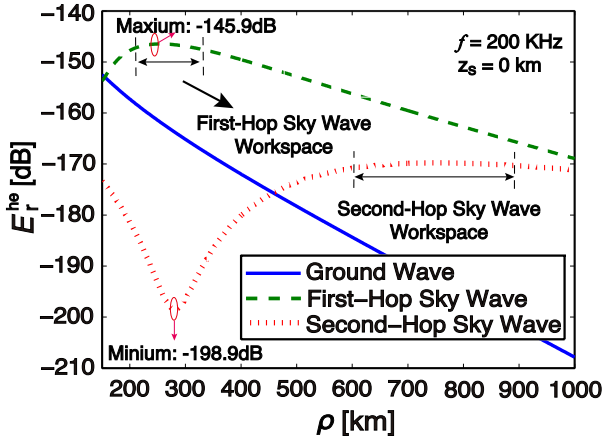

(a) f = 200 KHz

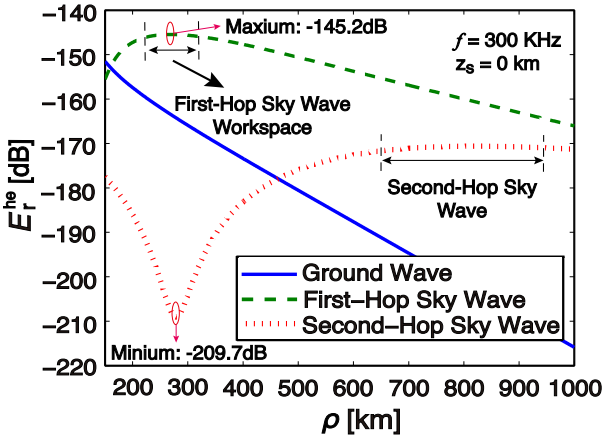

(b) f = 300 KHz

Fig. 2. Amplitudes of the electric field $\left|E_r^{he}(r,\theta)\right|$ in dB versus the propagating distances ρ due to unit horizontal electric dipole excitation; a = 6370 km, ε_r = 80, σ = 5 S·m^{-1}, and $z_r = z_s$ = 0 km; f = 200 KHz, 300 KHz, respectively.

(2) Similarly, for the second-hop sky wave, the propagation path $\overline{TAP_1BP_2R}$ in Fig. 4 (a) can be equivalent by the hop path $\overline{CAP_1BP_2R}$ excited by the image source C. Therefore, the propagation path is approximated in Fig. 4 (b) with the equivalent angular distance θ. By the triangle similarity of $\overline{PBA}$ and $\overline{PBC}$,

$$\frac{h-d}{h}=\frac{(\rho/a+\theta_1/2-2\theta_1)(a+d)}{a(\rho/a+\theta_1/2)}, \tag{26}$$

It leads to:

$$\theta_1=\frac{\rho d+\rho hd/a}{4ah-ad+3hd}. \tag{27}$$

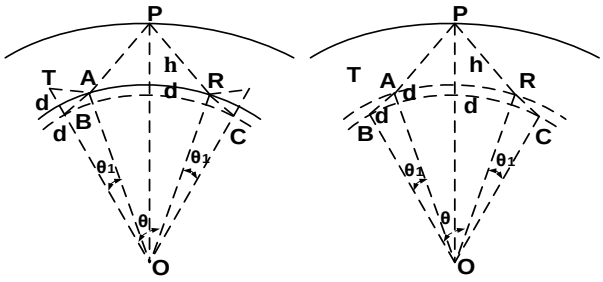

(a) First-hop sky wave (b) Equivalent model

Fig. 3. Propagation path for the first-hop sky wave when the receiving point and radiating source are located above the ground.

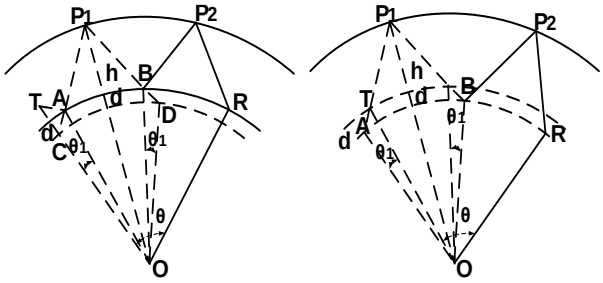

(a) Second-hop sky wave (b) Equivalent model

Fig. 4. Propagation path for the second-hop sky wave when the receiving point and radiating source are located above the ground.

(3) For the higher orders of sky waves, the equivalent angular distances will be more complicated to obtain. But for each sky wave vector, limited observable heights are requested for each hop wave due to the altered propagation path. In Table 1, the lowest observable heights are listed for the first-hop sky waves with propagation distances ρ = 100 km, ρ = 200 km, ρ = 300 km, and the radiating heights h = 10 m, h = 20 m, h = 30 m, respectively. It is seen that the lowest observable height restriction for the first hop sky wave is weakened as the increase of radial distance.

In Fig. 5, the electromagnetic field $\left|E_r^{he}(r,\theta)\right|$ are computed and plotted at the radiating height z_s = 5 km, radial distance ρ = 100 km due to unit horizontal electric dipole excitation, at the operating frequency f = 200 KHz and f = 300 KHz, respectively. It is shown that the maximum values and minimum values of the first two

hop sky waves occur periodically because of the interferences caused by the enhanced angular distances.

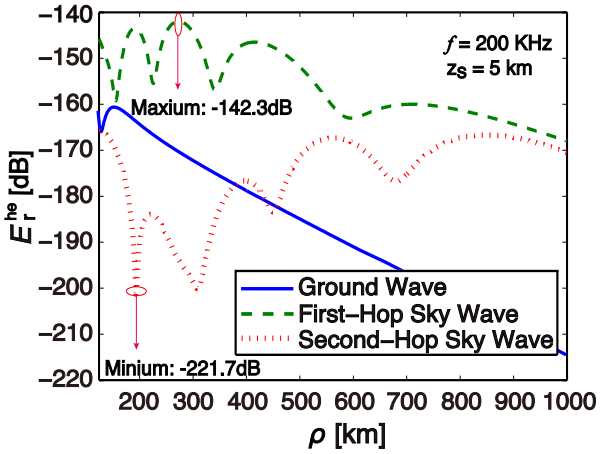

(a) f = 200 KHz; z_s = 5 km

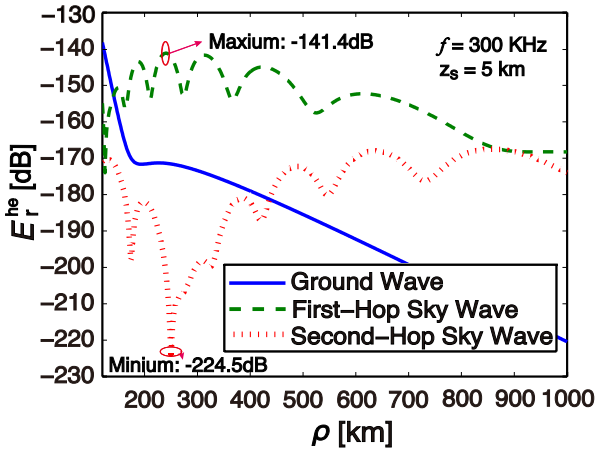

(b) f = 300 KHz; z_s = 5 km

Fig. 5. Amplitudes of the electric field $|E_r^{he}(r,\theta)|$ in dB versus the propagating distances ρ due to unit horizontal electric dipole excitation; a = 6370 km, ε_r = 80, σ = 5 S·m^{-1}, and z_s = 5 km; f = 200 KHz, 300 KHz, respectively.

C. Frequency-domain response

In Fig. 6, the electromagnetic components are evaluated by the variance of operating frequencies, with the radiating heights z_s = 0 km, 1 km, 5 km, and the distances ρ = 100 km, 200 km, 300 km, respectively. The equivalent height of the ionosphere assumed to be h = 90 km for summer day-time, electron density is N = 10^9 m^{-3}, electron collision frequency is ν = 10^7 s^{-1}, the ground which is characterized by the relative dielectric constant ε_r = 80 and electrical conductivity σ = 5 S·m^{-1}. It demonstrates that the radiation efficiency is improved by the enhancement of the radiating height. In the meanwhile, when the radiating source is located above the ground, the curves appear oscillatory decaying by the variance of frequencies.

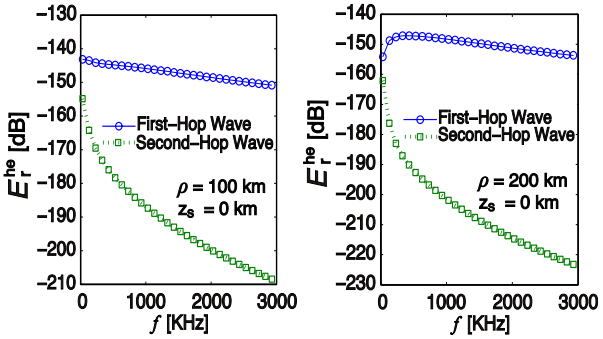

(a) ρ = 100 km; z_s = 0 km (b) ρ = 200 km; z_s = 0 km

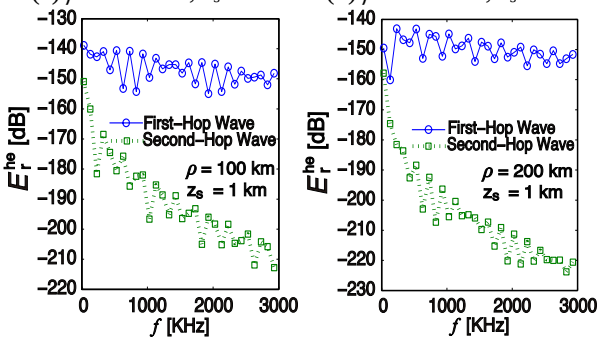

(c) ρ = 100 km; z_s = 1 km (d) ρ = 200 km; z_s = 1 km

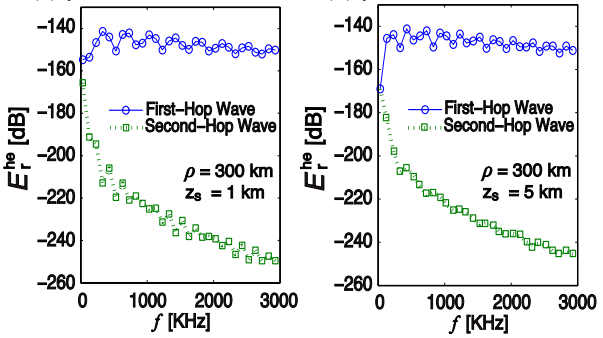

(e) ρ = 300 km; z_s = 1 km (f) ρ = 300 km; z_s = 5 km

Fig. 6. The electric field of sky waves due to horizontal unit electric dipole excitation versus the frequency; a = 6370 km, ε_r = 80, σ = 5 S·m^{-1}, and z_r = 0 km; ρ = 100 km, 200 km, 300 km, z_s = 0 km, 1 km, 5 km, respectively.

D. Time-domain response

Assuming that all parameters are same with those in Fig. 6, the characteristics of the transient electromagnetic field generated by a horizontal electric dipole are similar to those of vertical electric dipole case. The transient electric component $|E_r^{he}(r,t)|$ consisting of ground wave and two sky waves is computed by the inverse Fourier transformation excited by unit horizontal electric dipole and plotted in Figs. 7-8. This demonstrates the fact that excitation efficiency of a vertical dipole is much higher than that of a horizontal electric dipole for ground wave component, whereas with the increase of propagation distance, the sky wave part of the horizontal electric dipole radiation performance is better than vertical

electric dipole. Therefore, the radiating source is better described as a superposition of a vertical electric dipole representing for the ground wave and a horizontal electric dipole representing for the sky waves.

In Fig. 9, the ground wave and first two sky wave pulses are computed respectively. It appears that the ground pulse and sky waves arrive at distance ρ = 80 km and ρ = 150 km with different time-delays. Specifically, the time delay for each wave stay longer at the farther propagating distance.

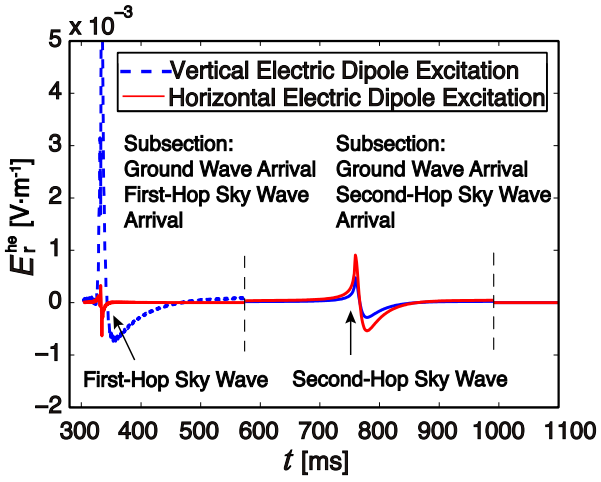

Fig. 7. The transient electric field $\left|E_r^{he}(r,t)\right|$ in V· m^{-1} due to a horizontal unit electric dipole; a = 6370 km, ε_r = 80, σ =5 S · m^{-1}, z_s =0 km, z_r = 0 km, ρ = 100 km, f = 200 KHz.

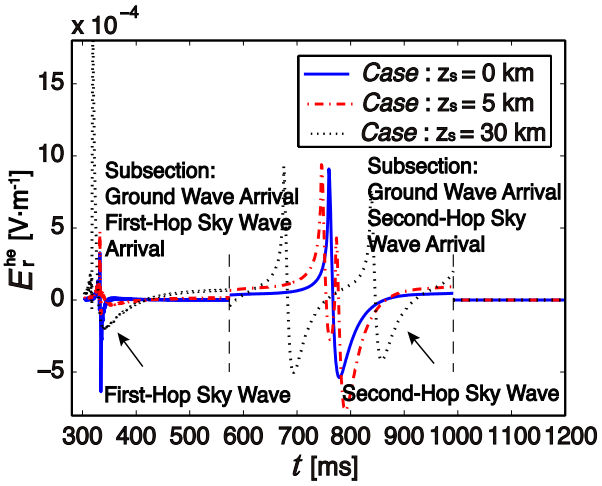

Fig. 8. The transient electric field $\left|E_r^{he}(r,t)\right|$ in V·m^{-1} due to a horizontal unit electric dipole; a = 6370 km, ε_r = 80, σ =5 S·m^{-1}, z_s =0 km, 5 km, 30 km, respectively, z_r = 0 km, ρ = 100 km, f = 200 KHz.

Table 1: Restriction on observing heights for first-hop sky wave

Distance (ρ/km)	HED Source (z_s/m)	Limit Observable Height at Receiving Point (z_r/m)
100	10	8.2777
	20	17.4862
	30	26.8464
200	10	6.7228
	20	15.1516
	30	23.8845
300	10	5.3333
	20	12.9931
	30	21.1103

**The limited observable heights are listed for the first-hop sky waves; for the higher modes of sky waves, the influence of revised angular distances are negligible compared to the first-hop wave. They are not listed.*

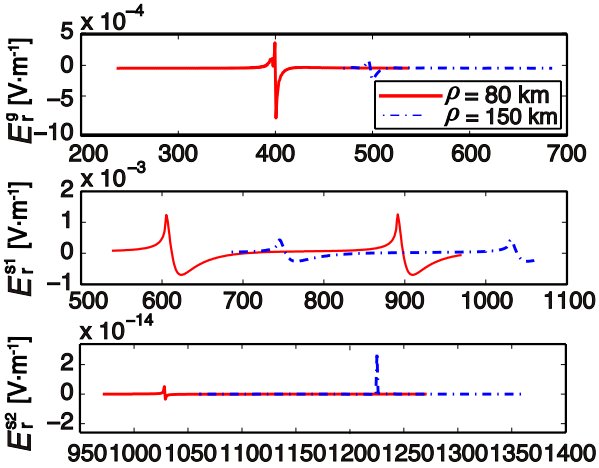

Fig. 9. The transient electric field $\left|E_r^{he}(r,t)\right|$ in V · m^{-1} due to horizontal unit electric dipole excitation; a = 6370 km, ε_r = 80, σ = 5 S · m^{-1}, and z_r = z_s = 0 km; ρ = 80 km, 150 km, respectively.

IV. CONCLUSIONS

The matter of LF sky wave propagation has been investigated by analytical approximation. In the present study, it is provided that: (i) Explicit formulas derived for the evaluations of LF ground wave and sky waves due to a horizontal electric dipole excitation; (ii) When both the observation point and the radiating source are located on the ground, it is demonstrated of high performance of radiation efficiency for ground wave by vertical dipole excitation over a horizontal electric one, while it is opposite for sky waves. (iii) The influence of LF radiation mechanism appears in time-domain

by different time-delays for the pulses. (iv) When the observation point and the radiating source are not located on the ground, the LF waves in variant of propagating paths are affected by the change of height factors and angular distances with restricted observable receiving heights for sky waves.

ACKNOWLEDGMENT

This work was supported by the [National Natural Science Foundation of China] under Grant [number 61271086, 61571389].

REFERENCES

[1] J. P. Casey, "Extremely Low Frequency (ELF) Propagation Formulas for Dipole Sources Radiating in a Spherical Earth-Ionosphere Waveguide," NUWC-NPT Technical Report 11,369, May 2002.

[2] S. Pal, "Numerical modelling of VLF radio wave propagation through earth-ionosphere waveguide and its application to sudden ionospheric disturbances," *Newweb.bose.res.in*, vol. 53, no. 2, pp. 33-37, May 2015.

[3] J. R. Wait, *Electromagnetic Waves in Stratified Media*. 2nd ed., New York: Pergamon, 1970.

[4] K. Li, *Electromagnetic Fields in Stratified Media.* Zhejiang University Press, pp. 409-415, 2009.

[5] G. Z. Li, T. T. Gu, and K. Li, "SLF/ELF electromagnetic field of a horizontal dipole in the presence of an anisotropic earth-ionosphere cavity," *Applied Computational Electromagnetics Society Journal*, vol. 29, no. 12, pp. 1102-1111, Dec. 2014.

[6] W. Y. Pan and K. Li, *Propagation of SLF/ELF Electromagnetic Waves.* Berlin Heidelberg: Springer, pp. 17-63, 2014.

[7] A. Nag and V. A. Rakov, "Lightning discharges producing very strong radiation in both VLF-LF and HF-VHF ranges," *2009 5th Asia-Pacific Conference on Environmental Electromagnetics*, vol. 427, no. 32, pp. 79-84, Oct. 2009.

[8] C. L. da Silva and V. P. Pasko, "Physical mechanism of initial breakdown pulses and narrow bipolar events in lightning discharges," *J. Geophys. Res. Atmos.*, vol. 120, no. 10, pp. 4989-5009, May 2015.

[9] A. Nag, V. A. Rakov, and D. Tsalikis, "New experimental data on lightning events producing intense VHF radiation bursts," *American Geophysical Union*, vol. 53, no. 12, pp. 199-204, Nov. 2008.

[10] CCIR Interim Method for Estimating Sky-wave Field Strength and Transmission Loss at Frequencies between the Approximate Limits of 2 and 30MHz. New Delhi: International Radio Consultative Committee; 1970. (CCIR Recommendation; no. 252-2).

[11] I. S. Gradshteyn and I. M. Ryzhik, "In table of integrals, series, and products," *Table of Integrals*, vol. 98, no. 3, pp. 1157-1160, Jan. 1980.

[12] D. M. Brink, "WKB Approximations," *Semi-classical Descriptions of Atomic & Nuclear Collisions*, vol. 13, no. 1712, pp. 241-251, 1985.

Hong Lei Xu was born in Jiangyin, Jiangsu, China, on June 7, 1990. She received the B.S. degree in Communication Engineering from Nanjing University of Posts and Telecommunications, Nanjing, China, in 2012, and the M.S. degree in Jiangsu University, Zhenjiang, China, in 2015, respectively.

She is currently working toward the Ph.D. degree in Electromagnetic Field and Microwave Technology with the College of Information Science and Electronic Engineering, Zhejiang University, Hangzhou, China. Her current research interests include radio wave propagation theory and its applications.

Ting Ting Gu was born in Leshan, Sichuan, China, on June 18, 1988. She received the B.S. degree and M.S. degree in Electromagnetic Field and Microwave Technology from Zhejiang University of Media and Communications, and Hangzhou Dianzi University, Hangzhou, China, in 2010 and 2013, respectively.

She is currently working toward the Ph.D. degree in Electromagnetic Field and Microwave Technology with the College of Information Science and Electronic Engineering, Zhejiang University, Hangzhou, China. Her current research interests include radio wave propagation theory and its applications.

Juan Zheng was born in Yulin, Shanxi, China, on October 6, 1992. She received the B.S. degree in Electronic Information Engineering from Xidian University, Xi'an, China, in 2015.

She is currently working toward the M.S. degree in Electromagnetic Field and Microwave Technology with the College of Information Science and Electronic Engineering, Zhejiang University, Hangzhou, China. Her current research interests include radio wave propagation theory and its applications

Kai Li was born in Xiao County, Anhui, China, on February 10, 1968. He received the B.S. degree in Physics from Fuyang Normal University, Anhui, China, in 1990, the M.S. degree in Radio Physics from Xidian University, Xi'an, Shaanxi, China, in 1994, and the Ph.D. degree in Astrophysics from Shaanxi Astronomical Observatory, the Chinese Academy of Sciences, Shaanxi, China, in 1998, respectively.

From August 1990 to December 2000, he was on the faculty of China Research Institute Radiowave Propagation (CRIRP). From January 2001 to December 2002, he was a Postdoctoral Fellow at Information and Communications University (ICU), Daejeon, Republic of Korea. From January 2003 to January 2005, he was a Research Fellow with the School of Electrical and Electric Engineering, Nanyang Technological University (NTU), Singapore. Since January 2005, he has been a Professor with the Department of Information Science and Electronic Engineering, Zhejiang University, Hangzhou, China. His current research interests include classic electromagnetic theory and radio wave propagation.

Li is a Senior Member of the Chinese Institute of Electronics (CIE) and a Member of the Chinese Institute of Space Science (CISS).

Radar Detection of Plasma-Covered Reentry Object Based on Crossed Two-Component LFM Signal

Xuyang Chen [1], Fangfang Shen [1], Yanming Liu [1], Xiaoping Li [1], and Wei Ai [2]

[1] School of Aerospace Science and Technology
Xidian University, Xi'an, Shaanxi 710071, China
xychen@mail.xidian.edu.cn, ffshen@mail.xidian.edu.cn, ymliu@xidian.edu.cn, xpli@xidian.edu.cn

[2] Science and Technology on Space Physics Laboratory
China Academy of Launch Vehicle Technology, Beijing 100076, China
27821126@qq.com

Abstract ─ A precise and efficient radar detection method based on crossed two-component LFM signal is proposed to deal with the detection problem of plasma-covered object. The method contains two segments: 1) design of transmitted signal, and 2) detection of object information (position and velocity) from the ambiguity function of the echo signal. For the first segment, the transmitted signal is designed to be a 2-component LFM signal with each component crossing with the other one in the time-frequency domain. The crossing design of the two components eliminates the disturbance term in solving the ambiguity function, guaranteeing the stability of detection. In the second segment, a mixed detection technique is proposed, which contains prior-information-based component classification and optimal parameters solution, maintaining both the accuracy and efficiency in detection. By the proposed method, both the efficiency in computation and accuracy in detection are achieved. The simulation results illustrate the validity of the method.

Index Terms─ Crossed two-component LFM signal, plasma sheath, radar detection, reentry object.

I. INTRODUCTION

The radar detection of plasma-covered reentry object arouses great attention in recent decade years with the development of applications like spacecraft recycle and radar surveillance. The emphasis in this research field lies in the study of the effect and its solution of plasma sheath on radar echo. Several researchers [1-6] carried out their work in this field and reveal some effect rules, including magnitude attenuation, dispersion in frequency, which may cause the deviation or failure in detection of object. However, these works mainly focused on the effect study of plasma sheath but few gave the way to overcome the effect. Certainly, there are some methods that can be used to deal with the plasma sheath effect to some extent, like appending magnetic field [7,8] and changing the antenna assembly of object [9]. Unfortunately, these methods are proposed to deal with the communication breakout problem but not suitable for the radar detection problem.

In our previous work [10], we proposed an idea of utilizing multi-component linear-frequency-modulation (LFM) signal to detect the radar echo of plasma-covered objects. The motivation of the idea is the consideration of the influence rule of plasma sheath on ambiguity function of the echo signal reflected by a plasma-covered object. The rule can be summarized as following: the plasma sheath can exert significant influence on the 2-D time-frequency position of the maximal point of ambiguity function, but its effect on the 2-D structure of energy distribution is trivial. Under this consideration, we found that, by using the multi-component LFM signal [11-16] as the transmitted signal, one can produce an ambiguity function with stable and detectable structure, which is a more suitable way to detect the plasma-covered object. However, the work in Ref. [10] is preliminary and leaves a key problem about how to detect the object from the echo for the case of multi-component LFM signal as transmitted signal.

There are several methods which can be used to detect the multi-component LFM signal, including fractional Fourier transform (FRFT) [12-14], Wigner-Hough transform (WHT) [15], Radon transform [16], etc. These methods are effective in solving the parameters of each component of the composite LFM signal. However, they have a common weakness, that is: the estimation precision of the parameters of components strongly relies on the setup of the increment of rotation angle and displacement quantity. A higher parameter precision means a smaller increment which implies a more complexity in calculation, restricting its real-time detection application. But the radar detection of reentry object, considered in this paper, requires both the

Submitted On: October 6, 2017
Accepted On: April 10, 2018

precision and real-time capability. Thus, these common methods mentioned above are not suitable for solving the detection problem in this paper.

Maintaining both the detection precision (or accuracy) and the real-time capability in the detection of multi-component LFM signal is an intractable problem. We tackle this problem only for the 2-component LFM signal in this paper. This is because the 2-component LFM signal is enough to acquire the stability and detectability in structure of the ambiguity function for the detection of plasma-covered object.

In this paper, we propose a precise and efficient radar detection method of plasma-covered object based on crossed 2-component LFM signal. The detection method contains two parts: 1) the design of transmitted signal, and 2) the detection of object information (position and velocity) from the ambiguity function of the echo signal reflected by a plasma-covered object. For the first part, the transmitted signal is designed to be a 2-component LFM signal with each component of the signal crossing with the other one in the time-frequency domain of ambiguity function. The crossing design of the two components eliminates the disturbance term in solving the ambiguity function, guaranteeing the stability of detection. For the second part, to maintain both the precision and efficiency in detection, we propose a mixed detection technique containing the prior-information-based component classification and the optimal parameters solution. By the proposed method, both the efficiency and accuracy in detection are achieved. The simulation results illustrate the validity of the method.

II. BACKGROUND OF RADAR DETECTION OF A PLASMA-COVERED OBJECT

Let a transmitted radar signal be $s(t)$. When the signal $s(t)$ meets with a plasma-covered reentry object, an echo signal $r(t)$ is generated. The relation of $r(t)$ and $s(t)$ can be expressed as follows [6]:

$$r(t) = [s(t) \otimes l(t) \otimes p(t)] \cdot \exp(j2\pi f_d t), \quad (1)$$

where t is the time variable within one pulse repetition interval (PRI) of a radar system, the sign '$\otimes$' represents convolution, $l(t)$ denotes the effect of space distance, $p(t)$ is the effect of the plasma surrounding the object to be detected, and f_d is the Doppler frequency caused by the velocity of the object.

Generally, the plasma effect on a radar echo is described by the reflection coefficient of plasma $\hat{p}(f)$ in frequency domain, expressed by

$$\hat{p}(f) = |\hat{p}(f)| \exp(j\varphi_p(f)), \quad (2)$$

where $|\hat{p}(f)|$ is the magnitude of $\hat{p}(f)$ and $\varphi_p(f)$ is the phase of $\hat{p}(f)$. Note, the $p(t)$ in (1) is a time-domain expression and it is the Inverse Fourier Transform of $\hat{p}(f)$.

The plasma affects a radar echo both on the magnitude and on the phase. Fiure 1 shows an example of the plasma effect based on the measurement data of 'RAM-C' experiment [17]. The label 'Diff. Phase' in Fig. 1 means the differential phase which reflects the change of phase. The 'Max Ne' denotes the maximal electron density of plasma, which is an important plasma parameter and is usually varying in a reentry flight of an object. Clearly, the plasma causes magnitude attenuation as well as phase jump in frequency domain, as shown in Fig. 1.

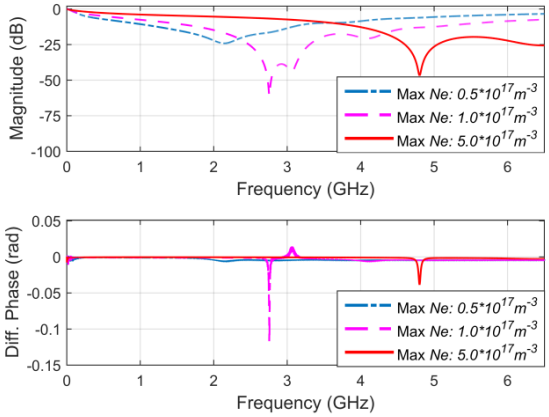

Fig. 1. An example of the plasma effect on echo signal both on magnitude (top figure) and on phase (bottom figure) in frequency domain.

To further reveal the plasma effect on radar detection, we then give the introduction of radar signal and that of ambiguity function analysis as follows. The LFM signal (with one component), as a common transmitted radar signal, is expressed as the form:

$$s(t) = A\exp(j(2\pi f_0 t + \frac{\pi}{T} Bt^2)), \quad (3)$$

where the symbols A, f_0, T, and B are the amplitude, center frequency, pulse width, and bandwidth of the transmitted signal, respectively.

The ambiguity function analysis of echo signal is a popular and useful method in radar detection, by which the object information about the position (reflected from the time delay) and the velocity (reflected from the Doppler frequency) of the object can both be determined. In addition, the resolution of the echo signal in the 2-D time-frequency domain can also be revealed from ambiguity function. Let the ambiguity function of echo $r(t)$ be $\chi(\tau, f)$, expressed by:

$$\chi(\tau, f) = \int_{-\infty}^{+\infty} s(t) r^{\dagger}(t+\tau) \exp(j2\pi ft) dt, \quad (4)$$

where the superscript '$\dagger$' denotes complex conjugation, and τ and f are the time delay and frequency shift,

respectively. By detecting the peak of the magnitude of $\chi(\tau, f)$, one can estimate the true time delay and the true Doppler frequency of an object to be detected. Certainly, the environmental interference or noise (such as the plasma effect considered here) may influence the estimation error.

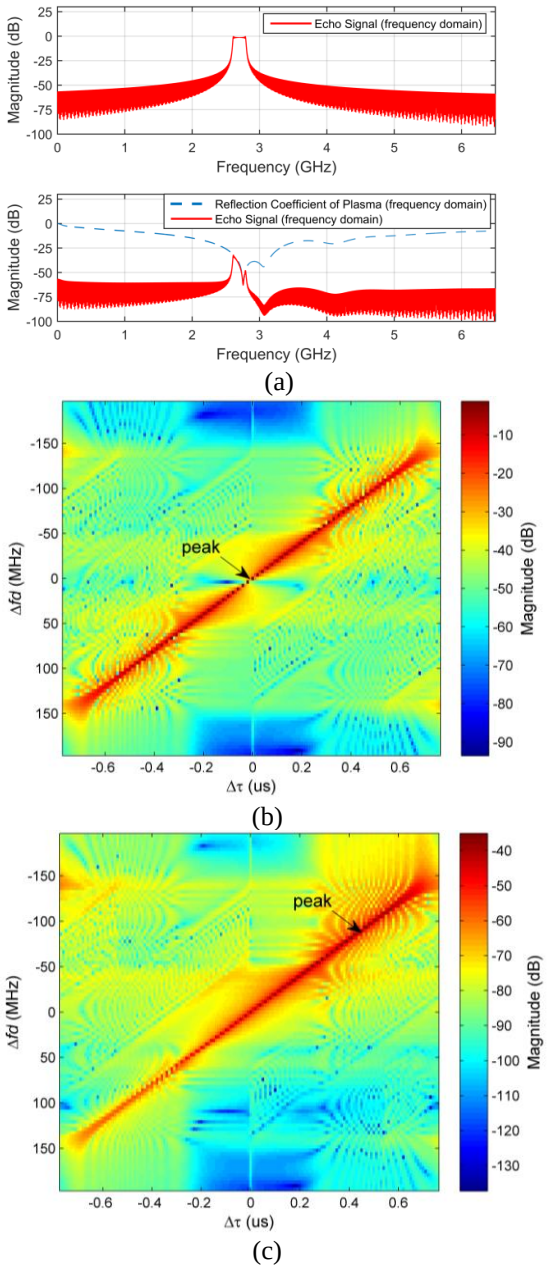

Fig. 2. Comparison of echo signal without plasma effect and that with plasma effect in magnitude. (a) Magnitude of echo signal without (top) and with (bottom) plasma effect in frequency domain. (b) Magnitude of echo signal without plasma effect in time-frequency domain. (c) Magnitude of echo signal with plasma effect in time-frequency domain.

Note: the echo signal $r(t)$ as well as the transmitted signal $s(t)$ in (4) are usually of intermediate frequency form in realistic radar system, which implies a down-conversion operation with a frequency f_{down}. Whatever f_{down} is, it only results in an additional oscillation with fixed frequency on the whole ambiguity function $\chi(\tau, f)$ but not affects the energy distribution of $\chi(\tau, f)$. With this in mind, we omit the down-conversion frequency f_{down} in (4).

Figure 2 shows a comparison of echo signal without plasma effect and that with plasma effect in the frequency domain and in the time-frequency domain solved by ambiguity function. The plasma effect in the figure is selected to be a severe case to obtain an obvious comparison (the same with that described by the purple dashed line in Fig. 1). The transmitted signal is selected to be a LFM signal with parameters: f_0 =2.7GHz, B=200MHz, and $T = 1us$. The horizontal coordinate and vertical coordinate of the ambiguity function (sub-figure (b), (c)) are the time axis (denoted by $\Delta\tau$) and frequency axis (denoted by Δf_d), respectively. Note: the true time delay and true Doppler frequency in the ambiguity function are both set to be zero here to make the comparison clear.

It can be found from Fig. 2 (a), compared with the echo signal in the top sub-figure, that in the bottom sub-figure has an obvious magnitude distortion and attenuation in frequency band due to the plasma effect. From the comparison of Fig. 2 (b) and Fig. 2 (c), it is clear that the peak of the ambiguity function is shifted largely in the time-frequency domain, also the magnitude of the major energy distribution is attenuated. The effect of plasma will result in distinct deviation in detection of the object in position and velocity.

III. RADAR DETECTION OF PLASMA-COVERED OBJECT BASED ON CROSSED TWO-COMPONENT LFM SIGNAL

A. Design of transmitted signal

As shown in the Introduction section, the proposed radar detection method contains two parts, shorted by signal design and object detection here. The object detection is obviously the key of the proposed detection method, by which the object information of an echo hidden in its time-frequency structure is extracted. Before the presentation of the object detection, the signal design has to be introduced firstly.

As indicated in our previous work [10], the peak point of ambiguity function of echo signal in magnitude is sensitive to the plasma effect, but its 2-D structure of energy distribution is insensitive to the plasma effect. Thus, if one can design a transmitted signal with a robust and detectable structure, the plasma effect will be reduced significantly. To meet this requirement, we

designed a 2-component LFM signal as follows:

$$s(t) = A\sum_{i=1}^{2} \exp(j(2\pi f_0 t + (-1)^i \frac{\pi}{T} Bt^2)),\ t \in [-\frac{T}{2}, \frac{T}{2}], \quad (5)$$

where A, B, T, and f_0 are the common amplitude, bandwidth, pulse width and center frequency of the two components. Note: the two components in (5) are designed to cross with each other in time-frequency domain, which suppresses the generation of disturbance term in time-frequency domain.

Figure 3 shows an example of ambiguity function for such an echo signal (without plasma effect). The setup of parameters is same with that in Fig. 2 except for the signal type changing to two-component LFM signal. As shown in Fig. 3, the two components of LFM signal cross with each other, with the crossing point at the center of each component, complying with (5).

The horizontal coordinate and vertical coordinate of the crossing point in Fig. 3 represent the true time delay (reflecting the true position of object) and the true Doppler frequency (reflecting the true velocity of object), respectively. Therefore, the object information (including the true position and velocity of the object) can be extracted by detection of the crossing point of the two components. Actually, detecting the crossing point of the two components is equivalent to detecting the structure of the 2-D energy distribution of the LFM signal in ambiguity function. This is because the crossing point, as a main quantitative expression of the crossing characteristic of the 2-D energy structure, possesses a stable and robust position (2-D coordinate), reflecting the stability of the structure. Clearly, the shift of the energy peak of any one component along its main energy region (a 'line') cannot affect the position of the crossing point, reflecting its stability.

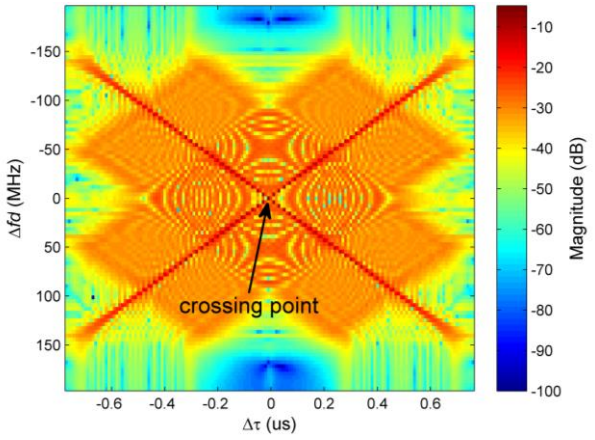

Fig. 3. The magnitude of ambiguity function of echo signal for the case of a two-component LFM signal as the transmitted signal (without plasma effect).

B. Detection method based on crossed two-component LFM signal

As stated in Sec. III-A, the crossing point of the two components of the LFM signal contains the information of true time delay and that of true Doppler frequency. However, the direct detection of the crossing point with high precision is a difficult problem. We tackle this problem from the following thinking: the parameters of the two components can be calculated at first, with which an equation set is generated; by solving the equation set, one can work out the crossing point. The key problem in the thinking is how to obtain an efficient and accurate estimation (or calculation) of the parameters of the two components.

To deal with the problem, we propose a mixed detection method containing prior-information-based component classification and optimal parameters solution. Different from the scenarios in Ref. [12-16], in the detection application of this paper, we have an important prior information about the echo signal reflected from a plasma-covered object. That is: the echo signal is initially produced from a transmitted signal whose parameters (center frequency, bandwidth, and pulse width) is known in advance. There are differences between the echo signal and the transmitted signal due to plasma effect. But, the differences are minor from the view of the whole 2-D time-frequency ranges where the main echo energy locates (see Fig. 3).

In detail, the available information which can be used as prior information is listed as two parts as below.

a) From the aspect of actual application, the Doppler frequency shift in an echo signal relative to the bandwidth of its corresponding transmitted signal is significantly small, making it possible to partition the 2-D time-frequency figure of the echo signal along the Doppler frequency axis.

b) The bandwidth B and pulse width T of the transmitted signal determine the slope of the two 'energy lines' of the main energy regions of ambiguity function to be $\pm\frac{B}{T}$.

By utilizing the 'part *a*' prior information shown above, we will classify all the available peak points in the two 'energy lines' of echo signal in the 2-D time-frequency domain. A schematic diagram about the procedure has been drawn in Fig. 4. As shown in the figure, we first partition the 2-D time-frequency figure along the time axis (horizontal axis) to obtain two valid regions and one fuzzy region. Then we pick all the valid peak points from the leftmost column to the rightmost column of the data in the valid region of $|\chi(\tau, f)|$. Only those peak points lying in the two 'energy lines' (marked by 'line1' and 'line2') are thought to be valid and can be picked. Note that the 'lines' composed of the picked

points are broken off by the fuzzy region, forming a fracture region along the vertical axis. Finally, we classify all the picked points into their corresponding 'energy lines' ('line1' or 'line2') according to separation effect caused by the fuzzy region and the fracture region.

'energy lines'. Actually, by using the 'part *b*' prior information of the transmitted signal listed before, we find that there are only two undetermined parameters b_1 and b_2, which comply with the following equations:

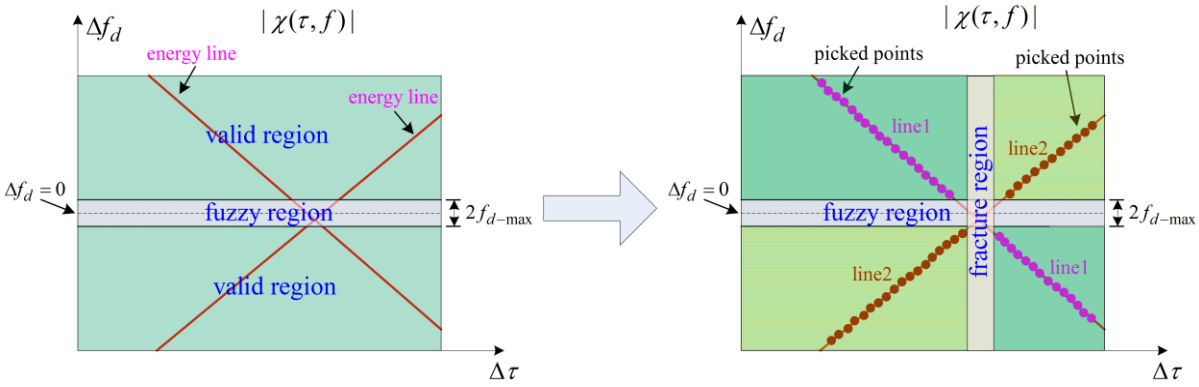

Fig. 4. Schematic diagram of peak points classification based on prior information of transmitted signal.

The determination of the range of the fuzzy region is indeed the determination of the maximal Doppler frequency $f_{d-\max}$. It is related to the maximal relative velocity $v_{\max}$ between the object to be detected and the radar station, complying with the following equation:

$$f_{d-\max} \approx \frac{|v_{\max}|}{c} f_0, \tag{6}$$

where c is the speed of light, and f_0 is the center frequency of transmitted signal. Usually, the velocity $v_{\max}$ is set as large as possible to ensure the validity of the classification shown in Fig. 4.

In the picking of the peak points in the 'energy lines', there is a magnitude threshold labeled by $M_{T(\mathrm{dB})}$ here (in 'dB' form). For one column of the data in the valid region of $|\chi(\tau, f)|$, only the maximal point larger than $M_{T(\mathrm{dB})}$ is thought to be a valid peak point (in an 'energy line') and is picked. The threshold is determined by the following equation:

$$M_{T(\mathrm{dB})} = |\chi(\tau, f)|_{\max(\mathrm{dB})} - C_{T(\mathrm{dB})}, \tag{7}$$

where $|\chi(\tau, f)|_{\max(\mathrm{dB})}$ is the maximum of $|\chi(\tau, f)|$ in 'dB' form, and $C_{T(\mathrm{dB})}$ is a const value in 'dB' form indicating the boundary of the main energy region of the components. The value $C_{T(\mathrm{dB})}$ is set as 6dB here. In some extreme case where the echo signal is extreme weak, one can consider to set a smaller $C_{T(\mathrm{dB})}$ (such as the half-power boundary 3dB) to obtain a more stable results.

After picking the points and classifying them, one can evaluate the undetermined parameters of the two

$$b_1 = f_{p1} + \frac{B}{T}\tau_{p1}, \tag{8a}$$

$$b_2 = f_{p2} - \frac{B}{T}\tau_{p2}, \tag{8b}$$

where (τ_{p1}, f_{p1}) and (τ_{p2}, f_{p2}) are the time-frequency coordinate of a picked point in 'line1' and that in 'line2', respectively.

The optimal b_1 and b_2 are labeled as $b_{1(opt)}$ and $b_{2(opt)}$, respectively. They are the solution of the following optimization problem:

$$b_{1(opt)} = \arg\min_{b_1} \sum_{n=1}^{N_1} \left(b_1 - \left(f_{p1(n)} + \frac{B}{T}\tau_{p1(n)} \right) \right)^2, \tag{9a}$$

$$b_{2(opt)} = \arg\min_{b_2} \sum_{n=1}^{N_2} \left(b_2 - \left(f_{p2(n)} - \frac{B}{T}\tau_{p2(n)} \right) \right)^2, \tag{9b}$$

where N_1 and N_2 are the number of picked points in 'line1' and that in 'line2', respectively, and $(\tau_{p1(n)}, f_{p1(n)})$ and $(\tau_{p2(n)}, f_{p2(n)})$ are the coordinate of the *n*-th picked point in 'line1' and that in 'line2', respectively.

The optimization problem (9a) and (9b) just can be solved by the least square method which can generate the optimal results in the sense of minimizing the energy of error. Whereas the undetermined parameter here is only one for one problem (9a) or (9b), so the solution form is simple, as shown below:

$$b_{1(opt)} = \frac{1}{N_1} \sum_{n=1}^{N_1} \left(f_{p1(n)} + \frac{B}{T}\tau_{p1(n)} \right), \tag{10a}$$

$$b_{2(opt)} = \frac{1}{N_2} \sum_{n=1}^{N_2} \left(f_{p2(n)} - \frac{B}{T}\tau_{p2(n)} \right). \tag{10b}$$

Replacing b_1 and b_2 in (8a) and (8b) by $b_{1(opt)}$ and $b_{2(opt)}$ respectively, then combining (8a) and (8b) to be simultaneous equations and solving the variables f and τ, we obtain the evaluation of the crossing point of the two components. By simplification of the result, the time delay τ_E and Doppler frequency f_{d-E} of the crossing point can be expressed as follows:

$$\begin{cases} \tau_E = \dfrac{(b_{1(opt)} - b_{2(opt)})T}{2B}, \\ f_{d-E} = \dfrac{b_{1(opt)} + b_{2(opt)}}{2}. \end{cases} \tag{11}$$

Obviously, τ_E and f_{d-E} correspond to the estimated time delay and estimated Doppler frequency of the object to be detected, respectively. The error of τ_E and that of f_{d-E} can then be defined as:

$$\begin{cases} \Delta\tau_E = \tau_E - \tau_{True} \\ \Delta f_{d-E} = f_{d-E} - f_{d-True}, \end{cases} \tag{12}$$

where τ_{True} and f_{d-True} denote the true time delay and true Doppler frequency of the object, respectively.

IV. SIMULATIONS

In this section, we will illuminate the validity of the proposed method. Also we will give a comparison of the method to the common FRFT-based method to show its superiority. The software for simulation is MATLAB R2014, and the computer hardware setting is as follows: CPU: Intel Core i5 3.3GHz, Memory: 8GB, OS: Windows7-64bit.

To show the validity of the proposed method, the noise is considered in the simulation. The signal-noise-ratio (SNR) is employed to measure the noise level, which is defined as follows:

$$SNR = 10\log_{10}(P_S / P_n), \tag{13}$$

where the unit of SNR here is dB, and P_S and P_n are the power of signal (echo signal without noise) and that of noise, respectively. As for each test SNR, we make statistical measures with 100 times (generating 100 noise samples). For each noise sample, we test four block sizes of the time-frequency matrix obtained by ambiguity function. Some common parameters settings are given as below. The center frequency of transmitted signal is $f_0 = 2.7\text{GHz}$, the model of transmitted signal is adopted as a 2-component LFM signal as shown in Sec. III. The plasma effect is selected to be the same case described in the purple dashed line in Fig. 1, which is a severe case for the selected transmitted radar signal. The default true time delay and Doppler frequency of an object is set as 3.5us and 342KHz, respectively.

A. Validation of the proposed method

A fixed transmitted signal is simulated with pulse width 50us and bandwidth 100MHz. One can find that the ambiguity resolutions of this transmitted signal in time delay and Doppler frequency are 10ns (1/100MHz) and 20KHz (1/50us), respectively. In the calculation of ambiguity function, the discrete size (or block size) of the generated function needs to be considered. Clearly, larger size can provide finer time-frequency structure which is helpful for estimation, but it will be more time-consuming. In contrast, smaller size case provides coarser time-frequency structure but is more efficient in calculation. As a simplification, the generated figures of ambiguity function are considered to be square (the same number of rows and columns). We select four different block sizes (number of rows or columns) for test: [500, 250, 125, 63], which are in a reasonable range for real-time radar detection. Figure 5 shows the estimation errors for the time delay and Doppler frequency by the proposed method for the four block sizes at SNRs of -20dB, -10dB, and 0dB, respectively. For each selected SNR and block size, there are 100 results generated corresponding to 100 noise samples and drawn in Fig. 5.

As shown in Fig. 5, the estimated time delay and Doppler frequency tend to concentrate with the increase of SNR. As for the block size, its influence on the concentration of estimation results is trivial, but it will affect the deviation of the results. Usually, the smaller the block size, the larger the deviation of estimated results.

Whereas the most important fact observed from Fig. 5 is that the proposed method can work in an acceptable way even at an extreme SNR of -20dB (see Fig. 5 (a)). In this extreme SNR case, the estimated results are still not over the ambiguity resolution (10ns in time delay and 20KHz in Doppler frequency) and have not generate 'bad point', which shows the high estimated accuracy and stability of the proposed method.

To show the deviation and error of the estimated time delay and Doppler frequency from a quantitative view, we calculate the average deviation and the std (standard deviation) of the estimated results. The tested SNRs are extended to five cases for sufficient test: -20dB, -15dB, -10dB, -5dB, and 0dB. Let $|\overline{\Delta\tau_E}|$ be the absolute average error of time delay and $|\overline{\Delta f_{d\text{-}E}}|$ be the absolute average error of Doppler frequency. Let $\delta_{\Delta\tau_E}$ be the std of time delay error and $\delta_{\Delta f_{d-E}}$ be the std of Doppler frequency error. Fig. 6 shows the statistic results of the average deviation and std.

As presented in Fig. 6, the average deviation of time delay and that of Doppler frequency are both insensitive to SNR. Whereas they can be affected by the block size distinctively. In general, larger block size is more possible to generate smaller estimated deviation, which conforms to the results in Fig. 5. As for the std of estimated error, the influence of SNR predominates.

With the increase of SNR, the stds of estimated errors both for time delay and Doppler frequency decrease.

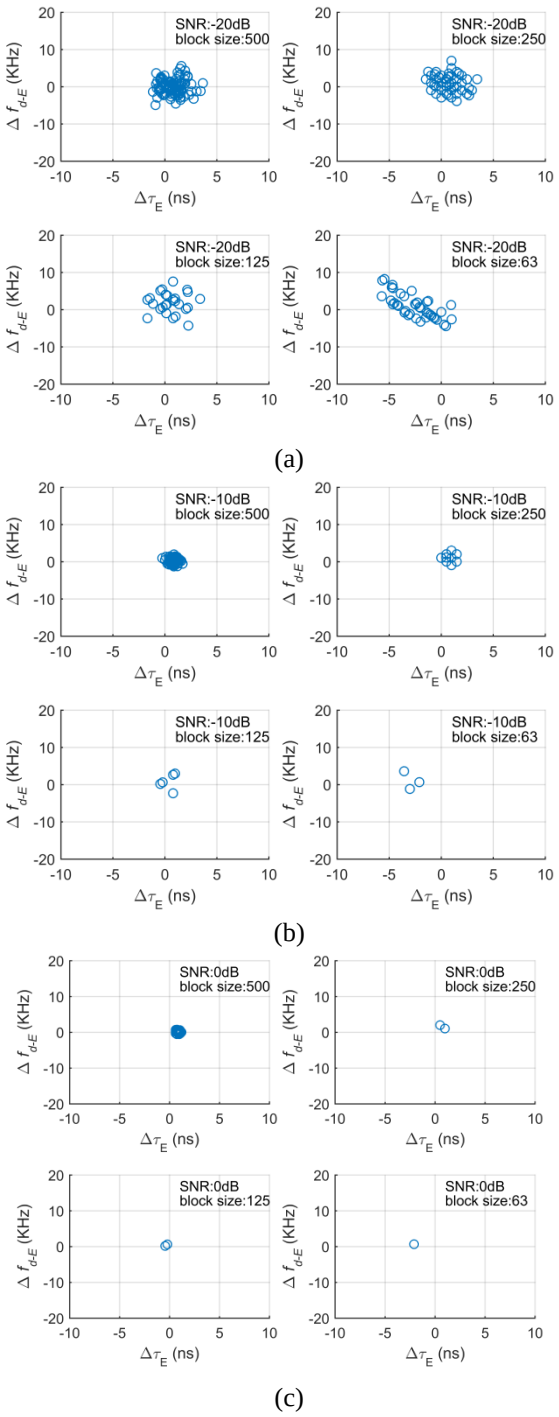

Fig. 5. The estimation errors for time delay $\Delta\tau_E$ and Doppler frequency Δf_{d-E} for 4 block sizes of time frequency matrix at different SNRs. (a) SNR=-20dB, (b) SNR=-10dB, and (c) SNR=0dB.

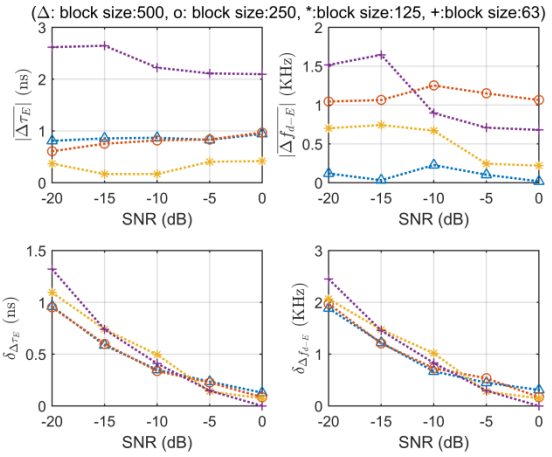

Fig. 6. Average deviation and std of the estimated time delay and Doppler frequency by the proposed method. Top left: absolute average error of time delay $|\overline{\Delta\tau_E}|$ vs SNR; top right: absolute average error of Doppler frequency $|\overline{\Delta f_{d\text{-}E}}|$ vs SNR; bottom left: std of time delay error $\delta_{\Delta\tau_E}$ vs SNR; bottom right: std of Doppler frequency error $\delta_{\Delta f_{d-E}}$ vs SNR.

One can also find that the maximal deviation of estimated time delay is not larger than 3ns and that of the Doppler frequency is not larger than 1.5KHz. Both of them are lower than the ambiguity resolution (10ns for time delay and 20KHz for Doppler frequency) significantly. As for the stds of estimated errors, they are also much lower than the ambiguity resolution even for the extreme SNR of -20dB.

For the time consumption, the proposed method also has superiority. Actually, the most time-consuming part of the method lies in the calculation of ambiguity function. In the simulation of Fig. 5, at any a fix SNR and a fixed noise sample, the algorithm consumes near the same time of about 0.5s for each block case without considering the calculation of ambiguity function. For the calculation of ambiguity function, it takes about 10.4s, 5.6s, 2.8s, and 1.6s for the block sizes 500, 250, 125, and 63, respectively. Certainly, in the calculation of ambiguity function, the fast algorithm is employed. However, one should note that the simulation in this paper does not utilize the parallel computing. Whereas in the realistic application, the parallel computing is highly suggested, which can further significantly reduce the consumed time.

B. Comparison of the proposed method to FRFT-based method

To evaluate the proposed method fairly, we employ the common FRFT-based method to estimate the time

delay and Doppler frequency. For fair comparison, the related parameters are set same with that by the proposed method shown above. The block sizes of the angle-shift region in FRFT are set as [500, 250, 125, 63], the same with that in Sec. VI-A. Figure 7 shows the estimated results for SNR=-20dB.

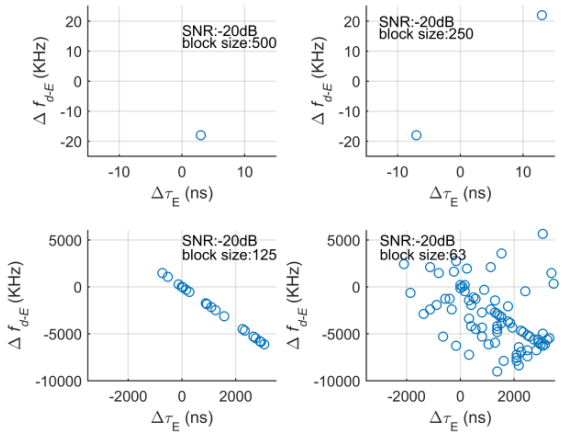

Fig. 7. The estimation errors for time delay $\Delta\tau_E$ and Doppler frequency Δf_{d-E} by FRFT for four block sizes at SNR=-20dB.

As for the block cases 500 and 250 as shown in Fig. 7, the maximal divergences of estimated results have reached about 20KHz for Doppler frequency and 10ns for time delay even though the results have better concentration. As for the cases with block sizes 125 and 63, however, the estimated results are flawed. Comparing these results with that by the proposed method as shown in Fig. 5 (a), one can find the resulting deviation by the proposed method is smaller (not larger than half of that by FRFT). Furthermore, as for the block sizes 125 and 63, the proposed method also generates acceptable result with smaller deviation.

The detailed estimated results for other SNRs are not shown here for saving space. Instead, we calculate the average deviation and the std of the estimated results for all the five candidate SNRs (including -20dB, -15dB, -10dB, -5dB, and 0dB) and present them in Fig. 8. Considering the huge estimation errors for blocks 125 and 63 at lower SNRs, we separate these blocks into two groups and plot the results in two sub-figures, as shown in Figs. 8 (a) and (b).

As shown in Fig. 8 (a), the average deviation and the std for the block sizes 125 and 63 do not reach a 'normal level' until the SNR gets to a larger level (≥ -10dB here). Yet the average deviation in the 'normal level' is still much larger than that by the proposed method in Fig. 6, even though the std reaches zero. Take a look at the case of SNR=0: for $|\overline{\Delta f_{d\text{-}E}}|$, the deviation reaches 141.9KHz for block size 63 and 19.4KHz for block size 125; for $|\overline{\Delta\tau_E}|$, it reaches 7.4ns for the two block sizes. For block sizes 500 and 250 in Fig. 8 (b), the estimated results appear to be stable ($\delta_{\Delta\tau_E} = \delta_{\Delta f_{d-E}} = 0$) for SNR≥-15dB. Whereas, the average deviations are nearly not affected by the SNR and are in a higher level than that by the proposed method in Fig. 6. For SNR≥-15dB, $|\overline{\Delta f_{d\text{-}E}}|$ reaches 18KHz for both the block sizes 500 and 250, and $|\overline{\Delta\tau_E}|$ reaches 7ns for block size 250 and 3ns for block size 500.

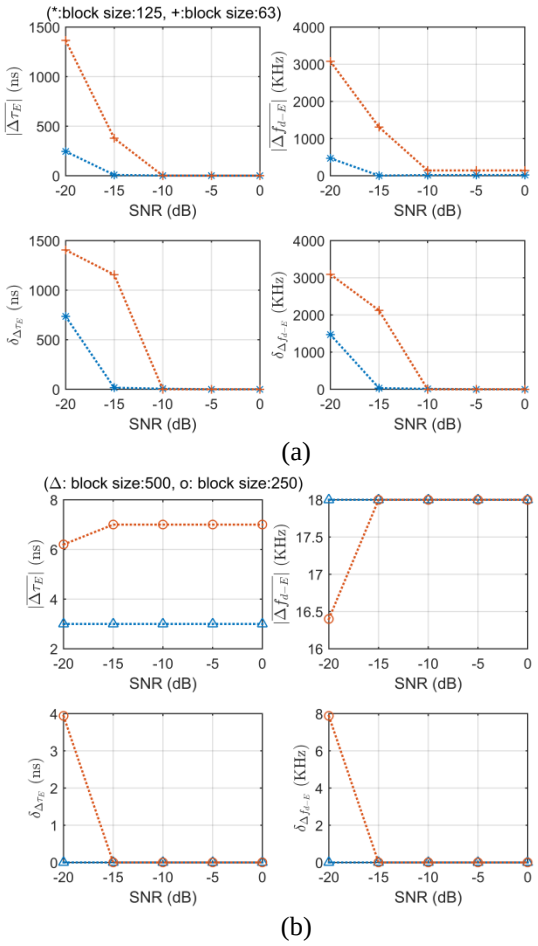

(a)

(b)

Fig. 8. Average deviation ($|\overline{\Delta\tau_E}|$ and $|\overline{\Delta f_{d\text{-}E}}|$) and std ($\delta_{\Delta\tau_E}$ and $\delta_{\Delta f_{d-E}}$) of the estimated time delay and Doppler frequency by FRFT. (a) Block sizes: 125 and 63. (b) Block sizes: 500 and 250.

The larger deviations of the estimated results by FRFT are mainly due to that the estimation precision mainly relies on the setup of increment (or the block size mentioned here), as indicated in the Introduction Section. Whereas, given the same block size, the proposed method makes full use of the block information (exactly, the 'energy line' information) and the prior information,

with the estimation results solved by an optimal scheme on those information. This results in a much higher improvement in estimation, as shown in Fig. 5 and Fig. 6.

For the time consumption, at any a fix SNR and a fixed noise sample, it is about 1210s for calculating all the four block cases in all, including 894s, 244s, 57s, and 15s for the block sizes 500, 250, 125, and 63, respectively. It is very time-consuming compared with the proposed method. The applicable fast algorithm of FRFT in the scenarios of this paper is in the consideration of our further work.

In all, the simulation results above show the validity of the proposed method in precision and efficiency. In addition, the results also illustrate the stability of the proposed method, in which acceptable estimation results are generated without 'bad point' even for SNR=-20dB. The comparison to FRFT-based method further shows the superior of the proposed method in solving the radar detection problem of plasma-covered objects.

V. CONCLUSION

In this paper, we proposed a precise and efficient radar detection method based on crossed 2-component LFM signal to deal with the detection problem of plasma-covered objects. By designing the transmitted signal to be a crossed 2-component LFM signal and detecting the object information from the ambiguity function of echo signal, the accuracy and efficiency are achieved. The simulation results illustrate the validity of the proposed method in accuracy, efficiency, and stability in estimating the object information (position and velocity). In our further work, some more extreme cases for plasma influence will be studied and also the detection of multiple objects will be considered.

ACKNOWLEDGMENT

This work was supported by the National Science Foundation of China under Grants 61701380, the Science and Technology on Space Physics Laboratory Funds, and the China Postdoctoral Science Foundation (No. 2016M592758).

REFERENCES

[1] J.-T. Li and L.-X. Guo, "Research on electromagnetic scattering characteristics of reentry vehicles and blackout forecast model," *J. Electromagnet. Wave*, vol. 26, no. 13, pp. 1767-1778, 2012.

[2] H. Torres-Silva, N. Reggiani, and P. H. Sakanaka, "Electromagnetic properties of a chiral-plasma medium," *ACES Journal*, vol. 12, no. 1, pp. 14-18, 1997.

[3] W. Liu, J. Zhu, C. Cui, and X. Wang, "The influence of plasma induced by α-particles on the radar echoes," *IEEE Trans. Plasma Sci.*, vol. 43, no. 1, pp. 405-413, 2015.

[4] S.-H. Liu and L.-X. Guo, "Analyzing the electromagnetic scattering characteristics for 3-D inhomogeneous plasma sheath based on PO method," *IEEE Trans. Plasma Sci.*, vol. 44, no. 11, pp. 2838-2843, Nov. 2016.

[5] M.-Y. Wang, H.-L. Li, Y.-L. Dong, G.-P. Li, B.-J. Jiang, Q. Zhao, and J. Xu, "Propagation matrix method study on THz waves propagation in a dusty plasma sheath," *IEEE Trans. Antenn. Propag.*, vol. 64, no. 1, pp. 286-290, Jan. 2016.

[6] X. Chen, K. Li, Y. Liu, Y. Zhou, X. Li, and Y. Liu, "Study of the influence of time-varying plasma sheath on radar echo signal," *IEEE Trans. Plasma Sci.*, vol. 45, no. 12, pp. 3166-3176, Dec. 2017.

[7] S. V. Bobashev and Y. P. Golovachov, "Deceleration of supersonic plasma flow by an applied magnetic field," *J. Propul. Power*, vol. 19, no. 4, pp. 538-546, July 2003.

[8] M. Kim, M. Keidar, and I. D. Boyd, "Analysis of an electromagnetic mitigation scheme for reentry telemetry through plasma," *J. Spacecraft Rockets*, vol. 45, no. 6, pp. 1224-1229, Nov. 2008.

[9] I. F. Belov, V. Y. Borovoy, V. A. Gorelov, A. Y. Kireev, A. S. Korolev, and E. A. Stepanov, "Investigation of remote antenna assembly for radio communication with reentry vehicle," *J. Spacecraft Rockets*, vol. 38, no. 2, pp. 249-256, Mar. 2001.

[10] Y. Zhou, X. Chen, K. Li, Y. Liu, and Y. Liu, "The application of multi-component LFM signals to radar detection of plasma-covered reentry object," in *2017 International Applied Computational Electromagnetics Society Symposium (ACES 2017)*, Suzhou, China, p. 1937, Aug. 2017.

[11] J. Su, H.-H. Tao, X. Rao, and J. Xie, "Coherently integrated cubic phase function for multiple LFM signals analysis," *Electron. Lett.*, vol. 51, no. 5, pp. 411-413, 2015.

[12] P. Wang, J.-Y. Yang, and Y.-M. Du, "A fast algorithm for parameter estimation of multi-component LFM signal at low SNR," *IEEE Int. Conf. Communications, Circuits and Systems Proceedings*, Hong Kong, China, vol. 2, pp. 765-768, 2005.

[13] H.-T. Qu, R.-H. Wang, W. Qu, and P. Zhao, "Research on DOA estimation of multi-component LFM signals based on the FRFT," *Wireless Sensor Network*, vol. 1, no. 3, pp. 171-181, 2009.

[14] F. Liu, H.-F. Xu, R. Tao, and Y. Wang, "Research on resolution between multi-component LFM signals in the fractional Fourier domain," *Science China: Information Sciences*, vol. 55, no. 6, pp. 1301-1312, June 2012.

[15] Q. Guo, Y.-J. Li, C.-H. Wang, and H.-Y. Cao, "Novel detection method for multi-component LFM signals," *Int. Conf. Pervasive Computing Signal Processing and Applications (PCSPA)*,

Harbin, China, pp. 759-762, Sept. 2010.
[16] Y.-X. Li and X.-C. Xiao, "Recursive filtering radon-ambiguity transform algorithm for detecting multi-LFM signals," *Chinese J. Electron.*, vol. 20, no. 3, pp. 161-166, May 2003.
[17] P. W. Huber, N. D. Akey, W. F. Croswell, and C. T. Swift, "The entry plasma sheath and its effects on space vehicle electromagnetic systems," *NASA, Washington, DC, USA, Tech. Note SP-252*, p. 1-630, 1971.

Xuyang Chen was born in Hebei, China, in 1980. He received the B.S., M.S., and Ph.D. degrees in Electronic Engineering from Xidian University, Xi'an, China, in 2005, 2008, and 2011, respectively. He joined the CAST-Xi'an Institute of Space Radio Technology, Xi'an, as an Engineer in 2011, where he is involved in radar detection and space navigation. He is currently a Teacher with the School of Aerospace Science and Technology, Xidian University. His current research interests include the radar detection of reentry vehicles covered by plasma sheath.

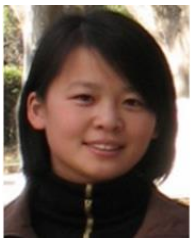

Fangfang Shen received the B.S., M.S. and Ph.D. degrees in Telecommunications Engineering from Xidian University, Xi'an, China, in 2006, 2009, and 2015, respectively. She is currently a Teacher with the School of Aerospace Science and Technology, Xidian University. Her research interests include high-resolution radar imaging and DOA estimation.

Yanming Liu was born in Shaanxi, China, in 1966. He received the B.S., M.S., and Ph.D. degrees from Xidian University, Xi'an, China, in 1989, 1993, and 2003, respectively. He is currently a Full Professor with the School of Aerospace Science and Technology, Xidian University. His current research interests include telecommunication network technology and wireless communication.

Xiaoping Li was born in Shanxi, China, in 1961. She received the B.S., M.S., and Ph.D. degrees from Xidian University, Xi'an, China, in 1982, 1988, and 2004, respectively. She is currently a Full Professor with the School of Aerospace Science and Technology, Xidian University. Her current research interests include telemetry, tracking and command technology.

Wei Ai was born in Shanxi, China, in 1977. He received the B.S. degree from North University of China in 2000, and M.S. degrees from China Academy of Launch Vehicle Technology in 2011. He is currently a senior Engineer with China Academy of Launch Vehicle Technology. His current research interests include communication technique and system integration design.

The Investigation of Backscattering Characteristics of 3-D Local Sea Surface with Time-varying Overturning Wave Crest

X. Meng [1], L. X. Guo [2], S. R. Chai [2], and Y. C. Jiao [1]

[1] National Key Laboratory of Antennas and Microwave Technology
Xidian University, Xi'an, Shaanxi 710071, China
mengxxidian@126.com

[2] School of Physics and Optoelectronic Engineering
Xidian University, Xi'an, Shaanxi 710071, China
lxguo@xidian.edu.cn, srchai1989@gmail.com, ychjiao@xidian.edu.cn

Abstract ─When there exists overturning wave crest on the sea surface, the sophisticated coupling effect between the overturning wave crest and sea surface may give rise to sea spikes. As sea spikes will cause the increase of radar false probability, the investigation of electromagnetic (EM) scattering characteristics of three-dimensional (3-D) local sea surface with time-varying overturning wave crest is meaningful for the remote sensing. In this paper, the influence of wind speed and time factor is taken into consideration when constructing the overturning wave crest, which is ignored in the traditional Longtank model. In addition, the Integral Equation Method (IEM) is adopted to calculate the EM scattering from a 3-D local sea surface with time-varying overturning wave crest for different incident angles and wind speeds. The simulation results are meaningful for analyzing the physical mechanism of sea spikes.

Index Terms ─ IEM, sea spikes, time-varying overturning wave crest.

I. INTRODUCTION

The sea spikes, which may cause the increase of radar false probability, have been hot issues during the past decades [1-6]. HH signals exceeding VV signals by as much as 10 dB or more is one of the characteristics of sea spikes. The overturning wave crest is thought to be a main reason to sea spikes, where the sophisticated coupling effect between sea surface and overturning wave crest may give rise to sea spikes. Therefore, the investigation of EM scattering from the 3-D local sea surface with time-varying overturning wave crest is of great importance for the physical mechanism analysis of sea spikes.

The Longtank model [7] has been widely used for the study of physical mechanism of sea spikes [3-5], which is generated by the University of California at Santa Barbara. The Longtank model is a series of numerically generated wave profiles, representing different profiles of overturning wave crest. These previous works indicated that multiple scattering from the crest and the front face of the overturning wave crest and the Brewster angle effect are the main reasons to HH signals exceeding that of VV signals. Actually, the multiple scattering also takes place between the sea surface and overturning wave crest. Therefore, it is necessary to investigate the EM scattering from the 3-D local sea surface with overturning wave crest. As the profile of sea surface is related to the wind speed, in order to combine the overturning wave crest with the generated sea surface, the wind speed should be taken into account when modeling. However, the Longtank model didn't consider the influence of wind speed. Therefore, the time-varying overturning wave crest model is applied to make a combination with the 3-D local sea surface in this paper, whose length and height are related to the wind speed and time factor. The 3-D sea surface is constructed by the Monte Carlo [8] method. Finally, the 3-D local sea surface with time-varying overturning wave crest can be built by the boolean operation, where the interpolation operation is adopted to avoid the discontinuity of the boundary.

To deal with the EM scattering from the 3-D local sea surface with time-varying overturning wave crest, the IEM [9]--an approximate method, is applied as a result of the limitation of numerical techniques [10-13] on the computer resource. The backscattering RCS and scattered electric field ratio of the 3-D local sea surface with overturning wave crest at different time sampling points are compared in detail. Meanwhile, the influence of wind speed on the backscattering characteristics is analyzed. Furthermore, the influence of overturning wave crest on the scattering characteristics of sea surface as well as the physical mechanism of sea spikes is also discussed. Compared with the previous literatures, our work focused on the variation of EM scattering of 3-D

Submitted On: December 28, 2016
Accepted On: May 1, 2018

local sea surface with overturning wave crest during the generation process, giving a detail analysis of sea spikes.

II. THEORY AND FORMULATION

In this section, a detailed description of the construction of 3-D local sea surface with overturning wave crest will be presented. Meanwhile, the EM scattering from the models was found using the IEM.

A. Time-varying overturning wave crest model

The two-dimensional (2-D) overturning wave crest is shown in Fig. 1, whose length and height are represented by *H* and *L*, respectively.

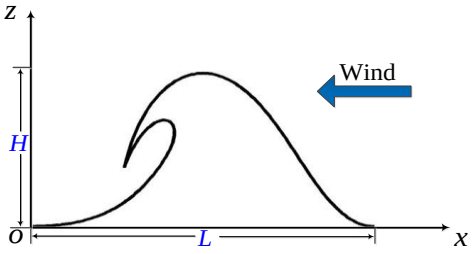

Fig. 1. The 2-D overturning wave crest.

According to [14], the height of wave is related to the wind speed, which can be expressed as:

$$H = 17.03 \cdot \exp(-\frac{\alpha^2}{18.3269}) + 2.361 \cdot \exp(-\frac{\beta^2}{8.8646}), \quad (1)$$

where $\alpha = u^{2/3} - 12.6549$, u is the wind speed.

S is defined as $S = H / L$. Therefore, the length of wave can be achieved by $L = H / S$.

The overturning wave crest takes place over a wide range of temporal and spatial scales. Therefore, the time factor is included to control its profile,

$$\begin{cases} x = L \cdot \left((0.5 - s_1)\cos(\phi) - r\sin(\phi) + 0.5 \right) \\ z = H \cdot z' / z_{\max} = H\left[(0.5 - s_1)\sin(\phi) + r\cos(\phi) \right] k_7 / z_{\max} \end{cases}, \quad (2)$$

$$\begin{cases} s_1 = \dfrac{(2s)^{k_1}}{2} \\ s_2 = (2s)^{k_2} \end{cases} (0 \le s \le 0.5), \begin{cases} s_1 = \dfrac{1 + (2s-1)^{k_1}}{2} \\ s_2 = 1 - (2s-1)^{k_1} \end{cases} (0.5 \le s \le 1), \quad (3)$$

where $s (0 \le s \le 1)$ is the input space parameter, which is splitted for the front and back of overturning wave crest. $k_1 \sim k_7$ can be obtained in [14]. It should be noted that *k* and *s* are related to the time factor, therefore the profile of overturning wave crest varies with time stepping. $r = k_2(1 + \cos((s_2 - 1)\pi)) / 2 + k_3 s_2^{k_4}$, $\phi = \pi k_5 s_2^{k_6} / 2$, $z_{\max} = \max\{z'\}$, and the period of overturning wave crest is $T = 2\text{s}$.

In this paper, the time-varying overturning wave crest model is obtained at sixteen different time sampling points as shown in Fig. 2. The wind speeds are $u = 5\text{m/s}$ and $u = 7\text{m/s}$, respectively. The direction of wind is along with $-x$ axis and $S = 1/3$. The time sampling interval is $\Delta t = 0.9 / 15(\text{s})$.

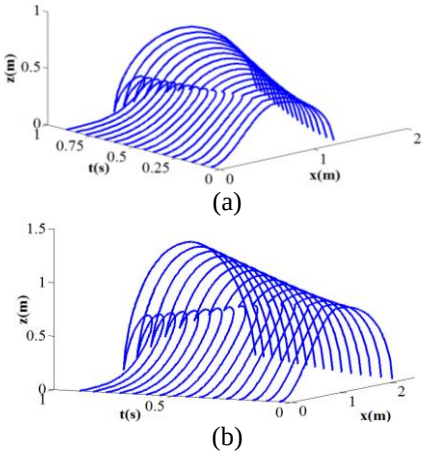

Fig. 2. The 2-D overturning wave crest for different wind speeds: (a) $u = 5\text{m/s}$ and (b) $u = 7\text{m/s}$.

As illustrated in Fig. 2, the profiles of overturning wave crest are obtained at sixteen time sampling points, which represented the temporal evolution of overturning wave crest. The height and length of overturning wave crest increased with wind speed. In addition, the overturning wave crest begins to generate at $t = \Delta t$, therefore its height and length are the smallest, which reached the maximum at $t = 16\Delta t$. When the 2-D time-varying overturning wave crest is constructed, the corresponding 3-D model can be achieved by extending the 2-D model in azimuth direction.

B. Construction of a 3-D local sea surface with overturning wave crest

The 3-D sea surface is modeled by the Monte Carlo method, where the Elfouhaily spectrum [15] is chosen to model the sea surface. The profiles of 3-D time-varying overturning wave crest are generated as described above. Then the 3-D overturning wave crest is combined with the 3-D sea surface by the boolean operation to build the composite model. In addition, the interpolation operation is adopted at the boundary between sea surface and overturning wave crest, avoiding the discontinuity at the boundary.

Figure 3 and Fig. 4 showed the 3-D local sea surface with overturning wave crest model at $t = \Delta t$, $10\Delta t$, $14\Delta t$, $16\Delta t$. The wind speeds are $u = 5\text{m/s}$ and $u = 7\text{m/s}$. As presented in Figs. 3 and 4, these are simplified models due to the complexiesity of the real overturning wave crest, which can briefly descibe the temporal evolution of the 3-D sea surface with overturning wave crest.

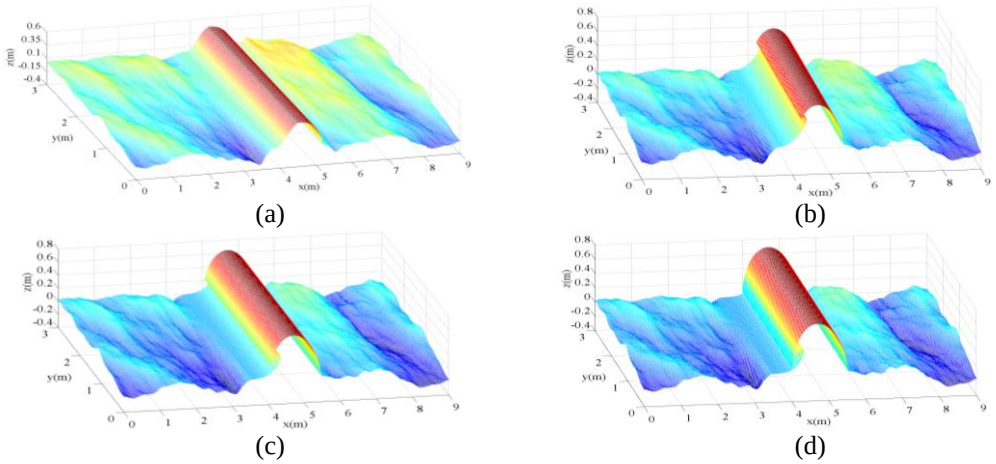

Fig. 3. The 3-D local sea surface with overturning wave crest ($u = 5$m/s): (a) Δt, (b) $10\Delta t$, (c) $14\Delta t$, and (d) $16\Delta t$.

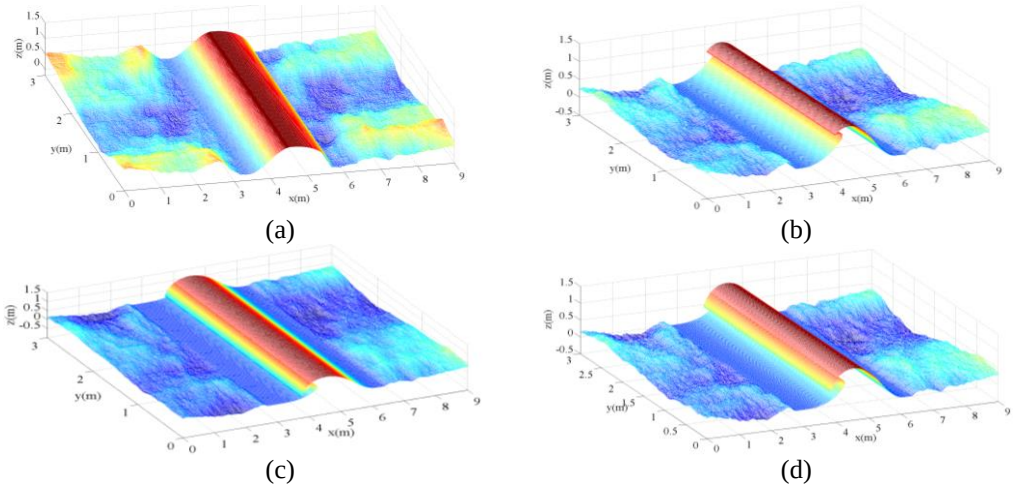

Fig. 4. The 3-D local sea surface with overturning wave crest ($u = 7$m/s): (a) Δt, (b) $10\Delta t$, (c) $14\Delta t$, and (d) $16\Delta t$.

C. IEM for the 3-D local sea surface with time-varying overturning wave crest

For the IEM, the governing equations for the tangential surface fields on a dielectric surface can be written as the sum of the standard Kirchhoff surface field and a complementary surface field,

$$\begin{cases} \hat{\boldsymbol{n}} \times \boldsymbol{E} = (\hat{\boldsymbol{n}} \times \boldsymbol{E})_k + (\hat{\boldsymbol{n}} \times \boldsymbol{E})_c \\ \hat{\boldsymbol{n}} \times \boldsymbol{H} = (\hat{\boldsymbol{n}} \times \boldsymbol{H})_k + (\hat{\boldsymbol{n}} \times \boldsymbol{H})_c \end{cases}. \tag{4}$$

The standard Kirchhoff surface field and the complementary surface field can be expressed as:

$$(\hat{\boldsymbol{n}} \times \boldsymbol{E})_k = \hat{\boldsymbol{n}} \times [(1+R_\perp)(\hat{\boldsymbol{p}} \cdot \hat{\boldsymbol{t}})\hat{\boldsymbol{t}} + (1-R_\parallel)(\hat{\boldsymbol{p}} \cdot \hat{\boldsymbol{d}})\hat{\boldsymbol{d}}]E^i, \tag{5}$$

$$\begin{aligned} \eta(\hat{\boldsymbol{n}} \times \boldsymbol{H})_k &= \hat{\boldsymbol{n}} \times [(1-R_\perp)(\hat{\boldsymbol{p}} \cdot \hat{\boldsymbol{t}})\hat{\boldsymbol{d}} - (1+R_\parallel)(\hat{\boldsymbol{p}} \cdot \hat{\boldsymbol{d}})\hat{\boldsymbol{t}}]E^i \\ &= \hat{\boldsymbol{n}} \times \{\boldsymbol{k}_i \times [(1-R_\perp)(\hat{\boldsymbol{p}} \cdot \hat{\boldsymbol{t}})\hat{\boldsymbol{t}} + (1+R_\parallel)(\hat{\boldsymbol{p}} \cdot \hat{\boldsymbol{d}})\hat{\boldsymbol{d}}]E^i\}, \end{aligned} \tag{6}$$

$$\begin{aligned} (\hat{\boldsymbol{n}} \times \boldsymbol{E})_c = -\frac{1}{4\pi}(\hat{\boldsymbol{n}} \times \hat{\boldsymbol{t}})\{\hat{\boldsymbol{n}} \times \hat{\boldsymbol{t}} \cdot \hat{\boldsymbol{n}} \times \int [(1+R_\perp)\boldsymbol{\varepsilon} + \\ (1-R_\perp)\boldsymbol{\varepsilon}_t]ds'\} - \frac{1}{4\pi}\hat{\boldsymbol{t}}\{\hat{\boldsymbol{t}} \cdot \hat{\boldsymbol{n}} \times \int [(1-R_\parallel)\boldsymbol{\varepsilon} + (1+R_\parallel)\boldsymbol{\varepsilon}_t]ds'\}, \end{aligned} \tag{7}$$

$$\begin{aligned} (\hat{\boldsymbol{n}} \times \boldsymbol{H})_c = \frac{1}{4\pi}(\hat{\boldsymbol{n}} \times \hat{\boldsymbol{t}})\{\hat{\boldsymbol{n}} \times \hat{\boldsymbol{t}} \cdot \hat{\boldsymbol{n}} \times \int [(1+R_\parallel)\boldsymbol{h} + \\ (1-R_\parallel)\boldsymbol{h}_t]ds'\} + \frac{1}{4\pi}\hat{\boldsymbol{t}}\{\hat{\boldsymbol{t}} \cdot \hat{\boldsymbol{n}} \times \int [(1-R_\perp)\boldsymbol{h} + (1+R_\perp)\boldsymbol{h}_t]ds'\}, \end{aligned} \tag{8}$$

where $\hat{\boldsymbol{n}}$ is the unit normal vector of surface, $R_\perp, R_\parallel$ are the Fresnel reflection coefficient, θ_i is incident angle.

$$\begin{cases} \hat{\boldsymbol{t}} = (\hat{\boldsymbol{k}}_i \times \hat{\boldsymbol{n}})/|\hat{\boldsymbol{k}}_i \times \hat{\boldsymbol{n}}| \\ \hat{\boldsymbol{d}} = \hat{\boldsymbol{k}}_i \times \hat{\boldsymbol{t}} \\ \hat{\boldsymbol{k}}_i = \hat{\boldsymbol{t}} \times \hat{\boldsymbol{d}} \end{cases}, \tag{9}$$

$$\boldsymbol{\varepsilon} = jk\eta(\hat{\boldsymbol{n}}' \times \boldsymbol{H}')G - (\hat{\boldsymbol{n}}' \times \boldsymbol{E}') \times \nabla' G - (\hat{\boldsymbol{n}}' \cdot \boldsymbol{E}')\nabla' G, \tag{10}$$

$$\boldsymbol{h} = (jk/\eta)(\hat{\boldsymbol{n}}' \times \boldsymbol{E}')G + (\hat{\boldsymbol{n}}' \times \boldsymbol{H}') \times \nabla' G + (\hat{\boldsymbol{n}}' \cdot \boldsymbol{E}')\nabla' G, \tag{11}$$

$$\boldsymbol{\varepsilon}_t = -[jk_t\eta_t(\hat{\boldsymbol{n}}' \times \boldsymbol{H}')G_t - (\hat{\boldsymbol{n}}' \times \boldsymbol{E}') \times \nabla' G_t - (\hat{\boldsymbol{n}}' \cdot \boldsymbol{E}')\nabla' G_t / \varepsilon_r], \tag{12}$$

$$\boldsymbol{h}_t = -[\frac{jk_t}{\eta_t}(\hat{\boldsymbol{n}}' \times \boldsymbol{E}')G_t + (\hat{\boldsymbol{n}}' \times \boldsymbol{H}') \times \nabla' G_t + (\hat{\boldsymbol{n}}' \cdot \boldsymbol{H}')\nabla' G_t / \mu_r]. \tag{13}$$

where $\hat{\boldsymbol{t}}, \hat{\boldsymbol{d}}, \hat{\boldsymbol{k}}_i$ are the local coordinate vectors, $\hat{\boldsymbol{n}}, \hat{\boldsymbol{n}}'$ is the unit normal vector of the surface, G is the Green's

function, ε_r, μ_r are the ratios of the permittivity and permeability of medium 2 to medium 1.

For the scattering of a 3-D local sea surface with time-varying overturning wave crest by IEM, the model is meshed into a great deal of triangles. For each lighted triangle, its Kirchhoff surface field and complementary surface field can be obtained according to Equation (5)~(13). The complementary surface field is a sum of the complementary surface field from the other lighted triangles, which represented the coupling scattering from the other triangles. In the end, the the scattered far fields are calculated by Stratton-Chu integral equation.

III. NUMERICAL RESULTS AND ANALYSIS

Firstly, the backscattering RCS of a 3-D local sea surface with overturning wave crest by IEM is compared with that of MoM in Fig. 5. The sea surface is 9m×3m, and $u = 5\text{m/s}$. The overturning wave crest is obtained at $t = 8\Delta t$. The frequency is $f = 0.456\text{GHz}$. The incident angle θ_i varies from -90° to 90°, and the incident vector is in xoz plane. When θ_i varied from -90° to 0°, it means upwind incidence, and 0° to 90° means downwind incidence. The relative permittivity of the sea water is $\varepsilon_r = (72.942, 178.069)$, which is obtained by the Debye model [16]. As seen in Fig. 5 (b), the backscattering RCS of 3-D local sea surface with overturning wave crest by the IEM shows a great agreement with that of MoM. Therefore, the validation of IEM is proved.

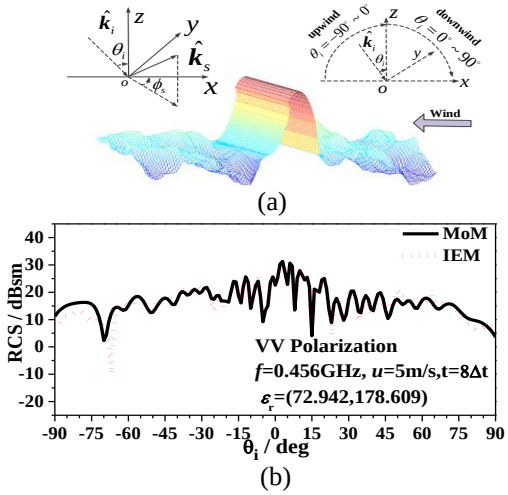

(a)

(b)

Fig. 5. Backscattering of a 3-D local sea surface with overturning wave crest: (a) model and (b) simulation results.

Figure 6 and Fig. 7 showed the backscattering RCS of a 3-D local sea surface with overturning wave crest by IEM for different wind speeds. Four profiles of overturning wave crest at $t = \Delta t$, $10\Delta t$, $14\Delta t$, $16\Delta t$ are considered. The sea surface is 9m×3m. The frequency of incident plane wave is $f = 0.456\text{GHz}$, and the relative permittivity is $\varepsilon_r = (72.942, 178.069)$. The incident vector is in xoz plane.

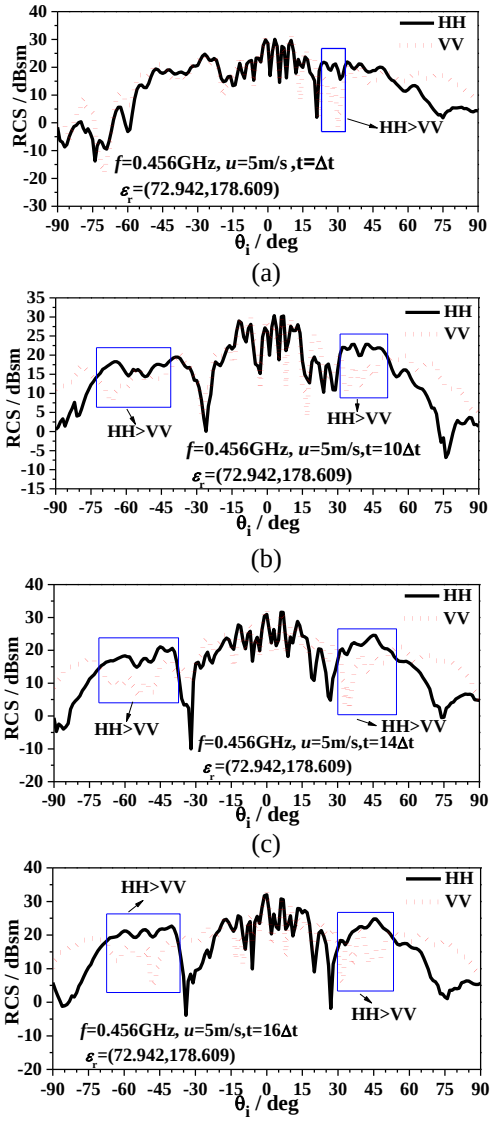

(a)

(b)

(c)

(d)

Fig. 6. Backscattering RCS for a 3-D local sea surface with overturning wave crest ($f = 0.456\text{GHz}$, $u = 5\text{m/s}$): (a) Δt, (b) $10\Delta t$, (c) $14\Delta t$, and (d) $16\Delta t$.

As shown in Fig. 6 the length and height of overturning wave crest are relatively smaller at the beginning of generation ($t = \Delta t$). Therefore, the sea surface scattering plays a major role, and backscattering RCS of HH polarization exceeding that of VV polarization is not observed except for $\theta_i = 20^\circ \sim 30^\circ$. However, the size of the overturning wave crest increased with time stepping, and its profile becomes

steeper. There is more incident angles for which HH scattering exceeding that of VV is observed. It is found that the sea-spike phenomenon is more likely to occur for upwind and large incident angle.

It can be seen from Fig. 7 that the backscattering RCS of HH polarization exceeding that of VV polarization becomes more obvious compared with that of $u = 5\text{m/s}$. The multiple scattering between the sea surface and overturning wave crest has a stronger contributor to the backscattering with the time stepping due to the increase of the size of overturning wave crest. Therefore, backscattering RCS of HH polarization exceeding that of VV polarization can be observed for the upwind and large incident angles, where the difference between HH and VV polarizations is larger than that of $u = 5\text{m/s}$. Meanwhile, this phenomenon also occurred for some incident angles when the incident wave is along with the downwind direction, but the difference is much smaller than that of upwind incidence. This means that the sea spikes are more likely to take place for the upwind incidence especially for the strong sea spikes, which is mainly caused by the multiple scattering between the sea surface and the overturning wave crest.

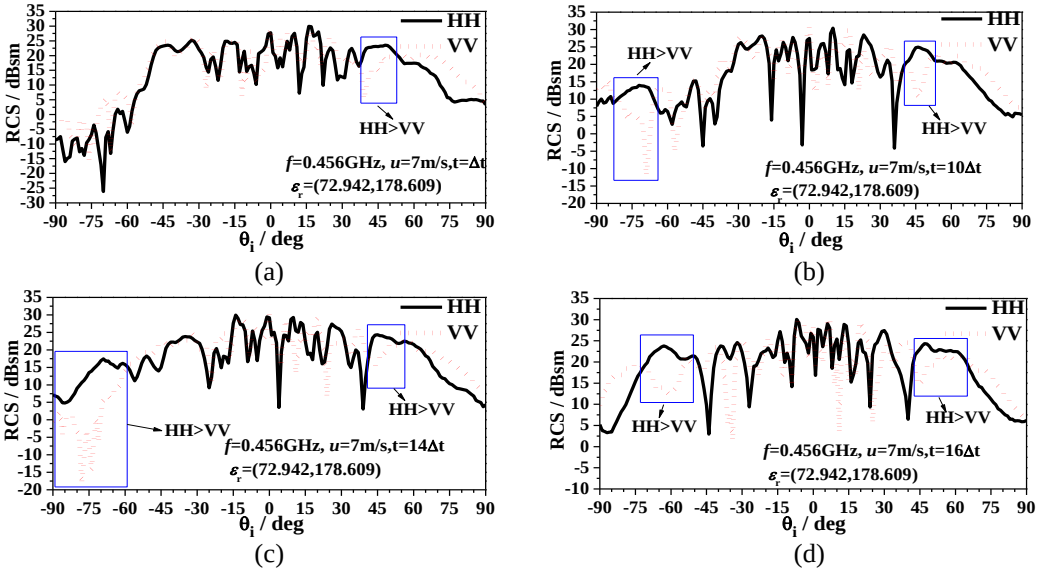

Fig. 7. Backscattering RCS for a 3-D local sea surface with overturning wave crest ($f = 0.456\text{GHz}$, $u = 7\text{m/s}$): (a) Δt, (b) $10\Delta t$, (c) $14\Delta t$, and (d) $16\Delta t$.

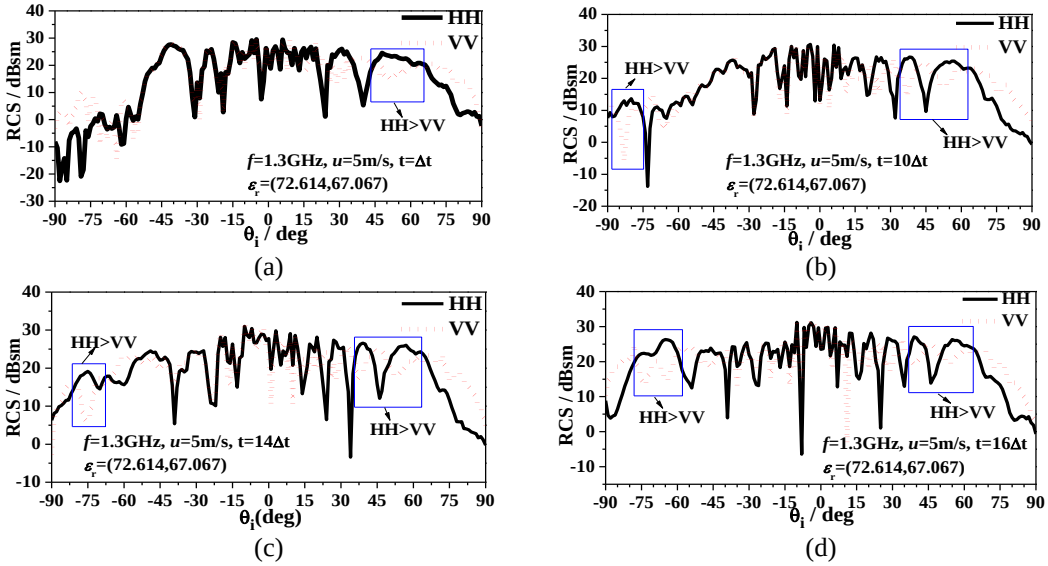

Fig. 8. Backscattering RCS for a 3-D local sea surface with overturning wave crest ($f = 1.3\text{GHz}$, $u = 5\text{m/s}$): (a) Δt, (b) $10\Delta t$, (c) $14\Delta t$, and (d) $16\Delta t$.

Figure 8 and Fig. 9 presented the backscattering RCS for $f = 1.3\text{GHz}$. The relative permittivity of the sea water is $\varepsilon_r = (72.614, 67.067)$, which is also obtained by the Debye model [16].

According to the simulation results from Fig. 8, it can be seen that when the profiles of the overturning wave crest model became steeper, the backscattering RCS of HH polarization larger than that of VV polarization becomes more obvious, and this is agree with that in Fig. 5. Therefore, it demonstrated that the overturning wave crest has a strong contributor to the backscattering from the sea surface and are particularly responsible for sea spikes. It should be noted that although overturning wave crest is a main reason to sea spikes, but not the sufficient condition, which is also related to the included angle of the overturning wave crest and sea surface as well as the incident angle.

As shown in Fig. 9, the backscattering RCS varies more quickly with the increase of radar frequency, compared with that in Fig. 6. The scattering of the sea surface has a main contributor to the backscattering RCS at $t = \Delta t$, then the RCS of VV polarization is larger than that of HH polarization. The RCS of HH polarization exceeding that of VV polarization occurred with the time stepping. At $t = 10\Delta t, 14\Delta t, 16\Delta t$, this phenomenon can be observed for the upwind and large incident angles, where the difference between the HH polarization and VV polarization reaches as much as 20 dBsm or more at $t = 14\Delta t$. Compared with the results in Fig. 6, the roughness of the sea surface and the size of the overturning wave crest increase with the wind speed. Therefore, the multiple scattering is more serious as well as the phenomenon of RCS of HH polarization exceeding the VV polarization.

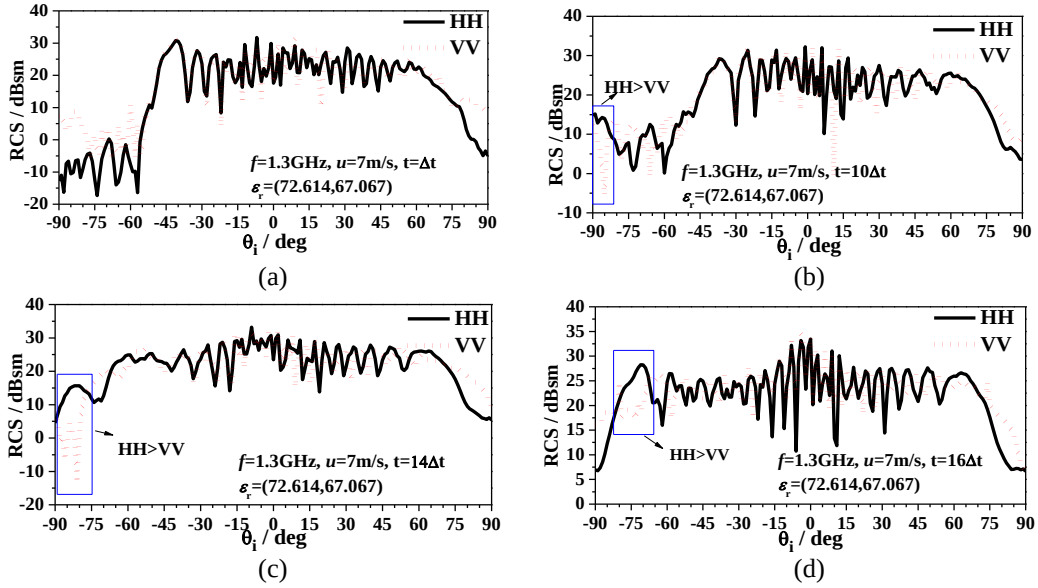

Fig. 9. Back scattering RCS for a 3-D local sea surface with overturning wave crest ($f = 1.3\text{GHz}$, $u = 7\text{m/s}$): (a) Δt, (b) $10\Delta t$, (c) $14\Delta t$, and (d) $16\Delta t$.

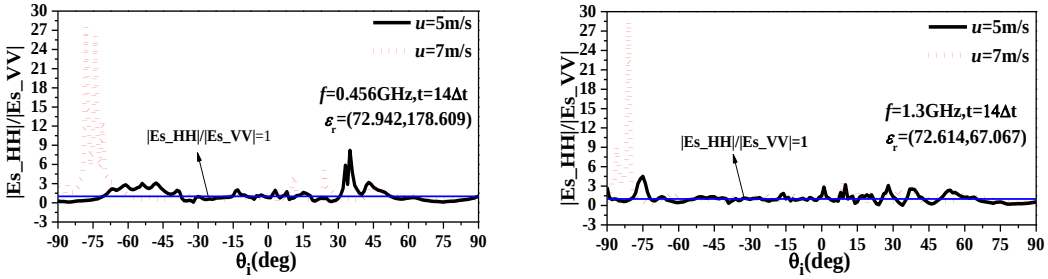

Fig. 10. Backscattering electric field ratio: (a) $f = 0.456\text{GHz}$ and (b) $f = 1.3\text{GHz}$.

The backscattering electric field ratio at $t=14\Delta t$ with different wind speeds and frequencies is depicted in Fig. 10. The blue line represents that the backscattering electric field ratio is equal to 1.

According to the simulation results in Fig. 10, with the increase of wind speed, there is more incident angles for which the strong sea-spike phenomenon is observed. Besides, a strong sea-spike phenomenon occurred for the incident angle between -90° and -65°, where the backscattering electric field ratio has nearly reached as much as 30. Therefore, it means that the strong sea spikes are more likely to take place for the upwind incidence, where the multiple scattering is more serious than that of the downwind incidence.

The comparison of backscattering electric field ratio from a 3-D local sea surface with and without the overturning wave crest is presented in Fig. 11, where the overturning wave crest are obtained at three different time sampling points and represents three different profiles of the overturning wave crest.

It is found that backscattering electric field ratio is much larger than 1 for some incident angles when there exists an overturning wave crest on the sea surface, which means a strong sea-spike phenomenon. While the backscattering electric field ratio is usually smaller than 1 when there is not an overturning wave crest, therefore the sea-spike phenomenon is difficult to take place in this situation. In other words, the overturning wave crest is one of the main reasons to sea spikes.

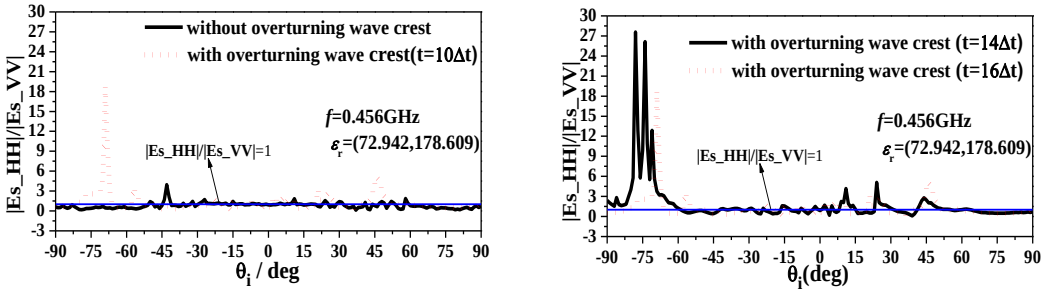

(a) (b)

Fig. 11. Backscattering electric field ratio: (a) without/with overturning wave crest ($t=10\Delta t$), and (b) sea surface with overturning wave crest ($t=14\Delta t,16\Delta t$).

IV. CONCLUSION

In this paper, the EM scattering characteristics of the 3-D local sea surface with the time-varying overturning wave crest is investigated based on IEM, where the overturning wave crest model is related to the wind speed and the time factor. The simulation results indicated that the overturning wave crest is particularly responsible for sea spikes. The size and profile of overturning wave crest also have a great influence on the backscattering RCS. When the length and height of overturning wave crest are relatively smaller at $t=\Delta t$, the sea surface scattering plays a domain role, and the sea-spike phenomenon is hardly to occur. While with the increase of the length and height of the overturning wave crest, the multiple scattering becomes obvious. When the incident angle is close to the Brewster angle of the sea water dielectric, the VV multipath is greatly attenuated and results in the sea spikes. According to the simulation results, the sea spikes are more easily to be observed for the upwind and large incident angles illumination. In addition, it should be noted that, as a result of the difficuly in the construction of real 3-D overturning wave crest, the 3-D local sea surface with overturning wave crest in this paper is a simplified model. Based on the present work, the further study will be carried on a more complex overturning wave crest model.

ACKNOWLEDGMENT

This work was supported part by the National Natural Science Foundation of China (Grant No. 61701378), part by the China Postdoctoral Science Foundation (Grant No. 2017M613069), part by the Aeronautical Science Fund (Grant No. 20170181004), part by the Fundamental Research Funds for the Central Universities.

REFERENCES

[1] L. B. Wetzel, *Electromagnetic Scattering from the Sea at Low Grazing Angles*. Surface Waves and Fluxes, vol. 8, pp. 109-171, 1990.

[2] D. B. Trizna, "A model for Brewster angle damping and multipath effects on the microwave radar sea echo at low grazing angles," *IEEE Trans. Geosci. Remote Sens.*, vol. 35, no. 5, pp. 1232-1244, 1997.

[3] J. C. West, "Low-grazing-angle (LGA) sea-spike backscattering from plunging breaker crests," *IEEE Trans. Geosci. Remote Sens.*, vol. 40, no. 2, pp. 523-526, 2002.

[4] D. Holliday, L. L. DeRead, Jr., and G. J. St-Cyr,

"Sea-spike backscatter from a steepening wave," *IEEE Trans. Antennas Propagat.*, vol. 46, no. 1, pp. 108-113, 1998.

[5] W. Yang, Z. Q. Zhao, C. H. Qi, et al., "Electromagnetic modeling of breaking waves at low grazing angles with adaptive higher order hierarchical Legendre basis functions," *IEEE Trans. Geosci. Remote Sens.*, vol. 46, no. 1, pp. 346-352, 1998.

[6] A. C. Patricio, C. H. Merrick, A. H. Robert, et al., "Optical and microwave detection of wave breaking in the surf zone," *IEEE Trans. Geosci. Remote Sens.*, vol. 49, no. 6, pp. 1879-1893, 2011.

[7] P. Wang, Y. Yao, and M. P. Tulin, "An efficient numerical tank for nonlinear water waves based on the multi-subdomain approach with B.E.M.," *International Journal for Numerical Methods in Fluid*, vol. 20, no. 20, pp. 1315-1336, 1995.

[8] I. T. Jonhson, J. V. Toporkov, and G. S. Brown, "A numerical study of backscattering from time-evolving sea surfaces: Comparison of hydrodynamic models," *IEEE Trans. Geosci. Remote Sens.*, vol. 39, no. 11, pp. 2411-2419, 2001.

[9] A. K. Fung, Z. Q. Li, and K. S. Chen, "Back-scattering from a randomly rough dielectric surface," *IEEE Trans. Geosci. Remote Sens.*, vol. 30, no. 2, pp. 356-369, 1992.

[10] R. F. Harrington and J. L. Harrington, *Field Computation by Moment Methods*. Macmillan, New York, 1968.

[11] J. Li, L. X. Guo, Y. C. Jiao, et al., "Investigation on wide-band scattering of a 2-D target above 1-D randomly rough surface by FDTD method," *Optics Express*, vol. 19, no. 2, pp. 1091-1100, 2011.

[12] J. Song, C. C. Lu, and W. C. Chew, "Multilevel fast multiple algorithm for electromagnetic scattering by large complex objects," *IEEE Trans. Antennas Propagat.*, vol. 45, no. 10, pp. 1488-1497, 1997.

[13] J. Hu, et al., "Fast solution of electromagnetic scattering from thin dielectric coated PEC by MLFMM and successive over relaxation iterative technique," *IEEE Microwave and Wireless Components Letters*, vol. 19, no. 12, pp. 762-764, 2009.

[14] W. L. Li, L. X. Guo, X. Meng, et al., "Modeling and electromagnetic scattering from the overturning wave crest," *Acta Phys. Sin.*, vol. 63, no. 16, pp. 164102-164102, 2014.

[15] T. Elfouhaily, B. Chapron, K. Katsaros, et al., "A unified directional spectrum for long and short wind-driven waves," *J. Geoph. Res.: Oceans (1978–2012)*, vol. 102, no. C7, pp. 15781-15796, 1997.

[16] P. Debye, *Polar Molecules*. Chemical Catalog, New York, 1929.

Xiao Meng received the B.S. degree in Electronic Information Science and Technology from Xidian University, Xi'an, China in 2011. She is currently pursuing the Ph.D. degree at the School of Science.

Her research has been on electromagnetic scattering from rough sea surface and GPU high-performance computing in remote sensing and computational electromagnetics.

Li-xin Guo (S'95-M'03) received the M.S. degree in Radio Science from Xidian University, Xi'an, China, and the Ph.D degree in Astrometry and Celestial Mechanics from Chinese Academy of Sciences, China, in 1993 and 1999, respectively.

During 2001-2002 he was a Visiting Scholar at School of Electrical Engineering and Computer Science, Kyungpook National University, Korea. He has also held appointments as Visiting Professor at d'Energetique des Systemes et Precedes (LESP), University of Rouen, France and Faculty of Engineering and Physical Sciences, University of Manchester, England. He is currently a Professor and Head of School of Science at Xidian University, China. His research interests mainly includes: electromagnetic wave propagation and scattering in complex system, computational electromagnetic and fractal electrodynamics.

Guo is a Senior Member of Chinese Institute of Electronics (CIE) and a Fellow of Physics Institute of Shaanxi Province, China.

A Propagation Model for Rough Sea Surface Conditions using the Parabolic Equation with the Shadowing Effect

Mengda Cui, Hao Cha*, and Bin Tian

College of Electrical Engineering
Naval University of Engineering, Wuhan, 430033, China
cuimd2050@sina.com, hydchj@sina.com*, sweetybox123@163.com

Abstract ─ In this article, an accurate and fast approach is proposed to calculate the electromagnetic wave propagation characteristics over the sea surface under tropospheric ducting conditions. The method is based on the parabolic equation and an asymptotic model of a rough sea surface and is used to calculate the electromagnetic characteristics and to model the sea surface reflection. In the proposed model, termed the extremum approximation of the shadowing effect (EA of SE) model, the shadowing effect is considered and simplified to improve the accuracy and shorten the computation time. The probability density functions and the propagation factors of different models are compared, the influence of the rough sea surface and the shadowing effect on the electromagnetic wave propagation is analyzed and the model accuracy and efficiency are evaluated. Some comparisons are made with experimental data. The results show that the average error is about 1 dB less after the shadowing effect is considered; and the proposed approach shortens the computation time about 600 times while maintaining a high accuracy.

Index Terms ─ Electromagnetic propagation, parabolic equation, rough sea surface reflection, shadowing effect, tropospheric duct.

I. INTRODUCTION

Electromagnetic (EM) waves are reflected, refracted, and diffused when propagating in the troposphere over a rough sea surface. This can result in the alteration of the radar performance, such as over-the-horizon radar detection and differences in the radar shadow [1,2]. In an informationalized battlefield at sea, the real-time evaluation of the radar performance effectively improves the radar usage and battlefield survivability. Therefore, it is important to model, predict, and analyze the EM propagation conditions rapidly.

It is computationally expensive to calculate precisely the EM field in a large region under certain tropospheric conditions and over a rough sea surfaces to satisfy military needs. However, the parabolic equation (PE) model, an approximation model of the Helmholtz scalar wave equation, can be used for rapid and accurate EM field calculations [3,4]. The rough sea surface reflection can be modeled with an asymptotic method based on the Kirchhoff approximation, in which the reflection field of the rough sea surface is regarded as the summation of the coherent field reflected by the sea surface at different heights. The probability density function (PDF) of the sea wave height is used to obtain the effective reflection coefficient of the rough sea surface [5].

The Ament and Miller-Brown (MB) models [6,7] are two routinely used rough surface asymptotic models integrated with the PE model [4]. The advantages of these models are their fast running times and high accuracies [8]. However, Fabbro et al. [9] demonstrated that the inaccuracies of these models are due to the non-consideration of the shadowing effect; therefore, the authors proposed the shadowing effect (SE) model, which is an another rough surface asymptotic model based on Ament model. Freund et al. [10] also analyzed the influence of the shadowing effect on the EM field and verified the accuracy of the model by simulations. However, this SE model requires integral calculations, which are time-consuming.

In this study, the influence of the shadowing effect on the EM propagation characteristics is analyzed and the extremum approximation of the shadowing effect (EA of SE) model is proposed to simplify the modeling of the shadowing effect. The proposed model is used by the PE to calculate the EM wave field in a complex sea environment. The simulation shows that the results are different after the shadowing effect is considered and the new approach has a similar result but a shorter computation time than the SE model. A comparison with the experimental data indicates that the consideration of the shadowing effect increases the precision of the results, and that the proposed method has higher computational efficiency than the SE model and a similar accuracy.

Submitted On: December 5, 2017
Accepted On: April 1, 2018

II. ELECTROMAGNETIC PROPAGATION OVER THE SEA

A. PE model

The PE model is a numerical computation method that is an approximation of the Helmholtz scalar wave equation [11,12]. The method can be used for the rapid calculation of EM wave propagation characteristics in a complex environment. Therefore, it is routinely used when EM propagation problems are investigated in a large region with complex environmental conditions. Using the Feit-Fleck approximation, the wide angle formulation of the PE is [13]:

$$\frac{\partial}{\partial x}u(x,z)=i\left(\sqrt{k_0^2+\frac{\partial^2}{\partial z^2}}-k_0\right)u(x,z)+ik_0(n-1)u(x,z), \quad (1)$$

where n is the refractive index, k_0 is the free-space wave number, x and z are the horizontal range and altitude respectively, and $u(x,z)$ is the wave function. The relationship between $u(x,z)$ and the scalar field $\Phi(x,z)$ is:

$$u(x,z)=\Phi(x,z)e^{-ik_0x}, \quad (2)$$

where $\Phi(x,z)$ represents the electric or magnetic field for the horizontal or vertical polarization, respectively. By using a Fourier transform with z at the range x and $x+\Delta x$, the split-step Fourier transform (SSFT) method for the PE can be deduced as:

$$u(x+\Delta x,z)=e^{ik_0\Delta x(n-1)}\Im^{-1}\left[e^{i\Delta x\left(\sqrt{k_0^2-p^2}-k_0\right)}\Im(u(x,z))\right], \quad (3)$$

where $\Im(\bullet)$ and $\Im^{-1}(\bullet)$ represent the Fourier transform and its inverse operator. p is a parameter in the spectral domain and is related to the EM propagation angle θ as $p=k_0\sin\theta$. Δx is the step length. By using the SSFT, $u(x+\Delta x,z)$ can be calculated if the $u(x,z)$ at the range x is known. The Discrete Mixed Fourier Transform (DMFT) can also be used instead of the SSFT in Eq. (3) to calculate electromagnetic wave under impedance boundary conditions [14]. For calculation the EM propagation over the rough sea surface, the effective reflection coefficient is used in DMFT [8].

B. Reflection from a rough surface

In the asymptotic models of a rough sea surface, the reflection coefficient are corrected using the Kirchhoff approximation. If Γ_0 represents the reflection coefficient of a smooth sea surface, ξ is the random variable of the surface height, $p(\xi)$ is the PDF of ξ, α is the grazing incidence angle, the effective reflection coefficient can be written as:

$$\Gamma_e=\rho\Gamma, \quad (4)$$

where the function ρ is the roughness reduction factor, which is defined as:

$$\rho(\alpha)=\int_{-\infty}^{+\infty}\exp(-2ik_0\xi\sin\alpha)p(\xi)\mathrm{d}\xi. \quad (5)$$

C. Asymptotic model of a rough surface

In the Ament approximation, the PDF of the sea surface heights is regarded as having a Gaussian distribution with zero mean and variance σ_ξ^2, written as:

$$p_{\mathrm{A}}(\xi)=\frac{1}{\sigma_\xi\sqrt{2\pi}}\exp\left(-\frac{\xi^2}{2\sigma_\xi^2}\right). \quad (6)$$

By inserting Eq. (6) into Eq. (4), one obtains:

$$\Gamma_{\mathrm{A}}(\alpha,\sigma_\xi)=\exp\left(-0.5\gamma^2\sigma_\xi^2\right)\Gamma_0, \quad (7)$$

where $\gamma=2k_0\sin\alpha$.

The PDF of the sea surface height is different in the MB model. The height of the rough sea surface is assumed to take the form $\xi=H\sin\varphi$, where the magnitude H has a Gaussian distribution with zero mean and variance σ_ξ^2 and the phase φ is uniformly distributed in the interval $[-\pi/2,\pi/2]$. Therefore, the PDF of the surface height is:

$$p_{\mathrm{MB}}(\xi)=\frac{1}{2\pi^{3/2}\sigma_\xi}\exp\left(-\frac{\xi^2}{8\sigma_\xi^2}\right)K_0\left(\frac{\xi^2}{8\sigma_\xi^2}\right), \quad (8)$$

where $K_0(\bullet)$ is a modified Bessel function of the second kind of order zero. By inserting Eq. (8) into Eq. (4), one can obtain the effective reflection coefficient of the MB model:

$$\Gamma_{\mathrm{MB}}=\exp\left(-0.5\gamma^2\sigma_\xi^2\right)I_0\left(0.5\gamma^2\sigma_\xi^2\right)\Gamma, \quad (9)$$

where $I_0(\bullet)$ is the modified Bessel function of the first kind of order zero.

D. Shadowing effect and its extremum approximation

The SE model is based on the Ament model. If α is the grazing incidence angle, the PDF of the illumination surface height is written as [10,15]:

$$p_{\mathrm{SHD}}(\xi;\alpha)=p_{\mathrm{A}}(\xi)S(\xi,\alpha,\sigma_\xi,\sigma_r), \quad (10)$$

where σ_r is the root mean square slope of the surface; $S(\xi;\alpha)$ is a function called the shadow factor and is defined as:

$$S\left(\xi,\alpha,\sigma_\xi,\sigma_r\right)= \frac{2B}{1-\exp\left(-2B\right)}\exp\left[-B\mathrm{erfc}\left(\frac{\xi}{\sqrt{2}\sigma_\xi}\right)\right], \quad (11)$$

$$B=\frac{\sigma_r}{2\sqrt{2\pi}\tan\alpha}.$$

Inserting Eq. (11) into Eq. (5) yields the roughness reduction factor with the shadowing effect:

$$\rho_{\mathrm{SHD}}\left(\alpha,\sigma_\xi\right)=\int_{-\infty}^{+\infty}\exp\left(-i\gamma\xi\right)p_{\mathrm{SHD}}\left(\xi\right)\mathrm{d}\xi = \frac{2B}{1-\exp\left(-2B\right)}\int_{-\infty}^{+\infty}\exp\left(-i\gamma\xi\right) \times\exp\left[-B\mathrm{erfc}\left(\frac{\xi}{\sqrt{2}\sigma_\xi}\right)\right]p_{\mathrm{A}}\left(\xi\right)\mathrm{d}\xi \quad (12)$$

Therefore, the reflection coefficient of the shadowing effect for the coherent reflected field can be written as:

$$\Gamma_{\mathrm{SHD}}=\rho_{\mathrm{SHD}}\left(\alpha,\sigma_\xi\right)\Gamma_0. \quad (13)$$

It is evident from Eq. (13) that the SE model is computationally expensive because an integral operator is needed for the calculation of the effective reflection coefficient. Since the PDF of the illumination surface height has an approximately Gaussian distribution, the PDF of the SE model can be simplified by assuming a Gaussian distribution [9]. However, the calculation of the mean and variance still require integral operators using the illumination height PDF $p_{\mathrm{SHD}}\left(\xi;\alpha\right)$. Therefore, an extremum approximation method is proposed in this study to obtain the reflection coefficient of the shadowing effect in a relatively short time.

Because the mean and variance of the Gaussian distribution are related to the extremum of the PDF, the illumination surface height PDF $p_{\mathrm{SHD}}\left(\xi;\alpha\right)$ can be Gaussian fitted at its extreme point.

If $h=\frac{\xi}{\sqrt{2}\sigma_\xi}$, the $p_{\mathrm{SHD}}\left(\xi;\alpha\right)$ can be expressed as:

$$p_{\mathrm{SHD}}\left(\xi;\alpha\right)=f\left(h\right)=A\exp\left[-B\mathrm{erfc}\left(h\right)-h\right], \quad (14)$$

where the parameter *A* is:

$$A=\frac{2B}{1-\exp\left(-2B\right)}\frac{1}{\sqrt{2\pi}\sigma_\xi}. \quad (15)$$

If calculating the derivative of $f\left(h\right)$ and making $f'\left(h\right)=0$; then the parameter *h* must satisfy:

$$\frac{B}{\sqrt{\pi}}\exp\left(-h^2\right)-h=0. \quad (16)$$

Transform Eq. (16) and it can be expressed as:

$$-2\ln\frac{\sqrt{\pi}h}{B}\times\exp\left(-2\ln\frac{\sqrt{\pi}h}{B}\right)=2\frac{B^2}{\pi}. \quad (17)$$

If $k=-2\ln\frac{\sqrt{\pi}h}{B}$, Eq. (17) can be written as:

$$k\exp\left(k\right)=2B^2/\pi. \quad (18)$$

The extreme point *h* in Eq. (14) can be calculated using the Lambert function:

$$k=\mathrm{L}\left(2B^2/\pi\right), \quad (19)$$

where $\mathrm{L}\left(\bullet\right)$ represents the Lambert function.

Therefore, the mean m'_ξ and root mean square σ'_ξ can be written as:

$$\begin{cases} m'_\xi=\sqrt{2}\sigma_\xi h \\ \sigma'_\xi=\dfrac{1}{\sqrt{2\pi}\,p_{SHD}\left(m'_\xi;\alpha\right)} \end{cases}, \quad (20)$$

Then, the PDF of the illumination surface height can be described as:

$$p_{\mathrm{E}}\left(\xi\,|\,\alpha\right)=\frac{1}{\sigma'_\xi\sqrt{2\pi}}\exp\left(-\frac{\left(\xi-m'_\xi\right)^2}{2\sigma'^2_\xi}\right), \quad (21)$$

and the effective reflection coefficient is:

$$\Gamma_{\mathrm{E}}=\exp\left(-iQm'_\xi-0.5\gamma^2\sigma'^2_\xi\right)\Gamma_0. \quad (22)$$

The phase of the effective reflection coefficient is related to the mean value of the surface height and its magnitude is related to the variance of the surface height. The Ament model and the MB model are only corrected with regard to the magnitude of the reflection coefficient but not the phase. However, in the SE model and the proposed model, the magnitude and phase of the coefficient are corrected.

III. SIMULATION AND VERIFICATION

In order to determine the precision and efficiency of the EA of SE model, the PDF and the propagation factor (PF) of the models are compared using a simulation. The simulation is performed in MATLAB 2016a on a computer with an Intel i5 3.2 GHz CPU.

A. Comparison of the PDF

The PDFs of the models are calculated and compared. Assuming that the grazing incidence angle α is 0.5°, the root mean square of the surface height and slope are calculated using the Elfouhaily wave spectrum at a wind speed of 7 m/s [16]. Figure 1 shows the PDFs of the different models.

In Fig. 1, the symbols p_{A}, p_{MB}, p_{SHD}, and p_{E} represents the PDFs of the Ament model, MB model, SE model, and EA of SEmodel respectively. The mean value and the root mean square of the p_{A} and p_{MB} are 0 and 0.3199. The mean values of the p_{SHD} and p_{E} are 0.4090 and 0.3989 and the root mean square values are

0.2233 and 0.2106 respectively. The results in Fig. 1 show that the mean value is higher for the p_{SHD} than the p_A. That is because the PDF of the Ament model only takes into account the wind speed (surface height variance σ_ξ^2) but the PDF of the SE model also takes in account the grazing incidence angle α and only the illumination surface is considered. As the value of α decreases, the illumination surface decreases, which results in an increase in the surface height mean value and a decrease in the root mean square of the p_{SHD}, as shown in Fig. 2. The curves of the p_{SHD} and p_E are similar but there are some differences because the PDF of the SE model does not have a perfect Gaussian distribution.

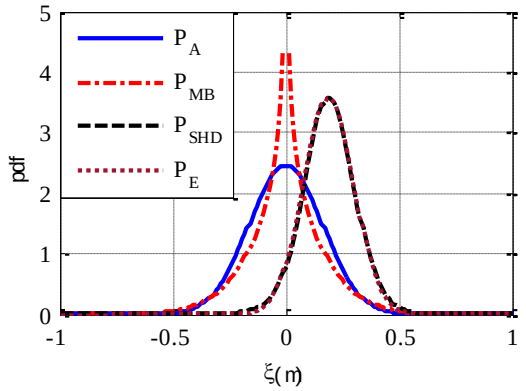

Fig. 1. PDF of surface height.

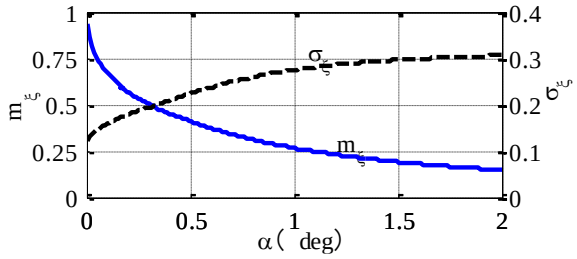

Fig. 2. Mean value and root mean square vs grazing incidence angle.

B. Comparison of the PF under simple conditions

A horizontally polarized 3-GHz line source at a height of 10 m was used to compute the PF over the sea using a geometrical optics (GO) two-ray model. In the simulation, the propagation range is 1 km, the height is 50 m, the number of height grid points is 250, the wind speed is 7 m/s, and the atmospheric effects and the earth's curvature are ignored. The PFs of the four models are shown in Fig. 3.

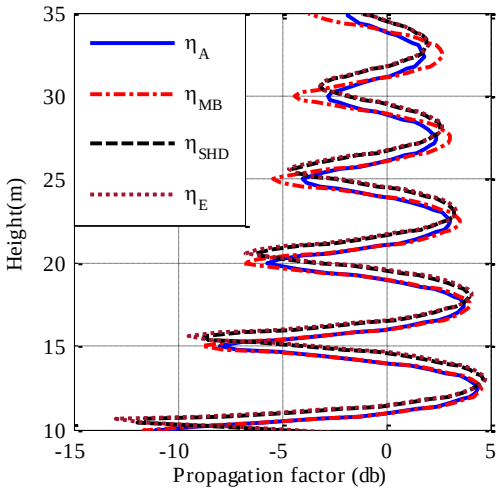

Fig. 3. Propagation factors under simple conditions.

The symbols η_A, η_{MB}, η_{SHD}, and η_E represent the PFs calculated by the Ament model, MB model, SE model, and the proposed model respectively. It is evident that, after the shadowing effect is considered, the results of η_{SHD} and η_A exhibit clear differences in the heights and maximums of the peaks and nulls. The heights of the PF peaks and nulls are determined by the phase of the reflection coefficient, which is different in the Ament model and the SE model. The mean value of the surface height is zero in the Ament model; therefore, its phase of the reflection coefficient is equal to that of a smooth surface. However, the phase is different in the SE model because only the illumination surface is considered, which results in different heights of the peaks and nulls. The maximums of the peaks and nulls are determined by the magnitude of the reflection coefficient. In the SE model, only the reflection field from the illuminated surface is considered and this results in an increase in magnitude of the effective reflection coefficient. The increase in the reflection field results in an increase in the maximums of the peaks and nulls. The heights of the peaks and nulls are identical in η_A and η_{MB} but the maximums are different, which means the phases of the reflection coefficient are identical in η_A and η_{MB} but the magnitude is larger in η_{MB}. A comparison between η_{SHD} and η_{MB} shows that the maximum of η_{SHD} is larger at a low altitude but smaller at a high altitude. This is attributed to the smaller grazing incidence angle α at a low altitude, which results in a larger effective reflection coefficient and maximums of the peaks and nulls in η_{SHD} than in η_{MB}; the opposite result is observed at high altitude. η_{SHD} and η_E have similar results with an average error of 0.07 dB, which indicates

that the EA of SE model has a similar precision as the SE model.

The computation times of the four models η_A, η_{MB}, η_{SHD}, and η_E are 0.002 s, 0.008 s, 8.94 min, and 0.781 s respectively. Because the integral operator is needed in the SE model, its computation time is much greater than that of the other models, which means the EA of SE model improves the efficiency while considering the shadowing effect.

C. Comparison of the PFs under complex conditions

The PE model and the asymptotic model of a rough surface are used to calculate the PF under tropospheric ducting conditions and a rough sea surface. A Gaussian antenna pattern is used with a 3° lobe width, 0° elevation, and 9 GHz frequency at 10 m height. The wind speed is 5 m/s and the duct height is 15 m. Because the EM energy is influenced by the tropospheric duct, some of the EM energy is trapped in the duct layer, which results in the increase in the PF over the sea. Four asymptotic models are used in the PE model to calculate the PF at a range of 100 km; the PFs are plotted versus the height and are shown in Fig. 4.

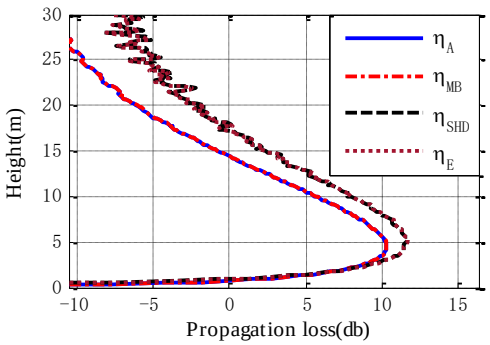

Fig. 4. Propagation factors under complex conditions.

The symbols η_A, η_{MB}, η_{SHD}, and η_E represent the PFs calculated by the PE with the Ament model, MB model, SE model, and the proposed model respectively. Figure 4 shows that η_A and η_{MB} have similar curves. However, the η_{MB}, which maximum is 10.277 dB, is slightly larger than the η_A, which maximum is 10.252 dB, as its magnitude of the reflection coefficient is larger in the MB model than in the Ament model, which results in a stronger reflection field in η_{MB}. It is also observed that the η_{SHD} is larger than the η_A and η_{MB}. The reason is that, when the EM energy propagates in the tropospheric duct, the grazing incidence angle α is small; therefore, the magnitude of the effective reflection coefficient is larger than that of the Ament model and MB model and the maximum of the η_{SHD} is about 1 dB larger than that of the η_A. However, the computation time of the η_{SHD} (11.43 min) is much longer than that of the η_A (0.495 s). The η_E and η_{SHD} have similar curves but the η_E has a shorter computation time (1.158 s), which means the approximation model is a more efficient model with similar results.

IV. EXPERIMENT AND VERIFICATION

The experimental data were obtained at Dachen Island in China in 2007 and are used for the verification of the models [17]. The atmospheric conditions and the tropospheric duct were measured using a weather balloon and a meteorograph. The radar transmitting antenna operating in the X band was mounted on the beach at a height of 15 m. A horn antenna was used as the receiving antenna and was mounted on a boat at a height of 2 m. A meteorograph was used on the boat for measuring the wind speeds, humidity, temperature, and pressure. The wind speed was 2–4 m/s during the experiment. The PE model and the asymptotic model of a rough surface were used to calculate the propagation loss and the results are shown in Fig. 5.

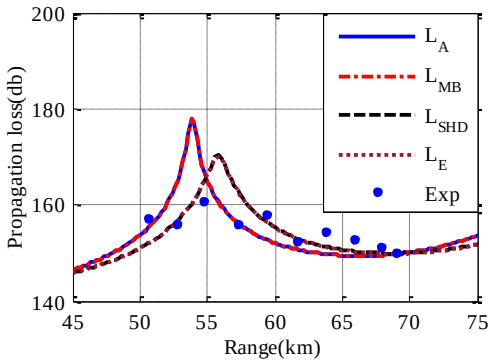

Fig. 5. Range versus propagation loss.

In Fig. 5, the blue points are the experimental results and the symbols L_A and L_{MB} represent the Ament model and MB model, whose curves are identical because the effective reflection coefficients are very close to the smooth surface reflection coefficient due to a low wind speed. The symbols L_{SHD} and L_E represent the SE model and the proposed model, whose curves are also identical. The effective reflection coefficients of the two models are close to the smooth surface reflection coefficient in magnitude but different in the phases, which results in the differences in the propagation losses for L_A and L_{MB}. The average errors of these models are shown in Table 1. Compared with the experimental results, the SE model and the proposed model have average errors that are nearly 1 dB lower than those of the other models. The computation time of the proposed model is about 600 times shorter than that of the SE model.

Table 1: Computation time and average error

Model	L_A	L_{MB}	L_{SHD}	L_E
Average Error (dB)	3.47	3.47	2.54	2.55
Computation Time	0.340 s	0.320 s	10.14 min	1.074 s

The results are close to the experimental results after the shadowing effect is considered but errors still remain. The errors may be caused by the following:

1) Measurement errors. The weather sensors in the weather balloon have a slow reaction time due to a 1-Hz sampling rate. The accuracy of the pressure sensor is 0.3 hpa, which means that the accuracy of the height calculated by the barometric formula is ± 3 m. Therefore, an error exists in the refractive index profile, even after using the noise reduction method.

2) Errors caused by the horizontal inhomogeneity and turbulence of the tropospheric duct. There are some random changes in the refractive index profile at different ranges and heights, which results in the errors of the propagation loss.

3) Model errors. The parameter of the grazing incidence angle α is needed at different ranges in the PE model and the SE model. The angle α is obtained by a ray-tracing method and errors may occur because it is an approximation method.

V. CONCLUSION

The Ament model and MB model are routinely used in the PE model for the rapid prediction of the EM propagation characteristics under tropospheric ducting conditions over the sea surface. However, the shadowing effect caused by the rough sea surface is not considered in these models. The SE model has a higher accuracy but is computationally expensive. In this study, a new approximation model is proposed to simplify the shadowing effect; this model has a higher computational efficiency and similar accuracy as the SE model. A comparison with the other models and the experimental results indicate that the EA of SE model used in conjunction with the PE is a fast and accurate model for the calculation of the EM propagation characteristics. Therefore, the proposed model satisfied the needs of the real-time evaluation of the radar performance to improve the battlefield survivability.

ACKNOWLEDGMENT

This work was supported by NSFC in China under Grant No. 41405009 and No. 41704034.

REFERENCES

[1] R. Douvenot, V. Fabbro, P. Gerstoft, et al., "Real time refractivity from clutter using a best fit approach improved with physical information," *Radio Science*, vol. 45, no. 1, pp. 1-13, 2016.

[2] X. F. Zhao, S. X. Huang, and D. X. Wang, "Using particle filter to track horizontal variations of atmospheric duct structure from radar sea clutter," *Atmospheric Measurement Techniques*, vol. 5, no. 11, pp. 2859-2866, 2012.

[3] R. Akbarpou and A. R. Webster, "Ray-tracing and parabolic equation methods in the modeling of a tropospheric microwave link," *IEEE Trans. Antennas Propagat.*, vol. 53, no. 11, pp. 3785-3791, 2005.

[4] Y. W. Shen, L. Zhang, D. K. Liu, et al., "Comparisons of ray-tracing and parabolic equation methods for the large-scale complex electro-magnetic environment simulations," *International Journal of Modeling Simulation & Scientific Computing*, vol. 3, no. 2, pp. 1-27, 2012.

[5] C. Bourlier, "Propagation and scattering in ducting maritime environments from an accelerated boundary integral equation," *IEEE Trans. Antennas Propagat.*, vol. 64, no. 11, pp. 4794-4803, 2016.

[6] D. E. Freud, N. E. Woods, H. C. Ku, et al., "Forward radar propagation over a rough sea surface: A numerical assessment of the Miller-Brown approximation using a horizontally polarized 3-GHz line source," *IEEE Trans. Antennas Propagat.*, vol. 54, no. 4, pp. 1292-1304, 2006.

[7] D. E. Barrick, "Grazing behavior of scatter and propagation above any rough surface," *IEEE Trans. Antennas Propagat.*, vol. 46, no. 1, pp. 73-83, 1998.

[8] A. R. Miller, R. M. Brown, and E. Vegh, "New derivation for the rough-surface reflection co-efficient and for the distribution of sea-wave elevations," *IEE Proceedings H - Microwaves Antennas Propagat.*, vol. 131, no. 2 pp. 114-116, 1984.

[9] V. Fabbro, C. Bourlier, and P. F. Combes, "Forward propagation modeling above Gaussian rough surfaces by the parabolic shadowing effect," *Journal of Electromagnetic Waves and Applications*, vol. 58, no. 1, pp. 243-269, 2006.

[10] D. E. Freud, N. E. Woods, H. C. Ku, and R. S. Awadallah, "The effects of shadowing on modelling forward radar propagation over a rough sea surface," *Waves in Random and Complex Media*, vol. 18, no. 3, pp. 387-408, 2008.

[11] D. D. Wang, X. L. Xi, Y. R. Pu, and J. Liu, "Parabolic equation method for Loran-C ASF prediction over irregular terrain," *IEEE Antennas and Wireless Propagation Letters*, vol. 15, pp. 734-737, 2016.

[12] G. Apaydin and L. Sevgil, "Matlab-based FEM-parabolic equation tool for path loss calculations along multi-mixed-terrain paths," *IEEE Antennas & Propagation Magazine*, vol. 56, no. 3, pp. 221-

236, 2014.
[13] D. J. Donohue and J. R. Kuttler, "Propagation modeling over terrain using the parabolic wave equation," *IEEE Trans. Antennas Propagat.*, vol. 48, no. 2, pp. 260-277, 2000.
[14] J. R. Kuttler and R. Janaswamy, "Improved Fourier transform methods for solving the parabolic wave equation," *Radio Science*, vol. 37, no. 2, pp. 5-1-5-11, 2002.
[15] N. Pinel, C. Bourlier, and J. Saillard, "Forward radar propagation over oil slicks on sea surfaces using the Ament model with shadowing effect," *Progress in Electromagnetics Research*, vol. 76, no. 1, pp. 95-126, 2007.
[16] C. Bourlier and G. Berginc, "Microwave analytical backscattering models from randomly rough anisotropic sea surface comparison with experimental data in C and Ku bands," *Progress in Electromagnetics Research*, vol. 37, no. 8, pp. 31-78, 2002.
[17] A. G. Liu and H. Cha, "Experiment study of electromagnetic wave propagation loss in oceanic evaporation duct," *Chinese Journal of Radio Science*, vol. 23, no. 6, pp. 1199-1203, 2008.

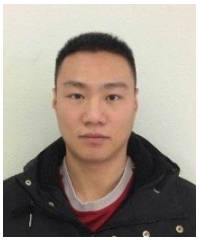

Mengda Cui received the B.S. degree in Radar Engineering and the M.S. degree in Signal and Information System from the Naval University of Engineering, Wuhan, China, in 2012 and 2014, respectively. He is currently pursuing the Ph.D degree at the Department of Electrical Engineering, Naval University of Engineering. His current research interests include atmospheric duct and Electromagnetic propagation.

Hao Cha received the M.S. degree and the Ph.D. degree in Communication and Information System from the Nanjing University of Aeronautics and Astronautics, Nanjing, China, in 1990 and 1993, respectively. Now he is a Professor in Naval University of Engineering and majors in radar system. He is responsible for many scientific research projects, such as military scientific research projects, and his research achievements gained the army science-technology advance reward many times.

Tian Bin received the M.S. degree in Electromagnetic Field and Microwave Technology and the Ph.D. degree in Communication and Information System from the Naval University of Engineering, Wuhan, China, in 2006 and 2010, respectively. He is now an Associate Professor in Naval University of Engineering. His main research direction is atmospheric duct and radar engineering. He is responsible for some scientific research projects, such as National Nature Science Foundation of China, and his research achievement gained the second medal in army science-technology advance reward.

A Novel Tunable Combline Bandpass Filter Based on External Quality Factor and Internal Coupling Tunings

Lixue Zhou [1], Shijie Liu [2], Jun Duan [1], and Min Xun [1]

[1] Microwave Engineering of Department
Xi'an Electronic Engineering Research Institute, Xi'an 710100, P. R. China

[2] Microwave Engineering of Department
Shanghai Aerospace Electronic Technology Institute, Nanjing 201109, P. R. China
Vesslan_zhou@163.com, lsjjs@163.com, nwpuduan@163.com

Abstract ─ A combline filter with quasi-elliptic performance with external quality factor and internal coupling tuning is presented in this paper. In this design, a wide center frequency tuning range with a constant 3-dB FBW (fractional bandwidth) and ABW (absolute bandwidth) is obtained. Also, it is demonstrated that the transmission zero located at the lower edge of passband can be adjusted with little effect on the passband characteristic. A prototype of the tunable filter with a tuning range of 1.27GHz to 2.25GHz is fabricated on a substrate with ε=10.2 and h=1.27mm. Through tuning internal coupling coefficient and external quality factor, one can make the filter operate over a wide center frequency tuning range, with a constant 3-dB FBW (fractional bandwidth) nearly kept at 54% or ABW (absolute bandwidth) nearly kept at 500 MHz.

Index Terms ─ Absolute bandwidth, coupling coefficient, fractional bandwidth, quality factor, tunable filter, transmission zero.

I. INTRODUCTION

Tunable bandpass filter is increasingly concerned in recent years, which is available to reduce the overall size and complexity of the modern communication and radar systems. Compared with other tunable filters, the combline topology is most frequently applied in the circuit design, due to its several advantages, such as miniaturization, one unique transmission zero in the upper band, convenience for integration and so on [1-9]. In [1-2], the designed method on the basis of the detailed formulas for a fundamental combline bandpass filter is presented, also its application is discussed. In [3-4], the resonator of SIR is utilized to keep the absolute bandwidth constant during the center frequency tuning. In [5], the short-circuited end of the resonator applied in combline filter is replaced by the lumped series resonator. And a wide tuning range can be achieved with only a small capacitance ratio of varactor. In [6], two coupled lines are introduced between the adjacent resonators to produce the source/load coupling and the multi resonator coupling. Then five tunable transmission zeros are created at the upper passband. In [7], the series *RC* unit is added to the first and last resonator to make the *Q* factor distribution of the resonator non-uniform. And then the passband flatness and selectivity of the filter are enhanced. In [8-9], the tunable filter with constant fractional bandwidth and absolute bandwidth is designed. Due to the cross coupling mechanism of the combline filter, transmission zeroes is always produced only at the upper passband edge, thus improving the selectivity of the filter at one side. However, the smoothing decrease of the rejection at the lower passband limits its practical application. Thus, another new transmission zero should be created at the lower passband to tackle the problem.

Several tunable combline filters with elliptic function performance have been designed [10-12]. In [10], a three-pole combline filter with two tunable transmission zeros located at two edges of the passband is presented. The additional transmission zero at the lower side is created due to a section line shunted with a varactor. In [11], a cross coupling between the non-adjacent resonators is produced, thus a new transmission zero is supposed to be generated to give the filter a quasi-elliptic performance. It is noted that [12] firstly demonstrates a four-pole combline filter with a pair of tunable transmission zeros at the two edges. And the phase difference between the main transmission path and other paths is analyzed to explain the production of the zeros. However, although some improvement is made to the performance of combline filter, how to simultaneously adjust the external quality factor and the internal coupling coefficient to control the bandwidth and control the position of the novel transmission zero is not discussed.

In this paper, a novel combline bandpass filter in Fig. 1 is presented. Varactors are employed to connect the adjacent resonators, the resonator and the I/O coupling

Submitted On: October 20, 2017
Accepted On: April 21, 2018

transmission line to tune the external quality factor and internal coupling tuning together. Therefore, the relative bandwidth and absolute bandwidth can be adjusted during the center frequency tuning, and in the paper *FBW* or *ABW* is nearly invariable in the process of the center frequency change. In addition, the application of a novel transmission line which produces the cross coupling between the I/O transmission lines creates a novel tunable transmission zero at the lower passband edge, thus, improving the selectivity of the designed filter. In this way, the tunable filter with fixed bandwidth can be used to connect with frequency synthesizer (PLL or DDS) which produces frequency-hopping signal of constant bandwidth to suppress spurious signal. And also, the filter is considered as a candidate for the switching-filter component which is frequently composed by several filters of adjacent passband. Detailed theoretical design, simulation, and experimental results for the tunable filter are demonstrated and discussed below.

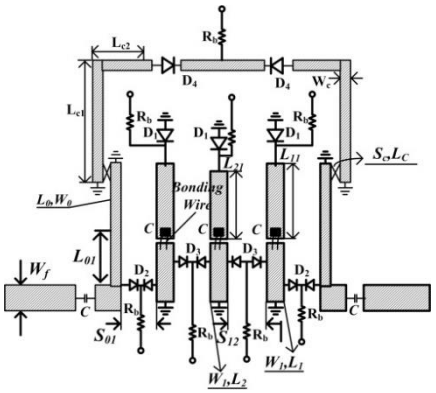

Fig. 1. Circuit of proposed tunable combline bandpass filter (W_f=1.2mm; W_0=0.4mm; W_1=0.8mm; W_c=0.4mm; S_{01}=0.3mm; S_{12}=0.2mm; S_c=0.2mm; L_{c1}=5.6mm; L_{c2}=1.5mm; L_c=2.8mm; L_1=6.8mm; L_2=6.4mm; L_{01}=1.45mm).

II. ANALYSIS AND DESIGN OF THE PROPOSED TUNABLE FILTER

In Fig. 1, the circuit configuration of the proposed tunable filter is shown. It can be seen that thirteen varactors marked as D_1, D_2, D_3, and D_4 are applied to satisfy the requirement for center frequency, internal coupling coefficient, external Q factor and the transmission zero tuning. Besides, to provide the *DC* power, several blocking capacitors *C* are utilized. What's more, a cross coupling path are introduced here to bring an additional transmission zero at lower passband. And, the characteristic impedances of the two microstrip lines at the input/output ports are both 50Ω.

It is clear from Fig. 1 that the varactor D_2 is applied to change the external Q factor of the filter, while D_3 used to tune the internal coupling coefficient. And the technique to calculate the Q factor and coupling coefficient can be found in [13-14]. Hence, Fig. 2 (a) is drawn to present the relationship between the Q factor and capacitance value of D_2, while the coupling coefficient vs. capacitance value of D_3 is given in Fig. 2 (b). In the figures, four capacitance values of D_1 that controls center frequency are considered. As is known, $Q=g_0g_1/FBW$ and $M_{i,i+1}=FBW/(g_ig_{i+1})$. Thus, various combination of Q and $M_{i,i+1}$ means different bandwidth. Taking D_1=1.2pF as an example, 52.3% of *FBW* which is the final result in this paper will be obtained when making D_2 and D_3 equal 1.1pF and 1.3pF.

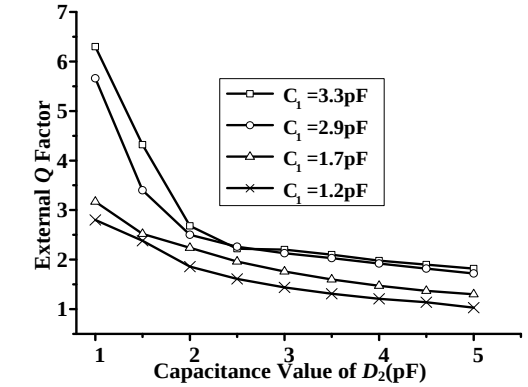

(a)

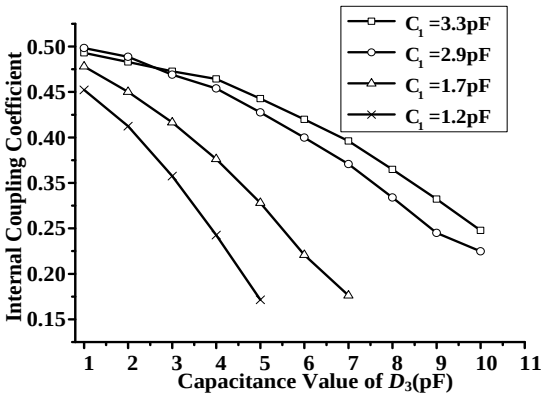

(b)

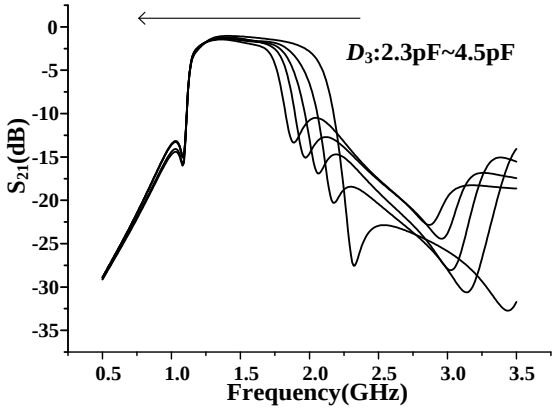

(c)

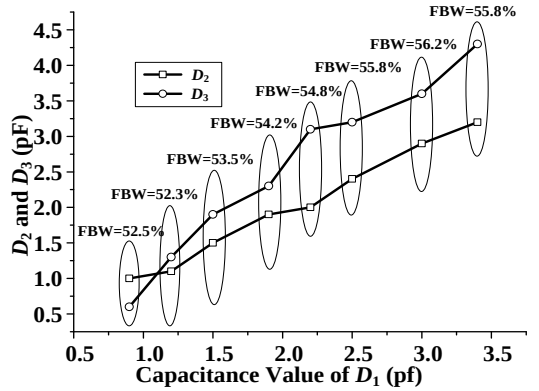

(d)

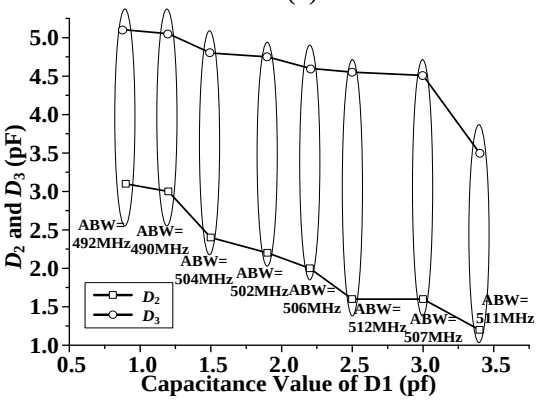

(e)

Fig. 2. (a) The relationship between external Q factor and capacitance value of D_2; (b) the relationship between internal coupling coefficient and capacitance value of D_3; (c) bandwidth change during the adjustment of D_2 and D_3; (d) the constant *FBW* during the center frequency moving; (e) the constant *ABW* during the center frequency moving.

To demonstrate the tunable characteristic for the bandwidth, Fig. 2 (c) which represents the variation process of bandwidth are plotted for the fixed value of D_1 (1.9pF) and D_4 (4.2pF). It is found that *FBW* is adjusted from 46.6% to 60.4% during the D_3's decreasing. And it should be remembered that a wider tuning range of *FBW* will be gotten, if expanding value's limit of D_2 and D_3. Figure 2 shows that the external Q factor and the internal coupling coefficient are inversely proportional to the capacitance value of D_2 and D_3. And for a fixed value of D_2 and D_3, the decrease of D_1 will lead to the decrease of Q factor and coupling coefficient [15-18]. Thus, to maintain the *FBW* as a constant, D_2 and D_3 should be adjusted simultaneously to keep the Q factor and coupling coefficient almost unchanged. Considering the element values $g_0=g_4=1$, $g_1=g_3=1.2275$ and $g_2=1.1525$ for Chebyshev lowpass prototype filters as an example, *FBW* of about 56% will be obtained when D_1 is made to be 3.4pF which tends to locate the center frequency of filter around 1.26GHz, while D_2 and D_3 which respectively determine the external Q factor and internal coupling coefficient are equal to be 3.2pF and 4pF. D_4 deciding the position of novel transmission zero is assigned 7.1pF on the basis of the technique involved below. And from Fig. 2 (d), with the decrease of the value of D_1, one should correspondingly reduce the values of D_2 and D_3 simultaneously to fix the *FBW* depending on Fig. 2 (a) and Fig. 2 (b). And, properly adjusting the values of D_2 and D_3, *FBW* can be almost unchanged in the whole process of center frequency tuning. What's more, it is seen from Fig. 2 (e) that properly adjusting D_2 and D_3 simultaneously, the absolute bandwidth (*ABW*) can also be almost unchanged during the D_1 change. To maintain a constant *ABW* during the increase of center frequency, the coupling coefficient should be decreased and the external quality increased.

For the conventional combline tunable filter, one transmission zero is always created at the upper passband edge, thus improving the selectivity of the filter at one side. So, another transmission zero should be produced at the lower passband to improve the rejection. In this paper, an additional signal propagation path whose equivalent circuit model is shown in Fig. 3 (a) is introduced from input coupling line to the output one. Hence, the quasi-elliptic performance is expected because of the multiple path cancellation. And the location of novel transmission zero is decided by the resonating frequency of the coupled lines.

Figure 3 (b) and Fig. 3 (c) show the odd mode and the even mode equivalent circuit. It is obvious from Fig. 3 (c) that even mode resonating frequency is non-adjustable. In this case, the odd mode resonating frequency which can be controlled by D_4 is used to adjust the novel transmission zero. S_{11o} of the odd mode equivalent circuit in Fig. 3 (b) can be written as $S_{11o}=(Y_o-Y_{ino})/(Y_o+Y_{ino})$, where Y_o is the characteristic admittance of the circuit, $Y_{ino}=(-Y_{11}\times Y_{in}-Y_{11}^2-Y_{12}^2)/(-Y_{in}-Y_{11})$, where Y_{11}, Y_{in} and Y_{12} can be found as below:

$$Y_{11}=Y_{22}=-j0.5(Y_{oe}+Y_{oo})\cot(\theta), \tag{1}$$

$$Y_{12}=Y_{21}=-j0.5(Y_{oe}-Y_{oo})\csc(\theta), \tag{2}$$

$$Y_{in}=j\,(Y_4\omega C+Y_4^{\,2}\tan(\theta))\Big/(Y_4-\omega C\tan(\theta))\,. \tag{3}$$

In the equations, Y_{oe} and Y_{oo} denote the even mode characteristic impedance and the odd mode characteristic impedance of the coupling line, $\theta=\theta_4=\theta_c$. And the odd mode resonating frequency which makes $S_{11o}=0$ true, identifies the location of transmission zero. And, the equivalent circuit simulation in *ADS* (Advanced Design System) also indicates the resonating frequency of odd mode and even mode. In addition, Fig. 3 (d) is presented to demonstrate how the value of D_4 influences the resonating frequency.

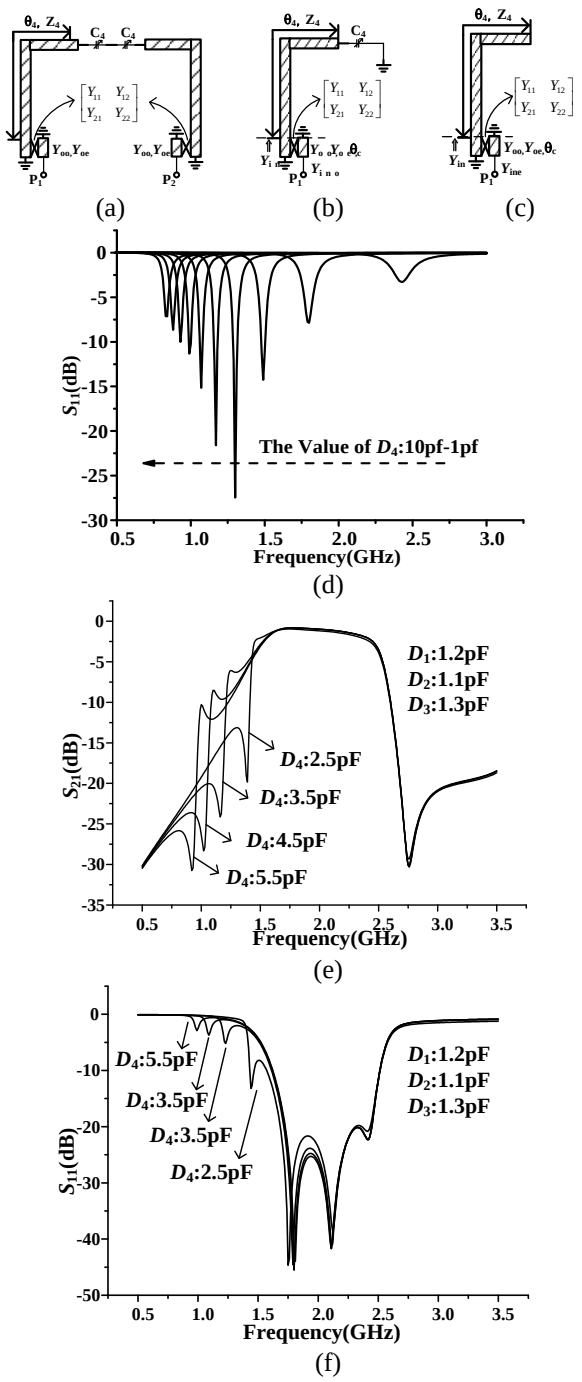

Fig. 3. (a) Equivalent circuit of the new transmission path; (b) the odd mode equivalent circuit; (c) the even mode equivalent circuit; (d) the odd mode resonating frequency of the added coupled line (Z_4=75.6Ω; θ_4=8.7°; Z_{oe}=107Ω; Z_{oo}=37Ω; θ_c=8.7° for f_0=1GHz); (e) S21 simulation result for D_1=1.2pF; (f) S11 simulation result for D_1=1.2pF.

In conclusion, the resonating frequency is inversely proportional to the value of D_4. To further demonstrate how the produced transmission zero is controlled by D_4, Fig. 3 (e) and Fig. 3 (f) are given. And, the proper value should be set to D_2 and D_3 based on Fig. 2 (a) and Fig. 2 (b). What is shown in Fig. 3 has proven that adjustment of D_4 results in the change of the transmission zero at lower band. However, as the novel transmission zero moved away from the passband, a resonating transmission pole becomes increasingly obvious. Hence, to tackle the problem, the value of D_4 is chosen carefully to make the lower transmission zero approach passband.

III. DESIGN OF THE TUNABLE FILTER

Based on the analysis above, the design parameters are determined as follows:

Step 1): Select the third-order low-pass prototype with elements. Then calculate the external quality factors Q_e and the coupling coefficient M_{ij} through $Q=g_0g_1/FBW$ and $M_{i,i+1}=FBW/(g_ig_{i+1})$, where FBW is the 3-dB fractional bandwidth.

Step 2): Determine the dimensions of the proposed tunable resonator. Initially, the impedance of the transmission line is conveniently selected as 72Ω (W_1=0.5mm is chosen initially), and the electrical length of the coupled line is set to 45 degrees at 1.7GHz (L=7.4mm), according to the required frequency tuning range. The spacing S_{12} between two resonators can then be determined. An initial value for S_{12} is chosen such that the coupling coefficient of the coupled resonators satisfies the bandwidth requirement at the center frequency.

Step 3): The rest of the design parameters are then determined. The coupling I/O structure is adopted to satisfy the constant bandwidth requirement over a wide tuning range because it has wideband matching behavior. The input/output line is typically chosen to be a high impedance line for tight coupling. S_{01} and W_0 are then chosen to satisfy external quality factors Q_e, using the well-known coupling coefficient/external Q_e method described in [13].

Step 4): An additional signal propagation path shown in Fig. 3 (a) is employed from input coupling line to the output one to create a novel transmission zero. And equivalent circuit technique is adopted to find the initial value of S_c and L_c. In the paper, short coupling lines of 15 degrees in length are chosen. And S_c is selected to be the same as S_{12} for simplicity.

Step 5): Finally, some necessary optimization is carried out, making use of electromagnetic EM simulation in SONNET. The estimated circuit dimensions from previous steps are substituted into a full wave EM simulator for including discontinuity, via-hole, and non-adjacent coupling effects. And when the center frequency is changed by D_1, another group of value for D_2, D_3 and D_4 units must be updated to keep the good passband performance based on Fig. 2 and Fig. 3.

A tunable filter of constant bandwidth is designed

on RT/Duroid 6010 with ε_r=10.2 and h=1.27mm with an overall size of 22×25mm^2. Electro-magnetic simulation software of SONNET is applied for the optimization. Three kinds of silicon junction varactor diodes produced by Nanjing Electronic Devices Institute are applied. *WB62* (C_t=0.45~4.23pF; R_s=1Ω; Q=3000 at 50MHz for C_t=1.07pF) is selected as D_1 to accomplish the center frequency tuning, while the wide tuning range varactor *WB2011H* (C_t=1.79~20.53pF; R_s=0.5Ω; Q=1200 at 50MHz for C_t=6.73pF) is chosen to adjust the location of the transmission zero. Besides, for the trivial space between the two adjacent resonators, the bondable chip varactor *W205* (C_t=0.8~11.54pF; R_s=1.2Ω; Q=800 at 50 MHz for C_t=3.55pF) is considered as the candidate for the coupling coefficient and external Q factor control, and the bonding wire is applied to finish the connection. Murata 0402 lumped components and 100pF chip capacitors are used for *DC* blocking and biasing.

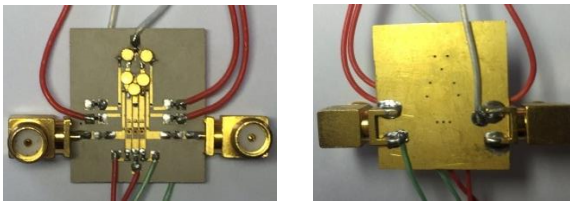

Fig. 4. Photography of the tunable combline filter.

In Fig. 4, the photography of the novel tunable filter is introduced. And the simulation and measured result in which the bandwidth is nearly kept unchanged are given in Fig. 5 and Fig. 6. The filter with the lowest center frequency 1.27GHz is optimized at the beginning (D_1=3.4pF, D_2=3.2pF, D_3=4.3pF, D_4=7pF). Then, D_1 is decreased to raise the center frequency to be 2.25GHz, while D_4 is reduced to move up the transmission zero correspondingly according to Fig. 3. Finally, D_2 and D_3 are adjusted monotonously to be 1pF and 0.6pF to keep a constant quality factor and coupling coefficient. Thus, nearly a constant fractional bandwidth can be acquired. And, for the case with unchanged absolute bandwidth during center frequency moving, D_2 and D_3 are tuned to be 1.2pF and 3.5pF.

According to [10], the following equation indicates that *FBW* and Q_u both mainly determine the insert loss of the filter:

$$IL(dB) = 4.343\sum_{i=1}^{n}\frac{g_i}{\Delta Q_u}, \tag{4}$$

where Δ stands for the fractional bandwidth and Q_u represents the unloaded quality factor of resonator. Again, g_0=g_4=1, g_1=g_3=1.2275 and g_2=1.1525 for Chebyshev lowpass prototype filters are considered and Q_u of the resonator covers the value range of 50 to 90 during center frequency tuning. Thus, *IL* is almost less than 2dB for most tuning cases. However, the measured insertion loss at the tuning range varies from 3dB to 5dB. This difference of *IL* is due to the *SMA* connector and the deviation of the diode's index.

Figure 5 and Fig. 6 demonstrate the simulated and measured results, with the center frequency turning from 1.27GHz to 2.25GHz. One can figure out that the filter achieves the quasi-elliptic performance. And the adjustment of D_4 makes the transmission zero close to the passband. Besides, D_2 and D_3 are changed correspondingly during center frequency tuning in order to keep the *FBW* and *ABW* invariant. As a result, the range of 52.5%~55.8% of the fractional bandwidth and absolute bandwidth of 490MHz~512MHz are obtained. To see the similarity, both the simulated and measured curves are plotted in one graph as shown in Fig. 5 and Fig. 6. Good agreement can be observed between the simulated and the experimental results. The slight frequency shift and difference of insert loss between measured and simulated results may be caused by the fabrication errors and the *SMA* connector. So, the comparing results given below have proven the advantage of the novel structure.

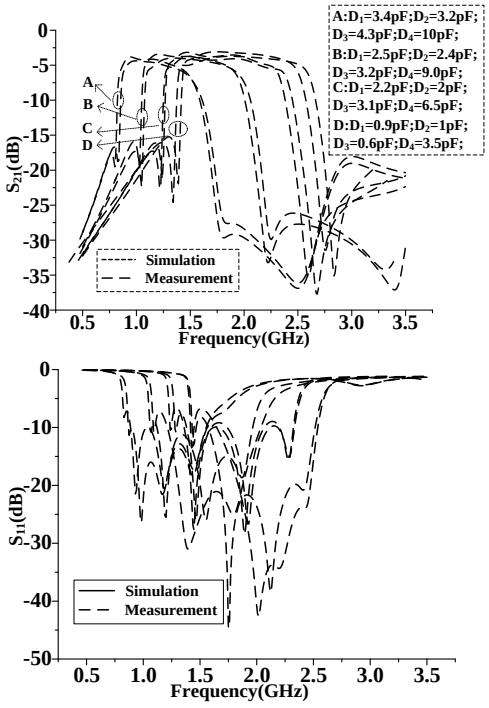

Fig. 5. Simulated and measured results of combline filter with constant FBW. (Voltage for the varactors during measurement is turning as below: V_1:5.1-0.9V; V_2:11.3-1.9V; V_3:17.6-2.9V; V_4:19.4-3.1V).

The comparisons of measured results for several tunable filters [5, 10-12] are shown in Table 1. It can be concluded that although the capacitance ratio for D_1 in this paper is not the smallest one, the tuning range of the

center frequency is wider than other compared structures. And as other tunable filters, the one introduced in the paper also have two transmission zeros at passband edges to improve the rejection. And the lower transmission zero can even be adjusted. Finally, being different from other tunable filters, *FBW* can almost be invariant during center frequency changing for the designed one in the paper.

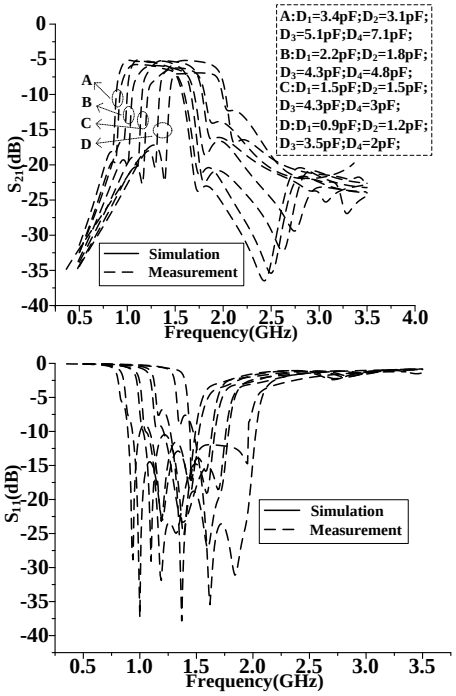

Fig. 6. Simulated and measured results of combline filter with constant ABW. (Voltage for the varactors during measurement is turning as below: V_1:5.1-0.9V; V_2:11.7-2.1V; V_3:9.2-1.6V; V_4:19.4-3.1V).

Table 1: Comparisons with wideband filters

Ref.	Tuning Range (GHz)	C Ratio	Size (λ_{g0}@2GHz)	Diode Number	Elliptic
[5]	1.7~2.2	2.6	0.35×0.51	4	No
[10]	1.5~2.2	6.7	0.20×0.28	9	Yes
[11]	1.75~2.25	6.7	0.18×0.26	5	Yes
[12]	1.55~2.1	5.6	0.21×0.30	10	Yes
This	1.27~2.25	3.8	0.37×0.42	13	Yes

IV. CONCLUSION

In this work, a 1.27~2.25GHz tunable combline bandpass filter based on external quality factor and internal coupling tuning is proposed. During the tuning of the center frequency, coupling coefficient and external quality factor are adjusted to keep the bandwidth as a constant value. Additionally, a novel transmission line is applied to generate the coupling between the *I/O* transmission lines to produce a new tunable transmission zero at the lower passband edge. Moreover, the quasi-elliptic performance can be observed at the simulation and measurement results. Therefore, the proposed filter exhibits good frequency selectivity, suggesting a good substitute for radio communication application.

REFERENCES

[1] I. C. Huncter and J. D. Rhodes, "Electronically tunable microwave bandpass filters," *IEEE Trans. Microw. Theory Tech*., vol. 30, no. 9, pp. 1353-1360, Sep. 1980.

[2] P. W. Wong and I. Huncter, "Electronically tunable filters," *IEEE Microw. Mag*., vol. 10, no. 6, pp. 46-54, Oct. 2009.

[3] B. W. Kim and S. W. Yun, "Varactor-tuned combline bandpass filter using step-impedance microstrip lines," *IEEE Trans. Microw. Theory Tech*., vol. 52, no. 4, pp. 1279-1283, Apr. 2004.

[4] L. Zhang, X.-H. Wang, Z.-D. Wang, Y.-F. Bai, and X.-W. Shi, "Compact electronically tunable micro-strip dual-band filter using stub-loaded SIRs," *J. Electromagn. Waves Appl*., vol. 28, no. 1, pp. 39-48, Jan. 2004.

[5] X. G. Wang, Y. H. W. Cho, and S. W. Yun, "A tunable combline bandpass filter loaded with series resonator," *IEEE Trans. Microw. Theory Tech*., vol. 60, no. 6, pp. 1569-1576, June 2012.

[6] S. R. Manuel, "High-selectivity tunable planar combline filter with source/load-multiresonator coupling," *IEEE Microw. Wireless Compon. Lett*., vol. 17, no. 7, pp. 513-515, July 2007.

[7] N. Jia, W. X. Tang, Z. C. Hao, and J. S. Hong, "An investigation of performance enhancement for tunable microstrip filter," in *2011 European Microw. Conf*., pp. 472-475, Oct. 2011,.

[8] D.-H. Jia, Q.-Y. Feng, X.-G. Huang, and Q.-Y. Xiang, "A two-pole tunable filter with constant fractional-bandwidth characteristics," *Inter. J. Electro*., vol. 101, no. 7, pp. 983-993, July 2014.

[9] B. Liu, F. Wei, Q. Y. Wu, and X. W. Shi, "A tunable bandpass filter with constant absolute bandwidth," *J. Electromagn. Waves Appl*., vol. 25, no. 11-12, pp. 1596-1604, Jan. 2011.

[10] Y. C. Chiou and G. M. Rebeiz, "Tunable three-pole 1.5–2.2-GHz bandpass filter with bandwidth and transmission zero control," *IEEE Trans. Microw. Theory Tech*., vol. 59, no. 11, pp. 2872-2878, Nov. 2011.

[11] Y. C. Chiou and G. M. Rebeiz, "A quasi elliptic function 1.75–2.25 GHz 3-pole bandpass filter with bandwidth control," *IEEE Trans. Microw. Theory Tech*., vol. 60, no. 2, pp. 244-249, Feb. 2012.

[12] Y. C. Chiou and G. M. Rebeiz, "Tunable 1.55–2.1 GHz 4-pole elliptic bandpass filter with bandwidth control and > 50 dB rejection for wireless systems,"

IEEE Trans. Microw. Theory Tech., vol. 61, no. 1, pp. 117-124, Jan. 2013.

[13] J.-S. Hong and M. J. Lancaster, *Microstrip Filters for RF/Microwave Applications*. New York: Wiley, 2001.

[14] D. M. Pozar, *Microwave Engineering*. 2nd ed., New York: Wiley, 1998.

[15] M. A. El-Tanani and G. M. Rebeiz, "Corrugated microstrip coupledlines for constant absolute bandwidth tunable filters," *IEEE Trans. Microw. Theory Tech*., vol. 58, no. 4, pp. 956-963, Apr. 2010.

[16] M. A. El-Tanani and G. M. Rebeiz, "High performance 1.5–2.5 GHz RF MEMS tunable filters for wireless applications," *IEEE Trans. Microw. Theory Tech*., vol. 58, no. 6, pp. 1629-1637, June 2010.

[17] Q. Xiang, Q. Feng, and X. Huang, "Tunable band-stop filter based on split ring resonators loaded co-planar waveguide," *Applied Computational Electromagnetics Society Journal*, vol. 28, no. 7, pp. 591-596, July 2013.

[18] Y. Ma, W. Che, W. Feng, and J. Chen, "High selectivity dual-band bandpass filter with flexible passband frequencies and bandwidths," *Applied Computational Electromagnetics Society Journal*, vol. 28, no. 5, pp. 419-426, May 2013.

Lixue Zhou received the M.S. degree in Electromagnetic Fields and Microwave Technology from Nanjing University of Science and Technology, Nanjing, China, in 2010 and the Ph.D. degree in Electrical Engineering Department of Xidian University, Xi'an, China, in 2017. Since 2010, he has been an Electronic Engineer in Xi'an Electronic Engineering Institute, where he developed the microwave and millimeter-wave circuit and RF component.

His research interests include microwave and millimeter-wave planar type circuit and multilayered circuit design and planner filter design in microwave and millimeter-wave frequency band.

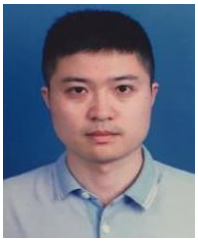

Shijie Liu received the M.S. degree in Communication and Information Systems from Nanjing University of Science and Technology, Nanjing, China, in 2010. Since 2010, he has been an Electronic Engineer in Shanghai Aerospace Electronic Technology Institute, where he worked on microwave circuits and radar systems research.

His research interests include microwave circuit and frequency synthesizer.

Jun Duan received the M.S. degree in Electronics and Information Systems from Northwestern Polytechnical University, Xi'An, China, in 2011. Since 2011, he has been an Electronic Engineer in Xi'an Electronic Engineering Institute, where he worked on microwave circuits and radar systems research.

His research interests include multiband antennas, dual-polarized antennas, waveguide slot antenna arrays.

Min Xun received the M.S. degree in Electronics and Information Systems from Northwestern Polytechnical University, Xi'An, China, in 2002. Since 2002, he has been an Electronic Engineer in Xi'an Electronic Engineering Institute, where he worked on microwave circuits and receiver research.

His research interests include microwave and millimeter-wave planar type circuit and multilayered circuit design.

FE Analysis on Temperature, Electromagnetic Force and Load Capacities of Imperfect Assembled GIB Plug-in Connectors

Xiangyu Guan [1], Xin Wei [1], Xianyong Song [2], Naiqiu Shu [1], and Hui Peng [1]

[1] School of Electrical Engineering
Wuhan University, Wuhan, 430072, China
xiangyuguan1986@163.com

[2] State Grid Hunan Power Supply Company
Yue yang, 414000, China
582583392@qq.com

Abstract ─ For purpose of providing effective method of optimal design and failure prediction of plug-in power connector with imperfect assembly conditions, this paper evaluate distributions of operation current, temperature rise and electromagnetic forces of gas insulated bus (GIB) plug-in connector by mechanical-electromagnetic-thermal multi-physics coupled finite element (FE) method. The FE procedure took current constriction effects among contact spots into account by imperfect contact bridge model. Effectiveness of numerical model was verified by physical experiments. Mechanical, electromagnetic and thermal behaviors of plug-in connector under various assembly conditions (preloading force, conductor insert depth and docking angle) were analyzed. Results show that due to the deviations of contact forces, operation currents and temperature rises among contact spots are not uniform. Influenced by overheating and electromagnetic force on several terrible contact spots with larger currents flow through, load capacity of plug-in connector could be reduced to 82%, 46% and 15% of design values with insufficient preloading contact force, insufficient conductor insert depth and docking angles deviation.

Index Terms ─ Electromagnetic force, finite element method, GIB, plug-in connector, short circuit current.

I. INTRODUCTION

The gas insulated bus (GIB) is favored by modern electrical industry for its large power transmission capacity, high operation reliability and well landscape coordination [1]. Spring type plug-in power connector is one of the most essential electrical connection parts inside GIB capsule. The main function of plug-in connector is to absorb misalignment caused by different thermal expansions between enclosure and conductor. However, mechanical slide able design makes the plug-in connector become weak component. As other power transmission/distribution equipment, safely operation of GIB relies on reliable connection of main electrical loop [2]. Internal insulation breakdown could be induced even contact deterioration/overheating happens on tiny part of the connector [3]. The fault of GIB equipment could be serious and power supply time is considerable due to its sealing structure. Therefore long term contact performance of plug-in connector should be accurately evaluated both in design and maintenance process to ensure safety of equipment.

Similar as other power connectors, the plug-in connector should have low and stable contact resistance and temperature rise. Mechanical structure should also be strong enough to resist the impact of short circuit current. Design-oriented closed formulas for the sliding GIB plug-in connector were given in [4], however deviation of contact performances among individual contact spots was ignored. Series works paid attention on electric, thermal and mechanical performances of power connectors during steady operation and pulse current impact by both closed formulas and numerical methods. Thermal effects of electrical contacts were analyzed by closed formulas in which the electrical connectors were modeled by lump components [5-6]. Numerical methods were conducted in order to obtain temperature distribution characteristics of electrical contacts [7-8]. Induced by current and surrounding electromagnetic field, electromagnetic repulsion forces acting on electrical connector are comprised of two parts: Holm repulsion force by the current constriction effect on contact interface [9] and Lorentz force by interaction between current carriers [10]. Focusing on electrical, thermal and mechanical field behaviors, some multi-physics models of electrical contacts were proposed in [11-12]. All of these works were based on static mechanical contact status. Forces on the contact interface were assumed as constant. However, it was noticed in [13] and our previous work [14] that transient movement on contact

Submitted On: July 31, 2017
Accepted On: April 21, 2018

interfaces of static power connector could be induced under cyclic loads such as operating current and environment temperature. Mechanical contact status of the GIB plug-in connector such as preloading contact force, conductor insert depth and docking angle can be changed with equipment service time, then make contact degeneration. Contact degeneration could reduce its load capacity. Traditional design methods paid few attentions on dynamic contact performance and load capacity of imperfect GIB plug-in connector after long time operation.

This work presents a mechanical-electromagnetic-thermal coupled physics FE method of large current GIB plug-in connector. Whole paper is organized as follows. Physical structure, test platform and numerical assumptions were described in Section 2. Multi-physics coupled FE model of imperfect assembled connector was built in Section 3. Results and experimental validation were shown in Section 4. Mechanical, electromagnetic and thermal contact behaviors of plug-in connector with various assembly conditions (preload contact force, conductor inserting depth and docking angle) under operation currents and short circuit current impact were discussed in Section 5. In Section 6, dynamic steady and fault load capacities of imperfect assembled GIB plug-in connector were discussed.

II. PHYSICAL STRUCTURE AND EXPERIMENT SET-UP

Thermal and electromagnetic force behaviors of spring type plug-in power connector used in GIB equipment were analyzed by multi-physics FE method. Physical experiments were also conducted to verify the effectiveness of the numerical model.

A. Physical structure and model assumptions

Physical structure of GIB plug-in connector is presented in Fig. 1 [4, 15-16]. GIB plug-in connector contains series pieces of contact fingers which are parallel arranged clockwise around the center axis of connector (A1). Mechanical contact forces on contact spots are supplied by series of holding springs. Conductor is made of aluminum alloy (6063-T6). The contact fingers are made of copper (T2-Y). Contact interfaces are plated with 20 μm sliver. Mechanical assembly conditions are defined as conductor insert depth H and conductor docking angle θ. Contact failure point locates on the edge chamfer of conductor plug. Geometric parameters of connector are listed in Table 1. Material properties are listed in Table 2. FE model of plug-in connector is based on the following assumptions.

- To reduce computational effort, some geometric features such as shield, bolt and other tiny chamfers (less than 0.5mm) were ignored.
- Quasi-static approximation of electromagnetic field could be used for low frequency current.
- Only mechanical contact area was considered for chemical stability of SF_6 gas. Mechanical contact was supposed occurs on one equivalent contact spot.
- During steady state analysis, electromagnetic force was omitted for its small amplitude. During short circuit fault analysis, it assumed no heat transfer occur between connector surface and environment due to the limited fault duration time.

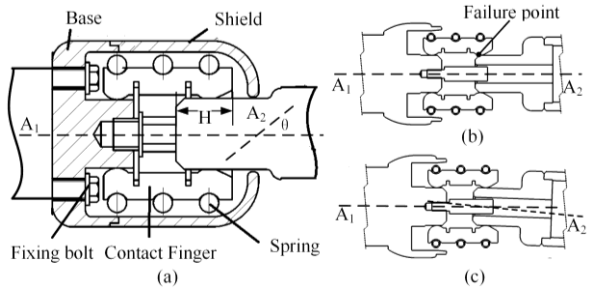

Fig. 1. Physical structure and mechanical assembly of GIB plug-in connector.

Table 1: Geometric parameters of GIB model

Conductor Material	Aluminum alloy 6063-T6
Finger Material	Copper alloy T2-Y
Conductor Length	391mm
Conductor Diameters	Φ85mm/Φ65mm
Finger Number	16
Spring Stiffness	980N/m
Spring Diameters	Φ85mm(free)/Φ108mm

Table 2: Material properties

Properties	6063	T2-Y
Density(kg/m^3)	2700	8900
Young's modulus (Gpa)	69	110
Poisson's Ratio	0.33	0.343
Resistivity (10^-8Ω.m)	3.3	1.7
Thermal conductivity(W/m/K)	209	388
Specific heat capacity (J/(kg.K))	902	391

B. Physical experiment set-up

Physical experiment set-up of prototype GIB plug-in connector was shown Fig. 2 (a). Test current was supplied by 2000A/5V current generator. Temperature rises on each contact finger were measured by k-type thermal couples. The temperature measure points were located on front sides of contact fingers nearby contact spots (Fig. 2 (b)). Analyzer was consisted of ampere meter, data acquisition (DAQ) card and Industrial Personal Computer (IPC) with LABVIEW software platform. Test currents were measured by ampere meter integrated inside the current generator. Temperatures collection interval was set as 1min.

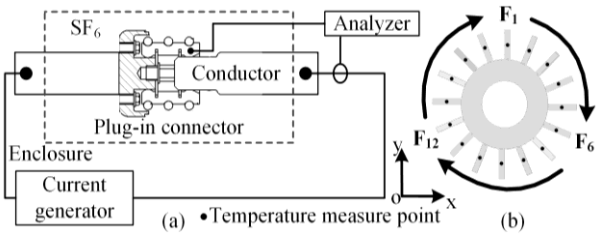

Fig. 2. Experiment set-up of GIB plug-in connector.

III. NUMERICAL MODELING

The FE analysis of GIB plug-in connector were conducted both steady state solution (operation current) and transient solution (short circuit fault). Numerical solution region is described in Fig. 3. The FE model includes contact fingers, conductors and surrounding gas medium (SF_6). Contact force F_n is influenced by the holding springs, gravity and electromagnetic force. The current I_n flows cross the contact interfaces through equivalent contact bridges.

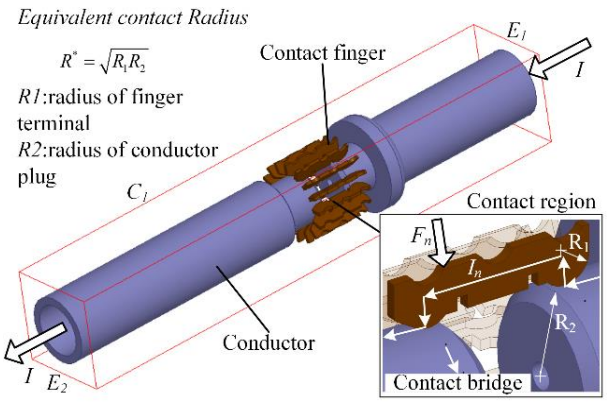

Fig. 3. Numerical solution region division and boundary conditions.

Multi-physics coupled FE analysis of GIB plug-in connector was realized by the sequent coupling (load transfer) method. Numerical calculation flowchart was described in Fig. 4. Nonlinear mechanical analysis was previous conducted to obtain initial mechanical contact parameters (forces and radiuses) on each contact spots of GIB connector with various mechanical assembly conditions. Using the radiuses $a_n(t)$ as contact bridge model parameters, electromagnetic (EM) field analysis was conducted to calculate power losses P(t) and EM force Fe(t). Temperature rise T(t) was calculated by thermal (TH) field analysis using power losses as load inputs. Contact status was updated through load step iterations during steady analysis and time iterations during transient short circuit fault analysis.

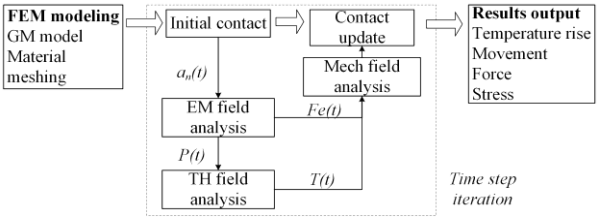

Fig. 4. Flowchart of multi-physics coupled FE procedure.

A. Field differential equations

Governing equation of electromagnetic field can be described as follows with magnetic vector potential **A**:

$$\mu\sigma\partial\mathbf{A}/\partial t - \nabla^2\mathbf{A} = \mu\mathbf{J}, \tag{1}$$

where μ is permeability, σ is electrical conductivity, $\boldsymbol{J}$ is current density. Boundary condition of electromagnetic field is as follows:

$$\mathbf{A}|_{c1} = 0. \tag{2}$$

Governing equation of thermal field can be described as follows combined with the current density as heating sources:

$$\rho c\frac{\partial T}{\partial t} - \lambda(T)\cdot\nabla^2 T = \int_V \frac{J^2}{\sigma}dV + 2\sum_{i=1}^{16} J_i^2 R_i, \tag{3}$$

where $\lambda(T)$ is thermal conductivity, ρ is material density and c is specific heat capacity, J_i is operation current on i contact spot.

Boundary conditions of thermal field include the heat fluxes on connector terminals and heat exchange between connector surface and environment:

$$\begin{cases} -\lambda(T)\dfrac{\partial T}{\partial n} = q_s \\ -\lambda(T)\dfrac{\partial T}{\partial n} = K_T(T - T_0) \end{cases}. \tag{4}$$

Equivalent heat transfer coefficient is set to consider the heat convection and radiation process:

$$K_T = (T - T_f)^{0.25} + \frac{\sigma_T \varepsilon_T}{(T - T_f)}(T^4 - T_f^4), \tag{5}$$

where σ_T is Boltzmann constant, ε_T is surface emissivity.

Self-acceleration relationship between contact resistance and contact temperature rise is as follows [17]:

$$R_c = R_0\left[1 + \frac{2}{3}\alpha_T(T - T_0)\right]. \tag{6}$$

Governing equation of mechanical field can be described as follows:

$$\begin{cases} \dfrac{\partial^2 u_i}{\partial t^2} + (\kappa + G)\dfrac{\partial e}{\partial i} = \mathbf{F_p} + \mathbf{F_g} + \mathbf{F_e} \\ \kappa = \dfrac{E\nu}{(1+\nu)(1-2\nu)} \\ e = \dfrac{\partial u_x}{\partial x} + \dfrac{\partial u_y}{\partial y} + \dfrac{\partial u_z}{\partial z} \end{cases}, \tag{7}$$

where u_i is the direction deformation along components of Cartesian coordinate system (i=x, y, z), κ is the lame constant, G is shear modulus, e is volume deformation, external forces include preloading force $\mathbf{F_p}$, conductor gravity $\mathbf{F_g}$ and electromagnetic force $\mathbf{F_e}$.

Pre-loading contact force on per contact spot can be expressed as:

$$F_p = 3K\pi^2 \Delta D / n, \tag{8}$$

where K is the spring stiffness and ΔD is the spring diameter increase after assembly.

Electromagnetic force induced by the interaction between current and magnetic field can be expressed as:

$$F_e = \int_V J \times B dV. \tag{9}$$

The GIB plug-in connectors are often fixed on the disc-type insulators, and the positioning design allows only axial freedom (direction of insert depth) and limited range of radial freedom (less than 2°).

Backward stepping scheme is adopted for the time discretization during the transient short circuit analysis:

$$(dx / dt)^{t+\Delta t} = (x^{t+\Delta t} - x^t) / \Delta t, \tag{10}$$

where x is the field nodal variables, t is the analysis time, the time step Δt is set as 1ms to simulate transient short circuit fault process.

B. Contact equivalent

The mechanical contact radius a_n on individual contact spot can be calculated by Hertz formula:

$$a_n = (3F_n R^* / 4E^*)^{1/3}, \tag{11}$$

where F_n is the contact force of n contact finger which equals to half of reactive force on individual contact spots, R^* is the equivalent contact radius (Fig. 3), E^* is equivalent Young's modulus.

The role of current constriction effect and contact resistance is usually considered by the contact bridge model. However, forces and radii on several contact spots are too small to be geometrically modeled. To simply contact spots of GIB plug-in connector under various assembly conditions, imperfect contact bridge model was constructed in our previous work [18] by two parameters: the equivalent contact radius r_n and the equivalent electric resistivity ρ_n:

$$\begin{cases} r_n = a_n & a_n \geq 0.1mm \\ r_n = 0.1mm & a_n < 0.1mm \end{cases}, \tag{12}$$

$$\rho_n = \eta \rho_{\text{silver}}, \tag{13}$$

$$\begin{cases} \eta = 1 & a_n \geq 0.1mm \\ \eta = 0.1 / a_n & 0 < a_n < 0.1mm \\ \eta = \infty & a_n = 0mm \end{cases}, \tag{14}$$

where η is electric resistivity ratio between n contact bridge and silver.

IV. FIELD RESULTS AND VERIFICATION

3-D FE model of GIB plug-in connector was built to describe mechanical, electrical and thermal field behaviors of GIB plug-in connector under operation current and short circuit current impact. The mechanical assembly condition was defined as 30mm of conductor insert depth, 0° of conductor docking angle under initial preloading contact force. Environmental temperature was 18℃. Operation current was 2000A and typical transient waveform of short circuit current was as follows:

$$i(t) = \sqrt{2} I (e^{-\alpha t} - \cos(\omega t)), \tag{15}$$

where I=10kA, ω=100π, α=22.311s^{-1}.

A. Field distributions

Mechanical field distribution of GIB plug-in connector is described in Fig. 5. Results show that the radial deformation happens on contact fingers for the over-travel design between connector and conductor terminal. Deformations on bottom contact finger are larger than upper ones for gravity. Influenced by uneven deformation of contact elements, mechanical stresses concentrate on contact spots and the maximum stress increasing from upper contact spots to bottom ones. Uneven mechanical contact forces can influence distributions of contact resistances and currents.

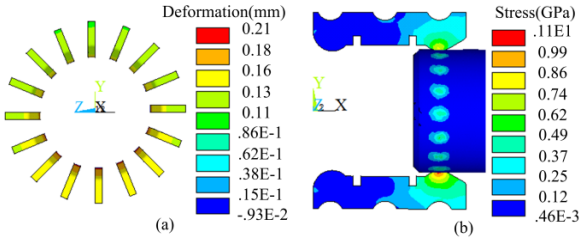

Fig. 5. Initial mechanical field distributions: (a) radial deformation and (b) von-Mises stress.

Distributions of current densities and temperature rises of GIB plug-in connector are described in Fig. 6. Results show that current density concentrates on contact spots for the limited electrical contact area. Local power losses and excessive temperature rises on contact spots can be induced by current. Temperatures on the bottom contact fingers are larger than those of upper ones for the deviation of operation current which is influenced by mechanical contact forces. It can be deduced that the mechanical assembly conditions could influence the thermal behaviors and load capacities of GIB plug-in connector.

Current and electromagnetic force densities of GIB plug-in connector concerning under peak value of short circuit current (t=10ms) are shown in Fig. 7. Results show the currents of lower contact fingers are larger than those of upper ones, which causes non-uniform electromagnetic forces. The electromagnetic force on contact finger is opposite to the preloading contact force. Real contact force can be reduced by increasing of

electromagnetic force under short circuit fault.

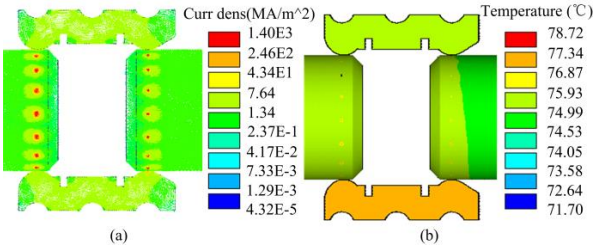

Fig. 6. Steady current and temperature distributions.

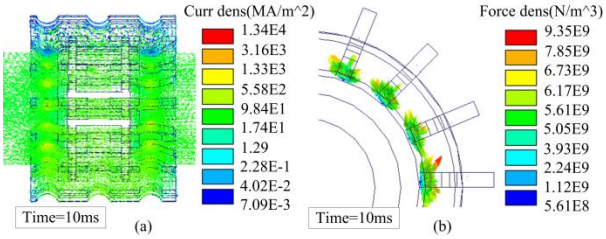

Fig. 7. Current and electromagnetic force distributions.

B. Transient characteristics under short circuit fault

Transient thermal responses of contact spot and conductor terminal under short circuit current impact are described in Fig. 8. Results show that temperature on contact spot follows the waveform of short circuit fault current for the small thermal constants. However, unlike contact spot, the transient temperature rise on measure points does not follow the fault current for the relative large thermal constants. Similar result has been found by research on similar connector structure [19].

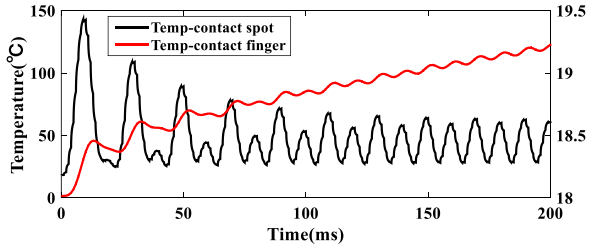

Fig. 8. Thermal response at contact spot and conductor.

Figure 9 shows the transient electromagnetic forces and temperature on the bottom contact spot (no.9 in Fig. 2) within the first three waveforms of fault current (60ms). FE results are compared with the well-known V-T relation [20] and design formula [4]. Results show that temperature by FE analysis lags behind the V-T relation for the difference between electric and thermal time constants of contact spot. Electromagnetic force contains 50Hz and 100Hz components, and force amplitudes by design formula are 50% smaller than FEM results for the Lorentz force is not considered.

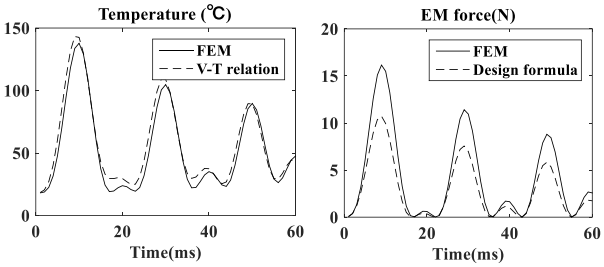

Fig. 9. Transient temperature rises and electromagnetic force on the bottom contact spot.

C. Results verification

Physical experiments were carried out in order to verify effectiveness of numerical model besides provide more information about thermal performance of GIB plug-in connector. Steady-state temperature rises on individual contact spots under different operation currents were obtained by both FE model and physical experiments. Calculated and the measured results are listed in Table 3. Both calculated and measured results follow the same trend as described in Fig. 6. The maximum deviation of calculation and test results is less than 15%. Errors are caused by approximation of heat transfer coefficient. Several thermal couples could be loosen due to higher test temperature.

Table 3: Temperature on individual contact spots (℃)

No	1000A		2000A		3000A	
	FEM	Test	FEM	Test	FEM	Test
1	35.4	36.3	58.6	66.9	92.4	105.2
2	36.2	36.3	60.6	67.1	100.0	105.3
3	36.4	36.4	63.3	68.4	100.1	106.1
4	36.6	36.6	65.3	68.8	101.6	106.9
5	37.4	36.8	65.8	70.6	103.4	108.0
6	37.5	36.9	66.7	71.8	104.5	108.9
7	38	37.1	67.4	72.6	105.0	109.6
8	38.8	37.1	71.7	73.0	105.2	110.0
9	38.3	37.2	73.8	73.2	107.8	110.2
10	38.1	37.1	68.8	73.1	107.1	110.1
11	37.7	37.0	67.2	72.4	106.2	109.4
12	36.4	36.9	66.8	71.8	104.6	109.0
13	36.3	36.8	65.9	70.7	101.3	108.2
14	35.8	36.6	63.4	68.8	99.6	107.1
15	35.5	36.4	62.9	67.4	97.5	106.1
16	35	36.3	60.9	66.7	92.6	105.5

V. CONTACT BEHAVIORS WITH VARIOUS ASSEMBLY CONDITONS

Distributions of mechanical contact parameters among contact spots across total assembly ranges are critical for electrical and thermal performance of GIB

plug-in connector. Using mechanical field analysis, distributions of initial mechanical contact forces and radii of plug-in connector with different mechanical assembly conditions are described in Fig. 10. Results show mechanical contact parameters on individual contact spots vary from each other. Deviation of contact parameters becomes larger with decrease of preloading contact forces, conductor insert depths, and increasing of conductor docking angles. Influenced by mechanical contact parameter deviations, contact resistances and currents among contact spots are different.

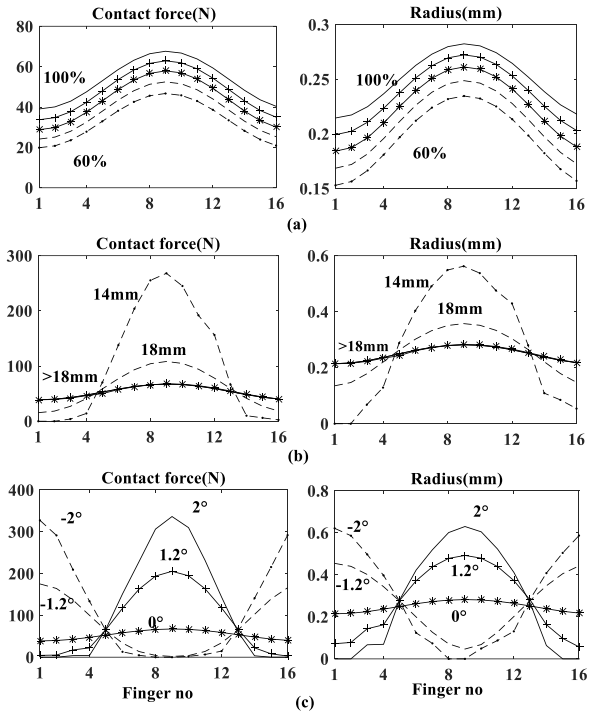

Fig. 10. Distributions of contact forces and radii: (a) preloading contact force, (b) conductor insert depths, and (c) conductor docking angle.

A. Contact behaviors under steady-state

Operation current up to several kA can lead to obvious temperature rise on contact spots. Ampacities of plug-in connector are constrained by the maximum temperature. Distributions of currents and temperature rises of GIB plug-in connector with different assembly conditions under 2000A current at 18℃ environmental temperature are shown in Fig. 11.

Distribution of currents and temperatures among contact spots with various preloading contact forces are described in Fig. 11 (a). Results show that the reducing of preloading contact forces by lower spring stiffness could make larger current deviations, which induce larger temperature rise on the bottom contact spots. However, the maximum temperature (94.5℃) could not exceed threshold (105℃), even the preloading contact force decrease to 60% of its initial value; which means that reducing of preloading contact force is not the main factor influencing contact performance of connector under steady-state operation current.

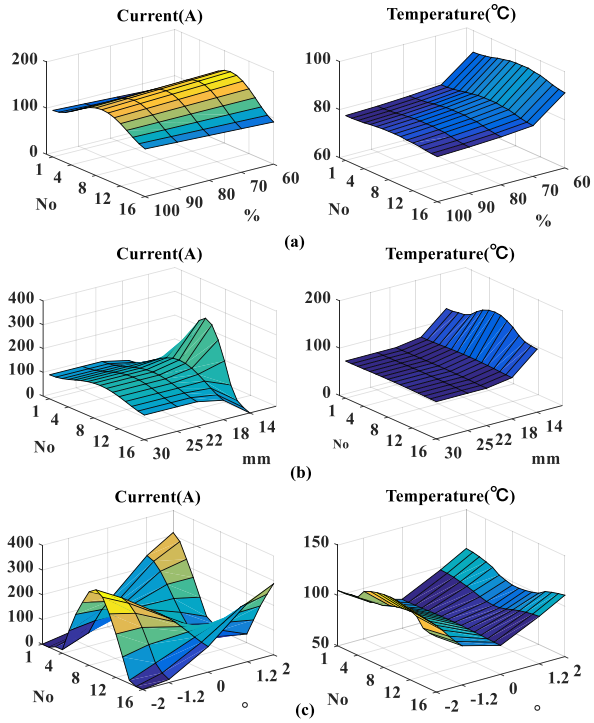

Fig. 11. Currents and temperatures on individual contact spots of GIB plug-in connector under steady state.

Distribution of currents and temperatures among contact spots with various conductor insert depths are described in Fig. 11 (b). Results show that deviation of currents and temperatures become larger with decrease of conductor insert depths. When conductor insert depth does not exceed failure point (18mm), the maximum temperature is below threshold value for nearly uniform contact parameters. However, when conductor insert depth exceeds failure point, current and temperature among contact spots significantly deviates. Overheating could be induced on several spots with larger currents.

Distributions of currents and temperatures among contact spots with various conductor docking angles are described in Fig. 11 (c). Results show that deviation of temperature becomes larger with increase of conductor docking angles. When docking angle deviation is below 1.2°, the maximum temperature is below threshold value for nearly uniform contact parameters. However, when conductor docking angle deviation exceeds 1.2°, temperature among contact spots significantly deviates. Overheating could be induced on several contact spots with larger currents flowing through. The maximum temperature at -2° docking angle is 11.3℃ larger than that at 2° docking angle due to the conductor gravity.

B. Contact behaviors under short circuit fault

Peak value of fault current under short circuit can reach up to tens of kA. Huge electromagnetic repulsion force and sharp increasing of temperature rise could be induced. Distributions of electromagnetic force and temperature of GIB plug-in connector with different assembly conditions under 25kA fault current impact at 18℃ environmental temperature are shown in Fig. 12.

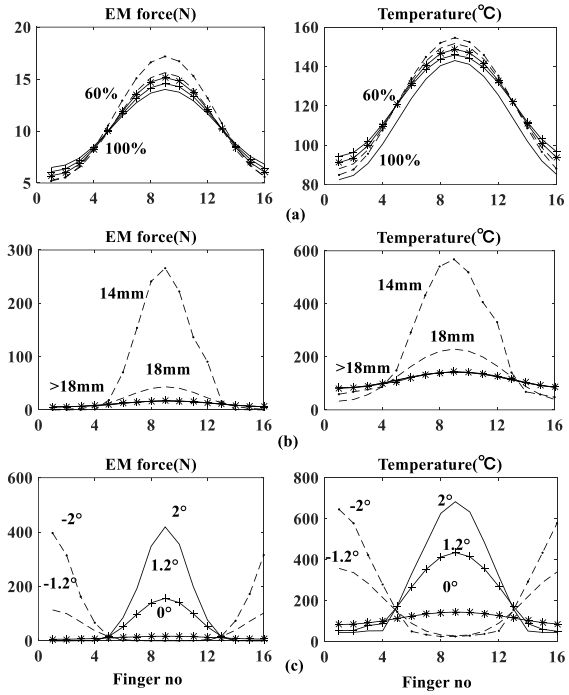

Fig. 12. Electromagnetic force and temperature under short circuit current impact.

Distributions of electromagnetic repulsion forces and temperatures among contact spots with various preloading contact forces are shown in Fig. 12 (a). It can be seen that deviation amplitudes of electromagnetic force and temperature increase with the decrease of preloading contact forces. However, even when the preloading contact force reduces to 60% of its initial value, the residual contact force still exists with the peak value of electromagnetic repulsion force (17.2N). The maximum temperature (154.6℃) does not exceed the threshold (200℃), which means that reducing of preloading contact force is not the main factor influencing contact performance under short circuit current impact.

Distributions of electromagnetic repulsion forces and temperatures among contact spots with various conductor insert depths are shown in Fig. 12 (b). It can be seen that deviation amplitudes of electromagnetic force and temperature rise increase with decrease of conductor insert depth. Preloading contact force on several serious contact spots could be totally offset by electromagnetic force together with seriously heating at 14mm conductor inserting depth, which means that the contact performance could be largely reduced by the insufficient conductor insert depth.

Distributions of electromagnetic repulsion forces and temperatures among contact spots with various conductor docking angles are shown in Fig. 12 (c). Results show that deviation of electromagnetic and temperature becomes larger with increase of conductor docking angles. When docking angle deviation exceeds 1.2°, preloading contact force on several serious contact spots could be totally offset by electromagnetic force, which means that the contact performance could be largely reduced by conductor docking angle deviation.

VI. LOAD CAPABILITY ASSESSMENT OF IMPERFECT PLUG-IN CONNECTOR

As part of series components in power grid, during entire equipment service life, contact system of GIB plug-in connector must be able to carry rated operation current besides withstand short circuit (SC) fault current without obvious contact degradation. According IEC 62271-1 and IEC 60865-1 [21-22], the maximum allowed temperatures for silver-plated contacts with long-term operation current and transient short circuit current impact is 105℃ and 200℃ separately.

During manufactory/install/operation process, GIB plug-in connector could be exposed to misalignment conditions such as preloading contact force reduction, insufficient conductor insert depth or conductor docking angle deviation. Imperfect assembly conditions could make higher temperature rise and electromagnetic force thus reduce the actual load capability comparing with its design value.

Load capabilities of GIB plug-in connector with various preloading contact forces are described in Fig. 13. Results show that the load capabilities reduce with decrease of preloading contact force. Load capacity of connector with 60% preloading contact force is 82% of its design value, which means that preloading contact force could not obviously influence load capability of connector with low relaxation ratio of holding spring across its service life.

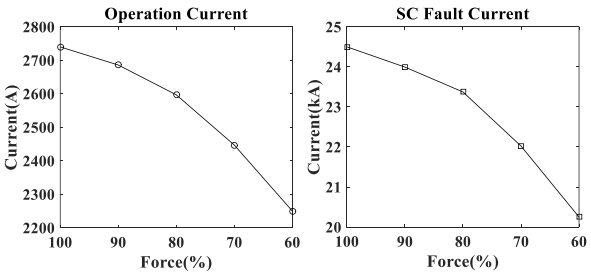

Fig. 13. Load capacities with preloading contact forces.

Load capabilities of GIB plug-in connector with various conductor insert depths are described in Fig. 14. Results show that as long as the conductor insert depth is below contact failure point (18mm), load capacities reduce slowly with decrease of conductor insert depth (87% of its design value at 18mm). However, when the conductor insert depth exceeds failure point, due to overheating and significant electromagnetic force on several contact spots, the load capacities reduce sharply (46% of initial value at 14mm).

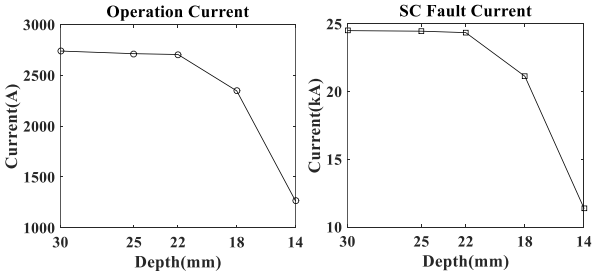

Fig. 14. Load capacities with conductor insert depths.

Load capabilities of GIB plug-in connector with various conductor docking angles are described in Fig. 15. Results show that due to overheating and significant electromagnetic force on several contact spots, the load capacities reduce sharply with the increase of conductor docking angle (15% of its design value at -2°).

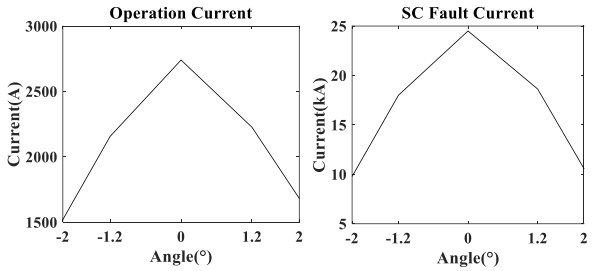

Fig. 15. Load capacities with conductor docking angles.

VII. CONCLUSION

By multi-physics coupled FE procedure, influences of imperfect assembly conditions on the mechanical, electrical and thermal contact behaviors of GIB plug-in connector under steady and short circuit current impact have been analyzed. Results show that when imperfect assembly condition happens, contact force, operation current, temperature rise and electromagnetic repulsion force deviate obviously among contact spots. The load capacity can be significant decreased by overheating on several contact spots. When insufficient preloading force (60%), insufficient conductor insert depth (14mm) and conductor deviation angle (-2°) happen, the actual load capability reduces to 82%, 46% and 15% of its design values. Result also indicates that insufficient conductor inserts depth and conductor docking angle deviation has the larger influence on load capacity of connector. FE model and results of this paper could help for optimal design and operation monitoring of GIB plug-in connector thus improve its reliability.

ACKNOWLEDGMENT

This work was supported by the Natural Science Foundation of China (51607124), the 60th China Postdoctoral Science Foundation (2016M602352), and the Fundamental Research Funds for China Central Universities (2042016kf1049, 2042017kf1011).

REFERENCES

[1] K. Mark, W. Christian, and G. Alfred, "The latest GIS and GIL developments for high voltage applications," *Proc. ICHVE*, pp. 56-59, 2008.

[2] M. Runde, "Failure frequencies for high-voltage circuit breakers, disconnectors, earthing switches, instrument transformers, and gas-insulated switchgear," *IEEE Trans. Power Delivery*, vol. 28, no. 1, pp. 529-530, 2013.

[3] Y. Mukaiyama, I. Takagi, K. Izumi, T. Sekiguchi, et al., "Investigation on abnormal phenomena of contacts using disconnecting switch and detachable bus in 300 kV GIS," *IEEE Trans. Power Delivery*, vol. 5, no. 1, pp. 189-195, 1990.

[4] A. E. Emanuel, H. C. Doepken, and P. C. Bolin, "Design and test of a sliding plug-in conductor connector for compressed gas-insulated cables," *IEEE Trans. Power Apparatus and Systems*, vol. 95, no. 2, pp. 570-579, 1976.

[5] M. P. Filippakou, C. G. Karagiannopoulos, D. P. Agoris, and P. D. Bourkas, "Electrical contact overheating under short-circuit currents," *Electric Power Systems Research*, vol. 57, no. 2, pp. 141-147, 2001.

[6] L. Koller, B. Novák, and G. Tevan, "Heating effects of short-circuit current impulses on contacts and conductors," *IEEE Trans. Power Delivery*, vol. 23, no. 1, pp. 221-227, 2008.

[7] B.-K. Kim, K.-T. Hsieh, and F.-X. Bostick, "A three-dimensional finite element model for thermal effect of imperfect electric contacts," *IEEE Trans. Magnetics*, vol. 35, no. 1, pp. 170-174, 2009.

[8] O. Bottaushort, "Numerical analysis of heating transient of electric contacts under short-circuit conditions," *IEEE Trans. Comp. Hybrids Manufact. Technol.*, vol. 16, no. 5, pp. 563-570, 1993.

[9] T. Ota, S. Suzuki, and K. Hirata, "Dynamic analysis method of repulsion forces on current-carrying contact using 3-D FEM," *IEEE Trans. Magnetics*., vol. 47, no. 5, pp. 942-945, 2011.

[10] S. Ito, Y. Takato, Y. Kawase, and T. Ota, "Numerical analysis of electromagnetic forces in low voltage ac circuit breakers using 3-D finite

element method taking into account eddy currents," *IEEE Trans. Magnetics*., vol. 34, no. 5, pp. 2597-2600, 1998.
[11] E. Carvou, R. EI Abdi, J. Razafiarivelo, N. Benjemaa, and E. M. Zindine, "Thermo-mechanical study of a power connector," *Measurement*., vol. 45, no. 5, pp. 889-896, 2012.
[12] A. Monnier, B. Froidurot, C. Jarrige, et al., "A mechanical, electrical, thermal coupled-field simulation of a sphere-plane electrical contact," *IEEE Trans. Comp. Packing Technol*., vol. 30, no. 4, pp. 787-795, 2007.
[13] Y.-Z. (Liza) Lam, J. W. McBride, C. Maul, and J. K. Atkinson, "Displacement measurements at a connector contact interface employing a novel thick film sensor," *IEEE Trans. Comp. Packing Technol*., vol. 31, no. 3, pp. 566-573, 2008.
[14] G. Xiangyu, S. Naiqiu, K. Bing, et al., "Multi-physics calculation and contact degradation mechanism evolution of GIB connector under daily cyclic loading," *IEEE Trans. Magnetics*., vol. 52, no. 3, pp. 1-4, 2016.
[15] Y. Ohshita, A. Hashimoto, and Y. Kurosawa, "A diagnostic technique to detect abnormal conditions of contacts measuring vibrations in metal tank of gas insulated switchgear," *IEEE Trans. Power Delivery*, vol. 4, no. 4, pp. 2090-2094, 1989.
[16] L. Bin, *SF6 High Voltage Electrical Design.* BeiJing, China Machine Press, 2007.
[17] J. Paulke, H. Weichert, and P. Steinhaeuser, "Thermal simulation of switchgear," *IEEE Trans. Comp. Packing Technol.*, vol. 25, no. 3, pp. 434-439, 2002.
[18] G. Xiangyu, S. Quanyu, et al., "Investigation on mechanical and magnetic field behaviors of GIB plug-in connector under different contact conditions," *Appl. Comp. Elec. Society Journal*, vol. 32, no. 3, pp. 275-282, 2017.
[19] M. Gatzsche, N. Lucke, S. Grobmann, T. Kufner, and G. Freudiger, "Evaluation of electric-thermal performance of high-power contact systems with the voltage-temperature relation," *IEEE Trans. Comp. Packing Manu. Technol*., vol. 7, no. 3, pp. 434-439, 2017.
[20] R. Holm, *Electric Contacts, Theory and Applications.* New York, Springer, 1979.
[21] High-Voltage Switchgear and Control Gear—Part 1: Common Specifications, Document IEC 62271-1 Edition 1.1 2011-08, 2011.
[22] Short-Circuit Currents—Calculation of Effects—Part 1: Definitions and Calculation Methods, Document IEC 60865-1 Edition 3.0 2011-10, 2011.

Xiangyu Guan received the B.S. degree of Environmental Science from Xinjiang Normal University, China, in 2010, the M.S. and Ph.D. degrees of Power System and Automation from Wuhan University, Hubei, China, in 2015.

He is currently a Lecturer at School of Electrical Engineering Wuhan University. He is Member of ACES and ICS and his research interests mainly focus on electrical contacts, numerical methods of coupling field calculation and condition monitoring of electrical equipment.

Xin Wei received her B.S. degree of Electrical Engineering from Fuzhou University, China, in 2016. She is currently a master candidate in School of Electric Engineering in Wuhan University. Her research interests include online monitoring technology and fault diagnosis of electric equipment.

Xianyong Song received the B.S. degree of Electrical Engineering from Hunan University, China, in 1994, the M.S degree in School of Electrical Engineering Wuhan University, Hubei, China, in 2015. He is currently a Senior Engineer in State Grid Hunan Power Supply Company and his research is working on electrical equipment monitoring and fault diagnosis technology.

Naiqiu Shu received the M.S. and Ph.D. degrees in Electrical Engineering from Wuhan University. He is currently a Professor in School of Electrical Engineering Wuhan University. His current research interests mainly focus on sensors technology and its application on condition monitoring of electrical equipment.

Hui Peng received the B.S., M.S. and Ph.D. degrees in Electrical Engineering from Wuhan University. He currently is an Associate Professor in School of Electrical Engineering. His current research interests mainly focus on condition monitoring of electrical equipment.

Comparison of Three Body Models of Different Complexities in Modelling of Equal-Sized Dipole and Folded Dipole Wearable Passive UHF RFID Tags

Toni Björninen

BioMediTech Institute and Faculty of Biomedical Sciences and Engineering
Tampere University of Technology, Tampere, 33720, Finland
toni.bjorninen@tut.fi

Abstract ─ We compare the performance of equal-sized dipole and folded dipole wearable passive UHF RFID tags using three different body models for the torso of an adult male: cuboid and anatomical models with and without internal structures. The results show that all models estimate the antenna impedance matching appropriately, but only the anatomical models predict the full spatial coverage of the tags properly. We present a novel metrics for analysing the coverage in simulations and compare the simulated and measured tag read ranges to validate our modelling results.

Index Terms ─ Dipole, e-textile, folded dipole, human body model, RFID tag, wearable antenna.

I. INTRODUCTION

Body area networks (BAN) have become an important trend in wireless communications and the development of wearable wireless technologies is offering marked benefits to numerous applications, such as medicine and healthcare, wellness and sports, and safety and security. Overall, the development is striving towards wearable intelligence: the body-worn sensing and energy harvesting platforms will provide wireless power and data to the human intranet consisting of implanted and body-worn devices [1–2].

Passive ultra-high frequency (UHF) radio-frequency identification (RFID) inspired technology is a compelling approach to energy- and cost-efficient wireless platforms for the future BANs [3–4]. In addition to identification, this versatile technology is adaptable for the purposes of wireless sensing, for instance [5–7]. Currently, perhaps the biggest challenges in the development of wearable wireless devices are the seamless cloth-integration and reliable and effective optimisation of body-worn antennas. Here, the regular printed circuit board is not a viable approach, and thus electrically conductive textiles (e-textiles) where conductive parts are patterned from metal-coated fabrics or embroidered with metal-coated sewing threads, for instance, have gained more attention. In the view of textile-compatible manufacturing, simple uniplanar antennas provide clear benefits over structures with multiple interconnected layers. Still, the presence of the body influences uniplanar antennas more and therefore we must optimise them affixed on a human body model.

The body is an extremely complex platform for electromagnetic modelling in terms of both the structure and materials. Thus, for effective simulation of wearable antennas, we must strike the right balance between complexity and prediction accuracy. In this letter, we address this question in the application of wearable RFID tags by comparing equal-sized tags based on dipole and folded dipole antennas using three different human body models of different complexities.

II. HUMAN BODY MODELS AND SIMULATION RESULTS

Figure 1 shows the tag antennas that we optimised using a simple cuboid body model in [8]. This work presents further analysis and comparison of the tag's performance and spatial coverage in more realistic body models illustrated in Fig. 2. The coordinate systems in Figs. 1–2 coincide and indicate the placement of the tag centred in the upper back at the level of the scapula. We first developed the structured anatomical model by adapting the full ANSYS human body model (adult male) by reducing it to the head and upper torso and then removing internal structures that we did not consider having significant size or were not located near the tag. We modelled the electromagnetic properties of the different tissue types using the four-term Cole-Cole dielectric relaxation model with the model parameters taken from IT'IS library [9]. In case of the solid anatomical model, we assigned the material in the whole body as skin (ε_r=41.4, σ=0.867 S/m at 915 MHz) since it is the tissue type nearest to the tag. Finally, we created the cuboid model by adapting the dimensions of a cuboid to fit the torso in the anatomical models as illustrated in Fig. 2 and assigned the dielectric properties of skin on the cuboid. The antenna substrate was EPDM (Ethylene-Propylene-Diene-Monomer, ε_r=1.26, tanδ = 0.007 at 915

Submitted On: September 15, 2017
Accepted On: May 13, 2018

MHz) cell rubber foam with the thickness of 2 mm and as conductors we used both 20-µm copper foil (conductivity: 58 MS/m) and nickel and copper plated Less EMF Shieldit Super Fabric (sheet resistance: 0.16 Ω/Sq.). The RFID IC we used was NXP UCODE G2iL RFID IC. It has the wake-up power of −18 dBm (15.8 µW) and we modelled it as a parallel connection of the resistance and capacitance of 2.85 kΩ and 0.91 pF, respectively [8].

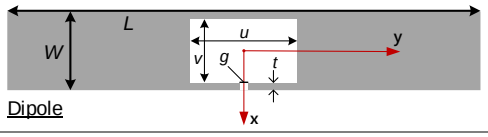

t	*g*	*L*	*W*	*u*	*v*
2	2	120	20	27	16

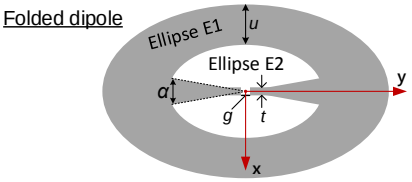

t	*g*	*α*	*u*	*q*
2	2	20°	10	1.65

Ellipse	Semi-minor axis	Semi-major axis
E1	$\sqrt{LW/(q\pi)}$	$\sqrt{(qLW)/\pi}$
E2	$\sqrt{LW/(q\pi)}-u$	$\sqrt{(qLW)/\pi}-qu$

Fig. 1. Structural diagrams of the studied antennas.

The main performance indicator of passive tags is the attainable tag read range (d_{tag}) that in passive UHF RFID systems is limited by the tag's capability to harvest energy from the reader's carrier signal. In free space,

$$d_{tag}=\frac{\lambda}{4\pi}\sqrt{\left\{\frac{4\,\mathrm{Re}(Z_A)\mathrm{Re}(Z_{IC})}{|Z_A+Z_{IC}|^2}\right\}\frac{\chi_p e_r D(\theta,\phi)EIRP}{P_{ic0}}}, \quad (1)$$

where λ is the wavelength of the reader's signal, the factor in curly brackets is the antenna-IC power transmission efficiency (τ) determined by the tag antenna and IC impedances Z_A and Z_{IC}, respectively, χ_p is the mutual polarisation loss factor between the tag antenna and the incident wave from the reader, e_r and $D(\theta,\varphi)$ are the radiation efficiency and directivity of the tag antenna, respectively, *EIRP* is the equivalent isotropically radiated power of the reader, and P_{ic0} is the wake-up power of the tag IC.

The complex electric field vector (**E**) of an electromagnetic wave can be expressed as a sum of orthogonal purely left and right hand circularly polarised components $\mathbf{E}_L$ and $\mathbf{E}_R$, respectively, by introducing a complex scalar (γ) called circular polarisation ratio such that: $\mathbf{E}=\mathbf{E}_L+\mathbf{E}_R=\mathbf{E}_L+\gamma\mathbf{E}_L$ [10]. With this notion, the mutual polarisation loss factor between a tag antenna and incident wave from a reader with an arbitrary elliptic polarisation is:

$$\chi_p=\frac{1+|\gamma_{inc}|^2|\gamma_{tag}|^2+2|\gamma_{inc}||\gamma_{tag}|\cos\Delta}{(1+|\gamma_{inc}|^2)(1+|\gamma_{tag}|^2)}, \quad (2)$$

where the complex scalars γ_{tag} and γ_{inc} are the circular polarisation ratios of the incident wave and the tag antenna, respectively, and Δ is the difference between the arguments of γ_{tag} and γ_{inc} [10]. Generally, RFID readers are equipped with circularly polarised antennas to eliminate the possibility of cross polarisation with tags that comprise almost invariably a linearly polarised antenna due the stringent requirements on size, cost, and manufacturing complexity. For the pure left and right hand circular polarisations, we have $\gamma_{inc}=0$ and $|\gamma_{inc}|\to\infty$, respectively. In these cases, Equation (2) yields the mutual polarisation loss factors:

$$\chi_{LH}=\frac{1}{1+|\gamma_{tag}|^2} \quad \text{and} \quad \chi_{RH}=\frac{1}{1+|\gamma_{ant}|^{-2}}. \quad (3)$$

For a perfectly linearly polarised tag antenna $\gamma_{ant}=1$ [10] and both loss factors in Equation (3) become equal to 1/2.

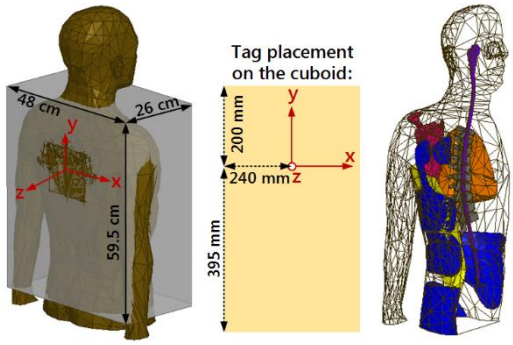

Fig. 2. Cuboid model visualised on top of the solid body model (left) and the transparent view of the structured body model (right). In the structured model, the material for the transparent part is skin. The red, dark grey, blue, yellow, and orange denote cortical bone (scapula), cancellous bone (thoracic vertebrae T3-T12), muscle, fat, and air (inside lungs), respectiely.

For further analysis, we define the read range coverage C_α with $0<\alpha<1$, so that in α percentage of the spatial observation angles $C_\alpha<d_{tag}(\theta,\phi)$. This means that when an incident wave from the reader impinges upon the tag, there is an α percentage probability for detecting the tag at a distance longer than C_α.

We used ANSYS HFSS v15 in modelling the antennas. Firstly, Fig. 3 shows the simulated τ. According to our parametric study, it was not possible to achieve higher τ with the dipole constrained in the 20×120 mm^2 footprint size by optimising the embedded inductive

matching loop (params.: u and v) due to the inherently elevated antenna resistance. This indicates that though widely applicable for tags in item level tracking applications, this impedance tuning approach has limited applicability in wearable tags. In contrast, we found that the folded dipole permitted good impedance matching within equal footprint area.

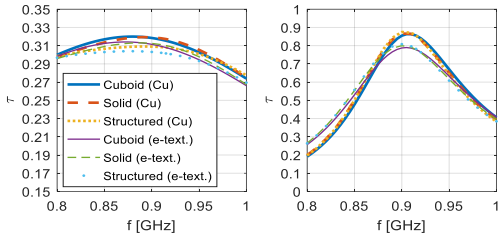

Fig. 3. Antenna-IC power transfer efficiency of the dipole (left) and folded dipole (right) tags.

Table 1: Radiation efficiency (%) and directivity (dBi) in the direction of the positive z-axis in Fig. 2

	Dip., Cu	Dip., e-textile	Folded, Cu	Folded, e-textile
Cub.	1.8%	1.7%	1.2%	1.0%
	7.6 dBi	7.6 dBi	6.2 dBi	6.2 dBi
Solid	1.8%	1.7%	1.1%	0.9%
	7.5 dBi	7.5 dBi	7.3 dBi	7.3 dBi
Struct.	1.7%	1.6%	1.0%	0.8%
	7.4 dBi	7.4 dBi	7.3 dBi	7.3 dBi

Overall, all the body models predicted very similar impedance matching, suggesting that a simplistic body model suffices for optimizing the antenna impedance. In addition, Table 1 shows that the radiation characteristics observed from the direction of the positive z-axis, are also very similar among all models, with the exception that the cuboid model predicted 1 dB lower directivity for the folded dipole compared with the anatomical models. Moreover, the antennas' radiation performance is characterised by low radiation efficiency in the order of 1% and high directivity – both due to the impact of the human body. The radiation patterns at other observation angles, however, differ notably between the cuboid and anatomical models as shown in Fig. 4. Consequently, the spatial coverage presented in Fig. 5 differs between these models suggesting that we need anatomically shaped models for the judicious analysis of the coverage and read range of wearable tags.

In the analysis of the spatial coverage, we assumed that a reader antenna may be located anywhere behind the person (θ = –90°…90°) within a 60° beam in the yz-plane (ϕ = –30°...30°). We discretised the ranges for θ and ϕ using steps of 2.5° and 1°, respectively, and extracted the directivity and left-hand circular polarisation ratio at each point. As shown in Fig. 5, the solid and structured anatomical models predicted nearly identical coverage, whereas the cuboid model yielded lower values. This is because the radiation patterns obtained from the anatomical models exhibit broader beams in the xz-plane (Fig. 4). Overall, in the anatomical models, the e-textile dipole and folded tags achieved the peak d_{tag} of approximately 2.0 m and 2.3 m in polarisation matched scenario and 1.4 m and 1.6 m in the case of a left-hand circularly polarised reader, respectively. The corresponding values of $C_{0.5}$ are 1.2 m and 1.4 m for χ_p = 1 and 0.9 m and 1.0 m for $\chi_p = \chi_{LH}$. Hence, even though the maximum d_{tag} is sufficient for practical applications of wearable tags, the important observation from the analysis of the spatial coverage is that the reliability of the detection, especially with a commonly used circularly polarised reader antenna, may still limit the applicability of the tags.

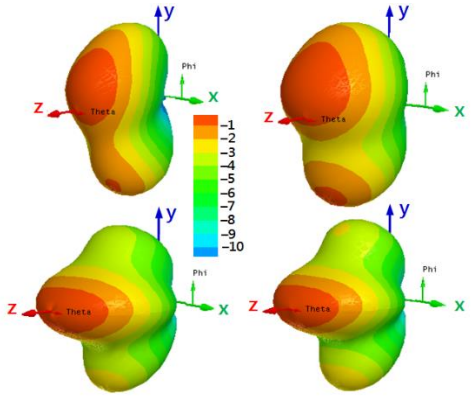

Fig. 4. Radiation patterns of the copper antennas in cuboid (top) and solid body models (bottom) at 915 MHz. Left dipole, right: folded dipole.

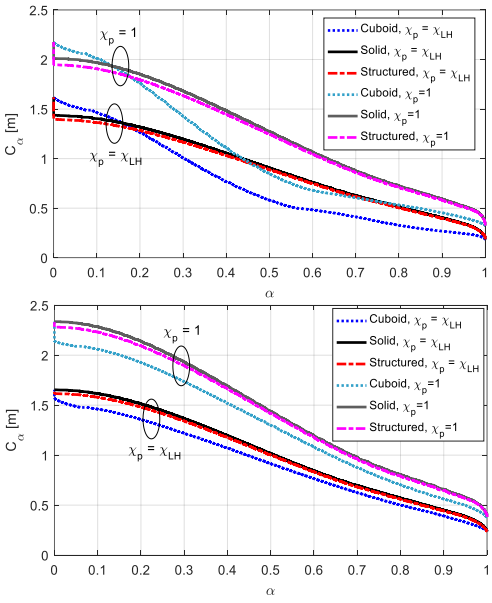

Fig. 5. Spatial coverage of the e-textile dipole (top) and e-textile folded dipole (bottom) at 915 MHz in the region where θ = –90°…90° and ϕ = –30°...30°.

III. RESULTS FROM TESTING

During testing, we affixed the tags on the skin in the upper back of a male test subject as described in Fig. 1 and tested them wirelessly using Voyantic Tagformance measurement system. It contains an RFID reader with an adjustable transmission frequency (0.8…1 GHz) and output power (up to 30 dBm) and provides the recording of the backscattered signal strength (down to −80 dBm) from the tag under test. During the test, we recorded the lowest continuous-wave transmission power at which a valid 16-bit random number from the tag was received as a response to the query command in ISO 18000-6C communication standard. In addition, the wireless channel from the reader antenna to the location of the tag under test was characterised using a system reference tag with known properties. As explained with details in [7], this enabled us to estimate the attainable read range of the tag. In the measurement, we used a linearly polarised reader antenna aligned for polarisation matching with the linearly polarised tags. Figure 6 shows the results referred to *EIRP* = 3.28 W. The excellent agreement between the simulations and measurement adds assurance to the modelling approaches presented in the previous section.

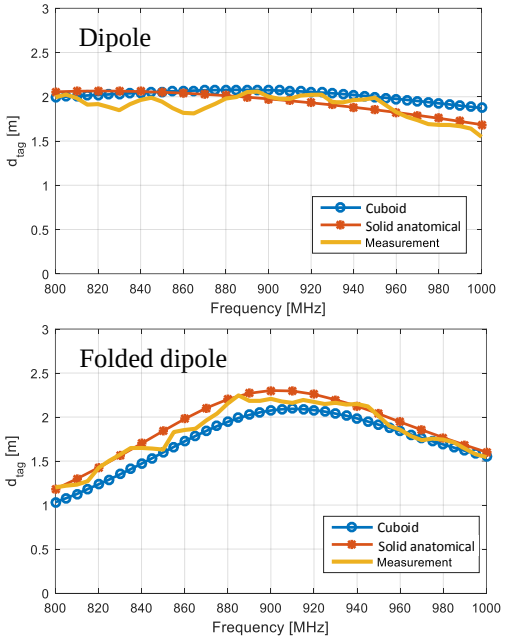

Fig. 6. Attainable read range toward +z-axis in Fig. 2.

IV. CONCLUSION

Wearable antennas couple electromagnetically to the human body making electromagnetic body models an indispensable tool for optimising them. We compared three different models for the torso: cuboid and anatomical models with and without internal structures, in the modelling of wearable RFID tags. We found little difference in antenna impedance obtained from the models, but the cuboid predicted notably different radiation pattern. Moreover, we found the difference in all performance indicators obtained from the solid and structured models negligible suggesting that the anatomical model without internal structures is the most effective one for our application.

REFERENCES

[1] J. M. Rabaey, "The human intranet—where swarms and humans meet," *IEEE Pervasive Comput.*, vol. 14, no. 1, pp. 78-83, Jan.-Mar. 2015.

[2] S. Lemey, F. Declercq, and H. Rogier, "Textile antennas as hybrid energy-harvesting platforms," *Proc. IEEE*, vol. 102, no. 11, pp. 1833-1857, Nov. 2014.

[3] A. Sani, M. Rajab, R. Forster, and Y. Hao, "Antennas and propagation of implanted RFIDs for pervasive healthcare applications," *Proc. IEEE*, vol. 98, no. 9, pp. 1648-1655, Sep. 2010.

[4] A. Yakovlev, S. Kim, and A. Poon, "Implantable biomedical devices: Wireless powering and communication," *IEEE Commun. Mag.*, vol. 50, no. 4, pp. 152-159, Apr. 2012.

[5] Z. Fu and F. Yang, "A slotted patch antenna integrated with thermal switch for high-sensitivity temperature monitoring," *IEEE Antennas Wireless Propag. Lett.*, vol. 14, pp. 998-1001, Jan. 2015.

[6] O. O. Rakibet, C. V. Rumens, J. C. Batchelor, and S. J. Holder, "Epidermal passive RFID strain sensor for assisted technologies," *IEEE Antennas Wireless Propag. Lett.*, vol. 13, pp. 814-817, Apr. 2014.

[7] F. Long, X. Zhang, T. Björninen, J. Virkki, L. Sydänheimo, Y.-C. Chan, and L. Ukkonen, "Implementation and wireless readout of passive UHF RFID strain sensor tags based on electro-textile antennas," in *Proc. 2015 European Conf. Antennas Propag*., 5 pages, 2015.

[8] X. Chen, L. Ukkonen, T. Björninen, and J. Virkki, "Comparison of e-textile dipole and folded dipole antennas for wearable passive UHF RFID tags," accepted in *PIERS*, Singapore, 19-22 Nov. 2017.

[9] IT'IS Fondation, Tissue Properties. Available: https://www.itis.ethz.ch/virtual-population/tissue-properties/downloads/

[10] T. A. Milligan: *Modern Antenna Design*. 2nd ed., John-Wiley & Sons, Inc., 2005.

N-Shaped Frequency Reconfigurable Antenna with Auto Switching Unit

Arun V. [1], KarlMarx L.R. [2], Jegadish K.J. Kumar [3], and Christy C. Vimlitha [1]

[1] Department of Electronics and Communication Engineering
Anna University Regional Campus Madurai, Madurai, 625019, India
arunece@autmdu.ac.in, cvimilitha@gmail.com

[2] Department of Electronics and Communication Engineering
Thiagarajar College of Engineering, Madurai, 625015, India
lrkarlmarx@tce.edu

[3] Department of Electronics and Communication Engineering
SSN College of Engineering, Kalavakkam, Chennai, 603110, India
jegadishkj@ssn.edu.in

Abstract ─ These days the need for reconfigurable antenna is widely increased in the field of multi band wireless communication. The proposed new design of N-shaped antenna structure consists of two PIN diodes for switching purpose. They are switched automatically by a pre-programmed Arduino microcontroller unit to attain the reconfiguration of four-different bands without changing the physical dimension of the antenna. The four switching bands are 3.5 GHz (WiMAX), 2.46 GHz (WLAN), 1.2 GHz (GPS) and 2.1 GHz (UMTS). It has a center stub with two N-shaped stub carrying PIN diodes. The stubs are connected with a 50ohm microstrip feed line. The measured return loss closely follows the simulation results. Also it exhibits a good impedance matching during the four switching states. The simulation has been done through Ansoft HFSS and measured results are obtained from a Vector Network Analyzer (VNA). The obtained VSWR value lies beneath 2 for all obtained bands. The radiation pattern of the antenna is bidirectional for all the four-switching states.

Index Terms ─ Auto switching antenna, multi frequency, N-shaped microstrip patch antenna, PIN diode antenna, reconfigurable antenna.

I. INTRODUCTION

In recent days, the reconfigurable antenna has been used extensively in the field of wireless communication, satellite communication, radio frequency (RF) devices and radar systems due to its functionality and versatility [1]. Normally a basic patch antenna works on a single or fixed band of frequencies [2]. But restructuring or reconfigurable antenna can work in various operating frequencies [3] and it can be used indifferent wireless applications such as Bluetooth, Wi-Fi, UMTS, GPS and WLAN. Polarization switching, pattern switching, bandwidth switching and frequency switching are the different switching operations performed by reconfigurable antenna [4]. In this paper, the concept of frequency switching is focused at large. For switching the various frequency bands, switches like PIN diodes [5], Varactor diodes [6], and RF MEMS [7] switches are being used.

Reconfigurable antennae with RF MEMS switches have the switching speed ranging from 1-200μsec. This is normally considered as low for most of the applications [8]. Antennae resorted with Varactor diode has variable capacitance due to varying bias voltage and it produces vast tuning ability. The design of biasing network with Varactor diode is in consideration to the reconfigurable antenna design [9]. Most of the reconfigurable antenna is designed with PIN diodes as it provides fast switching. The switching speed ranges from 1-100nsec. The fast switching provides dynamic reconfiguration ability [10] than other switching components. Hence, PIN diodes have been extensively used in reconfigurable antenna design.

In this paper frequency reconfigurable N-shaped antenna has been presented. Here two PIN diodes with an auto switching unit is used to obtain the multiple frequency bands. The frequency reconfiguration is achieved through switching ON/OFF the D1 & D2 diodes which is mounted on the patch. This paper covers six sections, where the Section I gives a common introduction about reconfigurable antenna. Section II describes the design of the proposed antenna and Section III gives the principle of auto switching unit using Arduino UNO board for the proposed N-shaped antenna. It is followed by Section IV, where the simulated and measured results of proposed antenna

Submitted On: March 27, 2017
Accepted On: May 13, 2018

have been briefly explained. Section V carries the comparison of proposed antenna with other factors. Finally, Section VI concludes the paper.

II. PROPOSED N-SHAPEDANTENNA DESIGN

The proposed frequency reconfigurable N-shaped antenna has dimension of 20mm*30mm as shown in the Fig. 1 (a). The antenna has a track width of 4mm all over the patch and it is fed by 50Ω microstrip feed line connected with a standard connector. The antenna's software model has been designed using Ansoft HFSS software and it is shown in Fig. 1 (b). The prototype antenna has been fabricated on FR4 epoxy material of dielectric constant 4.4 with a thickness of 1.6mm. The antenna has a ground plane with dimension as that of patch. The antenna is coated with Tin material as it provides improved frequency reconfigurability. RF PIN diodes namely SOD323 are used for switching the frequency in four different states. In HFSS the PIN diodes are designed with Lumped RLC boundary and it is indicated in Fig. 1 (b) as D1 and D2 position. Two PIN diodes D1 and D2 are mounted on the antenna radiating patches as shown in the Fig. 2 (a), and Fig. 2 (b) shows the ground plane of the antenna. The switching is provided with the help of auto switching unit which consist of a preprogrammed Arduino UNO board.

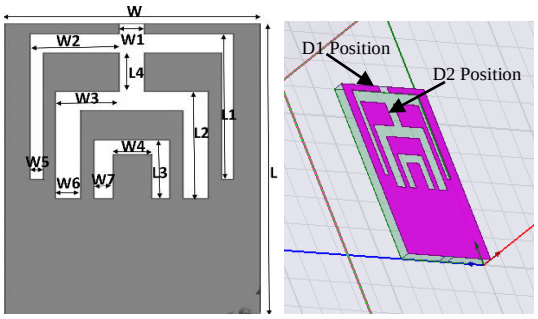

(a) (b)

Fig. 1. (a) Dimension of tree shaped antenna (all dimensions in mm) [W=20, W1=1.5mm, W2=7mm, W3= 5mm, W4=4mm, W5=1mm, W6=1.8mm, W7=1.5mm, L=30, L1=15mm, L2=12mm, L3=5mm, L4=3mm]; (b) simulation design in HFSS.

The length (l) and width (w) for designing the proposed N-shaped reconfigurable patch antenna is obtained from the following Equations from (1) to (4). The width (w) and effective dielectric constant (ε_{reff}) of the patch can be resolute through the Equations (1) and (2):

$$w = \frac{c}{2f}\sqrt{\left(\frac{2}{\varepsilon_r + 1}\right)}, \tag{1}$$

where c = free space velocity of light, f = resonant frequency, and ε_r = dielectric constant of substrate;

$$\varepsilon_{reff} = \frac{\varepsilon_r + 1}{2} \frac{\varepsilon_r - 1}{2} \left[1 + 12\frac{h}{w}\right]^{-\frac{1}{2}}. \tag{2}$$

The extension patch length (Δl) is given by the Equation (3) through which the actual patch length (l) can be calculated from Equation (4):

$$\Delta l = 0.412h \frac{(\varepsilon_r + 0.3)\left(\frac{w}{h} + 0.264\right)}{(\varepsilon_r - 0.258)\left(\frac{w}{h} + 0.8\right)}, \tag{3}$$

where w = width of the patch,

$$l = \frac{c}{2f\sqrt{\varepsilon_{reff}}} - 2\Delta l. \tag{4}$$

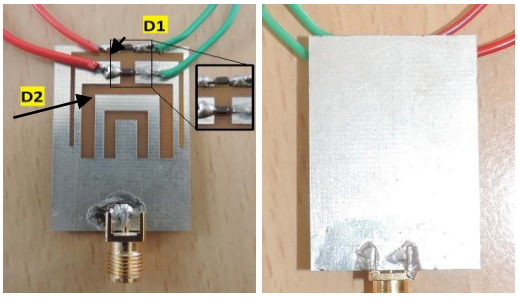

(a) (b)

Fig. 2. (a) Fabricated antenna with PIN diodes - front view, and (b) ground plane - back view.

III. AUTO SWITCHING UNIT

The auto switching unit consists of a pre-programmed Arduino Uno board connected with the proposed N-shaped antenna has been shown in Fig. 3. The output of the reconfigurable antenna is connected to the voltage multiplier unit which is designed with LTC3108. The output of multiplier unit is connected to the Arduino board's A_0 pin (Analog I/O port) and ground (GND) pin. The diodes D1, D2 of the proposed N-shaped reconfigurable antenna is connected with the Arduino board's Digital I/O ports 11, 12 respectively.

The pre-programmed Arduino board switches the diodes D1 and D2 consecutively. The received analog signal in the A_0 port is digitized through the inbuilt ADC unit. The diode reaches its next state one by one after 5s delay as per the program. Thus, the diode switching state starts with state 1 (0,1) where the diode D2 in ON and D1 in OFF condition. It is consecutively followed by the other states of PIN diode after every 5s delay as follows; (1,0), (1,1) and (0,0). The switching state of the PIN diodes (D1, D2) is given in the Table 1. In every switching state, the output of the reconfigurable antenna is read by the analog ports and the digitized value is compared with the previous stored value. Finally, the best value for the state where signal of the antenna is strong is selected and that switching state is chosen to remain as the antenna state for the RF harvesting.

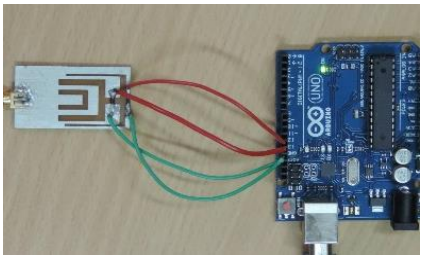

Fig. 3. Auto switching unit with the proposed antenna.

IV. RESULTS AND DISCUSSION

In this section the comparison of simulated result and measured result of prototype antenna has been discussed. The simulation and measured values are obtained through HFSS and VNA respectively. The various antenna parameters for the four switching states of the proposed antenna is presented as follows.

A. Return loss

The return loss for the state 1, state 2, state 3 and null state is shown in the Fig. 4, where the dotted line represents the simulated result and solid line represent the measured result. In state 1 (i.e.) D1 is in OFF and D2 in ON condition. In this state the frequencies of 3.5 GHz and 5.7 GHz are obtained. Thus this state can be used for WiMAX (3.5 GHz) application. The diode D1 is in ON and D2 in OFF represent the state 2. Here the frequency band of 2.4 GHz (Bluetooth) and 5 GHz has been obtained. Similarly, in the 3rd state both the diodes are in ON condition, the frequency of 1.2 GHz is obtained. Finally, in null state (i.e.) both the diodes are in OFF condition. In this state the antenna achieves 2.1 GHz and 6.8 GHz frequency. The frequency attained in state 3 can be used for GPS application and in null state can be used for UMTS application. The difference is attributed between simulation and measured result due the fabrication inacuuracy, effect of the material, PIN diode quality and realization environment. Howerever these results are acceptable.

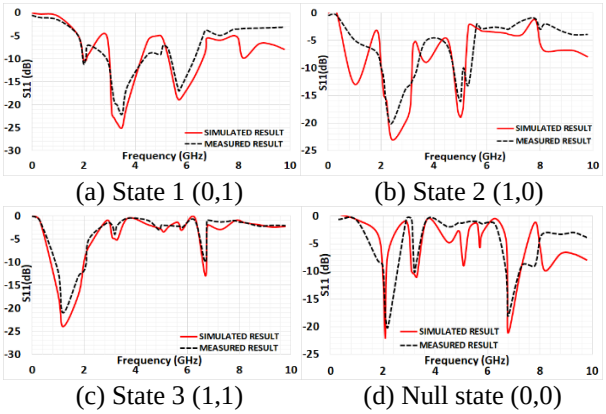

(a) State 1 (0,1) (b) State 2 (1,0)

(c) State 3 (1,1) (d) Null state (0,0)

Fig. 4. Simulated and measured return loss result.

Table 1: Comparison of various switching states

State	Diode	Operating Frequency
State 1 (0,1)	D1 OFF & D2 ON	3.5 GHZ, 5.7 GHz
State 2 (1,0)	D1 ON & D2 OFF	2.4 GHz, 5 GHz
State 3 (1,1)	D1 & D2 ON	1.2 GHz
Null state (0,0)	D1 & D2 OFF	2.1 GHz, 6.8 GHz

B. VSWR

The Voltage Standing Wave Ratio (VSWR) is obtained in minimum level in the permissible range (i.e.) below 2 for all the four switching condition of the diode D1 and D2. Hence, the simulated and measured result of the N shaped antenna for the null state is shown in the below Fig. 5.

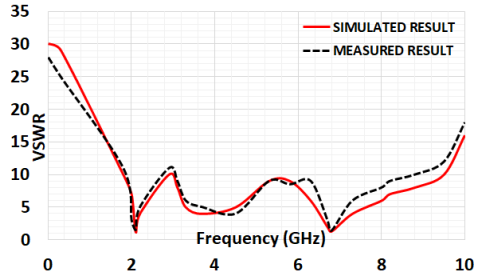

Fig. 5. Simulated and measured VSWR for null state.

C. Radiation pattern

The radiation pattern of proposed antenna in E-plane (x-z plane) and H-plane (y-z plane) at 2.1 GHz in null state is shown in Figs. 6 (a) and 6 (b) and also the 3-Dimensional radiation pattern is shown in Fig 7. Bi-directional radiation pattern is seen in both E- and H-plane of the proposed antenna in null state. Since the antenna has reconfigurable property, the radiation pattern will remain unchanged even though the operating frequency of the antenna is different.

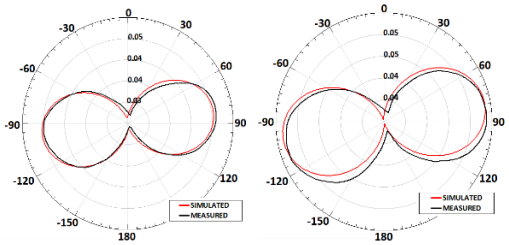

(a) (b)

Fig. 6. Radiation pattern at 2.1 GHz in null state: E-plane (x-z plane), and (b) H-plane (y-z plane).

D. Gain

The simulated and measured gain plot for all the switching states are shown in the Fig. 8. The observed discrepancy between simulated and measured curve is

mainly due to soldering effect of PIN diode. Table 2 shows the gain value obtained through simulation and measured in its operating frequency.

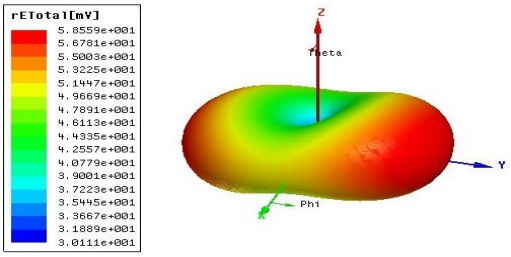

Fig. 7. Three-dimensional radiation pattern at 2.1 GHz.

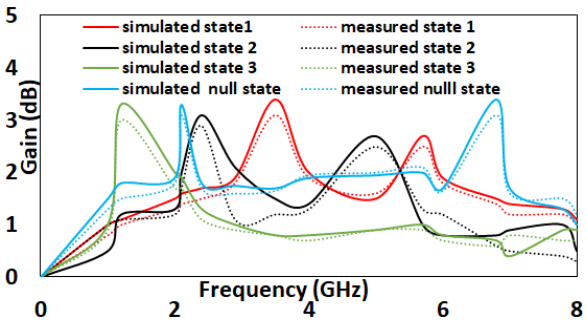

Fig. 8. Simulated vs. measured gain plot.

Table 2. Comparison of gain in various switching state

Diode State	Operating Frequency	Gain Simulated	Gain Measured
State 1	3.5 GHz	3.4 dB	3.1 dB
	5.7 GHz	2.7 dB	2.5 dB
State 2	2.4 GHz	3.1 dB	2.9 dB
	5 GHz	2.7 dB	2.5 dB
State 3	1.2 GHz	3.3 dB	3 dB
Null state	2.1 GHz	3.3 dB	2.9 dB
	6.8 GHz	3.4 dB	3.1 dB

V. ANTENNA COMPARISON

The obtained gain response of the proposed antenna design is stable (≈3dB) for all the switching states where as other antenna designs will not have such a kind of performance efficiency. The combined unit of proposed antenna with microcontroller is compact in size when compared with that of the existing methods and design standards [1], [9].

VI. CONCLUSION

In this paper, frequency reconfigurable N-shaped antenna for wireless communication application has been proposed and successfully implemented. The proposed antenna works on various wireless bands such as 3.5 GHz (WiMAX), 2.4 GHz (WLAN), 1.2 GHz (GPS), 2.1 GHz (UMTS) respectively. Two PIN diodes are automatically switches the different frequency band using Arduino board. Hardware prototype is tested in Lab setup with VNA. The radiation pattern of the antenna remains same for all the switching states of the diode and the antenna gain has been realized with maximum 3.4 dB and minimum of 2.7 dB gain. The measured results closely track the simulation result and confirms the antenna configuration.

REFERENCES

[1] C. G. Christodoulou, Y. Tawk, S. A. Lane, and S. R. Erwin, "Reconfigurable antennas for wireless and space applications," *Proceedings of the IEEE*, vol. 100, no. 7, pp. 2250-2261, 2012.

[2] N. J. Shimu and A. Ahmed, "Design and performance analysis of rectangular microstrip patch antenna at 2.45 GHz," In *Informatics, Electronics and Vision (ICIEV), 2016 5th International Conference on*, *IEEE*, pp. 1062-1066, 2016.

[3] P. K. Li, Z. H. Shao, Q. Wang, and Y. J. Cheng, "Frequency and pattern reconfigurable antenna for multistandard wireless applications," *IEEE Antennas and Wireless Propagation Letters*, vol. 14, pp. 333-336, 2015.

[4] V. Arun and L. R. Karl Marx, "Micro-controlled tree shaped reconfigurable patch antenna with RF-energy harvesting," *Wireless Personal Communications*, vol. 94, no. 4, pp. 2769-2781, 2017.

[5] N. Ojaroudi, S. Amiri, and F. Geran, "A novel design of reconfigurable monopole antenna for UWB applications," *Applied Computational Electromagnetics Society Journal*, vol. 28, no. 7, 2013.

[6] R. Tandon and T. Singh, "Varactor diode loaded reconfigurable patch antenna with adjustable slots," *International Journal of Computer Applications*, vol. 128, no. 14, pp. 36-39, 2015.

[7] K. Opalli, E. Erdil, O. A. Civi, S. Demir, S. Koc, and T. Akin, "Tunable dual-frequency RF MEMS rectangular slot ring antenna," *Sensors and Actuators A: Physical*, vol. 156, no. 2, pp. 373-380, 2009.

[8] J. Costantine, Y. Tawk, S. E. Barbin, and C. G. Christodoulou, "Reconfigurable antennas: Design and applications," *Proceedings of the IEEE*, vol. 103, no. 3, pp. 424-437, 2015.

[9] I. Rouissi, J. M. Floc'h, H. Rmili, and H. Trabelsi, "Design of a frequency reconfigurable patch antenna using capacitive loading and varactor diode," In *2015 9th European Conference on Antennas and Propagation (EuCAP), IEEE*, pp. 1-4, 2015.

[10] V. Rajeshkumar and S. Raghavan, "A compact frequency reconfigurable split ring monopole antenna for WLAN/WAVE applications," *Applied Computational Electromagnetics Society Journal*, vol. 30, no. 3, 2015.

Study of Phase and Patterns Characteristics of a Sub-Wavelength Broadband Reflectarray Unit Element Based on Triple Concentric Circular-Rings

Javad Nourinia, Changiz Ghobadi, Bahman Mohammadi, and Farzad Alizadeh

Department of Electrical Engineering
Urmia University, Urmia, WA 5756151818, Iran
{j.nourinia, ch.ghobadi, b.mohammadi, fa.alizadeh}@urmia.ac.ir

***Abstract*—**In this paper, phase and patterns characteristics of a sub-wavelength broadband reflectarray (RA) unit element are propounded. The unit element consists of triple concentric circular-rings on the Rogers 4003 substrate (H_2) that provide a nearly 615˚ linear phase range. To obtain a phase curve with a lower slope, a 3 mm thick Foam (H_1) is used and backed by a ground plane. A complete investigation analysis has been done to study the phase and patterns characteristics of the proposed sub-wavelength RA unit element. Results indicate that not only the incidence angle alter the element reflection phase, but also for oblique incidence, the element pattern deforms. It is shown, for sub-wavelength elements the combined effects of the mentioned factors are less severe.

***Index Terms* —** Broadband, concentric rings, patterns characteristics, unit element.

I. INTRODUCTION

A microstrip RA antenna consists of an array of microstrip patches and an illuminating feed antenna [1]-[3]. In the design of RA antenna, one of the most important issues is to achieve a phase shift of more than 360° to insure the required phase compensation. Different variations of phasing methods for a microstrip RA have been introduced. These include multilayer stacked patches [1], aperture coupled designs [1] and single layer multi-resonant elements [2].

II. DEISGN & CONFIGURATION

The layout of the proposed unit element is displayed in Fig. 1. The phase-shift mechanism is obtained by variation of diameter of rings. It consists of three concentric circular rings, where the radius of inner side of the ring is equal to the radius of the outer side of the ring multiplied by the factor of K_i. These elements are etched on a substrate with permittivity (ε_r) of 3.55 and thickness (H_2) of 0.813 mm. An element spacing of 15 mm (0.5 λ_0 at 10 GHz) is used to avoid grating lobes. To obtain a smoother phase curve, a Foam gap (H_1=3 mm) is considered between the substrate and the ground plane [4]. All the optimized parameters are specified as follows: $K_1 = 0.25$, $K_2 = 0.4$, $K_3 = 0.55$, $K_4 = 0.7$, $K_5 = 0.85$, $D = 2R$.

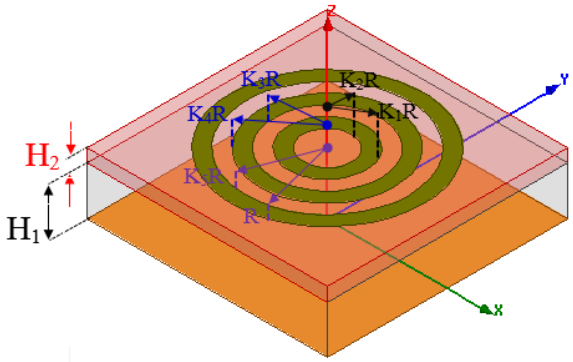

Fig. 1. Geometry of the triple concentric circular-rings.

In [5] and [6], four parameters presented to investigate the element efficiency. In this paper, we further dig into the range (ψ) and variation (β) of the reflection phase that affects the directivity [1]; the sensitivity to fabrication tolerances (σ) that affects the quantization errors [3]; and the phase variation rate versus frequency of the phase curve relative to the RA elements (α, dispersion [2]) that influences the gain bandwidth [6]. In this work, the polarization of the incident and reflected waves are the θ-polarized, that have the electric fields parallel to the plane of incidence (x-z plane) with E_x and E_z components and the magnetic field transverse to it (TM case) [7]. The mode to consider this scanning is the TM_{00} mode which is the zeroth-order Floquet modes and, therefore, the conventional plane wave [1].

In Fig. 2, the phase responses are plotted for λ/2 unit-element. Figure 2 (a) shows that incorporating of multi-resonance elements eases to reach wide range phase. Here, the bandwidth of the designed RA element is defined based on the evaluation of the frequency range by normalizing all the curves with respect to the central frequency (10 GHz), apart from a margin error $\Delta\psi$ which equals to ±45˚ [5]. As it can be observed, the resulting

Submitted On: January 27, 2017
Accepted On: September 22, 2017

bandwidth is equal to the value of about 6%, where the lower (9.7 GHz) and upper (10.3 GHz) bounds of bandwidth can be identified by dashed lines on Fig. 2 (c). Also, the bandwidth can be obtained by the frequency range within which all the phase curves computed for different values of the element size D are almost parallel [6].

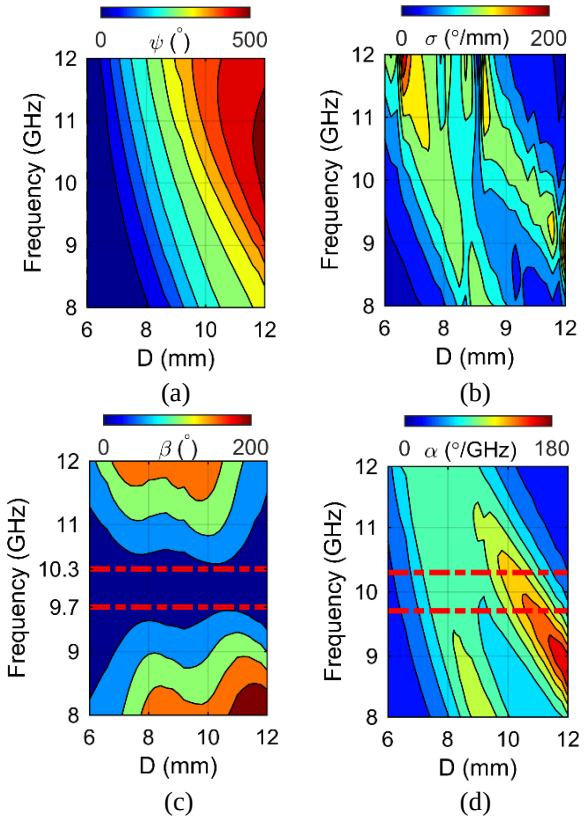

Fig. 2. The reflection phase characteristics of the λ/2 unit-element: (a) ψ, (b) σ, (c) β, and (d) α.

III. RESULTS & DISCUSSION

All elements in the RA must have proper spacing between adjacent elements in order to avoid the grating lobes in the radiation pattern. The element spacing should be governed by the following conventional array equation [1, 8]:

$$\frac{d}{\lambda} \le \frac{1}{\sqrt{\varepsilon_r} + \sin\theta}, \tag{1}$$

where d is the element spacing or unit cell size, ε_r is the relative dielectric constant and θ is either the incident angle from the feed or the main beam tilt angle from the broadside direction, whichever is larger. λ is the free-space wavelength of the highest frequency in the application. Offset-fed reflectarrays are more prone to grating lobe formation, in case the element spacing is much larger than 0.5 λ_0.

Another fundamental scanning property typical of phased arrays is known as scan blindness. It is caused by the resonance phenomenon that occurs when surface waves are excited in synchronism with the Floquet modes of the periodic structure [9]-[10]. Scan angle depends on the substrate thickness, the substrate relative permittivity and the inter-element spacing. The scan blindness occurs before the onset of the grating lobe, requiring the re-calculation of the element spacing to maintain keeping the scan blindness out of the required scanned area. The presence of the TM_0 surface wave causes scan blindness only in the E-plane [10]. The approximate angle at which scan blindness occurs is closer to broadside by the angle θ_{sc}, where

$$\theta_{SC} = \sin^{-1}\left(\frac{\beta_{SW}}{\kappa_0} - 1\right), \tag{2}$$

where θ_{sc} is the difference in angle between the onset of the grating lobe (1) and scan blindness, β_{sw} is the propagation constant of the surface wave TM_0, and K_0 is the free-space propagation constant. The value of the propagation constant for the dominant surface wave mode, TM_0, in a grounded-dielectric substrate, is given by the first root of the function $T_m(\beta)$ [9]. The implication of the phenomenon of scan blindness is to force a re-calculation of the element spacing, such that the scan blindness is out of the required scan area.

To improve the gain bandwidth of the structure [6, 11] and lower quantization phase error [3], sub-wavelength unit elements have been presented that have sizes and periodicity below the typical λ/2 spacing. In Fig. 3, the phase response is plotted for λ/4 unit-element. It is evident (Fig. 3 (a)) that the achievable reflection phase range decreases with spacing reduction. It is noticed in Fig. 3 (b) that the phase curves feature more linear behavior and are less sensitive to the size variation with the decrease of the element spacing [11]. Therefore, a good manufacturing tolerance is expected to be obtained with sub-wavelength elements. An impressive bandwidth improvement, from 6% to 13% around the design frequency f_0=10 GHz, is observed when decreasing the inter-element spacing from $0.5\lambda_o$ to $0.25\lambda_o$. Notice also the obvious similarity between the sensitivity to size (Fig. 3 (b)) and frequency dependency of dispersion (Fig. 3 (d)) in sub-wavelength element, confirming that dispersion and fabrication tolerance are deeply associate quantities. There is a similar lower sensitivity to the incidence angle of the incoming wave for the reduced spacing, as can be gleaned from Figs. 4 (a) and (b), which apply to the $\varphi_{inc} = 0^\circ$ case. The λ/2 spacing case in Fig. 4 (a) is more dependent on the value of the θ_{inc} than the reduced spacing λ/4 case in Fig. 4 (b), for large incidence angles [7].

Figures 5 (a)-(c) show the element patterns characteristics for different values of inter-element spacing at different frequencies. It can be seen that the

variations of element patterns for H-plane (y-z plane) are larger than E-Plane (x-z plane) case. Clearly, such variations are smaller for sub-wavelength RA elements than half-wavelength ones. It can be gleaned from Fig. 5, that the element pattern at H-plane for sub-wavelength case is more dependent on the value of the frequency. This observation stems from the fact that at frequencies below 10 GHz (the center-frequency), like 9 GHz, the element spacing becomes a smaller fraction of the wavelength compared to what it is at 10 GHz.

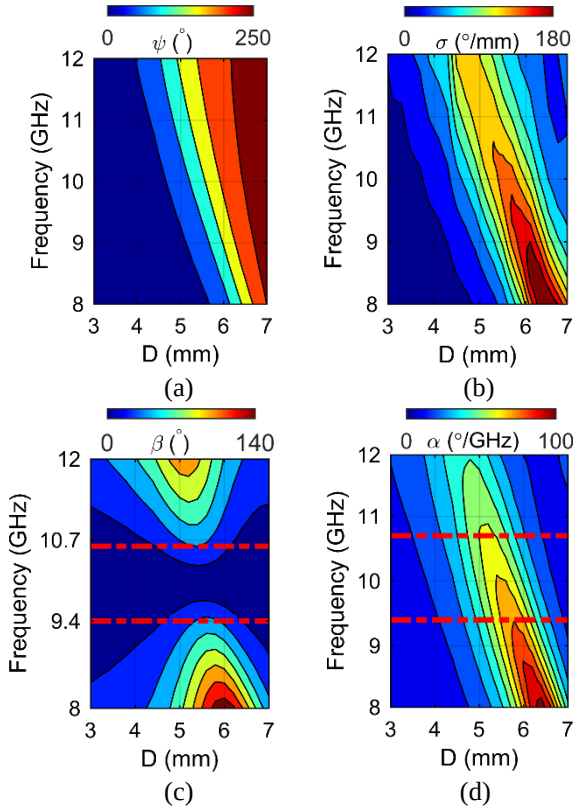

Fig. 3. The reflection phase characteristics of the λ/4 unit-element: (a) ψ, (b) σ, (c) β, and (d) α.

Figures 6 (a)-(b) show the element patterns characteristics for different values of inter-element spacing at different oblique incidence angles. It is immediately noticed that there is a narrowing of the element beamwidth when θ_{inc} increases from zero. Furthermore, the element pattern becomes deformed. Both beamwidth narrowing and deformation effects become less severe for the sub-wavelength lattice situation, therefore, one more reason for the superior behavior of sub-wavelength reflectarrays. The element patterns are important both from the point of view of coupling of the feed field to the elements, and the reradiated field from the elements [7].

The current amplitude distribution in the substrate region below the ring elements, at different frequencies is displayed in Fig. 7, when it is excited by an x-pol plane wave at normal incident angle for the element with different inter-element spacing. It can be noticed that the intense resonation occurs alongside the gap between the inner and outer rings [12]. In [12], it is shown that these radiating edges act as secondary sources and reradiates the required reflection phase. It is also observed that at λ/2 unit elements these currents are more dominant than at λ/4 sizes which indicates that the sub-wavelength unit elements have lower loss and more total performance [11-12].

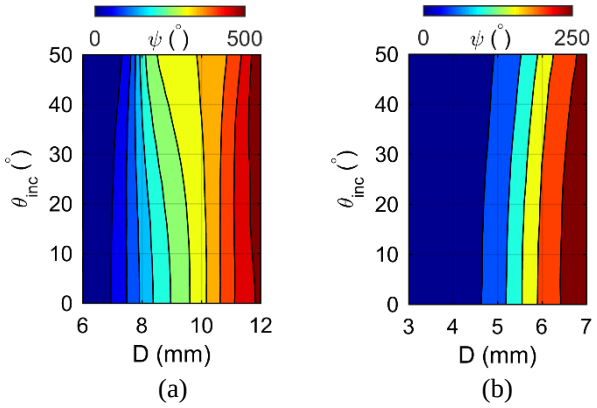

Fig. 4. The reflection phase characteristics at 10 GHz: (a) λ/2 unit-element, and (b) λ/4 unit-element.

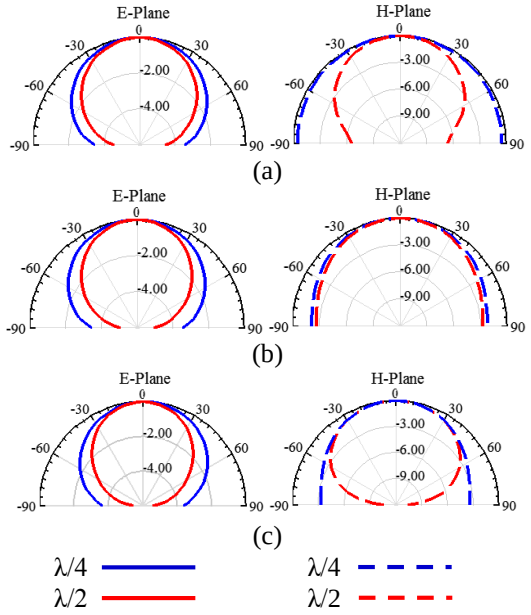

Fig. 5. Element patterns for different inter-element spacing: (a) 9 GHz, (b) 10 GHz, and (c) 11 GHz.

IV. CONCLUSION

In this paper, a sub-wavelength broadband RA unit element based on triple concentric circular-rings is evaluated. A complete investigation has been done

to study the phase and patterns characteristics of the proposed sub-wavelength RA unit element for oblique incidence angles. It is shown that the incidence angle alters the element reflection phase and the element patterns, but for sub-wavelength elements these effects are less intensive.

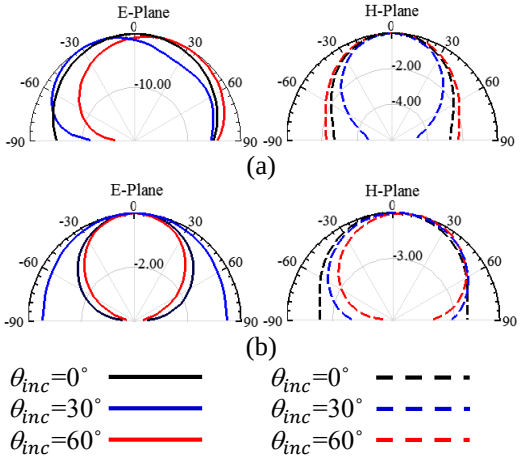

Fig. 6. Element patterns for different θ_{inc}: (a) λ/2 unit-element, and (b) λ/4 unit-element.

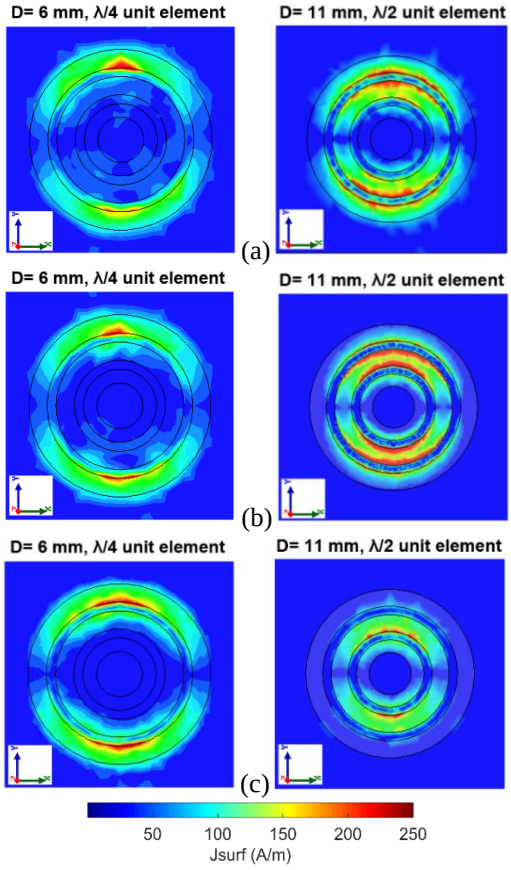

Fig. 7. Current distribution for normal incidence at: (a) 9 GHz, (b) 10 GHz, and (c) 11 GHz.

REFERENCES

[1] J. Huang and J. A. Encinar, *Reflectarray Antennas*. New York: IEEE/John Wiley & Sons, 2008.

[2] J. Shaker, M. R. Chaharmir, and J. Ethier, *Reflectarray Antennas, Analysis, Design, Fabrication, and Measurement*. Boston, London: Artech House, 2013.

[3] P. Nayeri, F. Yang, and A. Z. Elsherbeni, *Reflectarray Antennas: Theory, Designs, and Applications*. IEEE-Wiley, 2017.

[4] M. E. Bialkowski and K. H. Sayidmarie, "Investigations into phase characteristics of a single-layer reflectarray employing patch or ring elements of variable size," *IEEE Trans. Antennas and Prop*., vol. 56, no. 11, pp. 3366- 3372, Nov. 2008.

[5] M. Bozzi, S. Germani, and L. Perregrini, "Performance comparison of different element shapes used in printed reflectarrays," *IEEE Antennas and Wireless Prop. Letters*, vol. 2, pp. 219-222, 2003.

[6] F. Venneri, S. Costanzo, and G. Di Massa, "Bandwidth behavior of closely spaced aperture-coupled reflectarrays," *International Journal of Antennas and Propagation*, vol. 2012, Article ID 846017, July 2012.

[7] E. R. F. Almajali and D. A. McNamara, "Angle of incidence effects in reflectarray antenna design: Making gain increases possible by including incidence angle effects," *IEEE Antennas and Propagation Magazine*, vol. 58, no. 5, pp. 52-64, Oct. 2016.

[8] Y. Fujii, K. Ikarashi, Sh. Makino, T. Hirota, K. Noguchi, and K. Itoh, "High-efficiency and low-side-lobe reflectarray antenna," *Proceedings of ISAP 2014*, Kaohsiung, Taiwan, Dec. 2-5, 2014.

[9] D. M. Pozar and D. H. Schaubert, "Scan blindness in infinite phased arrays of printed dipoles," *IEEE Trans. Antennas Propag*., vol. 32, pp. 602-610, June 1984.

[10] P. D. Patel, "Approximation location of scan-blindness angle in printed phased arrays," *IEEE Antennas and Propagat. Magazine*, vol. 34, pp. 53-54, Oct. 1992.

[11] P. Nayeri, F. Yang, and A. Z. Elsherbeni, "Bandwidth improvement of reflectarray antenna using closely spaced elements," *PIER*, vol. 18, pp. 19-29, 2011.

[12] H. Rajagopalan, S. Xu, and Y. Rahmat-Samii, "On understanding the radiation mechanism of reflectarray antennas: An insightful and illustrative approach," *IEEE Antennas and Propagation Magazine*, vol. 54, no. 5, pp. 14-38, 2012.